Lawrence Berkeley National Laboratory
Lawrence Berkeley National Laboratory

Title
DENSITY VARIATION IN THE ELECTRON-HOLE LIQUID IN STRESSED GERMANIUM AND SILICON

Permalink
https://escholarship.org/uc/item/22w74127

Author
Kelso, Susan Mary

Publication Date
1979-08-01

eScholarship.org Powered by the California Digital Library
University of California

12/18

UC-34

LBL-8786 c.1

Lawrence Berkeley Laboratory

UNIVERSITY OF CALIFORNIA

Materials & Molecular Research Division

DENSITY VARIATION IN THE ELECTRON-HOLE LIQUID IN STRESSED GERMANIUM AND SILICON

Susan Mary Kelso
(Ph.D. thesis)

RECEIVED
LAWRENCE
BERKELEY LABORATORY

FEB 21 1980

LIBRARY AND
DOCUMENTS SECTION

August 1979

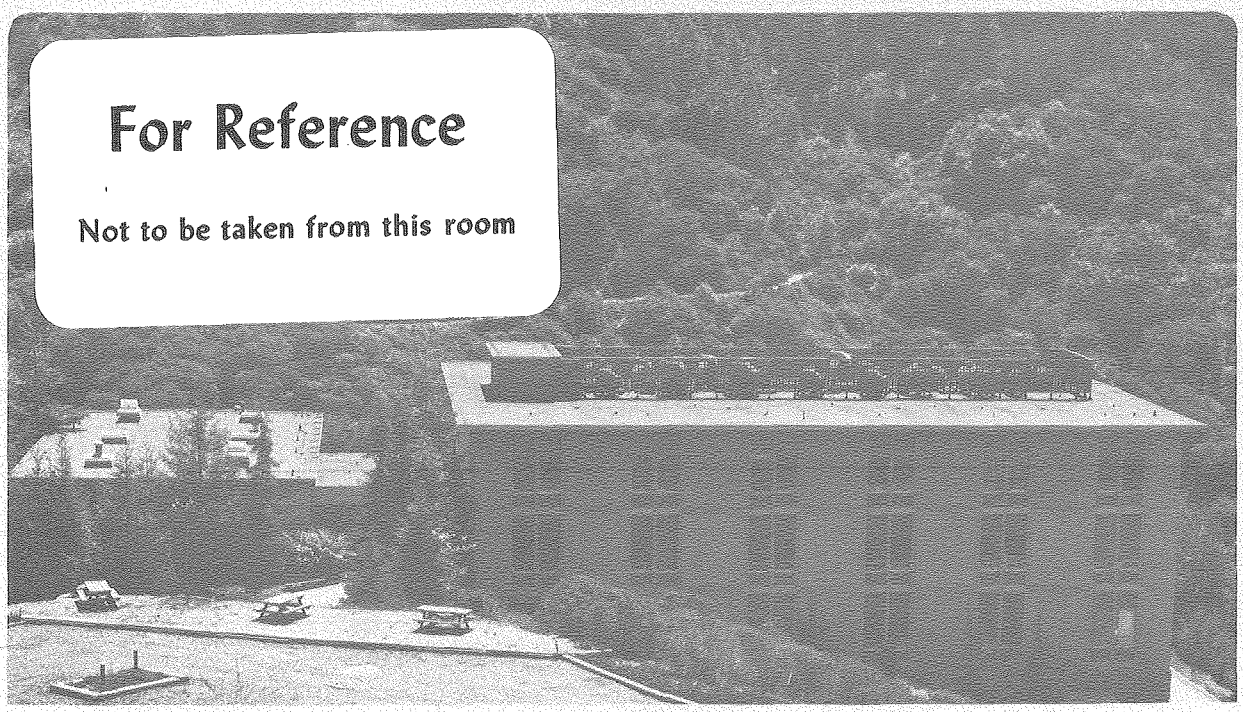

Prepared for the U.S. Department of Energy under Contract W-7405-ENG-48

LBL-8786 c.1

LEGAL NOTICE

This report was prepared as an account of work sponsored by the United States Government. Neither the United States nor the United States Department of Energy, nor any of their employees, nor any of their contractors, subcontractors, or their employees, makes any warranty, express or implied, or assumes any legal liability or responsibility for the accuracy, completeness or usefulness of any information, apparatus, product or process disclosed, or represents that its use would not infringe privately owned rights.

DENSITY VARIATION IN THE ELECTRON HOLE-LIQUID IN STRESSED GERMANIUM AND SILICON

TABLE OF CONTENTS

1. INTRODUCTION 1

2. CALCULATION OF PROPERTIES OF THE ELECTRON HOLE-LIQUID IN UNIAXIALLY STRESSED Ge AND Si 10

21. Introduction 10

22. Calculation of the Free Energy at Arbitrary Stress 15

22.1. Basic Thermodynamics 16

22.2. Hole Masses 23

22.3. Luminescence Lineshape 30

22.4. Calculation of the Kinetic Energy 35

22.5. Coulomb Energy 37

23. Results: Ground State Properties 42

23.1. Comparison of Models 43

23.2. Possible Phase Transition in Ge Involving the Electrons 49

23.3. Comparison with Experiment: The Approach to the Infinite Stress Limit 54

24. Results: Finite Temperature 64

24.1. Low Temperature Variations; Compressibility 65

24.2. The Critical Point; Phase Diagram 75

Appendix 2.1. Computer Program for the Hole Masses 87

Appendix 2.2. Calculation of the Kinetic Energy at Finite Temperature 94

3. EXPERIMENTAL DETAILS 96

31. Samples 96

32. Overall Setup 101

33. Detector 109

34. Imaging Technique 115

4. PROPERTIES OF THE STRAIN-CONFINED ELECTRON-HOLE LIQUID IN Ge . . . 125

41. Introduction 125

42. Spectroscopy of the Recombination Luminescence 129

42.1. The Liquid-Gas Phase Transition 129

42.2. Stress Dependence of the Luminescence 132

42.3. Luminescence Linewidth; Compression of the Strain-Confined Liquid 137

42.4. Determination of the Pair Density 140

42.5. Conduction Valley Degeneracy 144

43. Lifetime and Temperature Dependence 147

43.1. Enhanced Lifetime for the Strain-Confined Liquid . . . 147

43.2. Temperature Dependence of the Luminescence 150

44. Luminescence Profiles 151

44.1. Spatial Profiles of γ-Drops 152

44.2. Comparison with Clouds of α-Drops 156

44.3. Kinetics of the Luminescence Profiles 160

44.4. Magnetostriction of γ-Drops 162

5. DENSITY VARIATION AND COMPRESSIBILITY OF THE STRAIN-CONFINED ELECTRON-HOLE LIQUID IN Ge 166

51. Introduction 166

52. Characterization of the Strain Well 170

53. Theory 176

53.1. Prediction of the Variation in Pair Density with Position 176

53.2. Manifestation of the Density Variation in Luminescence Experiments 193

54. Experimental Results and Discussion 205

55. Density Dependence of the EHL Lifetime 218

6. SUMMARY AND CONCLUSIONS 230

ACKNOWLEDGMENTS 235

REFERENCES 237

TABLES 269

FIGURE CAPTIONS 280

FIGURES 301

DENSITY VARIATION IN THE ELECTRON-HOLE LIQUID IN STRESSED GERMANIUM AND SILICON

Susan Mary Kelso

Department of Physics
University of California
Berkeley, California 94720
and
Materials and Molecular Research Division
Lawrence Berkeley Laboratory
Berkeley, California 94720

ABSTRACT

A detailed study is presented of the variation in electron-hole pair density in the electron-hole liquid (EHL) in stressed Ge and Si. First, the variation of the density and other properties of the EHL is studied theoretically as a function of uniaxial stress in both Ge and Si. Second, the variation of the density with position is studied both theoretically and experimentally in the strain-confined electron-hole liquid (SCEHL) in Ge.

The first study represents an attempt to understand theoretically how EHL properties vary between their zero- and infinite-stress values, both at zero and at finite temperature, as continuous functions of stress, for ⟨111⟩ stress in Ge and ⟨100⟩ stress in Si. These properties include the ground state (T=0) equilibrium density, the ground state pair energy, the electron and hole Fermi energies, the luminescence linewidth, the electron-hole drop charge, and the liquid compressibility. The possibility

of a phase transition is discussed for the case of Ge; this phase transition would occur as the stress is varied, as the upper electron valleys become depopulated. The approach to the infinite-stress limit is discussed. The importance of including the nonparabolic valence band density of states in the fitting of the luminescence lineshape is emphasized. Theoretical results for the systematic low-temperature variation of the liquid density, Fermi energy, and chemical potential are presented. The high-temperature properties are also discussed, including the critical temperature and density. These theoretical results are found to be in reasonably good agreement with the available experimental data. The study of the EHL under uniform stress is a necessary prelude to the understanding of the EHL under nonuniform stress, i.e., confined in a strain well.

The properties of the strain-confined EHL are determined from measurements of the recombination luminescence with spatial, time, and spectral resolution, as a function of excitation level, magnetic field, temperature, and stress. A single drop of EHL forms in the strain well, with radius as large as $R \approx 0.7$ mm and volume greater than 1 mm^3. At high excitation levels the luminescence linewidth is found to increase and the recombination lifetime is found to decrease, indicating that the liquid becomes compressed. For smaller drop sizes ($R \lesssim 150$ μm), however, the equilibrium properties of the liquid may be studied: from a fit of the luminescence lineshape the density is found to be $n_o = 0.50 \pm 0.05 \times 10^{17}$ cm^{-3} for typical moderate stresses, and the lifetime is found from pulsed experiments to be $\tau \approx 500$ μsec. The enhanced lifetime is understood qualitatively as a result of the reduced density (compared to the values for unstressed Ge), while the reduction in

density is due to the stress. The size, shape, and kinetics of drops confined in strain wells are contrasted with the size, shape, and kinetics of clouds of EHD in unstressed Ge.

The compression of the SCEHL at higher excitation levels is investigated in detail. It is shown theoretically that the density should vary with position, with the magnitude of the variation increasing with drop size. Experimentally, density profiles are measured using luminescence spatial profiles (box scans) and an Abel transform. The density is found to be largest at the center of the drop, decreasing at the drop surface, as predicted theoretically. The density at the center of the drop is found to increase with drop size from the equilibrium value by approximately a factor of three, in agreement with theory. The liquid chemical potential is measured as a function of density by varying the drop size, providing a very stringent test of the many-body theories used to describe the EHL. The compressibility of the SCEHL is measured to be $K_T = 0.058 \, ^{+0.024}_{-0.012}$ cm^2/dyne. Finally, the liquid lifetime is studied as a function of density. The lifetime changes more slowly than the density, indicating that a density independent decay mechanism is significant. In addition, the Auger recombination coefficient is significantly reduced from its value in unstressed Ge.

CHAPTER 1. INTRODUCTION

When light is incident on a crystal of Ge electron-hole pairs are created. Electrons excited into the conduction band relax to the conduction band minima at the L point in the Brillouin zone, while holes relax to the valence band maxima at the center of the Brillouin zone (see Fig. 1.1). These carriers can move freely through the crystal. Because electrons and holes are oppositely charged, at low temperatures they bind into a hydrogen-like species via their Coulomb interaction. Such an electron-hole pair is called a free exciton (FE). For Ge the excitonic Bohr radius is large, $a_x \sim 100$ Å, so that the exciton wave function extends over many lattice sites; in this case the exciton is called a Mott-Wannier exciton.

At sufficiently low temperatures and high exciton concentrations, the exciton gas actually condenses into a liquid phase. The phase separation is analogous to that found in ordinary gas-liquid systems. In the liquid phase, however, the electrons and holes are no longer bound into pairs, thus the liquid phase consists of a metallic electron-hole plasma called the electron-hole liquid (EHL). This situation was suggested in 1968 by Keldysh,[1.1] in his interpretation of photoconductivity experiments by Asnin et al.[1.2] Keldysh's insight has since been confirmed both experimentally and theoretically. These studies of electron-hole droplets (EHD) have been the subjects of several reviews,[1.3-1.6] particularly the more recent articles by Hensel et al.[1.5] and by Rice.[1.6]

In unstressed Ge, a cloud of EHD is formed, each drop having a radius[1.7, 1.8] ≈1-5 μm and e-h pair density[1.9-1.12] $n \approx 2.3 \times 10^{17}$ cm^{-3}. Because an electron-hole pair (either in an exciton or in the liquid) represents an excitation of the crystal, the pair has a finite lifetime. Due to the indirect nature of the band gap in Ge, however, the lifetimes are relatively long: the droplet lifetime is ≈40 μsec, (Refs. 1.10, 1.13, and 1.14), while the exciton lifetime is ≈7 μsec (Refs. 1.3, 1.14, 1.15). As shown in Fig. 1.1, a free exciton is bound with respect to free carriers by the exciton binding energy[1.16] $E_x \approx 4$ meV. The liquid ground state energy per pair[1.11, 1.12] $|f_G|$ is ≈6 meV below that of free carriers. Thus the condensation energy[1.11, 1.12] of excitons into the liquid $\phi \approx 2$ meV. This gas-liquid system has a phase diagram, with a critical temperature $T_c \sim 6.5$ K.[1.17, 1.18] Hysteresis has been observed[1.19-1.21] in EHD thresholds, due to the surface tension[1.20-1.22] $\sigma \simeq 2.6 \times 10^{-4}$ erg/cm^2.

A convenient method to observe FE and EHD and measure their properties is to collect their characteristic recombination radiation lines at $\lambda \approx 1.75$ μm. The study of this luminescence yields a great deal of information about the FE-EHD system. Because of the indirect gap, the radiative recombination of an e-h pair is accompanied by the emission of a phonon. In Ge the LA phonon-assisted transition has the most intense luminescence and is studied the most. Figure 1.2 shows a luminescence spectrum[1.20] from unstressed ultrapure Ge at 2.10 K. At the selected excitation level, the FE and EHD peak intensities are nearly equal (LA phonon assisted). The bump on the low energy edge of the EHD line is the TO replica of the FE line. The EHL Fermi energy

$E_F \approx 6$ meV[1.11, 1.12] and condensation energy ϕ and the FE ground state energy E_x are indicated. The energies E_F and ϕ may be obtained from a careful analysis of the luminescence lineshapes; the equilibrium density is obtained from the Fermi energy. The experimental values given above are in good agreement with theory.[1.23-1.26, 1.6] In addition to this spectral information, the luminescence can be studied as a function of other parameters, such as position within the crystal, time, temperature, magnetic field, and stress.

The above discussion has dealt specifically with Ge and is now generalized slightly to include Si. This is an indirect gap material similar to Ge, except that the conduction band minima are located along the ⟨100⟩ directions, approximately 86% of the way out to the Brillouin zone edge.[1.27] In both Ge and Si, near the conduction band minima the surfaces of constant energy are ellipsoids of revolution. Due to symmetry, in unstressed Ge there are four equivalent conduction band minima, while in Si there are six. Two valence bands corresponding to light and heavy holes are degenerate at the zone center. Away from $\vec{k} = 0$, however, the constant-energy surfaces are warped, due to the strong interaction between the bands. A third valence band is split from the light and heavy hole bands, due to the spin-orbit interaction; the effects of this band can often be neglected in EHL calculations.

When uniaxial stress is applied to Ge or Si along one of the principal crystallographic directions (⟨111⟩, ⟨100⟩, or ⟨110⟩), changes occur in the band structure. For ⟨111⟩ compressional stresses in Ge, one conduction band is lowered in energy while the other three are raised, relative to the mean. For ⟨100⟩ compressional stresses in Si, two conduction bands are lowered and four are raised. These two cases are

illustrated in Fig. 1.3. In both cases, the valence bands are split and further warped by the stress.[1.28-1.31] For finite values of the stress, it is convenient[1.32] to designate the electronic configuration as Ge(ν_e:ν_h) or Si(ν_e:ν_h), where ν_e and ν_h are the number of electron bands and hole bands respectively whose minima are located below the EHL Fermi level. Thus, for example, unstressed Ge has the configuration Ge (4:2) while unstressed Si is Si (6:2). In both of the cases illustrated in Fig. 1.3, the conduction band degeneracy is lifted at a lower value of the stress than where the valence band degeneracy is lifted, due to the different electron and hole deformation potentials.[1.29] It is convenient to designate the stress at which the upper conduction band minima pass through the electron Fermi level as σ_e; it is shown in this thesis that $-\sigma_e \approx 2.6$ kgf/mm^2 for ⟨111⟩ stress in Ge and $-\sigma_e \approx 10$ kgf/mm^2 for ⟨100⟩ stress in Si. Here the convention is followed that compressional stresses are negative, and 1 kgf = 9.80665 Newton. Similarly, the stress at which the light hole band minimum passes through the hole Fermi level is designated σ_h; it is shown in this thesis that $-\sigma_h \approx 6.5$ kgf/mm^2 for ⟨111⟩ stress in Ge and that $-\sigma_h \approx 36$ kgf/mm^2 for ⟨100⟩ stress in Si. In addition, certain theoretical calculations have been performed[1.33, 1.34] for an idealized intermediate stress case in which the electrons are treated as for infinite stress while the holes are treated as for zero stress. This case does not correspond exactly to any value of the stress (it most closely approximates the stress σ_e), but may be referred to as the idealized Ge (1:2) or Si (2:2) system.

For the case of infinite uniaxial compression, the band structure again simplifies: one conduction band is occupied in Ge and two in Si, for the stress directions in Fig. 1.3; in addition, the single valence band becomes ellipsoidal at infinite stress. Indeed, due to symmetry considerations, the band structure becomes as simple as possible for these stress directions. Early theoretical treatments[1.23, 1.24] gave different conclusions about the existence of the EHL at infinite stress, i.e., whether or not the liquid would be bound with respect to free excitons. The most sophisticated treatment[1.26, 1.35] predicts that the EHL should be bound at infinite stress, in agreement with the experimental indications.[1.36, 1.10, 1.37-1.42]

This thesis presents the results of a detailed calculation[1.43] of properties of the electron-hole liquid in uniaxially stressed Ge and Si, for the stress directions of Fig. 1.3. This represents an attempt to understand how the properties vary between their zero- and infinite-stress values, as continuous functions of stress. In particular, rather rapid changes are predicted here to occur as the upper electron valleys empty out, at stresses just below σ_e. Additionally, significant changes should occur after the valence band degeneracy is lifted at σ_h, indicating the importance of the residual valence band nonparabolicity at fairly high stresses. These calculations are performed at finite temperature, as well as for the usual simpler case at $T = 0$, in order to study the critical point and the phase diagram.

While the above studies of the EHL in uniformly stressed crystals are extremely useful in their own right, they are also necessary in the understanding of the experiments on inhomogeneously stressed Ge

performed at Berkeley.[1.44-1.50] It has been shown[1.48, 1.49] that for a suitable stress geometry, a three-dimensional energy minimum for the EHL is formed in the interior of the crystal. In this case, the photoexcited e-h pairs (free carriers, FE, and EHD) are attracted into this strain well and coalesce into a large pool of electron-hole liquid. This is referred to as either a γ-drop[1.32] or, equivalently, the strain-confined electron-hole liquid (SCEHL). The EHD in unstressed Ge are referred to as α-drops.[1.32] Figure 1.4 shows a photograph of the luminescence from such a γ-drop: the drop diameter is $\approx$1.4 mm and the volume is over 1 mm^3. The method of obtaining the photograph and the faint luminescence tail extending below the drop are discussed later in this thesis.

The strain wells which contain large drops are located in regions of the crystal where the local strain tensor is approximately equivalent to a (111) uniaxial strain.[1.48, 1.49] Hence the properties of the SCEHL, at least for small γ-drop sizes, reflect the properties of the EHL in uniformly stressed Ge. These properties are conveniently studied via the SCEHL luminescence. Measurements of the equilibrium density $n_o \approx 0.5 \times 10^{17}$ cm^{-3} and lifetime $\tau \approx 500$ μsec are described in this thesis. The reduction in the liquid density is due to the stress, and the enhancement of the lifetime is understood qualitatively in terms of density dependent recombination mechanisms. (However, some interesting questions remain in the quantitative understanding of the EHL lifetime under stress.) In addition, studies of the threshold for EHL formation and the SCEHL condensation energy are presented here, as well as studies of the luminescence as a function of drop size, position within

the drop, temperature, magnetic field, time, and stress.

The understanding and interpretation of these luminescence experiments depends critically in many cases on the fact that the SCEHL in Ge is a single entity, i.e., a single pool of liquid, not a collection of smaller droplets.[1.51] Evidence for this has come from light scattering experiments,[1.52, 1.53] in which the large-angle scattering typical of Rayleigh-Gans scattering by small drops[1.7, 1.8] vanished, leaving only an in intense absorption near $\theta = 0$. Earlier evidence came from the microwave Alfvén resonances,[1.44, 1.45, 1.48, 1.54-1.56] which occur when the drop diameter is matched to a multiple of the microwave wavelength inside the drop. (There the wavelength is much shorter than in air, due to the high dielectric constant of the metallic liquid.) The Alfvén waves require a continuous medium in which to propagate; hence if the SCEHL consisted of small drops, the resonant frequency would not be characteristic of sizes ~30-300 μm. Further evidence for a single drop is its distortion in shape in an external magnetic field.[1.57-1.59] The observation and explanation of this remarkable phenomenon, which is discussed briefly in this thesis, relies on the production and imaging of a single large drop.

There are several advantages which result either from having a single drop of EHL or from the strain confinement geometry. The internal particle dynamics can be probed, including recombination currents and carrier-carrier collision times. Because the drop exists in a strain well, the strain gradient inhibits evaporation of excitons; thus the liquid lifetime can be measured even at high temperatures. In addition, since the drop is well separated from the crystal surfaces, the decay

is studied without the complications of surface recombination. While recent experiments[1.60] have shown that the FE lifetime in unstressed Ge can be as long as 30 μsec away from the crystal surface, the exciton lifetime in the strain well has been found[1.61] to be several hundred μsec, comparable to the SCEHL lifetime. The strain well provides a very convenient method to control the spatial distribution of the photo-excited carriers: excitons (and excitonic molecules in Si[1.42, 1.62]) behave like an ideal gas. On Si this fact has enabled a detailed study of excitons and excitonic molecules in equilibrium.[1.62]

Finally, it is shown in this thesis that in large drops the e-h pair density varies with position. This remarkable situation requires a single drop confined in a strain well. The density variation increases with drop size, and extends over a factor of 3 for the largest drops studied. This provides a unique feature of the SCEHL: the liquid is compressed directly by squeezing due to the strain gradient. This is in contrast to the case in unstressed Ge, where the density can be changed only by changing the temperature[1.11] (or by completly filling a small sample,[1.63, 1.64] in which the surfaces and sample heating provide complications). The compression is studied in detail in this thesis, both theoretically and experimentally. Theoretically, the density variation can be explained straightforwardly by assuming that the chemical potential is constant throughout the drop volume. Experimentally, e-h pair density profiles are measured for single EHD. Because the density variation is so large, properties of the SCEHL can be studied as a function of density. The density dependence of the chemical potential is measured, providing a sensitive test of the many-body

theoretical calculations. The compressibility of the SCEHL is measured, and is found to be an order of magnitude greater than for the EHL in unstressed Ge. Information on the density dependence of the EHL lifetime and on the relative importance of different recombination processes is obtained and discussed. The form and magnitude of the density variations are found to be in excellent agreement with the theory presented here.

Chapter 2 of this thesis presents the calculations of the stress dependence of EHL properties for Ge and Si. Experimental details are discussed in Chapter 3, including the special imaging techniques and the detector which were necessary for the experiments. In Chapter 4 an experimental study is presented of the basic properties of the SCEHL in Ge. The theoretical and experimental studies of the density variation and compressibility of the SCEHL are presented in Chapter 5. Finally, in Chapter 6 the results are summarized and some suggestions are made for further work.

CHAPTER 2. CALCULATION OF PROPERTIES OF THE ELECTRON-HOLE LIQUID IN UNIAXIALLY STRESSED Ge AND Si

21. Introduction

The first theories of the electron-hole liquid in semiconductors[2.1-2.3] were concerned with predicting and understanding the properties for systems in which the EHL had already been observed experimentally, namely unstressed Ge and Si. However, as described in detail in Chapter 1, since the band structure becomes much simpler in Ge under infinite uniaxial ⟨111⟩ compression and in Si under infinite uniaxial ⟨100⟩ compression, these cases were also considered,[2.1-2.3] in order to make the theories more tractable. These first calculations predicted that the EHL may not be bound with respect to excitons in the infinite-stress limit in Ge, or is just barely bound. The more sophisticated calculations of Vashishta et al.[2.4] indicated that the EHL should be stable and observable in this system. The electron-hole pain density is expected to be considerably reduced compared to unstressed crystals. Vashishta, et al.[2.5, 2.6] also performed a calculation for an ideal system, in which the electrons were treated as for infinite stress and holes as for zero stress. This system was expected to be approximately valid for intermediate stresses, and the experimental findings were indeed intermediate between the zero and infinite stress theories. In addition, the effect of temperature on EHL properties was estimated,[2.7] for zero and infinite stress, using an expansion valid at low T. Several estimates were made of the critical temperature at zero[2.7-2.10] and infinite[2.7] stress. Rice[2.11] has reviewed the theory of the EHL in semiconductors.

In the meantime, some experiments[2.12-2.14] were being performed on Ge and Si uniaxially stressed along the three principal crystallographic directions. These early experiments showed the existence of the liquid and the shift of the luminescence spectra under moderate stresses but were not analyzed in enough detail to determine the properties of the EHL. Additional experiments were performed at Berkeley[2.15] on inhomogeneously stressed Ge, in which the e-h pair density was found to be reudced from its value in unstressed Ge. More recently, careful experiments[2.16-2.18] have been performed on Ge uniaxially stressed along the ⟨111⟩ direction in order to study the stress dependence of the EHL properties. Less detailed experiments have been performed on uniformly[2.19] and nonuniformly[2.20, 2.21] stressed Si (⟨100⟩ stress). Hensel et al.[2.22] have reviewed the experimental results for stressed and unstressed crystals available prior to mid-1976.

It is of course highly desirable to have a theory applicable at finite stress and finite temperatures with which to compare experimental results. A first attempt at predicting the systematic variation of the ground state (T=0) properties of the EHL in ⟨111⟩-stressed Ge was made by Markiewicz and myself.[2.23] In this paper we treated the intermediate to high stress region: the electrons were treated as for infinite stress and the stress dependence of the holes was taken into account. Thus the results of Ref. 2.23 should be valid for stresses greater (in magnitude) than σ_e, the stress at which the upper conduction bands become depopulated; $|\sigma_e| \approx 2.6$ kgf/mm^2, as will be shown.

In this chapter I present a calculation[2.24] of a number of properties of the EHL in uniaxially stressed Ge and Si both at T=0 and at finite

temperature. This is the first calculation of the systematic stress dependence of EHL properties at T=0 in Si and at finite temperature in both Ge and Si. Kirczenow and Singwi[2.25] have independently performed a similar calculation, restricted to the ground state in Ge. In addition, Liu et al.[2.26, 2.27] have performed a calculation at two values of the stress, both for Ge and Si, including a low-T expansion to estimate the critical point.

For the kinetic energy, the full stress dependence of the conduction and valence bands is included, except that the split-off valence band is ignored (as is customary for Ge and common for Si). In order to describe the nonparabolicity of the valence bands, energy-dependent hole masses are introduced.[2.23, 2.28] These density-of-states and optical masses may be useful for other types of calculations. In particular, it is emphasized here that it is necessary to fit luminescence spectra including the nonparabolicity of the valence bands. If spectra are analyzed using the infinite-stress masses, the deduced densities can be substantially in error. The Coulomb energy, which describes the interactions between the carriers, is calculated according to several models, but is believed to be nearly independent of stress, following a suggestion by Vashishta.[2.29]

A rapid change in the ground state electron-hole pair density is predicted, associated with the emptying of the upper conduction bands at the stress σ_e. The possibility of the existence of two different types of EHL, with a phase transition as a function of stress, is discussed for the case of Ge. It is noted, however, that this phase transition is

unlikely to be observed experimentally, due to the effect of the temperature. Significant changes are predicted for all properties of the EHL at stresses beyond σ_h, where the upper valence band becomes depopulated. Since no further changes take place in the number of occupied bands (i.e. the configuration), the high-stress variation of EHL properties is due entirely to the residual nonparabolicity of the valence band, which remains important after the bands are well split in energy. Because of these significant changes in EHL properties, guidelines are given for extrapolation from finite stresses to the infinite-stress limit.

For finite temperatures, both low-T and high-T limits are considered. At low temperatures, the usual[2.30] expansion for the kinetic energy of a degenerate Fermi system is valid, except at stresses very near σ_e and σ_h. The systematic low-T variation of EHL properties is disucssed, using derivatives of the free energy versus density for the ground state. In order to estimate the critical point, however, the expansion is no longer valid. Thus the kinetic energy is calculated exactly at finite temperatures. A brief discussion is presented concerning the liquid-gas phase diagram and the nature of the gas phase near the critical point, in order to assess the validity of the model used. Other topics considered briefly include the effect on EHL properties of a renormalization of carrier masses, and the possibility that several quantities may have "universal" values, independent of the system. It should be noted that the compressional stresses considered here are taken to be negative, according to convention. Stresses are expressed in kgf/mm^2, where 1 kgf = 9.80665 Newtons.

Because the band structures of Ge and Si are so similar, it was possible to use the same computer programs for both materials. Results are presented for ⟨111⟩ stress in Ge and for ⟨100⟩ stress in Si. It would be straightforward to extend the calculations to the other principal stress directions, for which there are no experimental results at the present time. The directions considered here were chosen for several related reasons. Most importantly, the band configuration at high stress becomes the simplest: one conduction band for Ge and two for Si, and one (parabolic) valence band. Because the number of occupied conduction bands is the smallest allowed by symmetry considerations, the lower band or bands have the greatest energy lowering with stress relative to the "center of mass" of the bands. For the case of a suitable inhomogeneous stress geometry,[2.31] discussed in detail in later chapters, the EHL energy is lowest in a region of local ⟨111⟩ stress for Ge and local ⟨100⟩ stress for Si. Thus the strain-confined liquid collects in a potential well in a region of the crystal with these "locally uniform" stresses. It should be noted that it is necessary to first understand the effects of uniform stress on the properties of the EHL before considering the more complicated case of inhomogeneous stress. As a result of the above considerations, a growing body of experimental results is available for Ge stressed along the ⟨111⟩ direction and Si stressed along the ⟨100⟩ direction. These experimental results are compared with the theoretical predictions made here.

This chapter is divided into several sections. The calculation of the free energy of the electrons and holes is described in Section 22,

for arbitrary stress and temperature. The hole masses are introduced and described. A discussion is presented of the luminescence linshape, including the nonparabolicity of the valence bands. Several models are introduced for the Coulomb energy, but the proposal is made of a universal Coulomb energy. The results for the ground state properties are presented in Section 23. All models are compared for the density and ground state energy, and two are selected for further detailed comparison. The stress dependence of the exciton binding energy and the binding energy of the EHL with respect to excitons are estimated. The possible phase transition associated with the depopulation of the upper electron valleys in Ge is discussed. Other systems are suggested in which this might be observed. The results are presented for the electron and hole Fermi energies and the luminescence linewidth. The charge of electron-hole drops is predicted, and the effect of mass renormalization is considered. In addition, the approach to the infinite-stress limit is discussed. The theoretical results are compared with experiment. In Section 24, the finite-temperature results are presented. The low-temperature expansion is derived and its validity is discussed. Several quantities which describe the low-T variation of EHL properties are given. The critical point is defined and calculated. The results are compared with available experimental data. Finally, some remarks are made concerning the electron-hole fluid phase diagram and the scaling of certain quantities between different systems.

22. Calculation of the Free Energy at Arbitrary Stress

The results presented in Sections 23 and 24 are derived from a calculation of the free energy per electron-hole (e-h) pair of a neutral

plasma of electrons and holes as a function of pair density, temperature, and stress. In this section the calculation of the free energy is described. We begin with a discussion of some basic thermodynamics in Section 22.1. The calculation of the energy-dependent hole masses is described in Section 22.2. A discussion of the liminescence lineshape is given in Section 22.3, since this lineshape makes important use of the hole masses. For the electron-hole liquid, the free energy F is separated into kinetic and Coulomb energy contributions:

$$F = F_{kin} + F_{Coul} \tag{2.1}$$

(the free energy is defined below in Eq. (2.3)). The calculation of the kinetic energy is described in Section 22.4, and the Coulomb energy is descussed in Section 22.5.

22.1. Basic Thermodynamics

We begin with some basic thermodynamics. Consider a system consisting of N particles in a volume V, in equilibrium with a reservoir at temperature T. In an EHD experiment $N = N_e = N_h$ is the number of e-h pairs, electrons, or holes and is determined by the excitation level; V is the effective volume accessible to the e-h pairs; and T is the carrier temperature, assumed here to be the lattice temperature. A number of thermodynamic functions may be defined for such a system. It is convenient to begin with the grand potential, which is defined[2.30] as follows:

$$\Omega \equiv -PV = U - TS - N\mu \quad . \tag{2.2}$$

Here P is the pressure, U is the total energy, S is the entropy, and μ is the chemical potential. In addition, the Helmholtz free energy

is given by:

$$F \equiv U - TS = N\mu - PV \quad , \tag{2.3}$$

where the first part is the usual definition[2.30] and the second part uses Eq. (2.2). If the parameters N, V, and T are held constant, then the most probable configuration of the system is that for which F is a minimum with respect to any internal parameter of the system.[2.30] For the case of an electron-hole liquid in a semiconductor below the critical point, the e-h pairs can be in either the liquid or gas state. Then $F = F_\ell + F_g$ is a minimum with respect to changes in N_ℓ, N_g, V_ℓ, and V_g, such that $N_\ell + N_g = N$ = constant and $V_\ell + V_g = V$ = constant. That is, from Eq. (2.3) and the thermodynamic identity the differential

$$dF = \mu_\ell dN_\ell + \mu_g dN_g - P_\ell dV_\ell - P_g dV_g - S_\ell dT_\ell - S_g dT_g = 0 \, . \tag{2.4}$$

Thus we obtain a familiar result:[2.30]

$$T_\ell = T_g \, , \qquad \mu_\ell = \mu_g \, , \qquad P_\ell = P_g \, . \tag{2.5}$$

In equilibrium the temperatures, pressures, and chemical potentials of the two phases are equal. Now in general the free energy F is a function of N, V, and T. It is convenient to introduce the free energy per pair $f \equiv F/N$ and the e-h pair density $n \equiv N/V$ and to consider variations of f with n. Thus we can make the following definitions[2.30] and simplifications:

$$P \equiv -\left(\frac{\partial F}{\partial V}\right)_{T,N} = n^2\left(\frac{\partial f}{\partial n}\right)_{T,N} \tag{2.6a}$$

$$\mu \equiv \left(\frac{\partial F}{\partial N}\right)_{T,V} = f + n\left(\frac{\partial f}{\partial n}\right)_{T,V} \, . \tag{2.6b}$$

At sufficiently low temperatures, the gas density is essentially zero, so that the gas pressure and hence the liquid pressure are zero. Thus the equilibrium density for the liquid is that density for which f is a minimum, i.e., $\left(\frac{\partial f}{\partial n}\right)_{T,N} \approx 0$ for $T \approx 0$.

The preceding discussion has been for the most general case, in which both kinetic and Coulomb energies are included. We now specialize slightly and write down expressions which are appropriate for the kinetic energy; these are precisely the same expressions which are used to describe an noninteracting gas of particles. Again we begin with the grand potential, which may be written as follows for a gas of Fermi particles:[2.30]

$$\Omega = -kT\int_0^\infty \mathcal{D}(E) \ln\left(1 + e^{(E_F - E)/kT}\right) dE \tag{2.7a}$$

$$= -\int_0^\infty \left(\int_0^E \mathcal{D}(x)\, dx\right)\left(1 + e^{(E-E_F)/kT}\right)^{-1} dE \, . \tag{2.7b}$$

In this equation $\mathcal{D}(E)$ is the density of states, the number of states per unit energy E, and E is measured from the band edge. The second line is obtained via integration by parts. The second factor in the integrand of Eq. (2.7b) is just the Fermi distribution function

$$h(E,E_F,T) \equiv \left(1 + e^{(E-E_F)/kT}\right)^{-1} \, . \tag{2.8}$$

The Fermi energy E_F plays the same role as the chemical potential μ for a noninteracting gas. Other quantities and relations may be

derived from the grand potential:[2.30]

$$N \equiv -\left(\frac{\partial\Omega}{\partial E_F}\right)_{T,V} = \int_0^\infty \mathcal{D}(E)\, h(E,E_F,T)\, dE \quad . \tag{2.9a}$$

The Fermi energy is a function of temperature and is determined by this relation. At T = 0 we may write

$$N = \int_0^{E_F(0)} \mathcal{D}(E)dE \ , \quad (T = 0) \quad . \tag{2.9b}$$

The entropy is given by[2.30]

$$S \equiv -\left(\frac{\partial\Omega}{\partial T}\right)_{V,E_F} \tag{2.10a}$$

$$= k\int_0^\infty \mathcal{D}(E)\, \ln\left(1 + e^{(E_F-E)/kT}\right) dE \tag{2.10b}$$

$$+ \frac{1}{T}\int_0^\infty \mathcal{D}(E)(E - E_F)\, h(E,E_F,T)\, dE$$

$$= \frac{PV}{T} - \frac{NE_F}{T} + \frac{1}{T}\int_0^\infty \mathcal{D}(E)E\, h(E,E_F,T)\, dE \ , \tag{2.10c}$$

using Eqs. (2.7a) and (2.9a). From Eqs. (2.2) and (2.10c) the total energy U is given by

$$U = NE_F - PV + TS = \int_0^\infty \mathcal{D}(E)E\, h(E,E_F,T)dE \quad . \tag{2.11}$$

Equations (2.9a) and (2.11) are familiar results, but it is useful to see how they arise. In addition, as will be seen shortly, this general derivation is easily applied to the complicated case of the real band structure in stressed Ge and Si. First, however, we still require an expression for F, which is easily obtained from Eqs. (2.3) and (2.7b):

$$F = NE_F - \int_0^\infty \left(\int_0^E \mathcal{D}(x)\, dx\right) h(E,E_F,T)dE \quad . \tag{2.12}$$

The preceding equations are valid for any system which can be described using a density of states $\mathcal{D}(E)$. For the case of carriers in a semiconductor we require information about the conduction and valence band structure. First consider a single band of carriers; for this case[2.32]

$$\mathcal{D}(E) = \frac{V}{4\pi^3}\int k^2 \frac{dk}{dE}\, d\Omega \quad . \tag{2.13}$$

The integration is performed over solid angle (Ω is not to be confused with the grand potential of Eq. (2.2)), on a surface in k-space with energy E. If the band is parabolic, then Eq. (2.13) may be reduced to a simple form. If the band is not parabolic, the nonparabolicity may be taken into account by writing:

$$\mathcal{D}(E) = a^*V\, m_{dloc}^{3/2}(E)\, E^{1/2} \tag{2.14a}$$

where

$$a^* = \frac{\sqrt{2}}{\pi^2\hbar^3} \tag{2.14b}$$

Thus the nonparabolicity may be described through the use of an energy-dependent local density-of-states mass, which is defined by

$$m_{dloc}^{3/2}(E) \equiv \frac{1}{4\pi^3 a^* E^{1/2}}\int k^2 \frac{dk}{dE}\, d\Omega \quad . \tag{2.15}$$

An average or integrated density of states mass may also be defined, using Eq. (2.9b) and the analogy with the parabolic band case. Thus we may write

$$N = a^*V \frac{2}{3} (E_F(0))^{3/2} m_{dint}^{3/2}(E_F(0)) \quad , \tag{2.16}$$

where the integrated density-of-states mass is defined as follows:

$$m_{dint}^{3/2}(E) \equiv \frac{3}{2} E^{-3/2} \int_0^E m_{dloc}^{3/2}(x)\, x^{1/2}\, dx \quad . \tag{2.17}$$

Note that for the case of a parabolic band, both m_{dloc} and m_{dint} are just equal to a constant (in fact, the same constant) times the free electron mass m_0.

The actual situation is Ge or Si at arbitrary stress is more complicated, because both the conduction and valence bands are split by stress, as discussed in Chapter 1. Only the band(s) lowest in energy remain populated at high stress. Suppose that a set of ν_1 identical bands is lower in energy by E_{spl} than another set of ν_2 identical bands. (For example, for electrons in (111)-stressed Ge, $\nu_1 = 1$ and $\nu_2 = 3$; for electrons in (100)-stressed Si, $\nu_1 = 2$ and $\nu_2 = 4$; for holes in both cases, $\nu_1 = \nu_2 = 1$.) In this case the density of states can be written as follows:

$$\mathcal{D}(E) = a^*V \left\{ \nu_1 m_1^{3/2}(E) E^{1/2} + \nu_2 m_2^{3/2}(E)(E-E_{spl})^{1/2} \right\} \quad ; \tag{2.18}$$

here $m_1(E)$ and $m_2(E)$ are the local density-of-states masses for the two sets of bands. It is understood that $m_2(E) = 0$ for $E<E_{spl}$. This form for the density of states should be used in Eqs. (2.7), (2.9a), (2.10c), (2.11), and (2.12) for Ω, N, S, U, and F respectively. In particular, we may explicitly write

$$N = a^*V\nu_1 \int_0^\infty m_1^{3/2}(E) E^{1/2} h(E,E_F,T)\, dE + a^*V\nu_2 \int_{E_{spl}}^\infty m_2^{3/2}(E)(E-E_{spl})^{1/2} h(E,E_F,T)\, dE \tag{2.19}$$

and

$$F = NE_F - a^*V\nu_1 \int_0^\infty \left(\int_0^E m_1^{3/2}(x) x^{1/2} dx \right) h(E,E_F,T)\, dE - a^*V\nu_2 \int_{E_{spl}}^\infty \left(\int_{E_{spl}}^E m_2^{3/2}(x)(x-E_{spl})^{1/2}\, dx \right) h(E,E_F,T)\, dE \; . \tag{2.20}$$

Note that the same Fermi level is used for both sets of bands, indicating that both sets of carriers are in thermal equilibrium with each other. This will be the case when the interband and intervalley scattering times are short compared to the EHL lifetime (in a steady-state experiment), or when sufficient time has elapsed after EHL formation (in a pulsed experiment), corresponding to the equilibrium limit of Kirczenow and Singwi.[2.25] This may be contrasted with a situation[2.33-2.37] in which the recombination lifetime is shorter than the intervalley scattering time and carriers may be observed in the upper bands with a different Fermi level. Only the equilibrium limit is considered here.

Equations (2.19) and (2.20) can be used separately for electrons and for holes, with

$$N_e = N_h \quad \text{and} \quad F_{kin} = F_{kin}^e + F_{kin}^h \quad . \tag{2.21}$$

The electron and hole terms f^e_{kin} and f^h_{kin} in the kinetic energy contribution f_{kin} to the free energy per pair are obtained from Eqs. (2.19) and (2.20). Note that if the temperature is fixed (and the stress is fixed), then f^e_{kin} depends only on the electron Fermi level E^e_F, and f^h_{kin} depends only on the hole Fermi level E^h_F. In addition, $n_e = n_n$ depends only on E^e_F (or E^h_F). Thus we note that

$$\left(\frac{\partial f}{\partial n}\right)_{T,N} = \left(\frac{\partial f}{\partial n}\right)_{T,V} = \left(\frac{\partial f}{\partial n}\right)_T \quad . \tag{2.22}$$

2.2. Hole Masses

In order to compute the kinetic energy of the holes it is necessary to account for the warping of the valence bands through the energy-dependent mass introduced in Eq. (2.15). In this section the calculation of the density-of-states masses is outlined, and the related optical mass is introduced.

The valence bands in strained Ge and Si have been calculated near $\vec{k} = 0$ using the $\vec{k} \cdot \vec{p}$ formalism by Pikus and Bir.[2.38] The heavy and light hole bands are warped due to their interaction. This in turn arises from the degeneracy at zero stress at $\vec{k} = 0$. At infinite stress the bands are completely decoupled and are given by simple ellipsoids. However, as we shall see below and has been pointed out by Markiewicz and myself[2.23] and by Liu,[2.26] the residual nonparabolicity of the hole bands affects the properties of the EHL at stresses much greater than that required to merely depopulate the band raised in energy.

Measuring energies from $\vec{k} = 0$ for the lower band, the valence bands are given by[2.38, 2.39]

$$E(k) = Ak^2 + |E_{\epsilon\epsilon}| \pm \sqrt{E^2_{kk} + E^2_{\epsilon k} + E^2_{\epsilon\epsilon}} \tag{2.23}$$

where

$$E^2_{kk} = B^2k^4 + C^2(k_x^2k_y^2 + \text{c.p.}) \tag{2.24a}$$

$$E^2_{\epsilon k} = Bb\left[3(k_x^2\epsilon_{xx} + \text{c.p.}) - k^2\Delta\right] + 2Dd(k_xk_y\epsilon_{xy} + \text{c.p.}) \tag{2.24b}$$

$$E^2_{\epsilon\epsilon} = (1/2)b^2\left[(\epsilon_{xx} - \epsilon_{yy})^2 + \text{c.p.}\right] + d^2\left[\epsilon^2_{xy} + \text{c.p.}\right] \tag{2.24c}$$

Here A, B, and C are inverse mass band parameters,[2.40] $D = (3B^2 + C^2)^{1/2}$, b and d are deformation potentials, ϵ_{xy} and so on are strain components, $\Delta = \epsilon_{xx} + \epsilon_{yy} + \epsilon_{zz}$, and c.p. indicates cyclic permutation of the crystal coordinates x, y, and z.

A comment is in order on the labelling of the two hole bands. At zero stress both bands are parabolic in a given direction (so the warping is present as a function of angle); the designation heavy and light holes is determined by the relative curvature of the bands. Under compressive stresses (only compressive stresses are used in the experiments in this thesis) the light hole band actually moves "through" the heavy hole band,[2.41, 2.42] resulting in strong mixing. However, the band which is lower in energy and which remains populated at all

stresses always has a larger mass; thus this band, corresponding to the lower sign in Eq. (2.23), is referred to as the heavy hole band, even though at high stresses it has the character of the zero-stress light hole band. The upper sign then gives the energy for the light hole band, which becomes depopulated at high stress.

The strain components ε_{ij} in Eq. (2.24) are given by Hensel and Feher[2.43] for stresses along the principal crystallographic directions. For example, for ⟨001⟩ stress, which is used here for Si, Eqs. (2.24b) and (2.24c) simplify as follows:

$$E_{\varepsilon\varepsilon} = b\,\sigma_{001}/(C_{11} - C_{12}) \quad ; \qquad E^2_{\varepsilon k} = B\,E_{\varepsilon\varepsilon}(3k_z^2 - k^2) \quad . \tag{2.25}$$

Here σ_{001} is the stress along the ⟨001⟩ direction, which is the z-direction. For ⟨111⟩ stress, which is used here for Ge, Eqs. (2.24b,c) simplify as follows:

$$E_{\varepsilon\varepsilon} = d\,\sigma_{111}/(2\sqrt{3}\,C_{44}) \quad , \qquad E^2_{\varepsilon k} = \frac{2}{\sqrt{3}} D\,E_{\varepsilon\varepsilon}(k_x k_y + \text{c.p.}) \quad , \tag{2.26}$$

where σ_{111} is the stress along the ⟨111⟩ direction. In this representation the x, y, and z crystal coordinates are along ⟨100⟩ directions. In order to observe the expected 3-fold symmetry around the ⟨111⟩ direction, it would be necessary to perform a rotation of coordinates.

For the calculation of the masses, however, this step is actually unnessary, since from Eq. (2.15) the mass involves an integration over all angles. The values for all the parameters used for the calculation are given in Table 2.1. Also given is the energy splitting between the heavy and light hole bands at $\vec{k} = 0$ obtained from Eq. (2.25) for Si and Eq. (2.26) for Ge where $E^h_{spl} = 2|E_{\varepsilon\varepsilon}|$ in Eq. (2.23).

It can easily be seen from Eqs. (2.23)-(2.26) that the valence band energies scale with stress as E/σ and k^2/σ. Thus it is not necessary to compute the mass in Eq. (2.15) for every energy and stress, but only once as a function of reduced energy $E' \equiv E/|\sigma|$, where σ refers to ⟨111⟩ stress for Ge and ⟨100⟩ stress for Si. The calculations have been performed for compressional stresses σ, which are conventionally taken to be negative. Both the local density-of-states masses, Eq. (2.15), and the integrated density-of-states masses, Eq. (2.17), have been calculated for heavy and light holes. The results for Ge are shown in Fig. 2.1 and the results for Si are shown in Fig. 2.2, plotted as a function of reduced energy E'. Note that the structure present in the local masses is smoothed out in the integrated masses. Also, the local and integrated masses approach the same zero-stress values (indicated by the arrows) and infinite-stress values.

It is also possible to define optical or conductivity masses, as done originally by Lax and Mavroides.[2.44] They found, for a single band

$$\frac{n}{m_{ij}(E)} = \frac{1}{4\pi^3\hbar^2}\int \frac{\partial E}{\partial k_i}\,\frac{\partial E}{\partial k_j}\,\frac{\partial k}{\partial E}\,k^2\,d\Omega \quad , \tag{2.27}$$

where i and j are crystal coordinates x, y, z and the integral is taken over the k-space surface with energy E. Transverse and longitudinal masses can be defined, with reference to the stress direction, as follows. For ⟨001⟩ stress, with the z-axis along ⟨001⟩,

$$m_\ell^{-1} = m_{zz} \qquad (\langle 001\rangle \text{ stress}) \tag{2.28}$$

$$m_t^{-1} = \frac{1}{2}\left(m_{xx}^{-1} + m_{yy}^{-1}\right)$$

For ⟨111⟩ stress, using the same coordinate system as for the density-of-states masses above,

$$m_\ell^{-1} = \frac{1}{3}\left(m_{xx}^{-1} + m_{yy}^{-1} + m_{zz}^{-1}\right) + \frac{2}{3}\left(m_{xy}^{-1} + m_{yz}^{-1} + m_{xz}^{-1}\right) \qquad (\langle 111\rangle \text{ stress}) \tag{2.29}$$

$$m_t^{-1} = \frac{1}{3}\left(m_{xx}^{-1} + m_{yy}^{-1} + m_{zz}^{-1}\right) - \frac{1}{3}\left(m_{xy}^{-1} + m_{yz}^{-1} + m_{xz}^{-1}\right) \quad .$$

The longitudinal and transverse optical masses for the heavy and light holes are shown in Fig. 2.3 for Ge and in Fig. 2.4 for Si as a function of reduced energy E', defined previously. It is clear from Eq. (2.27) that the optical masses scale with stress in the same way as the density-of-states masses. The light hole in Ge has a remarkable change in the ratio m_t/m_ℓ just as the band depopulates, but this might be difficult to detect experimentally since less than 1/2% of the holes are in this band. At most stresses the holes are more anisotropic in Ge than in Si. The arrows in both figures indicate the zero-stress values, which are the same for transverse and longitudinal components for each hole band. This is a consequence of the cubic symmetry of the crystal. Consider for a moment the case of tension instead of compression. As the crystal passes through zero stress to tension (σ becomes positive) the symmetry is inverted. For example in Ge the hole is heaver in the transverse direction for compression and becomes heavier in the longitudinal direction for tension; for the same value of $E/|\sigma|$ the ratio m_t/m_ℓ just inverts.

The components of the optical masses given above are combined as follows:

$$m_{opt}^{-1} = \frac{1}{3}\left(2m_t^{-1} + m_\ell^{-1}\right) \quad , \tag{2.30}$$

$$\frac{n}{m_{oh}} = \frac{n_{HH}}{m_{oHH}} + \frac{n_{LH}}{m_{oLH}} \quad , \tag{2.31}$$

where n_{HH}/n is the fraction of holes in the heavy hole band and $n_{HH} + n_{LH} = n$. The densities are calculated as described in the previous section. The total optical masses m_{oh}, averaged over light and heavy hole bands and over longitudinal and transverse components, are shown in Figs. 2.3 (Ge) and 2.4 (Si). Due to the increasing importance of the light holes (with increasing E'), which is due in turn to the increasing fractional occupation, there is actually a maximum in the total optical mass. For Ge this occurs at $E' \sim 0.6$, but the maximum is not noticeable in the figure. For Si the maximum occurs at $E' \approx 0.30$ and is much more pronounced, partly because the light hole mass decreases more strongly as a function of E' and partly because the fractional occupation is larger compared to Ge. The total optical mass will be used later in one model for the correlation energy.

Some numerical results of the hole mass calculations are shown in Table 2.2. All mass values are multiples of the free electron mass m_o. The quantity frac_{LH} is the fraction of holes in the light hole band at zero stress. An overall density-of-states mass can be defined at zero stress, where the splitting between the two bands is zero, using Eqs. (2.16) and (2.19). Thus for zero stress

$$m_{dh}^{3/2} = m_{dHH}^{3/2} + m_{dLH}^{3/2}$$

The values for the density-of-states masses at zero stress agree with those calculated by Brinkman and Rice.[2.1] Under infinite stress the valence bands become elliposidal and can be completely characterized by longitudinal and transverse components m_ℓ and m_t. For this simplified case, the density-of-states mass is defined via

$$m_d = \left(m_t^2 m_\ell\right)^{1/3} , \tag{2.33}$$

and the optical mass is defined as in Eq. (2.30). For the type of band structure given by Eq. (2.23), the infinite-stress masses reduce to particularly simple forms:[2.41]

$$\left.\begin{aligned} m_t/m_o &= (A - 1/2\ B)^{-1} \\ m_\ell/m_o &= (A + B)^{-1} \end{aligned}\right\} \langle 100 \rangle \text{ stress} \tag{2.34a}$$

$$\left.\begin{aligned} m_t/m_o &= \left(A - \frac{D}{2\sqrt{3}}\right)^{-1} \\ m_\ell/m_o &= \left(A + \frac{D}{\sqrt{3}}\right)^{-1} \end{aligned}\right\} \langle 111 \rangle \text{ stress} \tag{2.34b}$$

$$m_{opt}/m_o = A^{-1} \qquad \text{all stress directions} \tag{2.35}$$

A check on the computer program is to note that the values in Table 2.2 agree with the experimentally measured mass parameters both for Ge[2.42] and for Si,[2.41] as they should. A description and listing of the program are given in Appendix 2.1.

2.2.3 Luminescence Lineshape

In order to compute the luminescence lineshape from the EHL in stressed Ge and Si, it is necessary to include the nonparabolicity of the valence bands, which involves the local density-of-states masses calculated in the previous section. For an allowed transition, the

luminescence intensity as a function of photon energy $\hbar\nu$ is given by[2.45, 2.46]

$$I(\hbar\nu) = I_o \int_0^\infty dE_e \int_0^\infty dE_h \mathcal{D}_e(E_e)\, \mathcal{D}_h(E_h)\, h(E_e, E_F^e, T) \times h(E_h, E_F^h, T)\, \delta(\hbar\nu - E_e - E_h + \hbar\omega_{ph} - E'_{BB}) \qquad (2.36)$$

for a single conduction band and valence band. The matrix element for the optical transition is independent of the electron and hole energies for an allowed transition[2.47] and has been absorbed into the constant I_o. In this equation $\hbar\omega_{ph}$ is the energy of the phonon emitted along with the photon in the indirect transition in order to conserve momentum and energy; and E'_{BB} is the energy of the bottom of the band within the EHL (see Fig. 1.1). The delta function merely expresses conservation of energy. The densities of states and Fermi distribution functions are defined in Eqs. (2.13) and (2.8). Thus the luminescence lineshape for an allowed transition is given by the joint density of occupied electron and hole states. The integral over E_e can be performed immediately, giving

$$I(\hbar\nu_{min} + \hbar\nu') = I_o \int_0^{\hbar\nu'} dE_h \mathcal{D}_e(\hbar\nu' - E_h)\, \mathcal{D}_h(E_h) \times h(\hbar\nu' - E_h, E_F^e, T)\, h(E_h, E_F^h, T) \qquad (2.37)$$

Here $\hbar\nu'$ is the energy above the minimum photon energy $\hbar\nu_{min} \equiv E'_{BB} - \hbar\omega_{ph}$. This lineshape formula is appropriate for single conduction and valence

bands or for sets of degenerate bands; it has been used extensively to analyze experimental lineshapes in unstressed Ge and Si.[2.22] The most intense luminescence is from the LA phonon-assisted transition in Ge and from the TO phonon assisted transition in Si.[2.48]

Several refinements have been suggested for fitting experimental lineshapes but will not be considered here. In Ge the main luminescence line is actually a composite, in which the intensity of the LO phonon assisted transition is approximately 8% of the intensity of the LA phonon-assisted transition.[2.49] Similarly, in Si the main line is also a composite, in which the LO component has approximately 10-15% of the intensity of the TO component.[2.50, 2.51] If the lines are analyzed as a single component, the e-h pair density is overestimated by a few percent. An additional contribution on the low-energy side of the line is a tail due to Auger processes modifying the recombination energies of carriers deep inside the Fermi sea.[2.52-2.55] This feature improves the fit but does not affect the value of the deduced density.[2.53] The effect of a renormalization of carrier masses is discussed in Section 23.3.

In stressed Ge and Si the situation is complicated because the two hole bands are split by an energy E^h_{spl} and because ν_1 electron valleys are lower in energy by E^e_{spl} than the other ν_2 valleys. (Conduction band parameters are given in Table 2.3.) The contributions must be added for transitions between each pair of bands. Thus

$$I(h_{min} + \hbar\nu') = I_o \int_0^{\hbar\nu'} (R_{e1} + R_{e2})(R_{HH} + R_{LH})\, dE_h \qquad (2.38)$$

where

$$R_{e1} = \nu_1 (h\nu' - E_h)^{1/2}\, h(h\nu' - E_h, E_F^e, T) \qquad (2.39)$$

$$R_{e2} = \begin{cases} \nu_2 (h\nu' - E_h - E_{spl}^e)^{1/2}\, h(h\nu' - E_h, E_F^e, T) & h\nu' - E_h > E_{spl}^e \\ 0 & h\nu' - E_h \leq E_{spl}^e \end{cases}$$

$$R_{HH} = m_{dHH}^{3/2}(E_h)\, E_h^{1/2}\, h(E_h, E_F^h, T)$$

$$R_{LH} = \begin{cases} m_{dLH}^{3/2}(E_h)(E_h - E_{spl}^h)^{1/2}\, h(E_h, E_F^h, T) & E_h > E_{spl}^h \\ 0 & E_h \leq E_{spl}^h \end{cases}$$

In this equation the local density-of-states masses are used, and some constants have been absorbed into I_o.

Figure 2.5 illustrates the importance of including the nonparabolicity of the hole bands. Two calculations are shown for typical conditions for the strain-confined EHL in Ge,[2.28] which will be discussed extensively in later chapters. (At low excitation, the liquid is in a region of essentially uniform (111) strain.[2.31]) The stress is -5.6 kgf/mm^2, n = 0.50 x 10^{17} cm^{-3}, and T = 1.8 K. The solid curve was calculated using the energy-dependent density-of-states hole masses shown in Fig. 2.1, while the dashed curve was calculated using a constant hole mass. The particular mass was $m_{dHH}(E_F^h)$ with E_F^h = 2.28 meV from the previous case. The shape of the line changes, though in this example the full width at half maximum ΔE only changes by about 0.1 meV. As can be seen from the

figure, in order to quantitatively analyze experimental lineshapes, the energy-dependent hole masses must be used.

In the above example, it was possible to choose an "appropriate" average mass, since the actual masses have already been calculated. However, up to now this has not been possible for spectra obtained from (100)-stressed Si,[2.19-2.21] and as a result there are significant errors in the reported densities. In these papers, the experimental lineshapes were fit using the infinite-stress hole mass. This seems like a reasonable thing to do if the stress is significantly larger than that required to completely depopulate the light hole band. (As discussed in Section 23, this critical stress is $-\sigma_{100} \approx 35$ kgf/mm^2.) For example, in the experiment of Gourley and Wolfe[2.20] on the strain-confined liquid, the stress was $-\sigma$ = 55 kgf/mm^2 and the full width at half maximum of the luminescence line was 6.8 meV. Using the infinite-stress mass, this linewidth corresponds to a density of 3.8 x 10^{17} cm^{-3} (T = 1.4 K). However, using the energy-dependent mass in Fig. 2.2, the same FWHM linewidth corresponds to a density of 5.6 x 10^{17} cm^{-3}. Thus by using the infinite-stress masses, the density can be underestimated by as much as 30%, even when the stress is 1-1/2 times the critical stress needed to depopulate the light holes. In the experiment of Kulakovskii and Timofeev[2.19] the maximum stress was $-\sigma_{100} \approx 35$ kgf/mm^2, so their deduced densities have a larger error.

The case just discussed is illustrated in Fig. 2.6. Here the solid curve represents the lineshape calculated using the energy-dependent mass and $-\sigma$ = 55 kgf/mm^2, while the dashed curve was calculated using the infinite-stress hole mass. In both cases the linewidth

ΔE = 6.8 meV. The two curves have been adjusted so that the energies $h\nu' = E_F^e + E_F^h$ coincide. Clearly the quality of the lineshape fit should change (hopefully, improve) when the correct theoretical lineshape is used. The nearly linear portion of the constant-mass spectrum occurs in the energy range $E_F^e \lesssim h\nu' \lesssim E_F^h$, and the peak occurs near $h\nu' \approx E_F^h$ (at low T). The resulting asymmetry of the line is rather pronounced here because the ratio $E_F^h/E_F^e = 2.17$ is fairly large. Using Eq. (2.16) for both electrons and holes, at T = 0 we find

$$\frac{E_F^h(0)}{E_F^e(0)} = \frac{m_{de}}{m_{dh}} \nu_e^{2/3} \qquad (2.40)$$

where for simplicity we only consider the zero and infinite stress cases. The values are listed in Table 2.3 for both Ge and Si. The asymmetry and pointed top should become very pronounced indeed in highly stressed Ge at low temperature. It should be noted that these features become rounded out with increasing temperature. Thus, for example, the discrepancies noted by Hammond, et al.[2.50] in their zero-stress lineshape fits in Si could possibly be explained by sample heating.

22.4. Calculation of the Kinetic Energy

Once the hole masses have been calculated as a function of reduced energy E', as described in Section 22.2, they can be fit to simple analytic formulas and used in other calculations. The local density-of-states masses $m_{dHH}^{3/2}(E')$ and $m_{dLH}^{3/2}(E')$ were fit to simple functions over several ranges of E', matching the functions and first derivatives at the crossover points between the ranges. Formulas for the integrated

density-of-states masses were then obtained using Eq. (2.17) by directly integrating the formulas for the local masses. Only in this way are the local and integrated masses consistent with each other. The total optical masses were fit to a ratio of polynomials. The masses for Ge and Si were fit to the same functional forms, so that in the final program it was only necessary to read in a new set of data in order to change materials. The optical masses were used in one model for the correlation energy, discussed in Section 22.5. The integrated density-of-states masses were used in another model for the correlation energy and in the zero-temperature kinetic energy. The local density-of-states masses were used in the calculation of the kinetic energy at finite temperature, as well as in fitting the luminescence lineshapes, as described in Section 22.3.

The kinetic energy contributions to the free energy per e-h pair were calculated using Eqs. (2.19) and (2.20) for electrons and for holes. At finite temperature the exact calculation was performed, rather than the T^2 expansion used by other authors.[2.7, 2.8, 2.27] In order for the T^2 expansion to be valid, it is necessary that $kT/E_F \ll 1$ or $kT/(E_F - E_{spl}) \ll 1$ for all occupied bands. At low temperature, this will not hold for certain ranges of stress. Near the critical temperature, the above conditions are necessary at the critical density and, as discussed in Section 24.2, are not true at any stress. At T = 0 the calculation is much simpler; the integrals in Eqs. (2.19) and (2.20) are trivial for electrons and involve the simple fitted functions discussed above for holes. In all cases, the calculation of f_{kin} proceeded as follows: (1) the hole Fermi energy E_F^h was chosen;

(2) the density was computed using Eq. (2.19) for holes; (3) the electron Fermi energy E_F^e was computed by inverting Eq. (2.19) for electrons; (4) the electron and hole kinetic energy contributions f_{kin}^e and f_{kin}^h were computed using Eq. (2.23). For electrons, at T=0 $f_{kin}^e = \frac{3}{5} E_F^e$. However, for holes, $f_{kin}^h \neq \frac{3}{5} E_F^h$ except at zero and infinite stress.

The calculations reported here involve finding a minimum in the free energy per pair f(n) or, as discussed in Sec. 24.2, finding the disappearance of a minimum in the chemical potential $\mu(n)$, defined in Eq. (2.6b). (In both cases the temperature is constant.) It turns out that the minimum is very shallow: at T = 0, for example, in order to find the equilibrium density to within 1% it is necessary to calculate f(n) to an precision of 1 part in 10^6. This is, of course, a mathematical [1] detail since the band structure is not known to such a high degree of precision; however, some care should be used in fitting the hole masses to ensure that the functions are sufficiently smooth. It is also possible, as discussed in Appendix 2.2, to evaluate the integrals in Eqs. (2.19) and (2.20) at finite temperature so that the kinetic energy contributions are adequately smooth.

22.5 Coulomb Energy

The free energy per e-h pair contains contributions from the kinetic energy and the Coulomb energy:

$$f = f_{kin} + f_{Coul} \quad , \tag{2.41a}$$

where the Coulomb energy is further separated into exchange and correlation energy contributions:

$$f_{Coul} = f_{ex} + f_{corr} \quad . \tag{2.41b}$$

At a given stress the Coulomb energy depends only on the density; in all calculations to date it is taken to be independent of temperature[2.9] and is calculated at T = 0. A detailed calculation of the Coulomb energy, including the band structure of Ge or Si at arbitrary stress, would be extremely difficult and has not been attempted. However, as we shall see here and in Section 23, it is not really necessary: the Coulomb energy is largely independent of band structure details, such as masses, degeneracies, and anisotropy, as long as both the exchange and correlation energies are calculated using the same band structure details. Markiewicz[2.56] has termed this statement the "ineffective mass theorem;" however, no formal proof of this theorem is known. This point was first discussed by Markiewicz and myself[2.23] and was based on a suggestion made by Vashishta[2.29] that the correlation energy should depend only weakly on mass. The idea has been used more recently by Kirczenow and Singwi[2.25, 2.35] in their calculations of the ground state properties of the EHL in stressed Ge. This apparent theorem may be illustrated by considering several models for the Coulomb energy. For zero or infinite stress the exchange energy is given by[2.2]

$$f_{ex} = -\frac{3e^2}{4\pi\kappa} (3\pi^2 n)^{1/3} \left[\frac{\phi(\rho_e)}{\nu_e^{1/3}} + \psi(\rho_h) \right] \tag{2.42}$$

where ν_e is the number of electron valleys. Combescot and Nozières[2.2] found that for an ellipsoidal Fermi surface

$$\phi(\rho) = \begin{cases} \rho^{1/6} \dfrac{\sin^{-1}\sqrt{1-\rho}}{\sqrt{1-\rho}} & \rho < 1 \\ \rho^{1/6} \dfrac{\sinh^{-1}\sqrt{\rho-1}}{\sqrt{\rho-1}} & \rho > 1 \end{cases} \qquad (2.43)$$

where $\rho = m_t/m_\ell$. At infinite stress the occupied hole band is also ellipsoidal, and for that case $\psi(\rho_h)$ is given by Eq. (2.43). For the holes at zero stress, it is necessary to take into account both the warping and coupling of the valence bands. This calculation has been performed exactly by Brinkman and Rice.[2.1] The values for $\phi(\rho_e)$ and $\psi(\rho_h)$ are listed in Table 2.3.

A total of six models have been used for the Coulomb energy; the first three were used in an earlier paper on stressed Ge.[2.23] Model 1 uses the exchange and correlation energies appropriate for ideal systems in which the electrons are treated as for infinite stress and the holes as for zero stress.[2.5, 2.6, 2.57] In the present model the kinetic energy of both electrons and holes is computed correctly, so that these ideal systems do not correspond exactly to any value of the stress for Ge or for Si. The correlation energy of Model 1 is the result of a detailed numerical calculation in a fully self-consistent (FSC) approximation[2.3, 2.4, 2.7] including multiple scattering and band anisotropy. The results were kindly provided by Dr. Vashishta.[2.57] The correlation energy was fit to a polynomial in the density, matched to a Wigner form. It is very similar to the form given recently by Kalia and Vashishta[2.58] except that the power series portion has more

terms and is valid over a wider range of density. In Model 2, this detailed calculation of the correlation energy is replaced by a simple empirical correlation energy, which is taken to be the sum of Wigner-type contributions from the electrons and holes:[2.59]

$$f_{corr} = -\frac{c}{n^{-1/3} + a/m_{oe}} - \frac{c}{n^{-1/3} + a/m_{oh}} \quad . \qquad (2.44)$$

In this model, as in Ref. 2.23, m_{oh} is taken to be the infinite-stress optical mass, which has been used in caluclations of the EHL ground state for zero stress.[2.1, 2.3] The constants a and c are chosen so that the value and first derivative of Eq. (2.44) agree with Model 1 at the equilibrium density for the ideal systems described above; the values for a and c are given in Table 2.3. The exchange energy is the same as for Model 1.

Models 3 and 4 represent two attempts to determine the effect of allowing the correlation energy to depend on the hole mass, which will vary with density and with stress. In Model 3 the correlation energy is given by Eq. (2.44), where m_{oh} is the total hole optical mass described in Sec. 22.2 (see Figs. 2.3 and 2.4); the constants a and are recalculated. Because the total optical mass is not a monotonic function of reduced energy E', this model undoubtedly overestimates the strain dependence of the correlation energy. In Model 4, the otpical mass is replaced by an average density-of-states mass (for both hole bands) calculated as an obvious extension of Eq. (2.16); a and c are again recalculated. This mass (not shown in the figures) a monotonic function of reduced energy E'; however, there is greater

variation between zero and infinite stress than for the optical mass (see Table 2.2). Thus it might be expected that this model also overestimates the strain dependence of the correlation energy. In both Models 3 and 4 the exchange energy is the same as for Model 1.

The last two models were chosen to illustrate two extreme cases in which the exchange and correlation energies are calculated using the same band structure details. Both models use FSC correlation energies given in Ref. 2.58. Model 5 uses the Coulomb energy appropriate for zero stress, while Model 6 uses the exchange and correlation energies appropriate for infinite stress. Models 5 and 6 are very similar to the two models used in Ref. 2.25 for Ge.

In order to compare the models, the Coulomb energies for Models 1, 2, 5, and 6 are shown as a function of density in Fig. 2.7 for Ge and in Fig. 2.8 for Si. Models 3 and 4 are not shown since the density dependence varies with stress. In accordance with the general idea of a universal Coulomb energy, it can be seen from the figures that for both Ge and Si the variation between the four models shown is rather small. Considering only the models based on the detailed calculations of Vashishta et al.,[2.3, 2.4, 2.7, 2.57, 2.58] a slight trend is apparent: at any density, the Coulomb energy increases in magnitude in going from Model 5 (zero stress) to Model 1 ("intermediate" stress) to Model 6 (infinite stress). It should also be noted that Model 2 is very similar to Model 1 over practically the entire density range for which the Model 1 detailed calculations were performed. Furthermore, suppose that the Coulomb energies are the densities are expressed in universal units (the excitonic Rydberg E_{Ryd} and the interparticle r_s)

$$E_{Ryd} = \frac{m_{eff}\, e^4}{2\kappa^2 \hbar^2} \tag{2.45a}$$

$$r_s = \left(\frac{3}{4\pi n}\right)^{1/3} \Big/ a_x \tag{2.45b}$$

where

$$a_x = \frac{\kappa \hbar^2}{m_{eff}\, e^2} \tag{2.45c}$$

is the excitonic Bohr radius and

$$m_{eff}^{-1} = m_{oe}^{-1} + m_{oh}^{-1} = m_{oe}^{-1} + A \quad . \tag{2.45d}$$

Then it is a remarkable fact that the Coulomb energies of all eight models displayed in Figs. 2.7 and 2.8 are spread by less than 15% in energy over a range of nearly two orders of magnitude in density. This simple comparison suggests that the Coulomb energy is relatively insensitive not only to band structure details but even to the material, as long as the entire calculation is done consistently. (The validity of this statement is untested for polar materials.) Further comparison between the models is made in the next section, where the results for the ground state properties are discussed. In addition, see the discussion in Section 54.

23. Results: Ground State Properties

In the previous section the procedure was described for computing the free energy per e-h pair as a function of pair density, for arbitrary stress and temperature. The kinetic energy was calculated exactly, taking into account the degeneracy and splitting of the conduction bands and the splitting and warping of the valence bands.

Six models were introduced for the Coulomb energy, and it was proposed that the Coulomb energy is relatively independent of band structure details. In this section the results will be presented for the ground state properties of the EHL in Ge uniaxially stressed along ⟨111⟩ and in Si uniaxially stressed along ⟨100⟩. The six models are compared in Section 23.1. In Section 23.2 a possible phase transition associated with the emptying of the upper electron valleys in Ge is discussed. The results of the calculations are compared with the available experimental data in Section 23.3, including guidelines for extrapolation to the infinite-stress limit.

23.1. Comparison of Models

The ground state of the EHL occurs at the density for which the free energy per pair f is a minimum, at T = 0. It is convenient to have the computer search for the associated zero in the pressure, given by Eq. (2.6a). In order to test out the proposed universality of the Coulomb energy, the ground state equilibrium densities n_o are shown as a function of stress in Fig. 2.9 for Ge and in Fig. 2.10 for Si. In both figures, part (a) shows the results for Models 1, 5, and 6, which are based onthe detailed correlation energy calculations of Vashishta, et al.;[2.3, 2.4, 2.7, 2.57, 2.58] part (b) shows the results for Models 2, 3, and 4, which are based on Wigner-type forms for the correlation energy. All six models were described in Sec. 22.5. In order to facilitate comparison between the models, arrows indicate the "correct" zero-stress (Model 5) and infinite-stress (Model 6) values for n_o.

Several conclusions may be drawn from these figures. First, as expected, all the models show the same general trends with stress: (1) A fairly rapid decrease in density occurs near the critical stress σ_e, where $E_F^e = E_{spl}^e$ and the upper electron valleys become depopulated. (In Ge $-\sigma_e \approx 2.6$ kgf/mm^2, while in Si $-\sigma_e \approx 10$ kgf/mm^2, as shown below; see Eqs. (2.49) and (2.50).) Note that there is a larger density change for Ge, due to the greater change in the number of occupied valleys. (2) There is a region of nearly constant density (the change is ≈ 30%) between the stresses σ_e and σ_h, where $E_F^h = E_{spl}^h$ and the light hole band becomes depopulated. (As shown below in Eqs. (2.49) and (2.50), $-\sigma_h \approx 6.5$ kgf/mm^2 in Ge and $-\sigma_h \approx 36$ kgf/mm^2 in Si.) (3) There is a slight kink at the stress σ_h, followed by (4) a further gradual decrease in density which is still apparent at stresses far beyond σ_h. Indeed, the equilibrium density changes by over a factor of 2 in ⟨100⟩-stressed Si and by approximately a factor of 4 in ⟨111⟩-stressed Ge after the light hole band occupation goes to zero. This point was emphasized by Markiewicz and myself[2.23] and by Liu[2.26] in preliminary calculations. In Models 1, 2, 5 and 6 the entire change in the pair energy f(n) with stress beyond σ_h comes from the hole kinetic energy f_{kin}^h and is due to the residual non-parabolicity of the occupied valence band. The valence bands do not become decoupled until they are split quite far apart in energy. Let us then check the validity of ignoring the split-off band, especially in view of the finding[2.41, 2.42] that this band interacts with the valence band remaining populated at high compressional stresses. As a result of this interaction the actual (bulk) masses differ from those

calculated in Section 22.2. Using the theory of Hasegawa[2.60] to first order, however, the density-of-states mass should decrease by ≈ 3% for $-\sigma_{111} \approx 40$ kgf/mm^2 for Ge and $-\sigma_{100} \approx 180$ kgf/mm^2 for Si, with smaller changes at lower stresses. For the stresses attained in experiments to date, this change should be negligible.

In Figs. 2.9 and 2.10, Model 3 shows an oscillation in the equilibrium density (noted in Ref. 2.23 for Ge[2.61]); this oscillation is associated with the structure in the hole optical mass (Figs. 2.3 and 2.4). It is perhaps surprising that the oscillation is not more pronounced in Si, since the structure in m_{oh} is more pronounced. However, the contribution from the holes to the correlation energy η (see Eq. 2.44) is relatively less important, since the hole and electron optical masses are more nearly equal. Model 4 does not exhibit an oscillation, since the averaged density-of-states hole mass changes monotonically with stress. The kink in the density vs. stress is associated with the depopulation of the light hole band and is more pronounced for Si since the fractional density of light holes is greater at low stresses. Both Model 3 and Model 4 appear to predict too great a decrease in density at high stress, due to the significant change in the hole mass and its probable overemphasis in importance in the correlation energy, Eq. (2.44). (Model 3 in Si is an exception, since from Table 2.2 the change in the optical mass is smaller than for the other cases in point.)

Comparison may also be made between Models 1, 5, and 6, which employ the detailed numerical calculations of Vashishta et al.,[2.3, 2.4, 2.7. 2.57, 2.58] for different ideal systems. As might

be expected from Figs. 2.7 and 2.8, at low stresses, the differences between Models 1 and 5 are smaller than the differences between both of these models and Model 6. The spread in zero-stress equilibrium densities, which is nearly 50%, is perhaps surprising. At large stresses all three models agree quite well; the infinite-stress equilibrium densities differ by only about 10%. Thus the proposed universality of the Coulomb energy is fairly well justified. The results of Kirczenow and Singwi[2.25] and of Liu et al.,[2.26, 2.27] are in good agreement with Models 5 and 6, which are nearly identical to the models used by these authors.

The ground state energy per pair f_G is shown in Fig. 2.11 for Ge and in Fig. 2.12 for Si, including all six models. A rather sudden change in slope occurs at the stress σ_e. This kink is more pronounced for Ge than for Si, due to the larger change in the number of occupied conduction bands. The binding energy of the liquid ϕ with respect to excitons is obtained from the following relation:

$$|f_G| = E_x + \phi \quad , \tag{2.46}$$

where E_x is the exciton binding energy (see Fig. 1.1). It is of limited value to describe the properties of the EHL if $\phi < 0$. Therefore let us consider the stress dependence of E_x. At zero stress the exciton structure is rather complicated, due to the degeneracy of the valence bands and the anisotropy of the conduction bands.[2.62] In Ge, two exciton states which are split by $\Delta \approx 1.01$ meV[2.63-2.65] and have a non-parabolic density of states[2.63, 2.64] are observed, in agreement with theory.[2.62, 2.66] This splitting is due to the conduction band

anisotropy.[2.62] In Si the splitting is found to be $\Delta \approx 0.35$ meV,[2.67-2.69] slightly smaller than the theoretical value $\Delta = 0.46$ meV;[2.62] the density of states is more nearly parabolic.[2.64, 2.66] The experimental values for the binding energy of the lowest exciton state are as follows, for unstressed Ge[2.70] and Si[2.71]:

$$\left.\begin{aligned} E_x &= 4.15 \text{ meV} \quad \text{(Ge)} \\ E_x &= 14.7 \text{ meV} \quad \text{(Si)} \end{aligned}\right\} \text{ zero stress .} \qquad (2.47)$$

The most recent theoretical values[2.62] are in good agreement with experiment. In the infinite-stress limit the exciton binding energy is nearly identical[2.72] to the excitonic Rydberg defined in Eq. (2.45), due to the simplified band structure. Thus

$$\left.\begin{aligned} E_x &= 2.65 \text{ meV} \quad \text{(Ge)} \\ E_x &= 12.85 \text{ meV} \quad \text{(Si)} \end{aligned}\right\} \text{ infinite stress.} \qquad (2.48)$$

At intermediate stresses the valence bands are split, and four exciton states are observed in absorption experiments.[2.39, 2.69] Only the lowest state is thermally populated in a low-temperature luminescence experiment. The binding energy of this state may be estimated at arbitrary stress by using an appropriate hole mass in the excitonic Rydberg, Eq. (2.45). For high enough stress the energy-dependent heavy hole optical mass $m_{oHH}(E')$ from Figs. 2.3 and 2.4 and Eq. (2.30) may be used, where $E' = E/|\sigma|$. The characteristic energy for excitons is kT, whereas it is E_F for the EHL. Even though this is a ground state calculation we use kT = 0.17 meV to indicate the effect of a typical

temperature. The results of this estimate are shown as dashed curves in Figs. 2.11 and 2.12. From the absorption data,[2.39, 2.69] this description appears reasonable for stresses greater than ≈ 5 kgf/mm^2 both for Ge stressed along ⟨111⟩ and for Si stressed along ⟨100⟩. In the figures the dashed curves terminate at this stress. It should be noted that the character of the lowest exciton state should change with stress. Indeed, the associated change in the exciton structure has been observed experimentally.[2.39, 2.69, 2.73, 2.74] It can be seen from Figs. 2.11 and 2.12 and Eq. (2.47) that ϕ is expected to decrease rather rapidly at low stresses; this has been observed in Ge by Ohyama et al.[2.75] and in Si by Ashkinadze et al.[2.76] At high stresses ϕ remains positive and the EHL is bound with respect to excitons for all models except Models 3 and 4 in Ge and Model 4 in Si.

For further calculations it is unnecessary to consider so many models. Among Models 1, 5, and 6, Model 1 gives the best overall agreement with the "correct" theories at both zero stress (where Model 5 is "correct") and at infinite stress (where Model 6 is "correct"), considering both the equilibrium densities and ground state energies for Ge and Si. This is of course reasonable, since Model 1 is based on an intermediate stress calculation. Thus Models 5 and 6 will not be considered further in detail. Models 3 and 4 apparently overestimate the effect of the changes in the valence band on the Coulomb energy, so they too will not be considered further. Thus Models 1 and 2 will be compared in detail. Numerical results for several selected values of the stress are given in Table 2.4 for these models. In addition the "correct" theoretical results are given for zero and infinite

stress, as well as experimental results for zero stress which are compiled in Ref. 2.22. The first stress is slightly greater in magnitude than σ_e (see Eq. (2.49)), so that the upper electron valleys are depopulated; this corresponds to the configurations Ge(1:2) and Si(2:2). Similarly, the second stress is slightly greater than σ_h (see Eq. (2.50)), so that only one valence band is populated; this corresponds to the configurations Ge(1:1) and Si(2:1). The final stress is just greater than the highest stresses obtained to date in experiments and serves to illustrate that further changes are expected before the infinite-stress limit is achieved.

23.2 Possible Phase Transition in Ge Involving the Electrons

In performing the calculations of the ground state density for Ge (Fig. 2.9) a surprising discovery was made: for Models 1, 5, and 6, in a very narrow range of stresses ($\Delta\sigma \leq 0.1$ kgf/mm^2) around the critical stress σ_e, there are <u>two</u> possible states for the EHL. That is, the free energy per pair has two minima as a function of density just as the upper electron valleys empty into the remaining (lower) valley. The higher density phase corresponds to partial occupation of the upper valleys, while the lower density phase corresponds to their complete depopulation. At T = 0, the true ground state of the system is the phase with the lowest ground state pair energy f_G, and there is a discontinuous change in the density as a function of stress, as the pair energy of the Ge(4:2)-like phase becomes greater than the pair energy of the Ge(1:2)-like phase. This is indicated in Fig. 2.9a by dotted lines. The possibility of such a discontinuous change in density has been noted independently by Kirczenow and Singwi,[2.25] but the sitution was less clear in their less precise calculations.

(This page for numbering sequence only.)

[Note added in proof: I have recently learned of another calculation by Kastal'skii[2.115] in which the possibility of two minima in the free energy in considered. However, this is a Hartree-Fock calculation (i.e. the correlation energy is omitted) and the changes in valence band structure with stress are neglected.]

It should be noted that the height of the energy barrier between the two minima is very small, only ≈0.004 meV ≈ 0.05 K; so that for a typical experiment at T = 1.5 to 2 K, it would be expected that both minima would be accessible to the e-h pair system. Mathematically, the double minimum can occur because the free energy is nearly constant over a wide range in density, i.e., $\left(\frac{\partial f_{kin}}{\partial n}\right)_T \approx -\left(\frac{\partial f_{Coul}}{\partial n}\right)_T$ over a wide range in density. Whether two minima result, as in Model 1, or only one minimum, as in Model 2, depends very sensitively on the details of the correlation energy. Because the Model 1 correlation energy was fit by a polynomial containing as many parameters as data points,[2,57] it is possible that the double minimum is a mathematical artifact.

Whether or not a discontinuous change occurs in the density, it is clear from Fig. 2.9 that the equilibrium density should change by a factor of two in a very narrow range of stress, perhaps 0.2 kgf/mm^2, showing very clearly the stress for which $E_f^e = E_{spl}^e$. It is difficult to draw firm conclusions from the available experimental data (discussed in the next section) in this very interesting range of stresses.

For the corresponding case of Si in Fig. 2.10, the density decrease associated with the depopulation of the upper electron valleys is somewhat smaller and is more gradual than Ge. In order to understand this, a series of artificial models was constructed for Ge-type bands. In each model, the hole kinetic energy and the Coulomb energy were calculated as in Model 1. The electron kinetic energy was computed in the usual way, with the following exception: instead of three bands being

raised in energy while the fourth band was lowered, ν_2 bands went up while one went down. The ground state equilibrium densities for these models are shown in Fig. 2.13. Thus, for example, the curve with $\nu_2 = 3$ corresponds to real Ge. The curve with $\nu_2 = 2$ corresponds (qualitatively) to Si, since the electron valley degeneracy changes by the same factor of 3. It is clear from this figure that the most important ingredient in the density change is related to the change in the degeneracy; more precisely, it is the change in the fractional occupation of the lowest band(s) between low and high stresses. For the extreme case considered in the upper curve, this fractional occupation changes between low and high stresses by a factor of 10; the discontinuous change at $-\sigma \approx 3$ kgf/mm^2 invovles a factor of 2 change in the fractional occupation accompanied by a factor of 5 change in the density. For real Ge, of course, the fractional occupation changes by an overall factor of 4 and for real Si by a factor of 3. Using similar reasoning we can also understand why there are only slight kinks in the curves of Figs. 2.9 and 2.10 associated with the depopulation of the light hole band. The fractional occupation of the light holes at zero stress (see Table 2.2) is only 14% for Si and 4% for Ge. Thus the heavy hole occupation is only slightly affected by the emptying of the other valence band. Indeed, the kink in the curves for Ge is even smaller than in the curves for Si.

It would be very interesting if nature provided a real system with a very large change in the fractional occupation of a band. In a particular alloy, Ge_{1-x} Si_x, with $x \approx 0.15$ to 0.20, the four Ge-like conduction band minima along ⟨111⟩ directions and the six Si-like

minima along ⟨100⟩ directions are degenerate.[2.77] Thus this system contains ten nearly equivalent electron valleys at zero stress (the masses of the two types of bands differ[2.78]). With the application of stress along the ⟨111⟩ direction, the (111) valley corresponding to the stress direction would be lowered in energy by $|\Xi_u\sigma/3C_{44}|$ with respect to the average band shift, the other (111) valleys would be raised by $|\Xi_u\sigma/9C_{44}|$ with respect to the average, and all the (100) valleys would be unchanged with respect to the average.[2.39] Thus the conduction band degeneracy would change from 10 to 7 to 1 under increasing ⟨111⟩ stress for this particular Ge-Si alloy. In such a system with a larger change of fractional occupation than in Ge, an experimental study vs. stress should give much insight into the nature of this proposed phase transition.

23.3. Comparison with Experiment: The Approach to the Infinite Stress Limit

Figure 2.14 shows the equilibrium density as a function of stress for Ge at T = 2K, a typical temperature used in experiments. The two curves correspond to Models 1 and 2. For this low temperature, it was assumed that the (exciton) gas pressure outside the EHL was still relatively low; consequently the equilibrium density of the liquid was assumed to be that corresponding to zero gas pressure, i.e. at the minimum of f(n). It can be seen that Model 1 predicts a discontinuous density change even at T = 2K, as discussed in Section 23.2 for the ground state. Also shown in the figure are several sets of experimental results, all obtained at temperatures in the range T = 1.8-2.1K. The solid circles are the data of Feldman, et al.;[2.16] the solid triangles are the result of Thomas and Pokrovskii;[2.18] the solid squares are the

results of Chou et al.[2.17] These experiments were all performed on uniaxially stressed Ge. The + symbol indicates the average result obtained in the Berkeley group[2.28, 2.80] for the strain-confined liquid. The data displayed in the figure were all obtained by fitting luminescence spectra using Eqs. (2.38) and (2.39), using the energy-dependent hole density-of-states masses from Fig. 2.1 (or a reasonable approximation). For the uniform-stress experiments, the stress was determined from the applied force and the cross-sectional area of the sample, while for the experiments on the strain-confined liquid the maximum strain at the bottom of the well was determined from the shift of the luminescence spectrum.[2.13] As can be seen from the figure, theory and experiment are in reasonable agreement over the entire range of stresses included in current experiments. The rapid or discontinuous density change associated with the emptying of the upper electron valleys is not as pronounced as predicted by theory. However, it is possible that at realistic experimental temperatures the rapid change is washed out due to the finite temperature. A definitive conclusion about this interesting range of stresses must await more detailed experiments and theoretical analysis of the effect of the temperature. At greater stresses, the general trend of the data is to decrease with stress more rapidly than the theoretical predictions. This point is discussed in somewhat more detail below.

A word is in order concerning possible sources of problems in interpreting the experimental results, due to stress inhomogeneity. It is always difficult to perform an experiment with really uniform stress. A region of high stress near the surface will attract EHD to

the surface, where there are rapid recombination centers. As a result, the EHL luminescence should exhibit a short lifetime and should be broadened due to the range of stresses being sampled. In the "uniform-stress" experiments discussed here,[2.16-2.18] care was taken to assure the uniformity of the stress. Any residual non-uniformity can be taken into account by noting that the densities will represent upper limits. For the case of the strain-confined liquid,[2.28] the strain gradient is understood[2.31] and the spectra are fitted only when the strain gradient has a negligible effect on the deducted density.[2.79]

Experimental measurements of the ground state energy f_G are generally not available, since this entails a measurement of the exciton binding energy E_x as well as the binding energy ϕ of the EHL with respect to excitons (see Eq. (2.46)). However, a few measurements of ϕ are available for stressed crystals and may be compared with theory. Ohyama et al.[2.75] found a reduction of several tenths of an meV between zero stress and $-\sigma \approx 4$ kgf/mm^2 in Ge. Quantitative comparison cannot be made with theory, however, since the results of Ref. 2.75 were analyzed using an incorrect zero-stress value for ϕ. Furneaux et al.[2,28, 2.80] found $\phi \cong 1$ meV for the strain-confined liquid at $-\sigma \approx 6$ kgf/mm^2, which can be compared with a theoretical value of 0.89 meV for Models 1 and 2. In uniformly stressed Ge, Feldman et al.[2.16] measured $\phi = 0.65 \pm 0.07$ meV for $-\sigma = 13$ kgf/mm^2, compared to 0.64 meV for Model 1 and 0.60 meV for Model 2. In Si, Wolfe and Gourley[2.21] measured $\phi = 1.5 \pm 0.5$ meV for the strain-confined liquid at a stress $-\sigma = 90$ kgf/mm^2; the theoretical values are 1.78 meV (Model 1) and 1.95 meV (Model 2). Agreement between theory and experiment is quite

satisfactory. All of the experimental values were obtained spectroscopically, by fitting the EHL and exciton luminescence spectra.

The electron and hole Fermi energies E_f^e and E_f^h, their sum E_F^{tot}, and the luminescence linewidth ΔE, defined to the full width at half maximum of a spectrum computed according to Eqs. (2.38) and (2.39), are shown for Model 1 at T = 2K in Fig. 2.15 for Ge and in Fig. 2.16 for Si. Also shown are the energy splittings E_{spl}^e and E_{spl}^h between the upper and lower bands for electrons and holes. The critical stresses σ_e and σ_h are as follows, for both Models 1 and 2:

$$\left.\begin{aligned} -\sigma_e &\approx 2.6 \text{ kgf/mm}^2 \\ -\sigma_h &\approx 6.5 \text{ kgf/mm}^2 \end{aligned}\right\} \quad \text{Ge, T = 0, (111) stress} \qquad (2.49)$$

$$\left.\begin{aligned} -\sigma_e &\approx 10 \text{ kgf/mm}^2 \\ -\sigma_h &\approx 36 \text{ kgf/mm}^2 \end{aligned}\right\} \quad \text{Si, T = 0, (100) stress} \qquad (2.50)$$

The general features in the two figures are similar. At low stress, the electron Fermi energy is forced to increase the the upper electron valleys depopulate; the hole Fermi energy remains nearly constant. For Si the relative increase in E_F^e is smaller, since the fractional occupation of the lower valleys has a smaller change. Before the stress σ_e is reached, however, the decrease in density becomes more pronounced and both Fermi energies begin to decrease. For stresses greater (in magnitude) than σ_e, the electron Fermi energy decreases following the decrease in density, since there are no further changes in the conduction band structure or degeneracy. Between the stresses σ_e and σ_h the hole Fermi energy increases as the light hole band depopulates, but this is a smaller effect than for the electrons at low stresses since the fractional

occupation changes by a smaller amount, as discussed in Section 23.2. The hole Fermi energy remains nearly constant between σ_h and $\approx 2\sigma_h$ while at the same time the density decreases, due to the residual nonparabolicity of the valence band. Eventually the nonparabolicity is reduced sufficiently that the hole Fermi energy and the density both decrease and finally level off. The origin of the decrease in density at high stresses is the change in the hole mass, which is due to the residual interaction between the valence bands. From Figs. 2.1 and 2.2, as the stress increases the average density-of-states hole mass decreases. When such a mass decrease occurs without a change in band degeneracy (as discussed below in the context of mass renormalization), the equilibrium density decreases and the Fermi energy decreases by a smaller amount.

Experimental results for the Fermi energies and linewidth in Ge have been omitted from Fig. 2.15, but the trends can be seen by comparison with Fig. 2.14. An initial increase in the electron Fermi energy is observed,[2.17, 2.18] followed by a gradual decrease for stresses greater (in magnitude) than σ_e. However, the magnitude of the increase is reduced, and the hole Fermi energy is actually observed to decrease, since the density decreases more quickly in experiment than predicted by theory in this stress range. The hole Fermi energy is found to be approximately independent of stress between $\approx\sigma_h$ and $\approx 2\sigma_h$, which approximately corresponds to the maximum stress used in the experiments.

The comparison between theory and experiment for stressed Si is less extensive than for Ge because less data are available. In addition, as discussed in Sec. 22.3, luminescence spectra have been fit using the

infinite-stress hole mass, with the resulting deduced densities substantially in error. Comparison can still be made using the luminescence linewidth, however, and the available data are shown in Fig. 2.16. The square is the zero stress result of Hammond, et al;[2.50] the circle is from Kulakovskii and Timofeev[2.19] for uniaxial stress; and the triangles are the data of Gourley and Wolfe [2.20, 2.21, 2.81] for the strain-confined liquid. The stress is estimated from the shift of the luminescence spectrum.[2.14] As for Ge, the equilibrium density apparently decreases more rapidly with stress than predicted by theory.

The Fermi energies in Figs. 2.15 and 2.16 can be used to predict the electric charge on EHD in stressed Ge and Si. An EHD can become charged because the chemical potentials of the electrons and holes differ. As discussed by Rice,[2.82] the electron and hole contributions to the Coulomb energy are nearly equal, so the sign of the chemical potential difference is given by the difference in Fermi energies. A further contribution from the surface dipole layer[2.82] should change the magnitude, but not the sign, of the predicted difference and hence of the charge.[2.58] According to this line of reasoning, if $E_F^h > E_F^e$, then holes are less tightly bound to the EHD than electrons. More holes than electrons will evaporate until the work functions and evaporation rates become equal, and the EHD will attain a negative charge. Thus from Fig. 2.15, EHD should have a negative charge for stresses smaller in magnitude than $\approx 2 kgf/mm^2$ or greater than ≈ 5.5 kgf/mm^2 and a positive charge for stresses between these two values, for Ge uniaxially stressed along the ⟨111⟩ direction. Note that the stresses

at which EHD are predicted to change sign are very close to the critical stresses σ_e and σ_h. In addition, since the ideal system, Ge(1:2), corresponds approximately to stresses just greater than σ_e, these predictions are in agreement with those of Kalia and Vashishta[2.58] for all the ideal systems they analyzed in detail. Pokrovskii and Svistunova[2.83, 2.84] have measured the charge on EHD in Ge uniaxially stressed along ⟨111⟩; they found that drops are negatively charged in unstressed Ge,[2.83] change sign at $-\sigma \approx 2$ kgf/mm^2,[2.84] and remain positively charged at least until $-\sigma \approx 9$ kgf/mm^2.[2.84] The last result is difficult to interpret since spectra obtained by the same authors at a similar stress indicate[2.18] that the hole Fermi energy is greater than the electron Fermi energy. Further experiments at higher stresses are needed to resolve this discrepancy. The results obtained at lower stresses, however, are in excellent agreement with these predictions. The charge on EHD in Si can be predicted from Fig. 2.16, using the same arguments. Since the hole Fermi energy is larger than the electron Fermi energy for all stresses, EHD are predicted to be negatively charged at all stresses, in contrast to the situation in Ge. Note however that the difference $E_F^h - E_F^e$ becomes rather small near σ_e so that the magnitude of the charge should be greatly reduced. The ideal intermediate-stress model, Si(2:2), considered by Kalia and Vashishta[2.58] does not correspond precisely to any point on the graph; however, their prediction of neutral charge for this configuration is consistent with the results presented here. There are no experimental results concerning the charge on EHD in Si.

It should be noted from Figs. 2.15 and 2.16 that the total Fermi

energy E_F^{tot} and the linewidth ΔE do not have the same stress dependence. The differences can be seen more vividly in Fig. 2.17, in which the ratio $E_F^{tot}/\Delta E$ is plotted as a function of stress for Models 1 and 2, both for Ge and for Si. The ratio tends to increase as one or more bands empty out and to decrease as the valence band non-parabolicity becomes less important. It is clear from this and from the discussion in Sec. 22.3 that it is important to fit luminescence spectra using the correct band structure at the actual experimental stress.

We now consider the observation that the density decreases more rapidly with stress than predicted by either Model 1 or Model 2. One possibility is that the Coulomb energy may not really be a universal function of density. It can be seen in Figs. 2.9 and 2.10 that Models 3 and 4 for Ge and Model 4 for Si predict significantly lower densities than Models 1 and 2 at high stresses. It is also noteworthy that for these models the EHL is unbound with respect to excitons for stresses greater than 12 kgf/mm^2 (Model 4) or 22 kgf/mm^2 (Model 3) in Ge or 44 kgf/mm^2 (Model 4) in Si, as in Figs. 2.11 and 2.12. However, luminescence from the liquid phase has been observed in both Ge and Si at stresses greater than that for which Model 4 predicts no binding. A second possibility is that the masses used in the kinetic energy could be incorrect. The masses described in Sec. 22 are correct for bulk Ge and Si, ignoring the effect of the split-off valence band. As mentioned in Sec. 23.1, the inclusion of the split-off band would result in a slightly smaller hole mass at high stresses

(for the bulk material). The possibility of the renormalization of the electron and hole masses within the EHL due to many-body effects was considered by Rice[2.85, 2.86] for the case of unstressed Ge. He found that both the electron and hole masses should be ≈10% larger in the EHL than in bulk Ge and that the renormalization is approximately isotropic. By studying luminescence spectra from unstressed Ge in magnetic fields up to 190 kOe, Störmer and Martin[2.52, 2.87] found that the electron and hole masses are indeed renormalized by about 10% in the EHL, in agreement with theory;[2.86, 2.87] a similar result was obtained from a study of the magnetoplasma resonance in unstressed Ge.[2.88] Neither theory nor experiment has been performed for stressed Ge or for Si.

It is straightforward to estimate the effect of a systematic (uniform) change in the carrier masses on the predicted ground-state properties of the EHL and on their stress dependences. Suppose that the electron and hole masses are multiplied by a factor β in the kinetic energy, and that the Coulomb energy is unchanged; then the minimum in the pair energy is recomputed as a function of stress. The resulting new curves for n_0 vs. stress are qualitatively very similar to the curves in Figs. 2.9 and 2.10 for both Models 1 and 2; however, for a mass increase of 10%, the equilibrium density increases by ≈30% and the Fermi energies and luminescence linewidth increase by ≈8%. On the other hand, in extracting the density from a fit of the luminescence lineshape, the experimental densities would increase by ≈15% for the same linewidth. Thus, for example, in Fig. 2.14, the agreement between theory and

experiment for unstressed Ge would be somewhat reduced but would still be satisfactory.

The impetus for studying the EHL in stress semiconductors is that the band structure becomes simpler and theoretical models become more accurate; for "high enough" stresses even the valence band becomes simple. However, in comparing experimental results obtained at finite stresses to theoretical predictions for the infinite-stress limit, it is of crucial importance to understand what constitutes a stress "high enough" that the valence band nonparabolicity has a negligible effect on the properties of the EHL, or else to have a good method for extrapolation to infinite stress. An important conclusion drawn from the preliminary calculation on Ge[2.23, 2.26] and re-emphasized above is that the ground state properties are still changing at stresses much greater than σ_h. This is illustrated in Figs. 2.18 and 2.19, where the equilibrium density and the luminescence linewidth are plotted as a function of $1/\sigma$ for Models 1 and 2. In Fig. 2.18 the densities for Ge, including data points, are replotted from Figs. 2.9 and 2.14 along with the linewidths from Fig. 2.15. Note, for example, that the density is still twice the predicted infinite-stress value at $-\sigma \approx 20 kgf/mm^2$ for Model 1 and at $-\sigma \approx$ kgf/mm^2 for Model 2. These stresses are greater than the maximum achieved to date in experiments. In order to obtain densities within 20% of the infinite-stress value, stresses greater than $-\sigma \approx 80$ kgf/mm^2 would have to be obtained. In Fig. 2.19 the densities for Si are replotted from Fig. 2.10 along with the linewidths from Fig. 2.16, including data points. For both Models 1 and 2 the density is still twice the infinite-stress value at $-\sigma \approx$ 35-40 kgf/mm^2 and approaches to within 20% of the infinite-stress

value at $-\sigma \approx 140$ kgf/mm^2. However, because the experimental densities apparently decrease more quickly with stress in both Ge and Si than predicted by theory, these guidelines for extrapolation to the infinite-stress limit may require modification. In addition, the extrapolation of Thomas and Pokrovskii[2.18] for Ge, which was based on a model similar to Model 2, must be regarded as approximate due to the relatively poor fit to the data. Experiments at higher stresses are clearly desirable in order to clarify the approach to the infinite-stress limit.

A further general observation can be made from Figs. 2.18 and 2.19. In part because the Fermi energy varies more slowly than the density at a given stress, and in part because of the variation of $E_F^{tot}/\Delta E$ with stress illustrated in Fig. 2.17, the linewidth ΔE approaches the infinite-stress value more rapidly than the density. Thus the apparent levelling off of the luminescence linewidth with stress does not necessarily indicate that the infinite-stress limit has been achieved.

24. Results: Finite Temperature

In the previous section the results fro the ground state (i.e., T = 0) properties of the EHL in stressed Ge and Si were presented and disucssed. For the purpose of comparison with experiment some data, for example the luminescence linewidth at low temperatures, were presented. In this section we extend the theory to the calculation of the variation of EHL properties with temperature. At low temperatures we shall be interested in the systematic variations, which involve derivatives of the pair energy near the minimum, while at higher temperatures we shall be interested in the critical point of the e-h gas-liquid system.

24.1 Low Temperature Variations; Compressibility

As noted in Sec. 22.5, in all calculations to date of properties of the EHL, the Coulomb energy has been taken to be independent of temperature;[2.9] the same assumption is made here. The entire temperature dependence of the free energy per pair is contained in the kinetic energy contribution:

$$f(n,T) = f_{kin}(n,T) + f_{Coul}(n,0) \quad . \tag{2.51}$$

The procedure for calculating the kinetic energy exactly was outlined in Sec. 22. At low temperatures, however, it is natural to treat the finite temperature as a perturbation and use an expansion. For example,[2.89] let

$$I(T) \equiv \int_0^\infty g(E)\ h(E,E_F,T)\ dE \quad , \tag{2.52}$$

where $g(E)$ is any function of the energy E and $h(E,E_F,T)$ is the Fermi distribution function from Eq. (2.8). If $0 < kT/E_F(T) \ll 1$ (i.e. if the system is degenerate[2.30]), then

$$\begin{aligned} I(T) &\approx \int_0^{E_F(T)} g(E)dE + \frac{\pi^2}{6}\, g'(E_F(T))(kT)^2 \\ &\approx \int_0^{E_F(0)} g(E)dE + g(E_F(0))(E_F(T) - E_F(0)) \\ &\quad + \frac{\pi^2}{6}\, g'(E_F(0))(kT)^2 \quad . \end{aligned} \tag{2.53}$$

Here the prime denotes a derivative with respect to E, and $g'(E_F) = g'(E)\big|_{E=E_F}$; the temperature appropriate for E_F is indicated explicitly. In the last line, it is assumed that $\left|[g'(E_F(T)) - g'(E_F(0))]/g'(E_F(0))\right| \ll 1$. Thus

$$\begin{aligned} I(T) &= I(0) + g(E_F(0))\ (E_F(T) - E_F(0)) \\ &\quad + \frac{\pi^2}{6}\, g'(E_F(0))\ (kT)^2 \quad . \end{aligned} \tag{2.54}$$

If $g(E) = \mathcal{D}(E)$, for example, then $I(T) = I(0) = N$ (see Section 22.1). Note that if some bands are raised in energy by E_{spl}, then an additional condition for the validity of this expansion is $0 < kT/(E_F(T) - E_{spl}) \ll 1$. For a finite temperature T, there will be a range of stresses for which this condition is not satisfied (see discussion below).

It is of interest to consider the low-temperature variations of three quantities: the equilibrium density, the chemical potential, and the total Fermi energy. It is customary[2.22] to define the parameters δ_n, δ_μ, and δ_E as follows:

$$n(T) = n_0[1 - \delta_n(kT)^2] \quad , \qquad \delta_n \text{ in meV}^{-2} \tag{2.55a}$$

$$\mu(T) = \mu(0) - \delta_\mu(kT)^2 \quad , \qquad \delta_\mu \text{ in meV}^{-1} \tag{2.55b}$$

$$E_F(T) = E_F(0)\ [1 - \delta_E(kT)^2] \quad , \qquad \delta_E \text{ in meV}^{-2} \quad . \tag{2.55c}$$

Because of the complications which are introduced due to the band splitting and nonparabolicity, the derivation will be outlined. It is

convenient to discuss the variation of the free energy with temperature by introducing the heat capacity at constant volume, which is defined as follows:[2.30]

$$C_v \equiv \left(\frac{\partial u}{\partial T}\right)_{N,V} = T\left(\frac{\partial S}{\partial T}\right)_{N,V} \quad . \tag{2.56}$$

We wish to make use of the expansion derived above. If $g(E) = \mathcal{D}(E)E$ then $I(T) = U(T)$ and

$$\begin{aligned} U(T) - U(0) &= E_F(0)\mathcal{D}(E_F(0))(E_F(T) - E_F(0)) \\ &+ \frac{\pi^2}{6}\left[\mathcal{D}(E_F(0)) + E_F(0)\mathcal{D}'(E_F(0))\right](kT)^2 \end{aligned} \tag{2.57}$$

In order to evaluate the quantity $E_F(T) - E_F(0)$, use the fact that N is to be held constant; i.e., use Eqs. (2.52) and (2.54) again, giving:

$$\mathcal{D}(E_F(0))(E_F(T) - E_F(0)) = -\frac{\pi^2}{6}\mathcal{D}'(E_F(0))(kT)^2 \quad . \tag{2.58}$$

Substituting into Eq. (2.57), we obtain

$$U(T) - U(0) = \frac{\pi^2}{6}\mathcal{D}(E_F(0))(kT)^2 \tag{2.59}$$

and thus

$$C_v = \frac{\pi^2}{3}\mathcal{D}(E_F(0))k^2T \quad . \tag{2.60}$$

It is convenient to rewrite the heat capacity as follows:

$$C_v = N\gamma T \tag{2.61}$$

where

$$\gamma \equiv \frac{\pi^2}{3}k^2\frac{\mathcal{D}(E_F(0))}{N} \quad . \tag{2.62}$$

From Eq. (2.56), if $C_v \propto T$, then $S = C_v$. Furthermore, using Eqs. (2.59), (2.60), and (2.3)

$$U(T) = U(0) + 1/2\ TS$$

$$F(T) = U(0) - 1/2\ TS = F(0) - 1/2\ TS \quad . \tag{2.63}$$

For the kinetic energy per particle, we obtain

$$f_{kin}(n,T) = f_{kin}(n,0) - 1/2\,\gamma T^2 \tag{2.64a}$$

$$= f_{kin}(n,0) - 1/2\left(\gamma^e(n) + \gamma^h(n)\right)T^2 \quad . \tag{2.64b}$$

Note that γ is a function of the density via the Fermi energy, and that the contributions from the electrons and the holes must be included separately. The density of states may be written explicitly in Eq. (2.62) from Eq. (2.18), yielding the following expression, for electrons or holes:

$$\gamma = \frac{\pi^2k^2}{2}\left[\frac{\nu_1 m_1^{3/2}(E_F(0))(E_F(0))^{1/2}}{\frac{3}{2}\nu_1\int_0^{E_F(0)} m_1^{3/2}(E)E^{1/2}dE}\right. \tag{2.65}$$

$$\left.\frac{+\ \nu_2 m_2^{3/2}(E_F(0))(E_F(0) - E_{spl})^{1/2}}{+\ \frac{3}{2}\nu_2\int_{E_{spl}}^{E_F(0)} m_2^{3/2}(E)(E - E_{spl})^{1/2}\,dE}\right] .$$

Usually the density of states per unit volume at the Fermi level, $\mathcal{D}(E_F(0)/V$, increases with density more slowly than the density $n = N/V$. However, when the fractional occupation of the upper ν_2 bands is small (but nonzero), the denisty of states changes faster than the density. Thus from Eq. (2.62) $\gamma^e(n)$ and $\gamma^h(n)$ are monotonically decreasing functions of the density except in a narrow range of densities just greater than those corresponding to $E_F^e(0) = E_{spl}^e$ or $E_F^h(0) = E_{spl}^h$. As a result we might expect anomolous features in quantities depending on $\gamma(n)$ at stresses just below σ_e and σ_h. The functions $\gamma^e(n)$ and $\gamma^h(n)$ are continuous at all densities but have a discontinuity in slope at the densities corresponding to $E_F^e(0) = E_{spl}^e$ and $E_F^h(0) = E_{spl}^h$, respectively. For these special densities, then, the conditions for the validity of the low-T expansion are violated. For all other densities, the conditions may be fulfilled by restricting the expansion to temperatures which are sufficiently low.

First consider the quantity δ_n, which describes the variation in the equilibrium density with temperature. Let

$$n(T) = n_o + \Delta n \tag{2.66}$$

be the equilibrium density at the temperature T (recall that $n(0) = n_o$). Using Eqs. (2.51) and (2.64),

$$f(n,T) = f(n,0) - (1/2)\,\gamma(n)T^2 \quad . \tag{2.67}$$

At low temperature $\left(\frac{\partial f}{\partial n}\right)_T = 0$ at the equilibrium density. Thus

$$\begin{aligned} f'(n_o+\Delta n,T) &= 0 = f'(n_o+\Delta n,0) - (1/2)\gamma'(n_o+\Delta n)T^2 \\ &= \Delta n f''(n_o,0) - (1/2)\,\gamma'(n_o)T^2 \end{aligned} \tag{2.68}$$

to first order, where the primes denote derivatives with respect to density with T held constant. The curvature of the free energy for the ground state is denoted

$$f_G'' = f''(n_o,0) \tag{2.69}$$

This curvature is related to the isothermal compressibility K_T, which is defined [2.30] via

$$K_T \equiv -\left(V\left(\frac{\partial P}{\partial V}\right)_{N,T}\right)^{-1} \tag{2.70a}$$

$$= \left(n\left(\frac{\partial P}{\partial n}\right)_{N,T}\right)^{-1} \tag{2.70b}$$

$$= (2n^2 f' + n^3 f'')^{-1} \quad . \tag{2.70c}$$

The last line uses the definition of the pressure given in Eq. (2.6a). Now Eq. (2.70c) is a general definition valid at any density and temperature. For the ground state

$$K_T(n_o) = (n_o^3\, f_G'')^{-1} \tag{2.71}$$

Using Eqs. (2.66)-(2.71) and the definition of δ_n in Eq. (2.55a), we

obtain

$$\delta_n = \frac{\gamma^{e'}(n_o) + \gamma^{h'}(n_o)}{2n_o f_G'' k^2}$$
$$= -\frac{n_o^2 K_T(n_o)\left(\gamma^{e'}(n_o) + \gamma^{h'}(n_o)\right)}{2k^2} \quad . \tag{2.72}$$

In order to understand δ_n, it is necessary to understand what happens to the compressibility as well as to γ^e and γ^h; the latter quantities are discussed above. Figure 2.20 shows the compressiblity of the ground state of the EHL versus stress for Ge; Fig. 2.21 shows the results for Si. In both Figs. Models 1 and 2 are shown. From Eq. (2.71), the compressibility depends on the density and on the second derivative f_G'' of the free energy. The second derivative was caluclated numerically. For Ge, the very large increase in the compressibility just below σ_e is due to the fact that the free energy versus density is nearly flat, as discussed in Sec. 23.2; as a result f_G'' becomes very small and K_T very large. Part of the increase in the compressibility is due to the decrease in the density. This also gives rise to the increase in K_T just below σ_e in Si and just below σ_h in both Ge and Si; the subsequent decrease in K_T is due to an increase in f_G''. Most experiments which are sensitive to the compressibility do not involve a <u>direct</u> measurement of K_T. (It should be noted that the measurement for Ge discussed in Chapter 5 requires a strain well and therefore only involves the EHL at stresses greater than σ_e). Since the predicted increase in the compressibility just below σ_e is so large both in Ge and in Si, it would be very interesting to obtain direct experimental

measurements in this range of stresses.

The results for δ_n are shown in Fig. 2.22a for Ge and in Fig. 2.23a for Si. The stress dependence appears rather complicated but is just a combination of the components in Eq. (2.72). Note that for most stresses γ^e and γ^h decrease with density, so that δ_n is positive. Thus, from Eq. (2.55a), the EHL expands slightly with temperature. This is of course the situation which is familiar from unstressed Ge and Si. However, at stresses just below σ_e and σ_h, δ_n becomes negative, implying an initial <u>increase</u> in density with temperature, i.e. thermal contraction. Because of the restricted range of conditions for which the thermal contraction is predicted, and becuase of the difficulties in the measurement of all of the quantities describing the systematic changes of EHL properties with temperature, the observation of a negative value for δ_n would be very difficult indeed (but very interesting).

Next consider the quantity δ_μ, which describes the variation in the chemical potential μ with temperature. At low temperature $\left(\frac{\partial f}{\partial n}\right)_T \approx 0$, so that using Eqs. (2.6b), (2.66), and (2.67) we have

$$\mu(T) = f(n(T),T) = \mu(0) - 1/2\ \gamma(n_o)T^2 \tag{2.73}$$

to first order. Using the definition in Eq. (2.55b),

$$\delta_\mu = \frac{\gamma(n_o)}{2k^2} = \frac{\gamma^e(n_o) + \gamma^h(n_o)}{2k^2} \quad , \tag{2.74}$$

where the contributions from the electrons and holes are indicated explicitly. The results for Ge and Si are shown in Figs. 2.22b and 2.23b. The enhancement just below the stresses σ_e and σ_h shows the behavior of $\gamma(n)$ at the associated densities. The structure near σ_e in Ge occurs in a narrower range of stresses than in Si because the large density change occurs in a narrower range of stresses, as seen in Figs. 2.9 and 2.10. The discontinuity in Model 1 for Ge arises from the discontinuity in the density, which was discussed in Sec. 23.2.

Finally consider the quantity δ_E, which describes the variation in the total Fermi energy $E_F^{tot} = E_F^e + E_F^h$ with temperature. Now the Fermi energy actually depends on both the density and the temperature, as can be seen from Eq. (2.19). Let

$$\begin{aligned} E_F(n(T),T) &= E_F(n(0),0) + [E_F(n(T),T) - E_F(n(0),T)] \\ &+ [E_F(n(0),T) - E_F(n(0),0)] \qquad (2.75) \\ &= E_F(n(0),0) + \Delta E_1 + \Delta E_2 \quad . \end{aligned}$$

Thus there are two contributions to the change in the Fermi energy: ΔE_1 is from the change in E_F with density, at constant temperature, while ΔE_2 is from the change in E_F with temperature, at constant density. At low temperature, the contribution ΔE_1 is the same as that for $T = 0$. Using Eqs. (2.66) and (2.55a), we obtain

$$\Delta E_1 = \Delta n \frac{\partial E_F(n = n_o,0)}{\partial n} = -n_o \delta_n \frac{\partial E_F(n_o,0)}{\partial n} (kT)^2 \quad . \qquad (2.76)$$

Note that this expression is true for E_F^e, E_F^h, and their sum. The second contribution may be obtained using Eq. (2.54) with $I(T) = I(0) = N$ for $g(E) = \mathcal{D}(E)$, as follows:

$$\Delta E_2 = -\frac{\pi^2}{6} \frac{\mathcal{D}'(E_F(n_o))}{\mathcal{D}(E_F(n_o))} (kT)^2 \quad . \qquad (2.77)$$

Separate contributions are required for electrons and for holes. Thus the variation in the total Fermi energy with temperature may be written as follows, using Eqs. (2.55c) and (2.75)-(2.77):

$$\delta_E = \delta_{E1} + \delta_{E2} \qquad (2.78)$$

where

$$\delta_{E1} = \delta_n n_o \frac{\frac{E_F^e(n_o,0)}{\partial n} + \frac{E_F^h(n_o,0)}{\partial n}}{E_F^e(n_o,0) + E_F^h(n_o,0)} \qquad (2.79a)$$

$$\delta_{E2} = \frac{\pi^2}{6} \frac{Q_e(E_F^e(n_o,0)) + Q_h(E_F^h(n_o,0))}{E_F^e(n_o,0) + E_F^h(n_o,0)} \qquad (2.79b)$$

$$Q_{e,h}(E_F) = \frac{\nu_1 \frac{d}{dE_F}\left(m_1^{3/2}(E_F)\, E_F^{1/2}\right) + \nu_2 \frac{d}{dE_F}\left(m_2^{3/2}(E_F)\,(E_F - E_{spl})^{1/2}\right)}{\nu_1 m_1^{3/2}(E_F)\, E_F^{1/2} + \nu_2 m_2^{3/2}(E_F)(E_F - E_{spl})^{1/2}} \quad . \qquad (2.79c)$$

In the last expression the density of states is written explicitly. The quantity δ_E is dominated by the first contribution δ_{E1}, due to the change in the equilibrium density, except at stresses just below σ_e

and σ_h, where δ_{E2} becomes more important, due to the rapid change in the density of states at the Fermi level. The results for δ_E are shown in Figure 2.22c for Ge and in Figure 2.23c for Si. These curves are very similar to the curves in Figs. 2.22a and 2.23a for δ_n, with the exception just mentioned. Note that it is easy to verify that the expressions given in Eqs. (2.72), (2.74), and (2.78) for δ_n, δ_μ, and δ_E simplify to the usual expressions[2.22] for unstressed Ge and Si.

Table 2.5 gives numerical results for these quantities at the same stresses for which the ground state results were given in Table 2.4. In comparing Models 1 and 2, it is useful to keep two things in mind: First, the two models are supposed to be similar, as discussed in Sec. 23.1. Secondly, however, the quantities displayed in Table 2.5[17] depend on derivatives of the free energy (and related quantities) and sometimes on high powers of the equilibrium density. Agreement for these quantities thus requires very detailed similarity between the models. The second remark also applies to comparison between theory and experiment. The experimental data are very sparse. Zero-stress values are listed in Table 2.5 and are in reasonable agreement with theory. Feldman et al.[2.16] have measured δ_n at 13 kgf/mm^2 in Ge and find $\delta_n = 6.7 \pm 2.0$ meV^{-2}, to be compared with theoretical values of 5.1 and 3.4 meV^{-2} for Models 1 and 2 at that stress. The agreement is reasonably good. No other experimental measurements of δ_n, δ_μ, or δ_E have been published for stressed Ge or Si.

24.2. The Critical Point; Phase Diagram

At low temperatures, as seen in the previous section, the properties of the electron-hole liquid vary as T^2. This is the usual situation for a degenerate Fermi system, such as an ordinary metal at room

temperature. For the EHL, at stresses which are not too close to σ_e or σ_h, the properties vary as T^2 over approximately the same temperature range for which the gas pressure outside the liquid is low enough to be considered negligible. At higher temperatures the gas in equilibrium with the liquid cannot be neglected. (If enough is known about the properties of the gas, the entire phase diagram can be constructed theoretically, using Eq. (2.5); a crude attempt is discussed later in this section). At sufficiently high temperatures, there is no longer a separation into liquid and gas phases. The liquid and gas become indistinguishable and the substance is usually called a fluid.[2.30] The temperature above which there is no phase separation is the critical temperature T_c, and the equilibrium density of the fluid at that temperature is the critical density n_c. Thermodynamically, the definition of the critical point is as follows:[2.30]

$$\left(\frac{\partial P}{\partial V}\right)_{T,N} = \left(\frac{\partial^2 P}{\partial V^2}\right)_{T,N} = 0 \quad . \tag{2.80}$$

Using the condition that the number of particles N is constant, the derivatives with respect to V may be transformed to derivatives with respect to n; then

$$\left(\frac{\partial P}{\partial n}\right)_{T,N} = \left(\frac{\partial^2 P}{\partial n^2}\right)_{T,N} = 0 \quad . \tag{2.81}$$

The definitions for P and μ in Eq. (2.6) may then be used, yielding a convenient definition of the critical point:

$$\left(\frac{\partial \mu}{\partial n}\right)_T = \left(\frac{\partial^2 \mu}{\partial n^2}\right)_T = 0 \quad . \tag{2.82}$$

Thus the critical point corresponds to the inflection point in the chemical potential versus density.

The critical point has been determined numerically as a function of stress for Ge and Si, using the exact calculation of $f_{kin}(n,T)$ described in Sec. 22, a temperature-independent Coulomb energy, and Eqs. (2.6) and (2.82). In order to obtain meaningful results for Model 1, it was necessary to modify the correlation energy. The correlation energy was originally fit to a power series, similar to those given in Ref. 2.58. As a result of this fitting procedure, there are slight anomolies in the higher derivatives; note that the definition of the critical point depends on the second and third derivatives of $f_{corr}(n)$. In order to avoid this mathematical problem, the original correlation energy was fit to a Wigner form (corresponding to Eq. (2.44) with only a single term) at intermediate densities and extended to higher and lower densities. This is reasonable since the correlation energy should be of this form for densities less than that corresponding to $r_s = 2$,[2.57] i.e., $n = 5 \times 10^{15}$ cm^{-3} for Ge and $n = 2.5 \times 10^{17}$ cm^{-3} for Si (r_s is defined in Eq. (2.45b)). This modified form for the Model 1 correlation energy was used only for the determination of the critical point.

The critical temperature and critical density as a function of stress in Ge are shown in Figs. 2.24 and 2.25, for Models 1 and 2. Similarly, the results for Si are shown in Figs. 2.26 and 2.27. The

results for the two models are quite similar, considering the sensitivity of the critical point to the details of the correlation energy. Both models show behavior that might be expected: a gradual decrease in both T_c and n_c with stress, including a more rapid change associated with the depopulation of the upper electron valleys. The reduction in T_c follows from the decrease in the magnitude of the ground state energy $|f_G|$ (see below), and the decrease in n_c approximately follows the decrease in the ground state density n_o, except in the immediate vicinity of σ_e.

Numerical results for the critical point at selected values of the stress are given in Table 2.5. Also included are experimental results at zero stress. Only a few experimental measurements have been made of the critical point in stressed Ge and Si. Feldman et al.[2.16] found $T_c = 3.5 \pm 0.5$ K and $n_c = 7.7 \pm 2.0 \times 10^{15}$ cm^{-3} at a stress of $-\sigma = 13$ kgf/mm^2 in uniaxially stressed Ge. Furneaux et al.[2.80] found $T_c = 4.7$-5.7 K at a stress of $-\sigma \approx 6$ kgf/mm^2 for the strain-confined liquid in Ge. Gourley and Wolfe have revised an early estimate[2.20] of $T_c \sim 4$K ($-\sigma = 55$ kgf/mm^2) to[2.21] $12\text{K} \leq T_c < 22\text{K}$ at $-\sigma = 90$ kgf/mm^2 for the strain-confined liquid in Si. For Ge, the calculations presented here apparently overestimate T_c and underestimate n_c. This discrepancy may be due to a temperature dependence of the Coulomb energy, which was ignored here. The results[2.90, 2.91] for T_c in unstressed Si are in remarkably good agreement with the theoretical values given in the table. For stressed Si the situation is less clear due to the uncertainty in the data. It should be noted in comparing results for the strain-confined liquid with theoretical or experimental values for uniaxially stressed crystals that the presence of the strain well does

not affect the critical point. This is easily seen from the form of the definition of the critical point which is commonly used for ordinary fluids:[2.30] above T_c only a single phase exists, no matter how great the pressure. However, the experimental manifestation of the approach to the critical point may be even more complicated than for uniaxially stressed or unstressed[2.92] crystals.

Comparison can also be made to other theoretical calculations of the critical point, which have been performed using Eq. (2.67), i.e., an expansion to T^2 in the kinetic energy. The results for this calculation are shown in Table 2.5 for Model 5 at zero stress and Model 6 at infinite stress. These models are practically identical to those used by Vashishta et al.[2.7] but the results are seen to differ substantially. This is due to an error in the calculation of Ref. 2.7, and those results have now been revised, in agreement with the values in the table.[2.57, 2.6] Other estimates made for unstressed Ge[2.8, 2.9, 2.93] and Si[2.8] are in remarkably good agreement with the values given here considering that different approximations were used for the Coulomb energy and that the critical point is so sensitive to the details of the Coulomb energy. A calculation[2.10] in which the kinetic and exchange energies were calculated at finite temperature and the correlation energy was neglected differs substantially, as might be expected. Liu and Liu[2.27] have recently calculated the critical point at two values of the stress for Ge and Si, using the T^2 expansion of Eq. (2.67) for the kinetic energy and a model similar to Model 6 for the Coulomb energy; taking this into account, their results are in reasonable agreement with the results presented in Figs. 2.24-2.27 at the same stresses. In an

alternate type of approach, the effect of the temperature may be approximated by including fluctuations in the density of the liquid and the gas at temperatures near the critical point.[2.94] Reinecke et al.[2.95,2.9] have recently used this approach to estimate the critical point for the ideal systems Ge(4:2), Ge(1:2), Ge(1:1), Si(6:2), Si(2:2), and Si(2:1). For all six cases, T_c is lower and n_c is higher than the values listed in Table 2.5, where the intermediate-stress model systems are compared with the stress which is close to σ_e. In the droplet fluctuation model[2.94-2.96] the calculation is based on a T^2 expansion.

It must be emphasized, however, that for calculations at temperatures near T_c the expansion in T^2 is no longer valid and should be replaced by an exact calculation such as that described in Sec. 22 and used here. The low-T expansion is only valid if $0 < kT/E_F$ and $kT/(E_F - E_{spl}) \ll 1$ for both electrons and holes. As discussed in Section 24.1, this condition breaks down even at relatively low temperatures at stresses just below σ_e and σ_h. In addition, the condition breaks down at the critical point for <u>all</u> stresses in both Ge and Si. The quantities $kT_c/E_F^e(n_c,T_c)$ and $kT_c/E_F^h(n_c,T_c)$ fall outside the range (0. to 0.25) for Model 1 in Ge, and outside the range (0. to 0.75) for Model 2; for Si these quantities fall outside the range (0. to 1.0) for both models. It is surprising, then, that reasonable agreement is obtained between calculations in which the kinetic energy is computed exactly and those using the expansion.

In all of the calculations presented here as well as in the calculations by other authors discussed above, it is assumed that near the critical point the carriers can be considered to be an electron-hole plasma in the form of a liquid, a gas, or, above T_c, simply a fluid. In order to determine the validity of such a calculation, even if the plasma is properly treated as (possibly) non-degenerate, it is necessary to consider the possibility that the gas and fluid phases are not simply an e-h plasma. At low temperature the gas phase in equilibrium with the EHL consists primarily of excitons rather than free carriers.[2.22] (Because the gas pressure is very small, however, this does not affect the low-T equilibrium properties of the EHL, such as those compared with experiment in Section 23.3.) As the temperature is raised, the excitons are expected to ionize in some way, perhaps through a finite-temperature analog of a Mott transition.[2.97] If the excitons are screened by Debye-HUckel screening, then such a metal-insulator transition is expected to occur at a density given by[2.92]

$$n_{MI}(T) = \frac{(1.19)^2}{16\pi} \frac{kT}{E_x} a_x^{-3} \qquad (2.83)$$

where

$$E_x = \frac{e^2}{2\kappa a_x} \qquad (2.84)$$

(see Eq. (2.45)). For zero and infinite stress, the values for the exciton energy E_x from Eqs. (2.47) and (2.48) may be used, with a_x obtained from Eq. (2.84) and $T = T_c$ estimated from Table 2.5. The results are as follows:

$$n_{MI}(7.5K) = 3.0 \times 10^{15}\ cm^{-3} \quad \text{(Ge: zero stress)} \quad , \qquad (2.85a)$$

$$n_{MI}(3.8K) = 6.3 \times 10^{14}\ cm^{-3} \quad \text{(Ge: infinite ⟨111⟩ stress)} \quad , \qquad (2.85b)$$

$$n_{MI}(27K) = 5.6 \times 10^{16}\ cm^{-3} \quad \text{(Si: zero stress)} \quad , \qquad (2.86a)$$

$$n_{MI}(18.5K) = 3.0 \times 10^{16}\ cm^{-3} \quad \text{(Si: infinite ⟨100⟩ stress)} \quad . \qquad (2.86b)$$

For unstressed Ge and Si, it can be seen that the metal-insulator transition is expected (for this model of the screening) to occur at a density which is approximately an order of magnitude below the critical density. Thus it is not surprising that other calculations[2.98-2.100] which attempt to treat both excitons and e-h plasma in the gas phase give results for the critical point which do not differ greatly from those given in Table 2.5. These calculations[2.98-2.100] and others[2.101-2.103] are concerned with the mechanisms by which excitons are screened. In addition, Rice[2.104] and Sander and Fairobent[2.99] have addressed the question of whether or not a metal-insulator transition occurs in the gas phase, separate from the gas-liquid phase transition, possibly associated with a second critical point.[2.105] Far-infrared experiments on Ge[2.106] and luminescence experiments on Ge[2.107] and on Si[2.90, 2.91]

have been interpreted in terms of an e-h plasma gas phase near the critical point. On the other hand, the more detailed luminescence experiments of Thomas et al.[2.92, 2.108] have been interpreted in terms of excitons, excitonic molecules (biexcitons) and trions (charged complexes of the form eeh or ehh); in the density range for which spectra have been fitted, the luminescence intensity from free carriers is expected[2.108] to be negligible. Apparently, excitons (and perhaps complexes) are present at densities greater than $n_{MI}(T)$ from Eq. (2.83), indicating that the real screening may be weaker than in this model.

The situation for stressed Ge and Si is less clear. According to Eqs. (2.85b) and (2.86b) and Table 2.5, for the case of (static) Debye-Hückel screening the metal-insulator transition is predicted to occur at a density which is only approximately a factor of 2 below the critical density, for infinite stress. If the screening is reduced, analogous to the zero-stress case, then the metal-insulator transition would be expected to move to a density greater than n_c, in which case the gas phase near the critical point would consist of excitons (or excitons, trions, and biexcitons).

Thus experiments near the critical point at high stresses,[2.109] while extremely difficult, would be very interesting. If it is the case that a revised $n_{MI}(T_c) > n_c$, then for high stresses the critical point cannot be computed as described above, i.e., considering the gas to be an e-h plasma.

A related consideration involves the small values expected for ϕ at T = 0 and high stresses, which can be seen from Figs. 2.11 and, 2.12. If the gas phase is considered to consist entirely of excitons,

then, unless kT is less than $\phi(T)$, boiloff of excitons would occur so rapidly than EHD embryos would be prevented from growing to macroscopic size. This could result in a reduction of T_c from the estimates given in Figs. 2.24 and 2.26. The quantity $kT_c/\phi(T_c)$ may be roughly estimated using a finite-temperature analog of Eq. (2.46), an assumption that E_x is independent of T, and Eq. (2.55b) for the ground state energy. This quantity ranges from ≈0.38 to ≈0.46 for Ge and Si under infinite stress, where the critical point is estimated as for the figures for Models 1 and 2. Thus this consideration apparently does not require a revision of T_c to lower values than those already given. More detailed understanding is needed of screening mechanisms in both stressed and unstressed Ge and Si.

If the nature of the gas in equilibrium with the EHL is understood, then a phase diagram can be constructed using the equality of the gas and liquid pressures and chemical potentials from Eq. (2.5). Although it is clear from the discussion in the preceding paragraphs that the gas is not yet well understood, a few qualitative remarks can be made. The simplest description of the shape of the phase diagram near the critical point is in terms of the law of corresponding states,[2.110] which is obeyed very nicely by many simple classical fluids for $T/T_c \geq 0.60$. The shape of the phase diagram has also been computed for the EHL in unstressed Ge using a spin-1 lattice gas model[2.111] and is very similar to the law of corresponding states. The droplet fluctuation model[2.94] has also been used and, while the results are again similar to the law of corresponding states, small systematic variations have been found[2.95, 2.96] for different model systems for

Ge and Si under zero, "intermediate," and infinite stress. Using the plasma model described above, with the finite-temperature kinetic energy computed exactly and the Model 5 correlation energy for unstressed Ge, the phase diagram turns out to be somewhat broader than that predicted by the law of corresponding states; the liquid density is larger by a factor of ≈1.3 and the gas density is smaller by a factor of ≈2.0 than the law of corresponding states prediction for $T/T_c = 0.9$. Thus the plasma model gives substantial deviations on both liquid and gas branches from the model for simple fluids. Two independent measurements of the liquid branch in unstressed Ge[2.9, 2.107] agree well with the law of corresponding states for different values for T_c; the possibility of systematic differences in the methods of determining the temperature should not be overlooked. In addition, two sets of data for the gas branch,[2.92, 2.107] which are interpreted using different models for the composition of the gas phase, give lower densities than those predicted by the law of corresponding states or the plasma model. The deviation from the simple fluid model had been suggested earlier.[2.112] It should be noted that the law of corresponding states was invented[2.110] to explain data on simple fluids, in which the particles have pairwise interactions. This simple model should not really be expected to be valid for the electron-hole fluid in a semiconductor, in which the correlations among all the particles are important.

Finally, let us briefly consider a different type of scaling. It has been suggested[2.22] that certain combinations of properties of the electron-hole liquid should scale from one system to another. For example, the quantities[2.22, 2.23] ϕ/kT_c, $T_c/n_o^{1/2}$, n_c/n_o and $n_o^2 f_G''$

have been proposed as approximate scaling quantities. More recently, Reinecke et al.[2.95] have suggested on the basis of theoretical arguments that the quantities n_c/n_o, $|f_G|/kT_c$, and $kT_c\kappa/n_o^{1/4}$ should scale rather well between systems. The validity of these ideas can easily be tested by computing these quantities as a function of stress for Ge and Si, using both Models 1 and 2. The quantities which are found to scale reasonably well in all of these systems are as follows:

$$\frac{n_c}{n_o} \approx 0.1 \quad , \tag{2.87a}$$

$$\frac{|f_G|}{kT_c} \approx 9 \quad , \tag{2.87b}$$

$$\frac{kT_c\kappa^2}{n_o^{1/4}} \approx 0.08 \text{ cm}^{3/4} \quad . \tag{2.87c}$$

The variation in these quantities is about ±15%, with somewhat larger deviations for stresses near σ_e, as might be expected from the previous discussions. Smaller systematic variations are found between the models. Thus the ideas of scaling which were originally proposed for model systems are found to work rather well at all stresses for Ge and Si.

APPENDIX 2.1. COMPUTER PROGRAM FOR THE HOLE MASSES

The computer program used to generate the hole masses was written in a general format in order to facilitate changing the stress direction or the material. It would be very easy, for example, to generate masses for ⟨100⟩ stress in Ge, although this has not been done. The parameters listed in Table 2.1 are supplied as data, along with a parameter specifying the stress direction (⟨100⟩ , ⟨110⟩, or ⟨111⟩). The value of the stress is also supplied as data, allowing calculations for tension (stress > 0) as well as compression (stress < 0). To obtain output as a function of reduced energy E' = E/|stress|, a value ±1 is generally entered for the stress. (The program does not perform the calculation using the unit E'.) However, other reduced units are used internally: k is given in units of $k_0 = 10^6$ cm^{-1} and energies are in units of $E_0 = \hbar^2 k_0^2/(2\, m_0) = 2.6247$ meV. In all output the energy is expressed in meV. The integrals are computed as described in Sec. 22.2. The optical mass components are calculated as in Eq. (2.27) and combined according to Eqs. (2.30) and (2.31). The local density-of-states masses are calculated as in Eq. (2.15). The integrated density-of-states mass is computed directly, not by integrating the local mass. Equation (2.9) can be written as an integral over k instead of energy:

$$N = \frac{V}{4\pi^3} \int_0^{k_F} \int k^2 dk d\Omega \qquad (2.1.1)$$

$$= \frac{V}{4\pi^3} \frac{1}{3} \int k^3 d\Omega \quad ;$$

in the second line the integral is performed over the k-space surface with energy E_F. Using the definition of the integrated mass in Eq. (2.16), then

$$m_{dint}^{3/2}(E) = \frac{\hbar^3}{4\pi(2E)^{3/2}} \int k^3 d\Omega \qquad (2.1.2)$$

where the surface now has energy E. Other quantities computed in the program include the density in each band and the fractional density in the light hole band. The program was written in FORTRAN IV and was run on the Berkeley CDC 6400 computer. A listing of the program follows.

```
      PROGRAM HOLES(INPUT,OUTPUT,PUNCH)
C        COMPUTE MASSES FOR TWO WARPED HOLE BANDS AS FOUND IN GE OR SI
C        READ IN MATERIAL MATER (A5 FORMAT)
C                INVERSE MASS PARAMETERS A, B, C IN UNITS OF
C                    (HBAR**2)/(2.*M0)
C                DEFORMATION POTENTIALS BD, DD IN MEV
C                LOW-TEMPERATURE ELASTIC STIFFNESS CONSTANTS C11, C12,
C                    C44 IN KGF/(MM**2)
C                STRESS DIRECTION PARAMETER NTD = 1 FOR (100), 2 FOR
C                    (110), 3 FOR (111)
C                NUMBER OF POINTS NT, NP FOR THETA, PHI INTEGRALS
C                LOWER AND UPPER INDICES IEFO, IEFM FOR COMPUTING FERMI
C                    LEVEL
C        SUPPLY SEPARATE FUNCTION ENRGY(IEF) TO COMPUTE FERMI LEVEL,
C            WHERE IEF RUNS FROM IEFO TO IEFM
C        COFF = 2.*M0/( (HBAR**2)(KO**2) )  IN MEV,
C            WHERE KO = 10**6 CM**-1
C        COFN = KO**3/(3.*PI**2)  IN CM**-3
      PI=3.141592?
      COFF=2.62465?
      COFN=3.377373E16
   99 READ 3, MATER
      IF(MATER.EQ.5H      ) GO TO 99
      READ 1, A,B,C,BD,DD,C11,C12,C44
      BD=BD*COFF
      DD=DD*COFF
      ASQ=A*A
      BSQ=B*B
      CSQ=C*C
      BBD=B*BD
      ENDD=2.*DD*SQRT(3.*BSQ+CSQ)
   91 READ 2, NTD,NT,NP,IEFO,IEFM,NPNCH
      IF(NTD.EQ.0) GO TO 99
      READ 1, TD
      CI=2./NT
      CJ=2.*PI/NP
      CIJ=CI*CJ
      CNCN=8.*PI/(3.*CIJ)
      GO TO (31,32,33),NTD
C        100 UNIAXIAL STRESS
   31 NDIR=5H1  0
      EPSY=-C12/((C11-C12)*(C11+2.*C12))*TD
      EPSZ=EPSY
      EPSX=-EPSY*(C11+C12)/C12
      EPSXY=0.
      EPSYZ=0.
      EPSZX=0.
      GO TO 40
C        110 UNIAXIAL STRESS
   32 NDIR=5H1 10
      EPSX=C11/(2.*(C11-C12)*(C11+2.*C12))*TD
      EPSY=EPSX
      EPSZ=-2.*C12/C11*EPSX
      EPSXY=-TD/(4.*C44)
      EPSYZ=0.
      EPSZX=0.
      GO TO 40
```



```
C        111 UNIAXIAL STRESS
   33 NDIR=5H1 1 1
      EPSX=TD/(3.*(C11+2.*C12))
      EPSY=EPSX
      EPSZ=EPSX
      EPSXY=TD/(6.*C44)
      EPSYZ=EPSXY
      EPSZX=EPSYZ
   40 CONTINUE
      EPSYX=EPSY-EPSX
      EXXYY=(EPSX-EPSY)**2+(EPSY-EPSZ)**2+(EPSZ-EPSX)**2
      EXYZ=EPSXY*EPSXY+EPSYZ*EPSYZ+EPSZX*EPSZX
      ETR=EPSX+EPSY+EPSZ
      EEESQ=.5*BD*BD*EXXYY+DD*DD*EXYZ
      EEF=SQRT(EEESQ)
      PRINT 10, NDIR,TD,MATER
      IF(NPNCH.NE.0) PUNCH 11, NDIR,TD,MATER
      PRINT 18, A,B,C,BD,DD,C11,C12,C44,NT,NP
      PRINT 12
C        FERMI ENERGY LOOP
      DO 80 IEF=IEFO,IEFM
      EFD=ENRGY(IEF)
      EF=EFD*COFF
      EF2=EF-2.*EEF
      EPR=EF-EEF
      EEP=EEESQ-EPR*EPR
      AINT01=0.
      AINT11=0.
      AINT21=0.
      AINT31=0.
      AINT41=0.
      AINT51=0.
      AINT61=0.
      AINT71=0.
      AINT02=0.
      AINT12=0.
      AINT22=0.
      AINT32=0.
      AINT42=0.
      AINT52=0.
      AINT62=0.
      AINT72=0.
      AN2=0.
      AMDL2=0.
      AM22=0.
C        PHI INTEGRAL
      DO 50 J=1,NP
      PHI=CJ*J
      CP=COS(PHI)
      SP=SIN(PHI)
      CP2=CP*CP
      SP2=1.-CP2
      SCP=SP*CP
      CSP=CP2-SP2
      P1=EPSX*CP2+EPSY*SP2
      P2=CP2*SP2
      P3=EPSZX*CP+EPSYZ*SP
```

```
      P4=SCP*CSP*2.
      P5=EPSYZ*CP-EPSZX*SP
C        THETA INTEGRAL
      DO 50 I=1,NT
      CT=CI*I-1.
      CT2=CT*CT
      ST2=1.-CT2
      ST=SQRT(ST2)
      SCT=ST*CT
      CST=CT2-ST2
      EEKSQ=BBD*(2.*(ST2*P1+CT2*EPSZ)-ETR) + ENDD*(ST2*SCP*EPSXY+SCT*P3)
      BPR=BSQ+CSQ*ST2*(CT2+ST2*P2)
      APR2=(ASQ-BPR)*2.
      DPR=EEKSQ*2.*A*EPR
      DP1=SQRT(DPR*DPR+APR2*2.*EEP)
C        1ST PART FOR PLUS SIGN IN SOLVING QUADRATIC. MINUS SIGN IN
C            EXPRESSION FOR E(K)
C        DENSITY-OF-STATES MASSES
      AKSQ=(DPR+DP1)/APR2
      ER=A*AKSQ-EPR
      DEDK=2.*A-(2.*BPR*AKSQ+EEKSQ)/ER
      AK=SQRT(AKSQ)
      AINTO1=AINTO1 + AK/DEDK
      AINT11=AINT11 + AK*AKSQ
C        OPTICAL MASSES
      ER2=2.*ER
      COFCT=2.*CSQ*SCT*(CST+2.*ST2*P2)
      COFCP=CSQ*ST2*ST*P4
      DEKDT=BBD*6.*SCT*(P1-EPSZ) + ENDD*(2.*EPSXY*SCT*SCP+CST*P3)
      DEKDP=BBD*6.*ST*SCP*EPSYX + ENDD*(EPSXY*ST*CSP+CT*P5)
      DEDT=-(AKSQ*COFCT+DEKDT)/ER2
      DEDP=-(AKSQ*COFCP+DEKDP)/ER2
      DEDR=ST*DEDK+CT*DEDT
      DEDX=CP*DEDR-SP*DEDP
      DEDY=SP*DEDR+CP*DEDP
      DEDZ=CT*DEDK-ST*DEDT
      AID=AKSQ*AK/DEDK
      AX=DEDX*AID
      AY=DEDY*AID
      AZ=DEDZ*AID
      AINT21=AINT21 + DEDX*AX
      AINT31=AINT31 + DEDY*AY
      AINT41=AINT41 + DEDZ*AZ
      AINT51=AINT51 + DEDY*AX
      AINT61=AINT61 + DEDX*AZ
      AINT71=AINT71 + DEDY*AZ
      AKSQ=(DPR-DP1)/APR2
      IF(AKSQ.LE.0.) GO TO 50
C        2ND PART FOR MINUS SIGN IN SOLVING QUADRATIC. PLUS SIGN IN
C            EXPRESSION FOR E(K)
C        DENSITY-OF-STATES MASSES
      ER=EPR-A*AKSQ
      DEDK=2.*A+(2.*BPR*AKSQ+EEKSQ)/ER
      AK=SQRT(AKSQ)
      AINTO2=AINTO2 + AK/DEDK
      AINT12=AINT12 + AK*AKSQ
C        OPTICAL MASSES
```



```
      ER2=2.*ER
      DEDT= (AKSQ*COFCT+DEKDT)/ER2
      DEDP= (AKSQ*COFCP+DEKDP)/ER2
      DEDR=ST*DEDK+CT*DEDT
      DEDX=CP*DEDR-SP*DEDP
      DEDY=SP*DEDR+CP*DEDP
      DEDZ=CT*DEDK-ST*DEDT
      AID=AKSQ*AK/DEDK
      AX=DEDX*AID
      AY=DEDY*AID
      AZ=DEDZ*AID
      AINT22=AINT22 + DEDX*AX
      AINT32=AINT32 + DEDY*AY
      AINT42=AINT42 + DEDZ*AZ
      AINT52=AINT52 + DEDY*AX
      AINT62=AINT62 + DEDX*AZ
      AINT72=AINT72 + DEDY*AZ
   50 CONTINUE
C        CALCULATE MASSES CORRESPONDING TO 1ST PART OF INTEGRATION
      AINTO1=AINTO1*CIJ/(2.*PI*SQRT(EF))
      AMDL1=AINTO1**(2./3.)
      AINT11=AINT11*CIJ/(4.*PI)
      AMD1=AINT11**(2./3.)/EF
      AN1=AINT11*COEN
      GO TO (51,52,53),NTO
C        OPTICAL MASSES FOR 100 STRESS
   51 AMOHHL=AINT21
      AMOHHT=.5*(AINT31+AINT41)
      GO TO 60
C        OPTICAL MASSES FOR 110 STRESS
   52 AMOHHL=.5*(AINT21+AINT31) + AINT51
      AMOHHT=.25*(AINT21+AINT31) + .5*AINT41 - .5*AINT51
      GO TO 60
C        OPTICAL MASSES FOR 111 STRESS
   53 Z=(AINT21+AINT31+AINT41)/3.
      ZZ=(AINT51+AINT61+AINT71)/3.
      AMOHHL=Z + 2.*ZZ
      AMOHHT=Z - ZZ
   60 CN=CNCN*AINT11
      AMOHHL=CN/AMOHHL
      AMOHHT=CN/AMOHHT
      AMOHH=3./(2./AMOHHT + 1./AMOHHL)
      PRINT 13, EF0,AN1,AMDL1,AMD1,AMOHHL,AMOHHT,AMOHH
      IF(NPNCH.NE.0) PUNCH 14, EF0,AN1,AMDL1,AMD1,AMOHHL,AMOHHT,AMOHH
      ANTOT=AN1
      AMOL=AMOHHL
      AMOT=AMOHHT
      AMO=AMOHH
      FRAC=0.
      IF(AINT12.EQ.0.) GO TO 75
C        CALCULATE MASSES CORRESPONDING TO 2ND PART OF INTEGRATION
      AINTO2=AINTO2*CIJ/(2.*PI*SQRT(EF2))
      AMDL2=AINTO2**(2./3.)
      AINT12=AINT12*CIJ/(4.*PI)
      AMD2=AINT12**(2./3.)/EF2
      AM2=AINT12*COEN
      GO TO (61,62,63),NTO
```

```
C        OPTICAL MASSES FOR 100 STRESS
   61 AMOLHL=AINT22
      AMOLHT=.5*(AINT32+AINT42)
      GO TO 70
C        OPTICAL MASSES FOR 110 STRESS
   62 AMOLHL=.5*(AINT22+AINT32) + AINT52
      AMOLHT=.25*(AINT22+AINT32) + .5*AINT42 - .5*AINT52
      GO TO 70
C        OPTICAL MASSES FOR 111 STRESS
   63 Z=(AINT22+AINT32+AINT42)/3.
      ZZ=(AINT52+AINT62+AINT72)/3.
      AMOLHL=Z + 2.*ZZ
      AMOLHT=Z - ZZ
   70 CN=CNCN*AINT12
      AMOLHL=CN/AMOLHL
      AMOLHT=CN/AMOLHT
      AMOLH=3./(2./AMOLHT + 1./AMOLHL)
      PRINT 13, EFO,AN2,AMDL2,AMD2,AMOLHL,AMOLHT,AMOLH
      IF(NPNCH.NE.0) PUNCH 14, EFO,AN2,AMDL2,AMD2,AMOLHL,AMOLHT,AMOLH
C        CALCULATE COMBINED OVERALL MASSES
      ANTOT=AN1 + AN2
      AMOL=ANTOT/(AN1/AMOLHL + AN2/AMOLHL)
      AMOT=ANTOT/(AN1/AMOLHT + AN2/AMOLHT)
      AMO=3./(2./AMOT + 1./AMOL)
      FRAC=AN2/ANTOT
   75 PRINT 15, EFO,ANTOT,FRAC,AMOL,AMOT,AMO
      IF(NPNCH.NE.0) PUNCH 14, EFO,ANTOT,FRAC,AMOL,AMOT,AMO
   80 CONTINUE
      GO TO 91
    1 FORMAT(10F8.2)
    2 FORMAT(16I5)
    3 FORMAT(A5)
   10 FORMAT(1H1,27X,A5,* STRESS TO = *,F8.2,* IN *,A5/)
   11 FORMAT(5X,A5,* STRESS T= = *,F8.2,* IN *,A5)
   12 FORMAT(6X,*E(MEV)*,14X,*N*,10X,*MDLOC*,10X,*MDINT*,9X,*MOLONG*,
     . 9X,*MOTRAN*,10X,*MOTOT*/38X,*FRAC*/)
   13 FORMAT(6X,F6.2,6(5X,E10.4))
   14 FORMAT(F6.2,6(1X,E10.4))
   15 FORMAT(6X,F6.2,2(5X,E10.4),15X,2(5X,E10.4)/)
   18 FORMAT(38X,*A = *,F5.2,5X,*B = *,F5.2,5X,*C = *,F5.2 / 38X,
     . *B' = *,F5.2,* MEV*,5X,*DJ = *,F5.0,* MEV* / 27X,*C11 = *,F6.0,
     . 5X,*C12 = *,F6.0,5X,*C44 = *,F6.0,* KGF/MM2* / 44X,*NT = *,I3,
     . 5X,*NP = *,I3 / )
   99 CALL EXIT
      END
```


APPENDIX 2.2. CALCULATION OF THE KINETIC ENERGY AT FINITE TEMPERATURE

The evaluation of the integrals in Eqs. (2.19) and (2.20) to the necessary precision at finite temperature is described in this Appendix. For electrons, the integrals are simply Fermi-Dirac integrals,[2.113] where

$$F_j(y) \equiv \int_0^\infty x^j (e^{x-y} + 1)^{-1}\, dx \qquad (2.2.1)$$

is the Fermi-Dirac integral of order j. (There should be no confusion in notation with the total free energy F.) For $y \leq 0$ and for $y \gg 1$ asymptotic expansions which coverge rapidly can be used. In the intermediate range, a 25-point Gaussian quadrature was found to be accurate. The crossover points separating the ranges of y were chosen so that the final functions were adequately smooth.

In the calculation of f^e_{kin}, the electron Fermi level is calculated given the density n, via Eq. (2.19). The inversion of this equation is equivalent to solving an equation of the form

$$g(x) - \text{const.} = 0 \quad . \qquad (2.2.2)$$

The Newton-Rapson iteration scheme,[2.114] for which

$$x_{n+1} = x_n - \frac{g(x_n) - \text{const.}}{\frac{dg}{dx}(x_n)} \quad , \qquad (2.2.3)$$

converges very rapidly since g(x) is a monotonic and "nice" function. The derivative dg(x)/dx is easily evaluated by noting that for $j > 0$ (Ref. 2.113)

$$\frac{dF_j(y)}{dy} = jF_{j-1}(y) \qquad (2.2.4)$$

The evaluation of Eqs. (2.19) and (2.20) for the holes involves the computation of "modified Fermi-Dirac integrals," in which x^j is replaced by a more complicated function. A 25-point Gaussian quadrature works very well for most values of E_F^h/kT. Because of the functional form used for the masses, asymptotic forms are not available; for $E_F^h/kT \gg 1$ it was necessary to use brute force (i.e., the trapezoidal rule) in order to avoid overflow on the computer.

CHAPTER 3. EXPERIMENTAL DETAILS

This chapter contains a description of the apparatus used in the experiments described in this thesis. All of these experiments involve the observation of recombination luminescence from the electron-hole liquid and from free excitions in stressed and unstressed Ge. The basic apparatus used here is standard for such luminescence experiments. However, a special imaging technique was used in order to study luminescence from small selected regions of the crystal. In addition, some effort was required to obtain a sensitive and reliable detector for monitoring small signals.

The Ge samples are described in Section 31, including their preparation, mounting, and the application of stress. The overall setup is described in Section 32. The detector is described in Section 33. Finally, the imaging technique and related calibrations are described in Section 34.

31. Samples

The samples used in the experiments described in this thesis were cut from large single crystals of ultra-pure Ge grown by W. L. Hansen and E. E. Haller[3.1] at the Lawrence Berkeley Laboratory. The starting material was zone-refined. The single crystals were pulled from the melt by the Czochralski method in a pure hydrogen atmosphere. The samples were cut from crystals which were dislocation-free; such crystals always contain hydrogen-vacancy clusters.[3.1, 3.2] The Ge grown at LBL is used primarily for gamma ray detectors, and much effort has been expanded in the characterization of the crystals. Information about electrically active centers is presented here. The role of these centers as recombination centers and the resulting effects on the (nonradiative) EHL lifetime

are discussed in Section 55.

Shallow impurities may be studied by far-infrared Fourier Transform Spectroscopy.[3.1] The main acceptor is Al (ionization energy 10.2 meV) and the main donor is P (ionization energy 12.0 meV). The material is not highly compensated, i.e.,

$$\frac{N_A + N_D}{|N_A - N_D|} \leq 10 \quad , \tag{3.1}$$

where N_A and N_D are the concentrations of acceptors and donors respectively. In addition, for the samples studied here,

$$|N_A - N_D| \leq 10^{11}\ \text{cm}^{-3} \quad . \tag{3.2}$$

Deep levels may be studied by means of Hall effect measurements or Deep Level Transient Spectroscopy.[3.3] (This is important for particle detectors, since deep levels trap free carriers effectively.) An acceptor level at ~80 meV is always present in dislocation-free crystals grown in hydrogen; this level is believed[3.2] to be due to the hydrogen-divacancy complex. The concentration of these acceptors is ~2-4 x 10^{11} cm^{-3} in as grown crystals. This is the only deep acceptor which occurs at a measurably large ($\geq 2 \times 10^{9}$ cm^{-3}) concentration.

Other impurities which are known to be present include O (concentration $\leq 5 \times 10^{13}$ cm^{-3}), Si (concentration $\leq 10^{16}$ cm^{-3}), and H (concentration $\leq 10^{14}$ cm^{-3}). The concentrations given are appropriate for crystals pulled from quartz crucibles in hydrogen. None of these impurities is electrically active.

The samples used in this thesis are listed in Table 3.1. They were cut from LBL Boule No. 145 or 146. These two single crystals (boules) were grown under the same conditions and have the same characteristics (see Eqs. (3.1) and (3.2) above). The samples were cut with a diamond saw, with the edges oriented along crystal symmetry axes as described below. The results presented here were primarily obtained from crystals shaped like rectangular parallelopipeds and stressed along the ⟨111⟩ direction, although a few experiments were performed on disc-shaped samples stressed along ⟨110⟩. A ⟨111⟩ stress geometry results in the production of a single strain well,[3.4] which is necessary for measuring density profiles. For these samples, the face used for excitation had edges parallel to the ⟨111⟩ and ⟨11$\bar{2}$⟩ directions, with dimensions approximately 4 mm x 4 mm (see Table 3.1). The direction perpendicular to this face was ⟨1$\bar{1}$0⟩, and the thickness ranged from ≈1.4 to ≈2.8 mm. The primary samples were CR38 (thickness 1.75 mm) and CR50 (thickness 2.8 mm). The latter sample was selected for studying density profiles because the strain well was well separated from all surfaces so that a good baseline was obtained in the imaging experiments. Samples used in ⟨110⟩ stress experiments were cut into ≈4 mm-diameter discs with a (100) face, using an ultrasonic cutting tool. These samples were stressed off-center along the thickness, so that only one strain well was formed within the crystal. All samples were first lapped to remove saw damage, then etched in a $3HNO_3$:HF solution ("White" etch) for 1 to 2 min, followed by a methanol rinse. In certain cases the faces being used for imaging were further polished with Syton. Different surface preparations had surprisingly little

effect on the image quality, as discussed in Section 34.

Samples with square faces were mounted in a sample holder shown in Fig. 3.1. The sample rested on a flat quartz plate and was stressed from above by a nylon rod with a rounded tip. This nylon plunger was threaded on the opposite end and screwed into a brass plug on the end of a piece of thin-walled stainless steel tubing, in order to facilitate changing plungers. The force on the plunger was transmitted by the stainless steel tube from a calibrated spring arrangement outside the helium cryostat, shown in Fig. 3.2. The force applied to the sample could be varied up to approximately 23 kgf, depending on the spring which was used.

The success of the experimental measurement of density profiles was contingent on the formation of a strain well with a "nice" shape, as symmetric as possible. When two objects are pressed together, the shear strain maximum occurs in the interior of the objects, rather than at the surface. This is part of the solution to the Hertz contact problem,[3.5] which is discussed more fully in Refs. 3.4 and 3.6. The distance between the shear strain maximum and the contact surface depends on the contact area. Thus for experiments using a nylon plunger, the following precautions were taken. The end of the rod was carefully machined to provide a rounded surface with a radius of curvature of several mm. The sample was stressed at room temperature, typically with a force of ≈9 kgf. This procedure resulted in a contact area of $\geq 1\ mm^2$. For the density profile measurements a plunger with an exceptionally large radius of curvature was used, a larger force was applied initially (≈18 kgf), and a thicker sample was used; as a result

the contact area was larger, and the strain well formed in this sample was well separated from all surfaces and had a large volume (see Section 52). For experiments in which a nylon plunger was used, after the sample and plunger were cooled to helium temperatures the contact area remained relatively insensitive to changes in the applied force, as discussed in Section 42.2. In one experiment described in the same section a slightly rounded brass plunger was used to contact the sample through a thin (0.002 in.) sheet of mylar, in order to provide a good contact area; the stress was again applied at room temperature. In this case the contact area was found to increase considerably with applied force. If the mylar sheet was omitted with the brass plunger or if the stress was applied after cooling, it was usually found that small regions of high strain were formed very near the contact surface, which attracted EHD to rapid recombination centers at the surface. In many such cases a strain well did not form at all. Thus the procedure described above was necessary for the experiment to work.

The sample holder shown in Fig. 3.1 was arranged so that the sample could be viewed from three different mutually perpendicular directions. Luminescence was collected directly from the square face ("face view"), from the bottom via a mirror oriented at 45° and located below the sample ("end view" or "bottom view"), or from the side via another mirror oriented at 45° next to the sample ("side view"). The 45° mirrors were constructed from glass prisms with right triangular cross section cut to appropriate size with a diamond saw. The surface corresponding to the hypotenuse of the triangle either had been "silvered" commercially or was coated with an evaporated Ag layer ≥5000Å thick to provide a highly reflective surface. The prisms were

oriented to be front-surface mirrors. The sample holder and side mirror were designed to accommodate samples up to $\approx 9 \times 9 \times 4$ mm^3. The viewing arrangement allowed the selection of the view or views most suitable for a particular type of experiment and thus gave increased experimental flexibility.

32. Overall Setup

A schematic diagram of the overall setup is shown in Fig. 3.3. The light source used for the creation of e-h pairs was a Coherent Radiation Model 52 argon-ion laser, operated CW. The laser has been equipped with several different plasma tubes; the most recent one had a maximum output of approximately 4 W when new. Immediately in front of the laser was mounted a glass microscope slide oriented at 45°, in order to direct a small fraction of the laser output into a Spectra Physics Model 401 C power meter equipped with a Si photocell. It was important that the laser output remained stable throughout an entire set of scans, up to a few hours in total duration. For this purpose a laser stabilizer constructed by A. D. A. Hansen[3.7] was used, which eliminated laser drift for virtually indefinite periods of time. The laser output was filtered through at least 2.5 cm of H_2O to attenuate infrared radiation from the plasma tube.

A special mechanical chopper ("laser razor") was constructed to modulate the laser light. The chopper contained a 6 in. diameter Dural wheel driven by an 1800 rpm synchronous motor. The wheel had several windows with razor edges made from 0.001 in. stainless steel shim stock supported from both sides. Thus there was a well-defined chopping plane. The laser was focused onto the chopping plane and then brought back to parallel by a pair of 12.5 mm focal length Schneider-Kreuznach f/2.7

movie camera lenses. After a good deal of use it was found that the laser was significantly attenuated by these lenses (possibly due to degradation of the cement between elements of compound lenses), so they were recently replaced by a pair of 10 mm focal length, 8 mm diameter, single element plano-convex lenses. These lenses are mounted on translators which facilitate positioning the lenses properly. In particular, the distance from the input lens to the chopping plane must be determined very precisely, as discussed below.

For studies of the EHL in stressed Ge it was desirable to have the length of a laser pulse be ~2 msec, with the turn-on time $\Delta t \lesssim$ a few μsec, so that kinetic studies on the latter time scale would be possible. The turn-on time is given by the time required for the razor edge to pass through the laser beam and can in principle be made shorter either by speeding up the wheel or by making the laser beam diameter smaller. However, in practice the motor speed given above was held fixed. The beam diameter may be estimated as follows. Suppose that the intensity profile of the laser beam is Gaussian (this should be the case if the laser operates in the TEM_{00} or fundamental mode). The beam emerges from the laser with wavelength λ and diameter D_1, measured to the radial distance at which the intensity is reduced from its peak value by $1/e^2$. Suppose that a lens with focal length f is placed a distance L_1 from the laser. Then the laser beam will be focused to a diameter D_2 given by[3.8]

$$D_2 = \frac{4\lambda f}{\pi D_1} (1 + x^2)^{-1/2} \qquad (3.3a)$$

where

$$x = \frac{4\lambda(L_1 - f)}{\pi D_1^2} \quad . \tag{3.3b}$$

For the case at hand, use λ = 514.5 nm, D_1 = 1.5 mm, and $L_1 - f \approx 30$ cm. This gives

$$D_2 = 4.4 \times 10^{-4} f \quad . \tag{3.4}$$

Thus for f = 12.5 mm, $D_2 \approx 5.5$ μm. The turn-on time Δt may be estimated as follows:

$$\Delta t = D_2/v \quad , \tag{3.5}$$

where v is the velocity of the razor blade edge as it passes through the laser beam. Suppose that the laser beam is positioned 5 cm from the axis of rotation of the wheel. Then from Eqs. (3.4) and (3.5), $v \approx 940$ cm/sec and $\Delta t \approx 0.6$ μsec. Another important parameter is the depth of focus: how accurately the first lens must be positioned relative to the chopping plane, or how accurately the chopping plane must be defined, in order to obtain an acceptable value for Δt. The depth of focus may be described by the confocal parameter b, which is twice the distance from the focal plane (where the beam diameter is D2) to the point where the beam diameter is $\sqrt{2}\, D_2$. The confocal parameter is given by

$$b_2 = \frac{\pi D_2^2}{2\lambda} \quad . \tag{3.6}$$

For the above numerical example b_2 = 92 μm ≈ 0.004 in. Thus the turn-on time should have an extremely well-defined minimum as the position of the first lens is varied with respect to the chopping

plane. In practice the minimum was not so well-defined, and the turn-on time Δt was measured to be ≤4 μsec, considerably longer than predicted above. However, it should be noted that the laser does not operate only in the TEM_{00} mode, and it is known[3.8] that higher modes are broader spatially. In any case, the observed Δt was fast enough for all experiments described here.

Several wheels were made for the chopper. The wheel used for studies of the EHL in stressed Ge had 8 windows. The resulting waveform was a square wave. The on-time was measured to be ≈2.2 msec, which corresponds to a chopping frequency of 227 Hz and a rotation frequency of ≈28 Hz. This is slightly slower than the nominal frequency mentioned previously, due to loading by the wheel. Note that this window length is nearly optimum: if the EHL lifetime $\tau \approx 500$ μsec (see Sections 43.1 and 55) then the laser stays on (and then off) for about 4.4 τ. Assuming exponential decay, for example, the signal would be reduced to $e^{-4.4} \approx 1.2\%$ of its original value before the laser came on again. A second wheel with 24 windows was constructed for studies of unstressed Ge, where the lifetime is much shorter. The lifetime-to-window length ratio is not as favorable from the standpoint of optimizing signal collection; however, it was impractical to have more holes.

Just after the chopper another glass microscope slide was located at 45° with respect to the laser beam in order to select a fraction of the (chopped) beam for use as a reference signal. This secondary beam was detected with a Hewlett Packard 5082-4220 Si planar PIN photodiode. An amplification circuit is shown in Fig. 3.4. In some cases the reference signal was further amplified, as required by the subsequent electronics.

Location of the chopper in the excitation path rather than in the luminescence path served two purposes. First, it was possible to perform either steady-state or time-resolved experiments without moving components in the optical path. (An AC signal is required for maximum detector sensitivity.) In addition, since the laser was actually incident on the sample only half of the time, sample heating was reduced.

In the experiments presented in this thesis the laser excitation was varied over nearly 5 orders of magnitude. The laser output could be varied by a factor of ≈250 using the laser stabilizer to regulate the power supply current. Additional attenuation was obtained by the use of up to 3 Corning 7-98 glass neutral density filters, each with transmission ≈15%.

The laser beam was steered by a mirror (Fig. 3.3) into the optical cryostat and was focused to a ≥100 μm spot on the Ge surface by a lens. Several lenses were used throughout the course of this work, with focal lengths 8-12 cm. For the experiments reported here, the spot size on the Ge surface was not critical. The focused spot was accurately positioned on the excited Ge face by translating the laser focusing lens and was usually positioned near the strain well, so as to yield the maximum drop size.

The Ge sample was located in an optical helium cryostat designed by L. F. Mollenauer and constructed by the Physics Department machine shop. Special features of this cryostat include two strain-free quartz windows[3.9] mounted on opposite sides of the Dewar, allowing a light collection cone with half angle $\theta \approx 14°$, and a built-in split-coil superconducting magnet which required 1.2 Amp/kOe and routinely produced

magnetic fields up to ≈25 kOe. The magnetic field is directed along the optical axis. The sample holder must fit into a slot with dimensions 1.190 in. x 0.333 in. Helium bath temperatures as low as $T \approx 1.6$ K were achieved by mechanically pumping the vapor above the helium bath; the bath temperature was determined using a Hg manometer or a Zimmerli gauge. Most experiments described here were performed either in the range T = 1.7-1.9 K or at T = 4.2 K. At the lower temperatures the properties of the strain-confined EHL are nearly independent of temperature, and the bath temperature drifted by up to ≈0.2 K during the course of a day's run.

Luminescence from the Ge sample was collected through the window opposite to the excitation. For most of the experiments described in this thesis, a precision lens (Fig. 3.3) formed a magnified image of the luminescence on the entrance plane of a spectrometer, steered by a deflection mirror. The imaging system is described in detail in Section 34. A Corning 7-56 glass filter was used to remove visible light. In addition, for the largest luminescence signals obtained, it was necessary to attenuate the luminescence via a 10dB neutral density filter, in order to prevent saturation of the electronics. The spectrometer was a 1/4-meter f/3.5 scanning grating spectrometer, Jarrell-Ash Model 82-410, equipped with a 590 grooves/mm grating blazed for 1.2 μm radiation. Although efficiency vs. wavelength data were not provided for this grating, it may be estimated from the data for other gratings that the efficiency is ≈60% for $\lambda = 1.75$ μm radiation.

Standard spectrometer slits were used for obtaining luminescence spectra. For studying power dependences, 250 μm slits were used, with resolution (full width at half maximum of the slit function)

0.66 meV. When spectra were to be fitted, 150 μm slits were usually used, with resolution 0.40 meV.

The output of the spectrometer was contained in a light-tight tube arrangement, collected by a 2-1/2 in. focal length, 2 in. diameter, plano-convex quartz lens, and focused onto the front surface of a cooled Ge photodiode using approximately 1-1 optics. This detector and the first stage of amplification typically had a combined response time of 10 μsec and are discussed in Section 33. The amplified signal was then fed into a signal averager, in conjunction with the reference signal from the photodiode located just after the mechanical chopper. The signal averager output was routined to one or more of the following devices: a strip-chart recorder, a teletype terminal, or paper tape punch.

Several different signal averaging systems were used, depending on the experiment and the available equipment. In order to obtain steady-state spectra or spatial images, such as much of the data shown in Chapter 4, a PAR single-channel (Model 160) or dual-channel (Model 162) boxcar integrator was used, with a gate width of ~0.5 msec. In order to obtain images at discrete times after turn-off of the excitation the boxcar gate width was reduced to 10 μsec. The delay times ranged from 5 μsec to 2 msec. Note in addition that this time resolution is fast enough to allow some useful kinetic information to be obtained for EHD clouds in unstressed Ge (see Section 44.3).

In order to obtain the density profiles shown in Chapter 5, several changes were made. Since steady-state images were required, a PAR Model 186A synchro-het Lockin Amplifier was used. In order to reduce the effect of the phase shifts due to the diffent lifetimes in different

regions of the drop, the chopper (wheel and lenses) described above was replaced with a simple wheel having a window length of ≈5.9 msec; this chopper also provided a reference signal. The lockin output was fed into an 8-bit A/D converter and then punched onto paper tape. The gain of the lockin was always selected to be the maximum possible without saturating the A/D converter. The paper tape was read into the Physics Department's IBM 1620 computer and punched onto cards. Further processing was performed by the University of California's CDC 6400 computer. This cumbersome two-step process was necessary because the final program was too large for the 1620 computer and it was not possible to read paper tape into the 6400 computer.

The data discussed in Section 55 on the EHL lifetime were obtained using a Tracor-Northern Model 575 Signal Averager. This unit had a 20-bit 2048-channel memory which could be divided into quarters, and a minimum time per channel of 10 μsec. For these experiments the original chopper was used, so that the turn-off time was well-defined. When the memory was filled, its contents were printed on a teletype terminal.

Several photographic images of the strain-confined EHL are shown in Chapters 1 and 4. In order to obtain these photographs, the setup shown in Fig. 3.3 was modified as follows. The deflection mirror was removed. The imaging lens and a 75 mm focal length f/1.9 Wollensak Oscillo-amaton oscilloscope camera lens were used to form an image of the luminescence on an infrared-sensitive vidicon equipped with a Hamamatsu type N214 Pb salt vidicon image tube. The tube has maximum sensitivity for visible wavelengths, but has ≈10% of its maximum sensitivity at 1.75 μm. A polished 0.5 mm thick Si disc filters out visible-wavelength radiation. The vidicon signal is fed into a CRT video monitor and then photographed.

33. Detector

In order to study EHL luminescence at low excitation levels it is necessary to have a sensitive and stable detector. As discussed below, the detector used here was somewhat less sensitive than another one used in this group for studying low-temperature threshold phenomena;[3.10] however, it is still significantly more sensitive than cooled, commercial PbS detectors commonly used in other laboratories. It has the added advantage of faster response time, allowing sensitive studies of the kinetics of droplet phenomena. (PBS detectors have response times >100 μsec.)

The detector used in the experiments presented in this thesis was a cooled Ge PIN device made from ultrapure Ge by E. E. Haller of the[11] Lawrence Berkeley Laboratory. The dimensions were approximately 4-1/2 x 4-1/2 x 9-1/2 mm^3. Two opposite 4-1/2 x 9-1/2 mm^2 faces had diffused Li n^+ and evaporated Cr Schottky barrier contacts. The procedure for making the detector is exactly the same as for making a nuclear radiation detector and is outlined in Ref. 3.1. The detector was mounted between sheets of In foil, with a small amount of GaIn eutectic on the Li contact, in a cold-finger Dewar equipped with a quartz window. Figure 3.5 shows the mounting arrangement. The mounted sample was attached to a Cu plate, with a thin piece of mica for electrical isolation and thermal contact. This sample mounting plate was partially thermally isolated from the liquid nitrogen cold finger by stainless steel tubing standoffs. The degree of thermal isolation was determined by the length of the standoffs, which could be varied. Because of black-body radiation from the

room-temperature walls of the Dewar and because of the imperfect vacuum, the temperature of the detector crystal was higher than 77 K. Additional temperature increases could be provided by a heater, which consisted of a Zener diode. The temperature was monitored using a chromel-alumel thermocouple attached to the sample mounting plate.

The operation of the detector for EHL luminescence is similar in some respects to its operation as a nuclear radiation detector. The device is operated as a reverse biased photodiode. Free carriers created in the region depleted by the bias voltage are swept to the contacts by the internal electric field. The depletion width is given by:[3.11]

$$W = \left(\frac{2\varepsilon_o \kappa (V_{bi} + V)}{eC}\right)^{1/2} \tag{3.7}$$

Here κ is the dielectric constant, V_{bi} is the built-in potential in the junction, V is the applied reverse bias voltage, C is the net impurity concentration in the intrinsic region of the crystal ($|N_A - N_D|$ in cm^{-3}), ε_o is the permittivity of vacuum, e is the electronic charge and W is the depletion width in cm. For Ge, $V_{bi} \sim 0.2$ Volt which is $<<V$ in most cases, and $\kappa \approx 15.7$ for $T \sim 160$ K,[3.12] so that

$$W = (1.73 \times 10^7 \text{ V/C})^{1/2} \quad . \tag{3.8}$$

For a typical detector crystal $C \approx 10^{10}$ cm^{-3}, and the voltage is chosen to be large enough that the entire crystal is depleted (e.g., $W \geq 4.5$ mm if $V \geq 120$ Volt). A bias voltage of -180 V was actually used (see Fig. 3.7). The time t required for carriers to be collected may be estimated as follows:

$$t = D/v \quad , \tag{3.9}$$

where D is the thickness of the device and v is the carrier drift velocity. The drift velocity increases with the internal electric field but saturates at $v \sim 10^7$ cm/sec.[3.13] For the parameters given above, the internal field $E \approx 400$ V/cm, for which $v \sim 2 \times 10^6$ cm/sec at the operating temperature $T \approx 160$ K.[3.13] Thus the collection time $t \sim 0.2$ μsec. (Note that if no external bias voltage is applied, the built-in junction potential $V_{bi} \sim 0.2$ Volt would result in an estimated collection time $t \approx 110$ μsec for this device.)

In order to sustain voltages of the magnitudes given above without inducing breakdown via conduction across the surfaces of the device, it is necessary to house the crystal in a clean vacuum system. Hydrocarbons, CO_2, abd H_2O are particularly undesirable. The detector used here was housed in a brass Dewar equipped with standard O-ring seals. The vacuum space was continually pumped by a mechanical roughing pump through a room-temperature molecular sieve trap, in addition to the cryopumping provided by the nitrogen-cooled surfaces. The cold finger was kept filled with liquid nitrogen in order to keep the detector as clean as possible and to minimize thermal cycling. Although a better vacuum could be obtained using other methods, the detector mounted in this Dewar was found to have satisfactory and stable performance for over two years.

The previous paragraphs have indicated some features of the detector which are similar to those of a nuclear radiation detector. Features relating to the detection of EHL luminescence are described next. The possibility of using a Ge crystal to detect radiation emitted

below the indirect gap at liquid helium temperatures is a result of the decrease in the band gap with increasing temperature. Whereas Ge is transparent to EHL luminescence at ~4 K, at higher temperatures this radiation can be absorbed via an indirect transition and the rate of thermal generation of carriers across the gap can still be reasonably low. Figure 3.6 shows the relative detector response as a function of wavelength for several different detector temperatures. The light source was an incandescent lamp. The light was filtered to remove the visible portion of the spectrum and then run through the spectrometer to the detector. The temperature of the detector was varied using the heater shown in Fig. 3.5. The peak wavelengths for free exciton (FE) and electron-hole droplet (EHD) luminescence are indicated by arrows in Fig. 3.6. The detector response falls off for wavelengths greater than ~1.66 μm because of the change in absorption length, due in turn to the indirect gap. Acceptable quantum efficiency can be obtained if the absorption length is ≤ the depth of the detector crystal, here ~1 cm. The quantum efficiency can be increased by raising the temperature of the detector, at the expense of an exponential increase in the dark current due to thermally generated carriers. It turns out that the signal-to-noise ratio is a maximum when the absorption length is ~ the depth of the crystal and when the noise due to the thermal dark current is comparable to the noise from the first amplification stage. For this detector, the optimum temperature was that of the lowest curve in Fig. 3.6, labelled T = 141 K. If the quantum efficiency is taken to be 1 for $\lambda \leq 1.66$ μm, then for EHD in unstressed Ge the quantum efficiency is ≈41% under operating conditions. The quantum

efficiency was marginally lower for the strain-confined EHL for typical stresses studied here, due to the reduction in the energy gap with stress. By comparison with Ref. 3.10 and with the absorption data of Macfarlane et al.,[3.14] apparently the detector crystal was about 20 K warmer than indicated by the thermocouple readings. Thus the actual operating temperature was T ≈ 160 K.

The change in the detector response with wavelength was found to have a negligible effect on the fitting of luminescence spectra. However, it is necessary to take the change in detector response into account when comparing signals with widely differing wavelengths, for example different phonon replicas or the same phonon replica for substantially different stresses.

Note that because the absorption length is ~1 cm, electron-hole pairs are created throughout the volume of the detector crystal. This is necessary in order to obtain the short collection times indicated above. If the absorption length is too short the collection time can become much longer, ~1 msec, due to surface channels which create undepleted areas near the surface. The electron-hole pairs are then created in field free regions and get collected slowly by diffusion.

The detector was connected (via DC coupling) to a sensitive current amplifier designed by Jan DeVries of the Space Sciences Laboratory, as shown in Fig. 3.7. The amplifier was shielded to reduce magnetic pickup. The response time is given by the feedback resistor and capacitor, usually 10 MΩ and 1 pF respectively, for $R_F C_F$ = 10 μsec. Throughout this thesis the luminescence intensity or signal is given

as the output of this amplifier, in mV. Although the signal is in general amplified further, e.g., by the boxcar or the lockin, this reference was chosen because it can be related to the luminescence flux incident on the detector, as follows:

$$V_{out} = P_{lum} A \eta e R_F / h\nu \quad . \tag{3.10}$$

Here P_{lum} is the luminescence incident on the detector, hν = 0.71 eV is the photon energy, A is the fraction of the luminescence absorbed into the Ge due to the index of refraction, η ≈ 0.4 is the quantum efficiency of the detector discussed above, and R_F = 10 MΩ. The quantity A may be estimated using

$$A = 1 - \left(\frac{n-1}{n+1}\right)^2 \quad ,$$

where n ≈ 4.1 is the index of refraction of Ge at 0.71 eV and T ≈ 160K.[3.15] Thus an amplifier output of 1 mV corresponds to 2.8×10^{-10} W incident on the detector.

An absolute measurement of the sensitivity of this detector has not been made. However, some experiments were performed using the apparatus described here and the apparatus described in Ref. 3.10, with the same sample. These experiments indicated that the sensitivity of this apparatus is about 6 times less than that of the other apparatus. Thus the detectivity may be estimated to be

$$D^* \approx 3 \times 10^{12} \text{ cm W}^{-1}\text{Hz}^{1/2} \tag{3.11}$$

for the detector used here. It should be noted that the detector output was quite reproducible from day to day. For a series of runs

extending over several weeks to collect the data presented in Chapter 5, the daily normalization factor varied by only ≈25%.

34. Imaging Technique

In order to measure density profiles for the EHL confined in a strain well, it was necessary to obtain detailed information about the spatial distribution of the luminescence emanating from the sample. As shown in Fig. 3.3, a precision imaging lens formed a sharp, 3x magnified image of the crystal onto the entrance plane of the spectrometer. In early experiments on unstressed Ge, Pokrovskii[3.16] and Martin[3.17] obtained spatial profiles by translating the laser spot across the sample, thus moving the image of the cloud of small EHD across the entrance slit of the spectrometer. Because the strain-confined liquid remains fixed in the crystal, it was necessary to modify the technique, as follows:[3.18, 3.19] The luminescence image of the entire sample was translated across the front of the spectrometer, using a deflection mirror (Fig. 3.3) precisely controlled by stepping motors. A scanner control circuit allowed precise digital positioning and recording of the mirror tilt, or image position. The motor-driven mirror and scanner control were constructed by J. E. Furneaux. A spectrometer slit could be mounted either vertically or horizontally, permitting only luminescence from a narrow strip of the crystal to enter the spectrometer. A luminescence profile obtained by scanning the luminescence image across a slit is called a slit scan. Alternatively, both vertical and horizontal slits could be mounted simultaneously, permitting only luminescence from a small region of the crystal to enter the spectrometer. Such a profile is called a box scan, since the crossed slits

were usually the same width. Box scans were used to obtain density profiles, as discussed in Chapter 5. This technique allowed the possibility of obtaining time- and wavelength-resolved image scans or spatially-resolved wavelength scans.

Slit scans and box scans could be obtained along three orthogonal spatial directions, using the mirrors (Fig. 3.1) to obtain different views of the sample. The views and the conventions for the labelling of crystal coordinates are shown in Fig. 3.8. A z-scan is obtained by scanning either the face view or the side view of the image vertically across a slit or box aperture. A y-scan is obtained by scanning either the face view or the end view horizontally across the aperture. An x-scan is obtained by scanning the end view vertically or the side view horizontally past the aperture. The zero-point of these scans is as follows: $z = 0$ at the face of the crystal contacting the plunger; $y = 0$ at the center of the crystal (below the plunger); and $x = 0$ at the face of the crystal illuminated by the laser. The distance the image was translated by one step of the stepper motor was different in the vertical and horizontal directions; these distance were about 8 μm (e.g., z-scan) and 12 μm (e.g., y-scan) respectively. Because the optical path lengths were slightly different for face, end, and side views, the step sizes were also slightly different.

The spatial resolution of the luminescence images depended on several factors: (i) the resolution of the lens and the focusing accuracy, (ii) the size of the slit or box aperture, (iii) the sweep speed used for the scans, and (iv) the optical quality of the crystal surface. Each of these factors is considered below.

A Zeiss Tessar 105 mm focal length f/3.5 camera lens was used to obtain high quality images, with the f/stop fully open for maximum sensitivity. The resolution of such a lens is, at the very worst, 50 lines/mm or 20 μm. The lens was mounted on an xyz translator equipped with micrometers and was positioned along the optical path to give the best focus, with the sample and spectrometer fixed. The best focus was indicated by the narrowest drop profile, for moderately low excitation. The focusing procedure was repeated for each view, due to the differing optical path lengths. It is necessary that the focusing be done using EHL luminescence, since the focal length of the lens changes with wavelength, due to the change in the index of refraction of the glass. Indeed, the characteristics of many optical glasses are similar;[3.20] the focal length is about 5% longer at 1.75 μm than at 0.5 μm.

The image blur resulting from an error in the lens position may be estimated as follows. The optical system consists of an object and an image plane separated by a fixed distance, and a lens with a particular focal length and aperture. At optimum focus for 1.75 μm radiation, the setup results in image magnification M = 2.9. Suppose that the lens is positioned a distance δ from the correct position. As a result of this misplacement, the plane actually containing a focused image is displaced from the intended image plane and the image is slightly blurred on the spectrometer slit. This image blur depends on the lens aperture A, on M, and on δ,[3.21] and may be referred back to an object size. The object blur b_{object} then refers to the minimum apparent object size and is given by

$$b_{object} = \frac{(M-1)}{MA_{IR}} \delta \quad . \tag{3.12}$$

Here A_{IR} is the lens aperture for 1.75 μm, which is about 5% greater than the value for visible light due to the change in focal length mentioned above. A reasonable upper limit for δ is 0.25 mm, from the focusing data. For the other parameters given above, the resulting object blur $b_{object} \leq 45$ μm.

A slightly different imaging problem occurs because the image planes for vertical and horizontal slits are displaced from each other by a distance $\Delta \approx 3$ mm, while the focussing procedure was performed for only one slit orientation. It is much more important to refocus for the different views, because in that case the error would be in the object distance (which is shorter than the image distance, due to the magnification). As mentioned above, the lens was indeed repositioned each time a different view was desired. The object blur resulting from a change Δ in the image distance is given by

$$b_{object} = \frac{\Delta}{M(M+1)A_{IR}} \quad . \tag{3.13}$$

For the values given above, the resulting object blur $b_{object} \approx 70$ μm. For future experiments using box scans it would be desirable to use a single-plane pinhole aperture, since the object blur given by Eq. (3.13) is greater than the effective aperture size given below.

In order to estimate the effect of the finite slit width, consider a spherical (or ellipsoidal) object with constant density. The luminescence profile from a slit scan of such an object (single drop of strain-confined EHL or cloud of small EHD in unstressed Ge) should be

$$I_{slit}(x) \propto (R^2 - x^2) \tag{3.14}$$

where x is the slit position and R is the radius. The full width at half maximum (FWHM) of the slit scan W_s related to R by

$$R = W_s/\sqrt{2} \quad . \tag{3.15}$$

These two relations are true if the width of the slit function is sufficiently small compared to R. For a slit (or box) scan, the slit function is rectangular, with width s equal to the slit width measured in sample coordinates. Equation (3.15) is true to within a few percent if $s \leq 0.7\ W_s$. For the case $s = 0.7\ W_s$ the shape of the profile is affected by the finite slit width, but the width (FWHM) of the profile is not significantly changed. The data presented in Chapter 4 were obtained using standard 250 μm or 150 μm spectometer slits, allowing resolution of radii ≥ 85 μm or 50 μm respectively, due to image magnification. In addition, Eq. (3.15) is used in Chapter 4 to obtain radii for the strain-confined EHL as well as for clouds of small EHD in unstressed Ge. This procedure is adequate for the semi-quantitative analysis presented there. For the data presented in Chapter 5, however, standard 100 μm spectrometer slits were used in order to provide the possibility of increased resolution (≈35 μm, including image magnification). Further, since the deviations from uniform density are considered in detail in this chapter, drop sizes are usually given in terms of W_s.

The sweep speed was always chosen so as not to affect the width of the scans. Indeed, in Chapter 5 the sweep speed was selected so that the dwell time per point was ≈4 times the instrumental time constant, in order to measure the shape of the profiles as accurately as possible.

The optical quality of the Ge crystal surface is the most difficult parameter to estimate quantitatively. In addition, it is very difficult to prepare an optically flat surface. Even with the most careful polishing procedures, scratches significantly larger than the nominal grit size are nearly always introduced. Further, since the index of refraction of Ge is ~4, the optical flatness is degraded by a factor of ~4 compared to the physical flatness. The problem is compounded by the fact that a relatively small intensity anomaly in a box scan is transformed into a much larger anomaly in the resulting density profile (see Section 54). Two different surface preparations were used on the two primary samples. For sample CR38, the primary sample used in Chapter 4, after the etching procedure described in Section 31 the faces through which luminescence was collected were polished with Syton. For sample CR50, the primary sample used in Chapter 5, the sample was prepared only as described in Section 31.

The overall spatial resolution may be estimated as follows. Slit scans along the x, y, and z directions are recorded and the radii R_x, R_y, and R_z are computed using Eq. (3.15). Then the drop volume $V = 4/3\ \pi R_x R_y R_z$ is computed as a function of excitation level, as shown later in Fig. 5.2 for sample CR50. The break in the slope for small drop sizes is evidence for loss of spatial resolution. From these data it can be seen that the slit scan FWHM is a good indicator of drop size for $W_s \geq 100$ μm (or $R \geq 70$ μm) for sample CR50 and for $W_s \geq 140$ μm (or $R \geq 100$ μm) for sample CR38. The difference between these values could be due to the surface preparation or to the other factors mentioned above. Because the variation in density with position is smaller for small drop sizes

(see Chapter 5), this resolution is satisfactory for the experiments described here.

This chapter is concluded with a discussion of several calibrations. The excitation level is given throughout this thesis by the actual laser power P_{abs} absorbed into the Ge sample. This was obtained by measuring the laser output at various points in the optical path using a Scientech calorimeter, which has flat response from the ultra-violet to the far infrared. It was verified that no significant infrared radiation from the laser plasma tube was transmitted through the H_2O filter. The procedure was repeated both with and without the laser razor equipped with lenses, as well as with and without the neutral density filters in place, since the transmission of the filters depended slightly on laser output. The laser output was measured before and after the helium cryostat so that the correction for only the entrance windows could be made. The transmission into the Ge sample was computed using the optical constants n = 5.06 and k = 2.50 at ≈5145Å and 120 K.[3.15] These coefficients are not expected to change appreciably at lower temperatures.[3.22] Thus only 47% of the incident laser light is absorbed into the Ge sample at 4 K.

The absorbed power P_{abs} was varied between 0.02 mW and 850 mW. For the higher excitation levels, the question of sample heating must be considered. Indeed, in order to interpret the experimental results obtained at the highest excitation levels, it is necessary to show that the EHL was not heated above the critical temperature, which is calculated in Section 24.2 to be $T_c \approx 5$ K for an appropriate value of the stress $-\sigma = 5$ kgf/mm^2 in Ge. The most extreme temperature increase would occur

if all the absorbed energy in a "pulse" of excitation went into heating of the sample. In this case the energy per pulse

$$U = P_{abs} \times \Delta t = 0.85\ \omega \times 6\ \text{msec} = 5.1\ \text{mJ} \quad .$$

The lattice heat capacity at low temperatures is given by[3.23]

$$C_v = \frac{12}{5}\pi^4 n_a V k \left(\frac{T}{\Theta_D}\right)^3 \quad , \tag{3.16}$$

where V is the sample volume, $n_a = 4.41 \times 10^{22}$ cm^{-3} is the number of Ge atoms per cm^3, and $\Theta_D = 360$ K is the Debye temperature for Ge. The temperature increase is then obtained from the following expression:

$$T_1^4 - T_o^4 = \frac{5\Theta_D{}^3}{3\pi^4 n_a k}\,\frac{U}{V} = 1.3 \times 10^6\,\frac{U}{V} \quad . \tag{3.17}$$

Here T_o is the initial (bath) temperature, T_1 is the final temperature, U is in Joules and V is in cm^3. For a sample with dimensions 4 x 4 x 3 mm^3, this results in a final sample temperature $T_1 \sim 19$ K! However, for such long pulse lengths the situation should be considered as for continuous excitation. In this case the temperature increase ΔT is given by[3.24]

$$\Delta T = \frac{RP}{A} \quad , \tag{3.18}$$

where P is the power input, A is the surface area of the sample, and R is the Kapitza resistance, which is the thermal resistance between the sample and the bath. Following Ref. 3.24, if the value $R = 50/T_o^3$ cm^{2}deg W^{-1} for a Cu-liquid He^4 interface is used, where $T_o \approx 1.9$K is the bath temperature, then $\Delta T \approx 7.7$K, so that the sample temperature would still be predicted to rise to $T_1 \approx 9.6$K.

Clearly a more direct measurement would be desirable. The most direct method to test for a relatively large temperature increase is via fitting the EHL luminescence lineshape. However, as discussed in detail in Chapter 5, for the highest excitation levels the density varies by a vactor of ≈3 with position in the drop, and a composite theoretical lineshape must be used in order to interpret the experimental lineshape. Thus far a satisfactory model for the composite lineshape has not been devised. If the high-energy half of the luminescence spectrum is instead fit to a single density (which would correspond to some <u>average</u> density), a crude estimate can be made of the EHL temperature by looking at the high-energy tail of the line. Such an analysis indicates that the EHL temperature may be slightly above the bath temperature of ≈1.9 K but is certainly less than 4 K.

In addition, it may be noted that Hansen[3.7] measured the temperature increase in a carbon resistance thermometer attached to a Ge sample with dimensions similar to the samples used here. Under 200 mW continuous incident excitation, which corresponds to $P_{abs} \approx 100$ mW, he measured a temperature increase of ≈0.15 K. If this temperature rise is simply scaled with excitation, as in Eq. (3.18), then for the highest excitation levels used here a temperature rise $\Delta T \approx 1.3$ K and a final temperature $T_1 \approx 3.2$ K would be expected. Thus it seems probable that the EHL temperature is somewhat higher than the bath temperature, perhaps by ≈1 K, but that it is certainly less than the liquid critical temperature $T_c \approx 5$ K.

Finally, an estimate may be made of the collection efficiency of the imaging optical setup, in order to relate the measured luminescence

signals to the actual radiated power. Consider the drop to be a radiating object imbedded in a medium with index of refraction ≈4. When the radiation reaches the interface, some is transmitted and the rest is reflected back into the Ge. It is assumed that only the radiation which is transmitted on this first pass contributes to a well-defined image of the drop; the rest results in a diffuse background. Then the luminescence intensity incident on the detector depends on the effective collection cone of the optics <u>within</u> the Ge sample, as well as the transmission of the various optical elements. The collection cone is determined by the imaging lens and has half-angle $\theta = 5.6°$, which corresponds to a collection cone with half-angle $\theta = 1.4°$ within the Ge, due to the index of refraction. The transmission of the windows, lenses, and mirror in the luminescence collection path was measured for visible light from the laser, as described previously. The spectrometer efficiency was estimated above to be ≈60%. Thus

$$P_{lum} = 2.4 \times 10^{-5}\ c\ P_{rad} \quad , \tag{3.19}$$

where P_{lum} is the luminescence power incident on the detector as in Eq. (3.10), and P_{rad} is the power radiated by the EHL. The factor c has been included to indicate that the transmission of the lenses and windows should be corrected for 1.75 μm radiation; the value of c is not precisely known but is approximately 0.5. Equation (3.19) may be combined with Eq. (3.10) to yield

$$V_{out} = 85\ c\ P_{rad} \quad . \tag{3.20}$$

This calibration is used in Section 55 to estimate the radiative efficiency of the strain-confined EHL.

CHAPTER 4. PROPERTIES OF THE STRAIN-CONFINED ELECTRON-HOLE LIQUID IN Ge

41. Introduction

The properties of the electron-hole liquid are expected to vary with stress, as discussed extensively in Chapter 2. Due to the reduction in the band gap with stress, the liquid energy is also reduced under stress. Thus in a non-uniformly strained crystal, EHD are attached to regions of maximum shear strain. It has been shown that, by applying a contact stress over a portion of the crystal surface, it is possible to create one or more energy minima within the interior of the crystal.[4.1-4.3]

The contact stress is produced by applying a moderate force to the sample with a rounded plastic plunger, as discussed in Section 31. Small EHD produced near the light excitation point are attached to the potential wells and coalesce into large masses of electron-hole liquid. The potential minima are located in regions of the Ge crystal where the local strain tensor is approximately equivalent to a ⟨111⟩ uniaxial strain,[4.1, 4.2] since the deformation potential is largest for uniaxial strain along the ⟨111⟩ axis. If the contact force is applied along a direction other than ⟨111⟩, potential minima occur along ⟨111⟩ axes radiating out from the point of contact. Thus, one, two, or four drops are produced when the contact force is applied along ⟨111⟩, ⟨110⟩, or ⟨100⟩ directions, respectively.[4.1-4.3] These multiple drops are found to have similar properties irrespective of the direction in which the contact force is applied, consistent with the idea that in each case the potential minima correspond to a local ⟨111⟩ uniaxial strain.

In addition, it has been shown[4.1, 4.2] that the shear strain maximum results in an energy lowering for the EHL only if the maximum ⟨111⟩ stress is greater in magnitude than σ_e, where the conduction band degeneracy is completely removed. As shown in Chapter 2, this occurs at $-\sigma_e \approx 2.6$ kgf/mm^2. Thus the strain-confined liquid is only observed if the maximum stress $|\sigma_M| > |\sigma_e|$. At stresses greater in magnitude than σ_h (where $-\sigma_h \approx 6.5$ kgf/mm^2) the valence band degeneracy is also removed. For most of the experiments described in this chapter, σ_M is between σ_e and σ_h, thus corresponding to the intermediate stress regime or Ge(1:2), in the notation given in Chapter 1.

The drop size is found to increase with excitation level. At moderate excitation levels, then, corresponding to drop radii ≤150 μm, the liquid occupies a region of strain sufficiently uniform that the equilibrium properties of the liquid may be studied. The results presented here are in reasonable agreement with the theoretical calculations presented in Chapter 2. At higher excitation levels and for larger drop sizes, the liquid is actually compressed by the strain well. A detailed description and understanding of this phenomenon is presented in Chapter 5. Since the compression affects many of the experiments, in this chapter only a semi-quantitative discussion is given of the results for large drop sizes.

The formation of macroscopic volumes of strain-confined liquid is a phenomenon quite distinct from the usual EHD formation in unstressed Ge. In this chapter, the strain-confined liquid is termed a γ-drop, in contrast to the small (~1-10 μm in size[4.4]) α-drops in unstressed Ge. If an unstressed sample of Ge is illuminated by a laser

beam focused to a point, the EHD produced by the light will form a cloud[4.5,4.6] of small droplets; this cloud increases in size as the laser intensity is increased. Experimental results presented in this chapter--infrared imaging, kinetic studies, and spectroscopy--show that a cloud of small drops is readily distinguishable from the strain-confined liquid. Experiments have been performed on both stressed and unstressed ultrapure dislocation-free Ge crystals. Where possible, direct comparisons are made between the γ-drop and a cloud of α-drops produced in the same sample when the stress is removed. Most of the results have been published previously.[4.7, 4.8] The measurements may be grouped into several categories:

1) Spectroscopy of the electron-hole liquid. The recombination luminescence was measured vs. wavelength at 1.8 K and 4.2 K for various laser excitation levels. The luminescence linewidth from the γ-drop is constant at low excitation levels, indicating a constant e-h pair density in the liquid. From these data at intermediate stresses an estimate is made of the equilibrium density n_γ(1.8 K $-\sigma \approx 6$ kgf/mm^2) = 0.50×10^{17} cm^{-3}, compared to the α-drop density n_α(1.8 K = 2.2×10^{17} cm^{-3}.[4.9] Luminescence from excitons in equilibrium with the strain-confined liquid was observed, giving an estimate of the exciton condensation energy, $\phi \approx 1$ meV. Aside from the spectral differences between α- and γ-drops, the intensity of the γ-drop luminescence was observed to be relatively independent of temperature between 1.8 and 4.2 K, indicating that the strain gradient inhibits boiloff from the liquid. In addition, many of these properties have been studied as a function of stress. Evidence is presented that only one conduction valley is occupied in γ-drops.

2) Decay kinetics. Time dependence of the total luminescence yields the volume decay time τ_γ = 400 to 600 μsec, compared to τ_α = 40 μsec for α-drops at 1.8 K. This enhanced τ_γ is relatively constant below 4.2 K, consistent with a reduced density and inhibited evaporation from the strain-confined liquid. The γ-drop lifetime is found to be greatly reduced in dislocated Ge.

3) Imaging of the recombination luminescence. Time-resolved spatial profiles of γ-drops and α-clouds are obtained by scanning the crystal image across the spectrometer slit. Under certain conditions, small EHD are observed flowing into the strain well in a sharply-defined stream. Taking into account the difference in γ-drop and α-cloud lifetimes, comparisons can be made between the γ-drop density and the average e-h pair density over the α-cloud. The cloud density is two orders of magnitude smaller. Under square-wave modulated excitation, decays of these luminescence profiles have been observed at 1.8 K. The radius of the γ-drop decays in time, as expected, whereas the cloud radius does not. Results are in agreement with previous Alfvén wave measurements.[4.10] The change in shape of a γ-drop in a magnetic field is described, including steady-state and kinetic behavior.

The experimental techniques were previously described in Chapter 3. In Section 42 the spectroscopic properties of γ-drop and free exciton luminescence are discussed, including the measurement of the γ-drop density and the exciton condensation energy φ. The stress dependence of the luminescence is also discussed. The lifetime and temperature dependences of the luminescence are discussed in Section 43. In Section 44 the spatial properties of γ-drops and α-clouds are compared,

including the dependence on the excitation level and on the time after turn-off of the excitation source. The section concludes with a discussion of the magnetostriction of γ-drops.

42. Spectroscopy of the Recombination Luminescence

In Ref. 4.1 it was shown that γ-drops form in 3-dimensional potential wells created by the inhomogeneous strain. The luminescence spectrum is shifted by the strain to lower energy than the spectrum of α-drops in unstressed Ge. Figure 4.1 shows a complete spectrum for a sample stressed in the ⟨111⟩ direction, showing the TO-, LA-, and TA-assisted phonon replicas. For the applied force of 9 kgf the spectrum is shifted by about 2.5 meV from the α-drop spectrum. In this section the intensity, lineshape, and energy of the γ-drop luminescence are studied under various experimental conditions.

42.1. The Liquid-Gas Phase Transition

In order to establish the existence of a liquid-gas phase transition it was necessary to observe the excitonic gas in equilibrium with the electron-hole liquid. At 1.8 K, however, the number of free excitons (FE) evaporated from the liquid was not sufficient to observe their radiation. The number of FE was presumably reduced by backflow into the liquid, caused by the stress-induced potential gradient at the liquid surface. Thus to observe the equilibrium excitons it was necessary to raise the temperature and reduce the excitation level, thereby creating a small drop in the shallow portion of the strain gradient. Figure 4.2 shows the luminescence spectra for several excitation levels at 4.2 K, revealing the existence of two distinct spectral lines which are interpreted as the liquid and gas phases. The EHL and FE peaks are closer than in an unstressed sample, indicating a reduced exciton

condensation energy.

The onset of the liquid-gas phase transition is clearly observed. At the lowest excitation levels only the exciton luminescence at 710.7 meV is present. As the exciton density is increased a distinct pumping threshold in the EHL luminescence intensity is observed. Figure 4.3 shows the EHL and free exciton intensities vs. excitation power showing that once the nucleation of the liquid phase has occurred, additional e-h pairs added to the system go predominantly into the liquid phase without greatly increasing the number of excitons. A similar threshold phenomenon has been studied extensively[4.11] for small EHD in unstressed Ge and is a characteristic property of drop nucleation from the saturated gas.

To confirm that both phases occur in the same region of the crystal, luminescence image scans were performed as described in Sections 34 and 44. Figure 4.4a shows a scan in the x-direction for the exciton phase near threshold, and Fig. 4.4b shows a similar scan for the liquid phase at a higher excitation level. It can be seen that both phases are spatially localized in the strain well.

The liquid, which has a higher equilibrium density, is concentrated near the center of the well, whereas the gas occupies the entire well. From the spatial distribution of the excitons, the shape of the strain well can be estimated. By treating the excitons as an ideal gas and setting the chemical potential equal to a constant, the gas density profile is expected to be

$$n(r) = n(0)\exp\left(-\frac{E_s(r)}{kT}\right) \quad . \quad . \quad (4.1)$$

As in Ref. 4.1, the strain energy is taken to be parabolic: $E_s(r) = \alpha r^2$ where $r = 0$ is the center of the strain well. It follows that the luminescence intensity in a slit scan is

$$I(x) = I(x_0) \exp\left(-\frac{\alpha(x-x_0)^2}{kT}\right) , \qquad (4.2)$$

where x_0 is at the center of the well. The open circles in Fig. 4.4a represent Eq. (4.2), with $\alpha = 11$ meV/mm^2. This value is in reasonable agreement with the 2-dimensional calculation of the EHL energy vs position presented in Ref. 4.1. However, α does vary with experiment, depending in particular on the stressing rod; see Section 52. Thus the shape of the free exciton distribution is satisfactorily explained in terms of an ideal gas, at the lattice temperature, in a potential energy gradient.

Because the free excitons are localized in the strain well, the effective volume of the gas is smaller than that which can be obtained in unstressed Ge with uniform pumping over a large surface area. Thus the exciton luminescence intensity at threshold is smaller for inhomogeneously-stressed samples, and the free excitons have so far been observed only at temperatures $T \geq 3.3$ K.

From the gas and liquid energy spectra, it is possible to measure the condensation energy ϕ lost by an e-h pair in the gas-liquid transition. As discussed in Section 23.3, it is theoretically expected that ϕ will be smaller in samples under ⟨111⟩ stress than in unstressed Ge. This is evident in Fig. 4.2, from the greatly reduced separation between the EHL and exciton luminescence lines, as compared to unstressed Ge. However, ϕ cannot be simply measured by the splitting between these

two lines: At such high temperatures, the EHL spectrum is broadened even near threshold, due to the enhanced compressibility of the liquid; and at all temperatures, the shape of the FE luminescence line must be corrected for broadening due to the strain gradient. A preliminary value of $\phi \approx 1$ meV has been measured[4.12] from the EHL and FE luminescence lineshapes and separation at a somewhat lower temperature ($T = 3.3$ K), using these modifications of the analysis. A similar value for ϕ was also measured[4.12] thermodynamically, from the temperature dependence of the exciton density at the threshold for drop formation. A detailed study of the strain-confined electron-hole fluid phase diagram would be interesting.[4.13] The value $\phi \approx 1$ meV should be compared with $\phi \approx 2$ meV ($T = 3.5$ K) in unstressed Ge.[4.14, 4.15]

42.2. Stress Dependence of the Luminescence

Figure 4.5a shows the variation of the luminescence peak energy as a function of applied force F. It can be seen that the peak energy shifts linearly with F, above a critical force F_c, similar to experiments on uniformly stressed Ge.[4.16] However, the origin of the discontinuity in slope is believed to be different in the two experiments.

A ⟨111⟩-uniaxial stress splits the conduction band degeneracy in Ge, raising three valleys in energy and lowering the fourth. At the critical stress σ_e this strain splitting becomes equal to the electron Fermi level inside the liquid (see Section 23.3). At higher stresses only the lowest valley is occupied, and the luminescence peak shifts to lower energies parallel to the shift of this conduction band edge. At lower stresses, when all four valleys are partly occupied, the luminescence peak position is almost independent of stress, and apparently

shifts slightly to higher energies. Only for stresses larger in magnitude than σ_e are EHD attracted by strain gradients toward regions of higher strain.

In the inhomogeneous stress experiments (Fig. 4.5), when the applied force is small, the maximum stress σ_M is smaller than σ_e in magnitude, so that EHD are not attracted to the point of maximum stress; indeed, they may be slightly repelled. For these low applied forces, the luminescence is due not to carriers inside the well, but to small droplets in a cloud near the laser spot. Thus the luminescence peak (Fig. 4.5a) is only weakly shifted by the stress, while the linewidth ΔE (defined as the full width at half maximum of the luminescence spectrum) (Fig. 4.5b) and lifetime τ (Fig. 4.5c) are characteristic of α-drops in unstressed Ge.

Once F exceeds some critical value F_c, however, the drops in the cloud are attracted to the stress maximum, forming a γ-drop with very different properties, as seen in Fig. 4.5. The force F_c is in general not the same as the force at which $\sigma_M = \sigma_e$, since the cloud of drops is localized near the crystal surface and will not be attracted into the well unless $|\sigma_M|$ is somewhat larger than $|\sigma_e|$. Once small drops are attracted into the well, a γ-drop forms, with a greatly enhanced recombination lifetime (Fig. 4.5c) and peak luminescence intensity (Fig. 4.5d), and a reduced linewidth (Fig. 4.5b), all characteristic of a reduced e-h pair density (see discussion in Sections 42.3 and 42.4).

For $F > F_c$, the luminescence is due to carriers inside the well, and the stress-dependent properties of γ-drops can be studied. The luminescence peak is seen to shift to lower energies approximately

linearly with $F(F > F_c)$. The magnitude of the strain at the bottom of the well cannot be measured directly,[4.17] but is estimated from the shift of the γ-drop luminescence peak, assuming that the stress at the bottom of the well is essentially a ⟨111⟩-uniaxial stress. As shown in Ref. 4.1 and in Section 52, this is a reasonable assumption. Using the peak energy vs. uniaxial stress data taken from Ref. 4.16, the resultant stresses are calculated and shown at the top of Fig. 4.5.

The changes in the properties of γ-drops with stress (for $F > F_c$ in Fig. 4.5) are not yet understood in detail. As shown in Section 23.1, the γ-drop density is theoretically expected to decrease with ⟨111⟩-stress; this result has been observed under uniaxial ⟨111⟩-stress,[4.18-4.20] where the luminescence linewidth was seen to decrease with increasing stress. In the strain well there are complications which can make this density change harder to observe. As discussed semi-quantitatively in the next section and in detail in the next chapter, the drop tends to compress, increasing the average pair density above the equilibrium value. The compression should be more significant at higher stresses for two reasons: first, the strain gradient is larger, and second, the compressibility of the liquid increases with stress, as the equilibrium density decreases (see Fig. 2.20). The luminescence linewidth, Fig. 4.5b, does not decrease as in the uniform stress experiments.[4.18-4.20] However, the pair recombination time does increase with increasing stress (Fig. 4.5c), suggesting a corresponding decrease in pair density, which may be masked in Fig. 4.5b by an inhomogeneous line broadening (see Section 42.3). Because of these complications, the lineshapes in Fig. 4.5b have not been analyzed to yield the liquid density. A systematic study of $n(\sigma)$ and $\tau(\sigma)$ for the

strain-confined EHL would be useful, both to complement the uniform-stress experiments[4.18-4.20] and to compare with the theory presented in Chapter 2. It should be noted that the sharp decrease in lifetime or intensity, which had been reported in earlier uniaxial stress experiments (Ref. 4.21), is not observed.

In Fig. 4.5a, the linear energy shift with applied force suggests that the contact area is relatively constant, unlike the classical Hertzian contact problem.[4.22, 4.1] An explanation of this is that the nylon plunger undergoes a plastic deformation when the 9 kgf force is initially applied at room temperature. The nylon becomes stiffer at liquid helium temperatures and retains the initial contact area for a wide variation in force. This conclusion is supported by birefringence data[4.1] which show that the position of the strain maximum is only weakly dependent on force.

By contrast, Fig. 4.6 shows the results of a different experiment, in which the stress was applied through a metal plunger. A slightly rounded brass rod contacted the crystal through a thin sheet of mylar. (The mylar interface reduced the effect of small high stress regions at the contact, caused by surface irregularities.) This case more nearly resembled the classical contact problem: an increase in the contact area with stress was observable in the birefringence, and the maximum stress point moved deeper into the crystal with increasing stress. The brass, being less deformable than nylon, made contact with the Ge over a smaller area A. This caused a larger maximum stress $\sigma_M = F/A$ and strain gradient for a given force, and accordingly a smaller threshold force for the formation of γ-drops. Note that the luminescence for F = 9 kgf has shifted as much as for F = 18 kgf with the nylon plunger.

(This is especially significant since the force was here applied along ⟨110⟩; see below). From the solution of the classical problem of two perfectly elastic contacting spheres, it is expected[4.22] that $A \propto F^{2/3}$. For this case $\sigma_M \propto F/A \propto F^{1/3}$, which is plotted as the solid curve on Fig. 4.6a. In this curve, the point F = 0 was shifted to give the best fit. Possible reasons for this shift are: (a) it was difficult in the experiment to determine precisely the point at which the rod first made contact with the crystal; and (b) at liquid helium temperatures, the mylar interface may have been distorted, giving an apparent minimum value of A > 0.

The effects of compression of the liquid are more evident in this metal-plunger experiment: the strain gradient is larger, and the drop size is larger due to an increased P_{abs}. The luminescence linewidth (Fig. 4.6b) increases and the lifetime (Fig. 4.6c) decreases with stress, corresponding to an increasing density with stress. Also the total luminescence decay is quite non-exponential, indicating that the density decreases as the drop size decreases.

In Refs. 4.1 and 4.2 it was shown that 1, 2, or 4 energy minima for the EHL can be formed by stressing along ⟨111⟩, ⟨110⟩, or ⟨100⟩ respectively. It was found that all of these cases actually correspond to drops forming in regions of local ⟨111⟩ strain, so that the properties of the strain-confined liquid should be independent of the direction of the applied force. Figure 4.7 shows a comparison of γ-drop luminescence spectra obtained for approximately equal applied forces along ⟨111⟩, ⟨110⟩, and ⟨100⟩ directions, as well as for α-drops in an unstressed sample. (The force is applied via the "permanent" stress

geometry as in Fig. 17a of Ref. 4.1.) Because γ-drops form in regions of local ⟨111⟩ strain, the energy shift should vary with the projection of a particular ⟨111⟩ axis on the applied force direction. This conclusion is qualitatively verified in Fig. 4.7 where the shift in the ⟨100⟩ and ⟨110⟩ stressed crystals is considerably less than for ⟨111⟩ stress.[4.23] The magnitudes of the shifts are approximately in agreement with the predictions of Ref. 4.1. Note that for all three stressed samples the luminescence linewidths are similar, and are narrower than the linewidth from the unstressed sample.

Because the properties of the strain-confined EHL are independent of the direction of the applied force, most of the experimental results presented in this thesis are for samples stressed along ⟨111⟩, since only a single drop forms. The rest of this thesis will deal with the properties of γ-drops at (approximately) a fixed value of the stress, $|\sigma_M| \approx$ 5-6 kgf/mm^2, corresponding in the experimental arrangement to an applied force F ≈ 9 kgf.

42.3. Luminescence Linewidth; Compression of the Strain-Confined Liquid

Assuming that a relatively constant fraction of the photoexcited carriers go into a single γ-drop, the properties of the strain-confined liquid can be studied as a function of drop size by simply varying the excitation level. Figure 4.8 shows the luminescence linewidth ΔE (full width at half maximum of an energy spectrum) plotted vs. absorbed laser power P_{abs}. The crystal was stressed along the ⟨111⟩ direction, with F ≈ 9 kgf and $|\sigma_M| \approx$ 5-6 kgf/mm^2, estimated from the energy shift of the luminescence spectrum. At low excitation levels, i.e., for sufficiently small drop size ($P_{abs} \leq$ 5 mW, R ≤ 200 μm), the linewidth

is constant, indicating a constant density within the liquid. In this regime the lineshape is used to estimate the e-h pair density, as discussed in Section 42.4. For higher excitation levels, i.e., larger drop size, the linewidth increases with P_{abs}. For comparison, Fig. 4.8 also shows the linewidth of the luminescence from α-drops in unstrained Ge. As anticipated, this width is independent of excitation level.

Several factors contribute to the power dependence of the γ-drop linewidth. The total luminescence is a superposition of the luminescence from different parts of the drop. Since the magnitude of the stress is a function of position in the well, the luminescence is shifted to higher energies near the surface of the drop, where the magnitude of the stress is lower. From Ref. 4.1, the strain energy is approximately parabolic, with

$$E_s(r) = \alpha r^2 \qquad (4.3)$$

measured from the bottom of the well, with α ≈ 8 meV/mm^2 for typical experimental conditions. Thus for a 400 μm radius drop, the luminescence energy would vary by ~1.3 meV across the drop.

Since the strain gradient acts as a restoring force on electrons and holes, a deep potential well also acts to compress the liquid, resulting in an increased pair density and luminescence linewidth.[4.24] It can be shown[4.25] that for small variations from the equilibrium density n_o, the density variation within a γ-drop is approximately given by

$$n(r) = n_o[1 + \hat{\alpha}(R^2 - r^2)] \quad , \qquad (4.4)$$

where R is the drop radius, $\hat{\alpha} = \alpha/n_0^2 E_0''$ and $E_0'' = (d^2E/dn^2)_{n=n_0}$ is related to the compressibility of the liquid. The quantity $n_0^2 E_0'' \approx 0.36$ meV for a stress $-\sigma = 6$ kgf/mm^2, using Model 1 in Chapter 2. Thus the density is greatest at the center of the drop and falls to the equilibrium value n_0 at the surface of the drop. According to Eq. (4.4), for a 400 μm-radius drop, $n(r=0) \approx 4.5\ n_0$. For such a large drop the deviation from the equilibrium density is no longer small; Eq. (4.4) must be regarded as only approximate and should be replaced by the exact theory described in Chapter 5. The density variation across a 100 μm-radius drop, however, is only about 20%. It is clear that such a large compression has an important effect on many properties of the γ-drop; indeed, it is the subject of the next chapter. In the following sections of this chapter, however, several instances where the data show evidence of compression are noted.

Figure 4.9 illustrates the effect of the strain inhomogeneity at the highest light levels. Trace (a) is the spectrum from the center of a large drop at moderately high excitation, $P_{abs} = 58$ mW; spectrum (b) is from a small region near the edge of the same drop; and spectrum (c) is from a smaller drop for which $P_{abs} = 1.4$ mW. The narrowest spectrum is from the small drop, where the density and strain are uniform to within ≈10%. Spectrum (b) represents the liquid near the surface of the drop: Here the luminescence line is still somewhat broadened by the strain gradient over the observed slit aperture. The peak of the luminescence is shifted to higher energies, since the local strain is smaller than that at the bottom of the well. Spectrum (a) is a superposition of spectra from liquid at all depths

in the well. Spectra (b) and (c) may be used to give another estimate of the strain well parameter α, as follows: Since trace (b) was obtained at $r = y \approx 320$ μm (see Sec. 34 for definition of coordinates), Eq. (4.3) yields $\alpha \approx 7$ meV/mm^2. This is in reasonable agreement with the estimate in Section 42.1 and the prediction in Ref. 4.1. These data clearly illustrate the role of spatial inhomogeneities in the line broadening at higher excitation levels.

42.4. Determination of the Pair Density

Figure 4.8 showed that at low excitation levels the luminescence linewidth ΔE, which is a measure of the electron plus hole Fermi energies, is independent of power. This means that for sufficiently small drops ($R \lesssim 150$ μm), the strain is relatively uniform across the drop and the e-h density is constant. This constant density is characteristic of a liquid phase.

The luminescence linewidth of γ-drops obtained for $P_{abs} < 5$ mW is actually ≈30% smaller than the linewidth of α-drops, measured from the same sample with the stress removed. This occurs in spite of the fact that in stressed Ge the electron degeneracy is reduced. The electron Fermi level depends on the density n as

$$E_F^e \propto \left(\frac{n}{\nu_e}\right)^{2/3} \tag{4.5}$$

where ν_e is the conduction valley degeneracy. Since the γ-drop does not form until the electron degeneracy is removed (ν_e reduced from 4 to 1), the observed decrease in ΔE for the γ-drop implies that the density must be considerably lower than in α-drops. Indeed, such a reduction in density is predicted theoretically in Chapter 2.

The equilibrium e-h pair density in a γ-drop may be determined by fitting the luminescence lineshape at low laser pump intensity. The luminescence intensity for the LA phonon-assisted line is given by Eq. (2.38) and (2.39), which include the splitting of the conduction and valence bands with strain and the nonparabolicity of the valence bands. Figure 4.10 shows a fit of the LA phonon-assisted luminescence line for P_{abs} = 0.17 mW,[4.26] $-\sigma_M$ = 6.8 kgf/mm^2, and T = 2.0 K. The theoretical points are for a density of $n = 0.50 \times 10^{17}$ cm^{-3}. By analyzing several lines, the following average value was obtained:

$$n_\gamma = 0.50 \pm 0.05 \times 10^{17} \text{ cm}^{-3} \quad (T = 1.8\text{-}2.0 \text{ K}, \; -\sigma_M = 5\text{-}7 \text{ kgf/mm}^2) \quad . \qquad (4.6)$$

This is in good agreement with the theoretical result according to Model 1 from Chapter 2: $n = 0.43 \times 10^{17}$ cm^{-3} for $-\sigma = 6$ kgf/mm^2 and T = 2K.

The low-energy tail in Fig. 4.10 is present in all γ-drop spectra, and is more pronounced than the tail observed in unstressed Ge (see Fig. 5.7). In unstressed Ge, as discussed in Section 22.3, this tail has been interpreted as partly due to Auger processes modifying the recombination energies of carriers deep inside the Fermi sea.[4.27] Also, an additional contribution may arise from a "forbidden" luminescence line associated with LO phonons.[4.28] It is not likely that the magnitude of either effect could be enhanced in γ-drops.

In addition to an analysis of the luminescence lineshape, other methods have been used to estimate the e-h pair density. In a magnetic field, the carrier energy is quantized into Landau levels, and many properties of the carriers have a quasi-sinusoidal modulation with period $\propto 1/H$. That is, the property undergoes a change whenever $(j + 1/2)\hbar\omega_c = E_F$, where $\omega_c = eH/m_c^* c$ is the cyclotron frequency, m_c^* is the cyclotron mass of the carrier and j is an integer. In experiments on α-drops in unstrained Ge, periodic oscillations have been observed in the luminescence intensity[4.29, 4.30] and far-infrared absorption[4.31, 4.32] and emission.[4.31] There should be separate sets of oscillations due to electrons and holes, but so far only oscillations due to electrons have been resolved.[4.33] Similar magneto-oscillatory effects are expected for properties of γ-drops.

Indeed, magneto-oscillations in the luminescence intensity of γ-drops have been observed by Furneaux.[4.34] These oscillations are apparently due to oscillations in the pair recombination time τ_o as in unstressed Ge.[4.29, 4.30] The data were analyzed assuming that the oscillations were due to the electrons and that only one electron valley was occupied. From the analysis the electron Fermi energy was found to be $E_F^e = 2.3 \pm 0.12$ meV (T = 1.6 K) for low excitation ($P_{abs} \approx 3$ mW) and a stress $-\sigma_M \approx 6$ kgf/mm^2; this yielded a value $n_\gamma = 0.52 \pm 0.05 \times 10^{17}$ cm^{-3} for the e-h pair density, in good agreement with the fit of the luminescence lineshape. At higher excitation levels the period of the oscillations was observed to increase, corresponding to a larger electron Fermi energy and a higher average density, due to compression of the liquid.

Ohyama, Hansen, and Turney[4.35] observed oscillations in the attenuation of longitudinal ultrasound by γ-drops in a magnetic field. These

oscillations should have the same period as the oscillations in luminescence intensity. From the period of the oscillations they derived the electron Fermi level and hence the density inside the γ-drop. The density they obtained was $n_\gamma = 0.62 \pm 0.04 \times 10^{17}$ cm^{-3} (T = 1.8 K). However, they were using moderately high excitation ($P_{abs} \approx$ 20-40 mW), so that compressional effects should have been significant, explaining the higher value. Indeed, they too found[4.36] that the period of the oscillations varied with excitation.

The pair density has also been estimated by Markiewicz, et al.[4.2,4.10, 4.37-4.40] from Alfvén resonances in the microwave absorption of γ-drops. Standing electromagnetic waves are set up inside the drop, and a resonant absorption occurs when the Alfvén wavelength approximately matches the drop diameter. The resonant magnetic field should provide a measure of the quantity ($n_\gamma R^2$). Determining R from a simultaneous imaging experiment, these data imply $n_\gamma \approx 0.7 \times 10^{17}$ cm^{-3} (T = 1.8 K).[4.41] This represents some kind of an average value, since the dependence of the density on drop size was not considered in the analysis. As such it is in reasonable agreement with the estimate of Ohyama, et al.[4.35] However, the analysis is complicated since the theory has only been done for spherical drop shape, while the γ-drop becomes markedly non-spherical in a magnetic field, as discussed in Section 44.4.

The γ-drop density has also been estimated from experiments on the absorption of 3.39 μm infrared light.[4.42-4.44] The densities quoted are higher than those observed in other experiments: Pokrovskii and Svistunova[4.42, 4.43] found $n_\gamma \approx 1 \times 10^{17}$ cm^{-3}; Mattos et al.[4.44] found $n_\gamma \approx 2 \times 10^{17}$ cm^{-3}. However, the results rely on an absolute measure

measure of the hole interband absorption cross-section σ_a at 3.39 μm, and the two groups disagree on the appropriate value to use.[4.45] (It is even possible that this cross section changes with stress.) Until this point is clarified, it is difficult to know the accuracy of these results. It should be noted that the drops observed in Refs. 4.42 and 4.43 were large enough that there could have been some compression, and apparently the stress was not determined.

Finally, the pair density was measured by Aurbach, et al.[4.46] from observation of far-infrared plasma absorption. This experiment yielded $n_\gamma \approx 4 \times 10^{16}$ cm^{-3} for F ≈ 9 kgf. The size of the drop could not be readily determined, although the peak position of the IR absorption did not shift significantly when the power was reduced by an order of magnitude, suggesting n ≈ constant. No correction was made for additional absorption due to transitions between the two hole bands (Refs. 4.47-4.51). Consequently, this value may require some modification.

With the qualifications mentioned above, these measurements of the equilibrium density are in reasonable agreement. The most reliable and accurate measurement is obtained from the fit of the luminescence lineshape, however, and that value agrees well with the theoretical prediction made in Chapter 2.

42.5. Conduction Valley Degeneracy

Theoretically, it is clear that a large ⟨111⟩-stress should split the four conduction band valleys by a large enough amount that only a single band is occupied. This gives a clear explanation of the break in the slope of EHD peak luminescence vs. stress, observed by Alekseev, et al.[4.21] and Benoît à la Guillaume, et al.[4.16] Similarly,

it explains the sudden jumps observed in nonuniformly stressed samples in E_o, ΔE, τ, and I as functions of applied stress (Figs. 4.5 and 4.6). That is, the point of maximum shear stress in the sample does not become an energy minimum for the EHL until after the conduction valley degeneracy is removed. However, it is of interest to consider the direct experimental evidence that only one conduction valley is occupied in γ-drops.

The most direct evidence is given by the angle dependence of the ultrasonic attenuation, reported by Hansen.[4.52] The data were taken in a (110)-plane over a range within 20^o of the ⟨100⟩-direction, and show only a single series of magneto-oscillations. The angle dependence of the oscillation peaks is consistent with the variation of cyclotron mass (Ref. 4.53) in the occupied valley. If all four valleys were occupied, there would be two other sets of peaks, corresponding to the cyclotron masses of the other valleys.

The conduction valley degeneracy ν_e can also be inferred indirectly by comparing the data on the luminescence linewidth and the magneto-oscillations of the luminescence (Sec. 42.4). The first measures the sum of the electron and hole Fermi energies $E_F^e + E_F^h$, while the second measures only the electron Fermi energy E_F^e. Specifically, $E_F = E_F^e + E_F^h \approx 4.66$ meV from the luminescence linewidth, and $E_F^e \approx 2.30$ meV from the magneto-oscillations. This yields $E_F^h \approx 2.36$ meV which corresponds to $n \approx 0.47 \times 10^{17}$ cm^{-3} (for T = 2.0 K and $\sigma_M = -6.8$ kgf/mm^2). This density in turn corresponds to $E_F^e = 2.15$ meV (for $\nu_e = 1$), 1.35 meV (for $\nu_e = 2$), or 0.85 meV (for $\nu_e = 4$). (These calculations all contain the assumption that the masses are unchanged

from bulk Ge.[4.54]) Assuming for the moment that E_F^h may be approximately described by a scalar hole mass m_{dh}, this argument can be restated more quantitatively. Let $\gamma = m_{de}/m_{dh}$. Then

$$E_F = E_F^e \left\{1 + \gamma\, \nu_e^{2/3}\right\} \quad . \tag{4.7}$$

Using the values $E_F = 4.66$ meV (luminescence linewidth), $E_F^e = 2.30$ meV (magneto-oscillations), $m_{de} = 0.22\ m_o$, and $m_{dh} = 0.201\ m_o$ (the <u>average</u> hole density-of-states mass for the lineshape calculation of Fig. 4.10), Eq. (4.7) gives $\nu_e = 0.91$.[4.55] Thus the values measured for E_F and E_F^e are consistent only if $\nu_e = 1$.

This degeneracy $\nu_e = 1$ can also be inferred from the angle dependence of the Alfvén resonances. The experimental result is quite striking:[4.56] The resonance approximately follows the angle dependence of the electron cyclotron resonance in a single ellipsoid, having 180° symmetry in a (110)-plane characteristic of $\nu_e = 1$, rather than the 90° symmetry which would occur if $\nu_e = 4$. This angle dependence is expected theoretically.[4.40]

Finally, the cyclotron resonance of electrons outside the drop has been observed by Markiewicz.[4.2, 4.7] This experiment showed that most of the electrons are located in a single valley corresponding to the same ⟨111⟩ direction as that associated with the drop. The experimental result is interpreted[4.7] as further evidence that $\nu_e = 1$ for the strain-confined liquid.

43. Lifetime and Temperature Dependence

43.1. Enhanced Lifetime for the Strain-Confined Liquid

The lifetime of the liquid phase is governed by several processes: (1) direct radiative recombination of electrons and holes; (2) (non-radiative) Auger recombination of an e-h pair, whereby kinetic energy is given to other carriers; (3) non-radiative recombination due to impurities or lattice defects; and (4) evaporation of free excitons or carriers from the surface of the EHL. In unstressed Ge, surface evaporation has been observed above about 2 K and is characterized by a non-exponential decay and a cutoff time; below this temperature the volume decay mechanisms usually predominate. Even though the binding energy ϕ of the EHL with respect to FE is reduced under stress, the boiloff of excitons is less important, because of the much larger drop size and increased volume-to-surface ratio and because the strain gradient inhibits boiloff. A cutoff time is not usually observed for the strain-confined liquid, due to the difficulty of observing luminescence from a single drop of sufficiently small size. Thus the effects of boiloff will be neglected in this section. (See, however, the end of Section 43.2.)

In addition, it is known that the α-drop lifetime is unchanged in samples containing a density of up to 10^{15} cm^{-3} shallow impurities,[4.57] or up to $\sim 10^{3}$ cm^{-2} dislocations.[4.58] The samples used in this thesis are ultrapure and dislocation free, as discussed in Section 31. Thus the impurity and defect contributions to the e-h pair recombination time will also be neglected in this section. This will allow a semi-quantitative understanding of the γ-drop lifetime. A more detailed

analysis is undertaken in Section 55.

In this section, then, only radiative and Auger processes are considered. To first order, the two-particle radiative recombination rate depends linearly on the e-h pair density of the liquid phase, whereas an Auger rate depends on higher powers of the density. A reduced e-h pair density in the liquid, obtained by stressing the crystal, would diminish the Auger contribution to the total recombination rate more than the radiative contribution. Thus the lifetime would be expected to become longer and the radiative efficiency would be expected to increase.

Figure 4.11c shows the decay of the total EHD luminescence for an unstressed sample after the light was switched off. The α-droplet lifetime at 1.8 K was found to be 36 μsec for this sample, in good agreement with published values.[4.16, 4.59-4.61]

Figures 4.11a and 4.11b show the much longer decay times characteristic of γ-drops. At low excitation levels (Fig. 4.11a, P_{abs} = 1.1 mW) the decay is exponential, with $\tau \approx 530$ sec. At higher excitation levels (Fig. 4.11b, P_{abs} = 119 mW) the decay is noticeably non-exponential. A non-exponential decay is expected if the liquid is compressed: Initially, when the drop is larger, the decay is faster, suggesting a high average pair density. As the drop shrinks, the average density decreases and the instantaneous decay rate becomes slower. For very long delay times, the decay typically becomes exponential, with a time constant comparable to that found in Fig. 4.11a for smaller drop size. Figure 4.12 shows the change of initial decay time τ_i with pumping power. If the decay were purely radiative

($\tau \propto n^{-1}$), such a change in τ would suggest that the average density is approximately doubled in the largest drops (R = 400 μm). For smaller drop sizes the density becomes uniform and τ_γ approaches an equilibrium value. This value is somewhat sample dependent, but $\tau_\gamma \approx 550$ μsec as shown in Fig. 4.12 is typical.

Considering only radiative and Auger processes, a simple model may be used to understand the increased γ-drop lifetime. The volume decay rate is written as the sum of two terms:

$$\tau^{-1} = \tau_{rad}^{-1} + \tau_{Aug}^{-1} = Bn + Cn^s \quad . \tag{4.8}$$

The coefficients B and C are considered for the present to be constants, and s = 2 or greater, depending on the dominant type of Auger process. The radiative efficiency is defined as follows:

$$\varepsilon_{rad} = \tau/\tau_{rad} \quad . \tag{4.9}$$

For α-drops, estimates of the radiative efficiency $\varepsilon_{rad\alpha}$ range from ≈25% to ≈80%.[4.30, 4.62-4.64] In order to be specific, Pokrovskii's more recent value[4.65] ≈30% will be used in this discussion, along with standard values[4.9] $n_\alpha \approx 2.2 \times 10^{17}$ cm^{-3} and $\tau_\alpha \approx 40$ μsec. These values and Eq. (4.8) yield values for B and C, which may be used along with $n_\gamma \approx 0.50 \times 10^{17}$ cm^{-3} from Eq. (4.6) to predict the γ-drop lifetime. Using s = 2, this analysis gives τ_γ = 380 μsec and $\varepsilon_{rad\gamma}$ = 65%, while for s = 3, τ_γ = 520 μsec and $\varepsilon_{rad\gamma}$ = 90%. For both cases the radiative efficiency of γ-drops is found to be considerably higher than for α-drops. In addition, the lifetime is predicted to be greatly enhanced, in semi-quantitative agreement with the measured lifetimes.

The simplified model discussed here neglects several things: (1) the density dependence of the radiative enhancement factor ρ, which is a measure of the spatial electron-hole correlation; (2) other possible stress dependences of the coefficients B and C; (3) a density-independent nonradiative decay process present both in stressed and unstressed Ge, which might be negligible for α-drops but not for γ-drops. A more detailed model of the recombination processes is the subject of Section 55, in which the density variation discussed in earlier sections of Chapter 5 will be utilized.

43.2. Temperature Dependence of the Luminescence

So far results have been presented for samples in superfluid liquid He^4 (T ≈ 1.8 K). At higher temperatures, the α-drop lifetime is considerably shortened due to boiloff of excitons.[4.59] For γ-drops the effects of boiloff are greatly reduced by the strain gradient: an exciton which boils off the surface of the γ-drop will be pulled by the strain back into the drop in a time short compared to the exciton recombination time.[4.2] The force of an exciton due to the strain gradient is approximately $\vec{F} = -2\alpha\vec{r}$, where α is the strain parameter of Eq. (4.3). The exciton thermal velocity $v_T = \sqrt{3kT/m_x} \approx 6.4 \times 10^6$ cm/sec at T = 4.2 K, using $m_x = 0.05\ m_o$. If an exciton evaporates from a γ-drop of radius R = 100 μm and moves radially away at the thermal velocity v_T, then it will be accelerated back into the drop in 0.02 μsec, or less than 1% of its lifetime, assuming $\alpha \approx 8$ meV/mm^2. Thus, even at 4.2 K, shortening of the γ-drop lifetime due to boiloff of excitons is greatly inhibited. This explains the very small number of FE observed in the well even at 4.2 K (see Section 42.1). Figure 4.13 shows the luminescence intensity vs. temperature for γ-drops and for

α-drops at two different light levels. The γ-drop signal is relatively independent of temperature, while the α-drop signal is strongly temperature-dependent, due to boiloff.

Figure 4.14 shows the initial decay time τ_i as a function of excitation level at 4.2 K, for the same ⟨111⟩ stressed sample as in Fig. 4.12 (Sample CR38). The shorter initial time at higher excitation levels is evidence of compression. At all powers the lifetime is longer at 4.2 K than at 1.8 K (Fig. 4.12), and it levels off to around 670 μsec for small drop size. An increase in lifetime is expected to accompany a decrease in the γ-drop equilibrium density at higher temperatures; the temperature dependence of the density is discussed in Section 24.

The lifetime of γ-drops at 4.2 K depends sensitively on the details of the strain well configuration. In sample CR38, when the stress was reduced by 1/2, the decay was nonexponential, qualitatively having the characteristic time dependence for boiloff-limited lifetime.[4.59] For crystals stressed along a ⟨100⟩-direction, the strain well is usually quite shallow, and strongly temperature-dependent lifetimes have been observed.[4.46]

44. Luminescence Profiles

The spatial position, size and shape of a γ-drop in Ge are observed most directly by a vidicon image[4.66] of the recombination luminescence. Figure 4.15 shows a series of γ-drop photographs obtained at different excitation levels for ⟨111⟩-stressed sample. At low excitation levels an approximately spherical mass of liquid is formed in the bottom of the potential well. At higher excitation levels, the increased volume of e-h liquid fills a larger portion of strain well, displaying a

non-spherical shape. For typical values of the liquid surface tension ($\sigma_s \approx 10^{-4}$ erg/cm^2)[4.67] and strain parameter ($\alpha \approx 8$ meV/mm^2), the strain and surface energies are equal when the drop radius $R \approx 30$ μm. Since the strain energy increases as R^5, while the surface energy increases only as R^2, for large drops the strain energy dominates. Consequently the drop shape conforms to a surface of constant strain energy.

A more quantitative measurement of the luminescence intensity as a function of position in the sample is obtained by the slit-scanning method described in Section 34. This technique also permits a time-resolved observation of the luminescence profile after the excitation is switched off.

44.1. Spatial Profiles of γ-Drops

Figure 4.16 shows a set of μ-drop slit scans at two different laser excitation levels. These slit scans, obtained with ≈85 μm spatial resolution, clearly show a large increase in the volume of the EHL as the excitation is increased. The boundaries of the crystal are well defined by scattered luminescence light.

The drop radius is plotted vs. absorbed laser power P_{abs} in Fig. 4.17, using Eq. (3.12) to obtain R from the FWHM of a slit scan. For constant e-h pair density and laser production efficiency the simplest model would predict that the drop volume is proportional to P_{abs}, or $R \propto P_{abs}^{1/3}$. The measured radii deviate from the simple $P_{abs}^{1/3}$ power dependence at both the highest and lowest excitation levels. The apparent leveling off of the drop radius at low laser levels is likely due to the finite slit width and the irregular etched surface of the sample, which limit the resolution. (From Alfvén resonances in a

similar sample, the radius was measured down to ~30 μm.) It is observed that the drop is not spherical, i.e., $R_x \approx R_y \geq R_z$, reflecting the anisotropy of the strain well.

In order to observe the total luminescence from the whole drop without spatial selection, the total EHL luminescence intensity was measured with no slits in place. This "total" luminescence intensity is plotted as a function of absorbed power in Fig. 4.18, which shows that the total intensity varies approximately linearly with P_{abs} over nearly three orders of magnitude. This is expected for the case where the production efficiency ϵ_{prod} (the number of e-h pairs in the drop per photon absorbed) and the radiative efficiency ϵ_{rad} (the fraction of pairs which decay radiatively) are constant. For constant ϵ_{prod}, the number of e-h pairs in the drop is simply proportional to P_{abs}. It can be seen from Fig. 4.17 that for $P_{abs} \geq 10$ mW the drop volume $V \propto R_x R_y R_z$ increases more slowly than P_{abs}, while the total luminescence intensity in Fig. 4.18 is still linear with P_{abs}. This is further evidence that the liquid is compressed by the strain well for $R \geq 150$ μm, and is consistent with the increased luminescence linewidth, reduced lifetime, and shifted magneto-oscillations observed at higher P_{abs}. For comparison, Fig. 4.18 also shows the total EHL luminescence intensity for the same crystal after the stress was removed; this represents the total luminescence intensity from a cloud of α-drops. The deviations from linearity are undoubtedly due to the complex mechanisms of cloud formation.

An estimate of the e-h pair production efficiency can be made from the data obtained for low excitation. For a steady-state experiment the number of e-h pairs in the drop is given by

$$N = \bar{n}V = \frac{P_{abs}\,\tau_N\,\epsilon_{prod}}{E_{ph}} \quad , \tag{4.10}$$

where $\bar{n}$ is the average pair density, V is the drop volume, τ_N is the initial decay time for N, and E_{ph} is the energy per photon of laser light. For low excitation, where the density is constant, $\bar{n} = n \approx 0.50 \times 10^{17}$ cm^{-3} from Eq. (4.6) and $\tau_N = \tau_i \approx 550$ μsec from Fig. 4.12. For this sample (sample CR38) $\epsilon_{prod} \approx 30\% \pm 10\%$, when the laser was focused to a position close to the strain well. The value of ϵ_{prod} decreases as the laser spot is moved further from this position or if the beam is significantly defocused.

At the very highest excitation levels, interesting new phenomena occur as the strain well becomes nearly filled with liquid. In Fig. 4.15, the final photograph shows the drop obtained for $P_{abs} = 800$ mW. The shape of the drop is non-spherical, reflecting the shape of the strain well. In addition, there is a well-defined "tail" of luminescence extending below the drop, approximately parallel to the ⟨111⟩ stress direction. This luminescence tail is rather sharply defined both in the face view shown in Fig. 4.15 and in the side view (not shown). It probably consists of small EHD, originally created near the laser spot, being collected into the strain well.

This explanation is supported by the following considerations. At such high excitation levels the EHD created near the laser spot are

propelled throughout a 4 x 4 x 3 mm^3 crystal, as discussed in the next section for the case of zero stress. Consider those droplets which are driven into the lower part of the crystal. They are attracted to the well by the strain gradient, with the channeling of their motion induced by the carrier mass anisotropy, as discussed by Markiewicz.[4.68] This is illustrated by Fig. 4.19, which is reproduced from Ref. 4.68. Figure 4.19a shows the results of a two-dimensional calculation of the EHL energy shift in a crystal non-uniformly stressed along ⟨111⟩. The force on a droplet would be normal to these constant energy contours. However, because of the carrier mass anisotropy, the acceleration of an EHD is not necessarily parallel to the force. Figure 4.19b shows contours of constant "acceleration potential" E^*.[1] The droplet acceleration should be normal to the contours shown in Fig. 4.19b. Thus droplets in the lower part of the crystal first move perpendicular to the stress direction, as they cross several acceleration potential contours rather rapidly; then they move parallel to the stress axis into the well, moving more slowly across fewer contours.

This channeling has been observed[4.68] at lower excitation levels by positioning the laser below the strain well. However, in Fig. 4.15 the tail was observed with the laser spot close to the well. If the excitation point is chosen in the lower portion of the sample and translated in the y direction (perpendicular to the stress axis), the bottom of the tail is observed to move also. However, the tail moves away from the laser spot, as illustrated in Fig. 4.20. This figure shows three spatial y-scans, obtained with spatial resolution ≈35 μm

in the y direction and ≈700 μm in the z direction, with the image centered at $z_I \approx 2.8$ mm below the top of the crystal. The scans were obtained for different laser pump positions, shown on the inset. For Fig. 4.20c the laser was positioned near the well, while for Figs. 4.20a and 4.20b it was positioned near the bottom of the crystal near opposite sides. The broad features in scans (a) and (b) are part of the cloud surrounding the excitation point. It can be seen that the EHD tail shifts by ≈0.4 mm when the laser is translated from point a to point b. It seems clear that a directional force associated with the laser pumping position is involved. Such a force could be provided by a wind of phonons coming from the excitation point. The interaction of EHD with phonons has been the subject of a number of recent experimental and theoretical studies,[4.69-4.74] primarily in connection with the formation processes of a cloud of EHD in unstressed Ge. It is likely that a phonon wind is responsible for the motion of the EHD tail illustrated in the figure.

44.2. Comparison with Clouds of α-Drops

The results for unstressed samples are considerably different from the results of the previous section. Previous experiments have shown that in unstressed Ge a cloud of small drops (each with radius 1 to 10 μm) is formed,[4.5, 4.6, 4.75, 4.76] for point excitation. The average density of e-h pairs in the cloud has been estimated by light scattering to be ~10^{15} cm^{-3}, indicating ~1% filling factor of EHD.[4.5] The cloud size increases with increasing excitation level, contrary to a simple model of EHD or FE diffusion into the crystal. The mechanisms of the cloud formation are not presently understood in detail,

although there is increasing evidence that a phonon wind, originally proposed by Keldysh,[4.69] is responsible for many general features of α-clouds.[4.70-4.74, 4.77] In addition, if the excitation is very well focused, striking anisotropies have recently been observed[4.73] in the cloud shape, which are reasonably well explained by the channeling of phenons in elastically anisotropic Ge,[4.72] and by the anisotropy of the electron-phonon interaction.[4.74, 4.78]

The results presented in this section illustrate some general features of α-clouds and show that they are easily distinguishable from γ-drops via the spatial distribution of the luminescence. Figure 4.21 shows a set of slit-scans for the same sample before and after the stress is removed, for P_{abs} = 2.8 mW. The α-cloud peak intensity is much lower, and the size of the profile is significantly larger, than for the γ-drop, indicating a much lower average density of e-h pairs in the cloud than in the γ-drop. For the stressed samples, the largest drop was always obtained when the laser was focused near the strain well. For the scans taken after the stress was removed, the laser spot was translated to a position near the center of the pumped face of the crystal.

Luminescence profiles for the cloud in the unstressed sample are shown in Fig. 4.22 for three different laser intensities. For low and moderate excitation (P_{abs} = 0.45 mW and 5.1 mW in the figure) the cloud has a fairly well-defined surface, as observed by others (Refs. 4.5, 4.6, 4.75, 4.76). Figure 4.23 shows a profile for the x direction under increased spatial resolution (≈50 μm, compared to ≈85 μm in Fig. 4.22), for moderate excitation (P_{abs} = 11 mW). The peak

of the distribution is distinctly separate from the edge effect peak at x = 0, the surface on which the laser is incident. This result is in contrast to earlier results,[4.5, 4.76] in which no such separation from the crystal surface was observed.

At higher excitation levels (P_{abs} = 47 mW in Fig. 4.22), the cloud seems to nearly fill the 4 x 4 x 2 mm^3 crystal. (The lumps on these slit scans may be due to imperfections on the crystal face or possibly to anisotropy in the cloud shape.[4.73]) The increasing effect of the contribution to the phonon wind associated with the excitation point is illustrated in Fig. 4.24, which shows three x-scans for P_{abs} = 29, 83, and 290 mW. As the power is increased, the droplets are more forcefully blown away from the pumped surface. It should be noted that some of the phonon wind effects are observed here only at high excitation because the laser was not very well focused; when the laser is focused more carefully, the peak of the distribution moves well into the crystal and the cloud anisotropies are apparent at lower excitation levels.[4.73]

Figure 4.25 shows the measured dependence of the cloud radius on excitation level, for low and moderate excitation only. The radius in the x direction was obtained from the half-width at half maximum of the slit scans, measured from the peak of the distribution deeper into the sample. It is clear from these data and from the above discussion that the shape of the α-cloud is complex: it is neither spherical nor hemispherical, and it does not scale in a simple way with excitation. However, a hemispherical cloud model is least inaccurate at low excitation and provides a concrete way to estimate the average e-h pair density within the cloud by comparison with the γ-drop. The

scans in Fig. 4.21 give α-cloud and γ-drop radii at the same (low) excitation level, P_{abs} = 2.8 mW. Using these radii, the measured lifetimes τ_α = 36 μsec and τ_γ = 450 μsec, and the measured γ-drop equilibrium density and estimated production efficiency, Eq. (4.10) gives $n_{ave}/\varepsilon_{prod} \approx 1 \times 10^{15}$ cm^{-3} for the cloud of α-drops. This is consistent with the result of Voos, et al.,[4.5] if ε_{prod} is close to 100% for α-drops.

In addition to the above analysis, an estimate can be made concerning the relative radiative efficiencies for α-drops and γ-drops, as follows. The integrated luminescence intensity, measured with the slits removed, is proportional to $P_{abs} \times \varepsilon_{prod} \times \varepsilon_{rad}$. This quantity can also be estimated from the area under a slit scan. The areas under the curves in Fig. 4.21 indicate that $I_\gamma \approx 3.8\ I_\alpha$, and hence

$$\frac{\varepsilon_{rad\alpha}}{\varepsilon_{rad\gamma}} \approx 0.3\ \frac{\varepsilon_{prod\gamma}}{\varepsilon_{prod\alpha}} \quad . \tag{4.11}$$

The total intensities I_γ and I_α are both nearly proportional to P_{abs} over a wide range, so Eq. (4.11) holds over a wide range. Widely differing estimates have been given for $\varepsilon_{prod\alpha}$ for the case of surface excitation, ranging from ≈15%[4.79] to ≈100% (above). However, it should be noted that the production efficiency is likely to be lower for γ-drops than for α-drops, due to the added difficulty of getting into the well. Thus Eq. (4.11) shows that the radiative efficiency of α-drops is unlikely to be greater than about 30%, somewhat lower than previous estimates (Refs. 4.30, 4.62-4.65). Indeed, using the estimates $\varepsilon_{prod\gamma} \approx 30\%$ and $\varepsilon_{prod\alpha} \approx 100\%$ given above, Eq. (4.11) has a value ≈0.1, which must

be considered to be a lower limit on the ratio of radiative efficiencies. In addition, it is important to note that the comparison is made here for γ-drops and α-drops produced in the same sample in a single run, in order to eliminate sample dependences and signal variations between runs.

44.3. Kinetics of the Luminescence Profiles

The size of γ-drops and α-clouds has also been observed as a function of time after the laser light is turned off. In the experiments, the laser light was square-wave modulated at 225 Hz, and the luminescence was sampled with a boxcar integrator at discrete times t after laser cut-off. Typical luminescence x-scans are shown for γ-drops in Fig. 4.26 (t = 0 and t = 1000 μsec) and for α-clouds in Fig. 4.27 (t = 0 and t = 100 μsec), while Fig. 4.28 shows the radius vs delay time for x-, y-, and z-scans for both cases. It is clear that the time behavior of γ-drops and α-clouds is quite different.

In Figs. 4.26 and 4.28a the γ-drop radii are measured at a relatively high light level P_{abs} = 100 mW. The decay is precisely what would be expected for the quasi-equilibrium decay of a single drop: as the drop shrinks, its shape approximately corresponds to the steady-state shape of successively smaller drops (Fig. 4.17). The radius decay is non-exponential, analogous to the decay of the total luminescence at a similar excitation level (see Fig. 4.11b).

Figure 4.29 shows the decay of the γ-drop radius for a sample stressed along ⟨110⟩, with P_{abs} = 96 mW. This sample was stressed in the "permanent stress" geometry described in Ref. 4.1, so that both luminescence imaging and Alfvén resonance experiments could be done,

using different experimental setups, for the same strain conditions. Shown also is an average radius inferred from Alfvén wave resonance (Refs. 4.2, 4.10, 4.38, 4.40). The resonant absorption occurs at a magnetic field ($H \parallel \langle 100 \rangle$) which varies with the drop size: $H \propto R$; and so the resonance shifts to lower fields as the drop decays. The Alfvén resonances were detected in a pulsed excitation experiment which resulted in a smaller initial drop size. The resonance decay times measured in these two experiments are in good agreement. As expected (if compressional effects are not large), the radius decay time is approximately equal to three times the luminescence decay time.

On the other hand, the cloud of α-drops in unstressed Ge decays in a quite different manner, as shown in Figs. 4.27 and 4.28b. The size of the cloud does <u>not</u> decay in time at low temperature, implying that after the initial cloud formation the droplets individually decay at a relatively fixed position in the cloud. In Fig. 4.27, after 100 μsec delay the width of the luminescence profile is unchanged, even though the peak intensity has decreased by over a factor of 10. In Fig. 4.28b, the line corresponds to exponential decay with τ = 105 μsec. This is three times the luminescence decay time, which would be the expected radius decay time if the cloud decayed as a single body with n_{ave} = constant. Clearly the cloud does not shrink in time: in fact, the data indicate the interesting possibility that the cloud size may initially <u>grow</u> after the light is switched off. Indeed, this can be understood using a recent phonon wind theory of Markiewicz.[4.74]

In principle, the same techniques described here to study the decay of γ-drop and α-drop profiles can also be used to study their buildup. However, the buildup process is much more complex than decay: In unstressed Ge, the rate of cloud expansion has been observed to depend on excitation level for a square wave excitation experiment,[4.73] while a kind of ballistic expansion at ≈ the speed of sound has been observed for intense pulsed excitation.[4.80] In nonuniformly stressed Ge, the buildup is complicated still further, because the small EHD created near the laser spot must collect in the strain well. Preliminary studies of the total luminescence intensity show that for the square-wave excitation used in this thesis the buildup time varies with P_{abs}, somewhat similar to the decay time (e.g., Fig. 4.12). However, at the highest excitation levels buildup occurs more rapidly than decay. In a pulsed experiment, the γ-drop has been observed[4.81] by Alfvén wave resonances to grow from zero to final size within ≈1 μsec. Clearly much remains to be learned about the formation of γ-drops; however, greater understanding is first needed of the processes by which α-drops are propelled in unstressed crystals, before the details of their collection in the strain well can be understood.

44.4. <u>Magnetostriction of γ-Drops</u>

In a magnetic field the shape of a γ-drop has been observed to change,[4.82-4.85] as illustrated in Fig. 4.30. Part b shows vidicon images for zero field for $P_{abs} \approx 50$ mW. Both face and end views are shown, for the viewing arrangement of part a. Parts c and d show that in a field of 20 kOe the drop flattens along the applied field direction, for $H \parallel \langle 11\bar{2} \rangle$ and for $H \parallel \langle 1\bar{1}0 \rangle$. Figure 4.31 shows the distortion more quantitatively as a function of magnetic field for low excitation,

P_{abs} = 3 mW, and for the field orientation of Fig. 4.30d. The radii parallel and perpendicular to the magnetic field direction were measured using luminescence slit scans, as in Section 44.1. The shape was observed to begin to change in fields of a few kOe and to saturate at fields ≤20 kOe. This general behavior has been observed for different field orientations, values of the stress, and drop sizes.[4.82] The field at which saturation occurs depends on the last two variables, as does the saturated drop shape. In Fig. 4.31, for example, at 20 kOe the ratio $R_\perp/R_\parallel \approx 2.3$, for a zero-field drop radius of ≈170 μm. Since the strain gradient acts as a restoring force, it may be expected that in a shallower strain gradient the magnetostriction would be more pronounced. This is indeed the case. In the sample and configuration of Fig. 4.15 the strain well parameter α of Eq. (4.3) was relatively small. For an excitation level comparable to Fig. 4.31, at 20 kOe the ratio $R_\perp/R_\parallel \approx 3$ to 4, measured approximately from a vidicon image.

The observed shape change may be understood as follows. Because of the continuous recombination of e-h pairs within the bulk of an EHD, a drop can be maintained in steady state only if there is a net flow of e-h pairs inward from the surface, supplied from the cw laser excitation. This recombination current was proposed by Kaminskii and Pokrovskii[4.86] and is illustrated in Fig. 4.32 for the case of spherically symmetric collection of pairs onto the drop surface. Figure 4.32a shows the electron and hole recombination currents for zero field, while Fig. 4.32b shows how they are deflected by the Lorentz force in an applied magnetic field. Electrons and holes are deflected in opposite directions, giving a net current azimuthal about the magnetic field axis. This current in turn results in a net positive

(paramagnetic) magnetization $\vec{M}_R$, with a contribution $E_m = -1/2\ \vec{M}_R \cdot \vec{H}$ to the drop energy. Thus the drop can lower its energy by increasing the magnetization, i.e., by flattening along the magnetic field axis and growing perpendicular to that axis. The flattening is balanced by restoring forces due to the strain gradient and the surface energy. A detailed magnetohydrodynamic theory has been developed by Markiewicz et al.[4.68, 4.87] which describes the magnetostriction quantitatively, including high-field saturation and the effect of nonuniform flux onto the drop surface.

The decay of γ-drops is strongly affected by the fact that carriers can move parallel to the field much more easily than perpendicular to it. Very shortly after the square-wave excitation is switched off, there is no net particle flow into the drop, and the decay of an isolated drop in a magnetic field can be determined. Figure 4.33 shows the drop radii parallel and perpendicular to H as a function of time after the excitation was switched off, with ≈85 μm spatial resolution. The drop dimension parallel to the field decays more rapidly than the dimension perpendicular to the field. (For smaller drops $R_\perp$ has been observed to decay, having a decay rate comparable to that for $R_\parallel$ at long delay times.) It is clear that the γ-drop shape depends on the dynamic internal particle currents, which can be affected by an external magnetic field.

Magnetostriction is also expected[4.68] to occur in α-drops in unstressed Ge. However, it is more difficult to observe because of the extreme difficulty of studying individual droplets. If EHD are in motion in a lossy medium, the magnetic field could damp droplet motion perpendicular to the field axis. Although the size and shape of α-clouds

have not been observed to change significantly in a 20 kOe field,[4.68] p-n junction experiments[4.88] may have shown evidence for such damping of motion. It would be desirable to perform an experiment in which the α-drop motion was well-defined but which avoids the complications of junction fields. The last photograph in Fig. 4.15 shows a large drop with a stream of small EHD flowing into the well in a sharply-defined direction. When a 20 kOe magnetic field was applied perpendicular to the direction of the EHD flow, the vidicon image of the tail was observed to become brighter, indicating that the drops were moving more slowly. In this case, then, droplet motion transverse to the field was damped. It is possible that the crystal was lossier due to a larger concentration of free carriers at the very high excitation level which was used, compared to the usual α-cloud experiments in unstressed Ge.

CHAPTER 5. DENSITY VARIATION AND COMPRESSIBILITY OF THE STRAIN-CONFINED ELECTRON-HOLE LIQUID IN Ge

51. Introduction

Chapter 4 of this thesis presented a discussion of some of the properties of the strain-confined electron-hole liquid (SCEHL) in Ge. In particular, it was shown that the equilibrium density and lifetime can be measured for the small drop sizes obtained at low excitation intensities. In addition, evidence was presented that at higher excitation levels the liquid may actually become compressed by the strain well: the luminescence linewidth was found to increase and the luminescence decay time was found to decrease with increasing drop size.

In this chapter the compression of the SCEHL by the strain well is investigated in detail. The theoretical background is presented, and experimental results are presented for two samples. Sample CR38 was studied in Chapter 4; however, because the experiments for the present chapter were performed under different stress conditions, the strain well was not completely characterized. On the other hand, Sample CR50 was carefully characterized.

Some qualitative evidence for the compression of the SCEHL is reviewed in Figs. 5.1-5.4, all of which show experimental results for Sample CR50. Figure 5.1 shows the total luminescence intensity I_{tot} from the entire drop without spatial selection, the peak luminescence intensity in a slit scan I_{slit}, and the peak luminescence intensity in a box scan I_{box}, all as a function of absorbed power P_{abs}. The procedure for obtaining slit and box scans is indicated schematically

in the inset and is discussed in Section 34. Figure 5.2 shows the drop size and drop volume vs. power. The drop size is given by the full width at half maximum of a slit scan. As discussed later, this is related to the drop radius via Eq. (3.15) if compressional effects are not important. The drop volume is obtained from the radii for three mutually perpendicular directions: $V = 4/3\pi\ R_x R_y R_z$. To aid in the interpretation of these data, straight lines are drawn in Figs. 5.1 and 5.2 to indicate the trends, for P_{abs} between ≈0.1 and ≈5 mW. Consider the trends expected for the case of spherical drops with a constant e-h pair density. The total luminescence intensity is a measure of the drop volume and thus should vary with power as R^3.[5.1] The peak intensity in a slit scan represents a slice through the center of the sphere and should vary as R^2. Similarly, the peak intensity in a box scan represents a core section through the center of the sphere and should vary as R. It is clear from the slopes given in the figures that these simple relationships are not found to be true. Firstly, the two measures of the drop size, I_{box} and W_s, have very different power dependences (the slopes are 0.67 and 0.41 respectively). Secondly, the two measures of the drop volume, I_{tot} and V, also have different power dependences (the slopes are 1.44 and 1.24 respectively[5.1]). Thirdly, the slopes for I_{box}, I_{slit}, and I_{tot} have the relation 0.67:1.12:1.44, which does not correspond to the expected relation 1:2:3. It will be shown later in the chapter that these apparent inconsistencies can be explained in terms of a compression of the liquid. It may be noted that in order to obtain valid comparisons of the luminescence intensities, as in Fig. 5.1, it was necessary to have

a detector which was reliable and stable and gave reproducible results. Some of the requirements for such a detector are discussed in Section 33.

Additional qualitative evidence is shown in Figs. 5.3 and 5.4. Figure 5.3 shows the full width at half maximum ΔE of luminescence spectra for the LA-assisted line as a function of absorbed power. As was the case in Fig. 4.8 for Sample CR38, the linewidth is found to increase at high excitation levels. This broadening is due to the strain gradient as well as to an increase in the (average) density with drop size. In addition, Fig. 5.4 shows the initial luminescence decay time τ_i as a function of absorbed power, analogous to the data in Fig. 4.12 for Sample CR38. The lifetime is again observed to decrease with excitation level. Such a change in the lifetime must be accompanied by a change in the e-h pair density. Thus the average density must increase with drop size.

In order to interpret the above luminescence data, as well as the data presented in later sections of this chapter, it is necessary to characterize the strain well. The strain inhomogeneity which is known to be present must be accounted for in some way, and the variation in the EHL energy with position must be measured. This procedure is discussed in Section 52.

In Section 53 the theoretical background is presented. The idea that the e-h pair density should vary with position is presented in Section 53.1, including the origin, form, and magnitude of the density variations. This is found to be a large enough effect to account for the kinds of effects shown in Figs. 5.1-5.4. The manifestations of the density variation in luminescence experiments are

discussed in Section 53.2. Predictions are made concerning the shapes and power dependences of spatial slit and box scans. A method is described which is later used to measure density profiles directly. It is shown that the density measurements can be used to measure the EHL chemical potential as a function of density, thus providing a sensitive test of the theories used to describe the EHL. In addition, it is shown that the liquid compressibility can be measured, since the density is varied by squeezing the liquid at a fixed temperature.

The experimental results for Samples CR50 and CR38 are presented in Section 54. Measured e-h pair density profiles are shown for different drop sizes. The form of the density variation with position is found to be in good agreement with the theoretical predictions, as is the magnitude of the variation with drop size. The measurements of the chemical potential and compressibility are presented. These constitute the most stringent tests of the theory which was presented in Chapter 2. Since some differences are observed, this may be an indication that a modified model for the Coulomb energy should be used. However, the differences are not considered to be serious.

Finally, in Section 55 a discussion is presented of the density dependence of the EHL lifetime. Various models are presented in order to explain the observed lifetime variation with drop size. The lifetime of the SCEHL is found to vary more slowly than the density, in contrast to the case for unstressed Ge where Auger recombination dominates. A density independent recombination mechanism is shown to be possible. However, it appears that in order to explain the experimental results for both unstressed and stressed Ge, the Auger coefficient must be rather sharply reduced under stress.

Some of the material presented in this chapter has been published in preliminary or abbreviated form.[5.2, 5.3] More complete discussions of the density variation and compressibility[5.4] and of the density-dependent lifetime[5.5] are currently in preparation.

52. Characterization of the Strain Well

In order to quantitatively understand the variation of the e-h pair density with position in the SCEHL, it is necessary to characterize the strain well. This requires several steps which are described in this section, along with additional information presented in Section 53.1. First the degree to which the stress is uniaxial is discussed. Next the maximum stress σ_M at the center of the well is determined, along with the equilibrium density n_o, for Sample CR50, which is the sample discussed in the greatest detail in this chapter. Then the shape of the strain well is discussed, both for excitons and the electron-hole liquid.

It is clear that the stress geometry used here and described in Section 31 results in a distribution of stress which is highly nonuniform. Indeed, Markiewicz[5.6, 5.7] has numerically calculated the distribution of shear strain components in inhomogeneously strained Ge. Other quantities may be calculated once the shear strains are known. Figure 5.5 shows the result of such a calculation, which was performed using a two-dimensional model of the system. Thus part (a) of the figure represents a slice parallel to a 4×4 mm^2 $(1\bar{1}0)$ face of the Ge crystal, while part (b) represents a slice parallel to a 4×3 mm^2 $(11\bar{2})$ face of the crystal. (These are approximately the dimensions of Sample CR50.) In each case the slice is

selected which passes through the center of the well. Information about the actual three-dimensional distribution can be inferred from the pair of two-dimensional distributions. Figure 5.5 shows σ_{111}, the component of stress along the ⟨111⟩ direction, as a function of position. The parameters of the program were chosen to approximately reproduce two experimental features of the well: the maximum stress $-\sigma_M \approx 5$ kgf/mm^2 (see below), and the position $z_o = 0.8$ mm of the well relative to the face where the plunger touches the sample (see also Fig. 4.15). As noted in Section 31, for this sample a plunger with a rather large radius of curvature was used, and the initial force applied at room temperature was greater than usual. As a result the contact area between the plunger and the sample was ~2 mm^2, and the well was an unusually large distance below the stressed surface.

The computer program also evaluates other stress components. If the stress direction is z and the perpendicular direction is y, the program computes the stress components σ_{zz}, σ_{yy}, and $\sigma_{yz} = \sigma_{zy}$. The component of stress along the ⟨111⟩ direction is given approximately[5.8] by $\sigma_{111} \approx \sigma_{zz}$, and the component of stress along other directions is given approximately[5.8] by $\sigma_{\text{non-111}} \approx -\sqrt{\sigma_{yy}^2 + 2\sigma_{yz}^2}$ (recall that compressional stresses are negative). Thus a measure of the deviation from uniaxial stress is given by the ratio $|\sigma_{\text{non-111}}/\sigma_{111}|$. This quantity is shown in Fig. 5.6 for the geometry and parameters of Fig. 5.5. It can be seen that the stress is very highly uniaxial: even for the largest drops studied, the quantity $|\sigma_{\text{non-111}}/\sigma_{111}| \lesssim 0.3$. Thus the assumption of uniaxial ⟨111⟩ stress throughout the region of the crystal occupied by the SCEHL is well justified.

The next step in characterizing the strain well is to determine the maximum stress σ_M at the center of the well. For the inhomogeneous geometry used here the stress cannot be simply obtained from the applied force and the contact area. Instead, as discussed in Section 42.2, σ_M may be estimated from the shift of the peak energy of a luminescence spectrum measured at low excitation, by comparison with the uniaxial stress data of Benoît et al.[5.9] This procedure is illustrated in Fig. 5.7, which shows a luminescence spectrum from Sample CR50 for $P_{abs} = 0.8$ mW and a spectrum from an unstressed Ge crystal for $P_{abs} = 25$ mW. The shift of the luminescence peak $\Delta E_{peak} = -1.93$ meV. The ⟨111⟩ stress data of Benoît et al.[5.9] can be fit by the following expression (see Fig. 4 of Ref. 5.7):

$$\Delta E_{peak} = 1.62 + 0.68\sigma \quad (2.5 \lesssim -\sigma \lesssim 13) \qquad (5.1)$$

where σ is measured in kgf/mm^2 and ΔE_{peak} is in meV. Using this method, $-\sigma_M = 5.2$ kgf/mm^2 for sample CR50.

It is really more fundamental to measure the change in the liquid ground state energy, which is given by $h\nu_{min} + E_F^e + E_F^h$ in the notation of Section 22.3. This spectroscopic energy E_{spec} (sometimes called μ' in the literature[5.10]) is measured from an energy $\hbar\omega_{ph}$ above the valence band maximum, where $\hbar\omega_{ph}$ is the energy of the phonon emitted with the photon in the indirect transition (see Fig. 1.1). The phonon energy is assumed to be independent of stress. The data of Benoît et al.[5.9] have not been analyzed in sufficient detail to yield the spectroscopic energy E_{spec} as a function of stress. However, the shift of E_{spec} with stress can be calculated using the results of Chapter 2, as follows:

$$\Delta E_{spec} = \Delta E_{gap} - \Delta f_G \quad . \tag{5.2}$$

Here E_{gap} is the change in the minimum band gap with stress, and the ground state energy f_G is measured with respect to the lowest conduction band minimum. For Ge the change in the minimum gap is given by[5.11]

$$\Delta E_{gap} = \Delta E_{gap}^{mean} + 3/4\ E_{spl}^{e} + 1/2\ \Delta E_{spl}^{h} \quad . \tag{5.3}$$

The mean band gap E_{gap}^{mean} is the energy difference between the mean of the conduction bands and the mean of the valence bands. It changes with stress as $\Delta E_{gap}^{mean} = -\ 0.098\ \sigma$,[5.11] while E_{spl}^{h} and E_{spl}^{e} are given in Tables 2.1 and 2.3 respectively. Thus $\Delta E_{gap} = 0.87\ \sigma$. The ground state energy f_G is shown in Fig. 2.11 for Ge. The change in this quantity with stress, Δf_G, is nearly identical for Models 1 and 2 and may be fit over range of stresses to yield the following:

$$\Delta E_{spec} = 1.81 + 0.77\sigma \quad (2.5 \leq -\sigma \leq 9) \quad . \tag{5.4}$$

The spectroscopic energies shown in Fig. 5.7 were obtained from a fit of the luminescence lineshapes (see below) and yield $\Delta E_{spec} = -2.67$ meV. Using this method, $-\sigma_M = 5.8$ kgf/mm^2. The reasonable agreement with the result of the first method indicates that the change in f_G with stress is described well by Models 1 and 2 of Chapter 2. The two methods thus give an average value $-\sigma_M = 5.5 \pm 0.3$ kgf/mm^2 for the stress at the center of the well in Sample CR50. It is shown in Section 53.1 that the analysis of this chapter is not sensitive to small variations in σ_M. Thus the theory is presented for $-\sigma_M = 5.0$ kgf/mm^2.

The luminescence spectra in Fig. 5.7 were fit to the lineshape formula given by Eqs. (2.38) and (2.39). In both cases the slit resolution (0.66 meV FWHM) and the detector response versus wavelength were included. For the unstressed sample the best fit was obtained for $n = 2.20 \pm 0.05 \times 10^{17}$ cm^{-3}, in reasonable agreement with other published values.[5.10] For the stressed sample the best fit was obtained for

$$n = 0.47 \pm 0.03 \times 10^{17}\ \text{cm}^{-3} \quad (-\sigma_M = 5\ \text{kgf/mm}^2,\ T = 1.9\text{K}). \tag{5.5}$$

Since this spectrum was measured at low excitation, the deduced density is the equilibrium density for this stress. The density obtained for this sample is typical for samples stressed under similar conditions (see also Section 42.4). In the figure the open circles give the theoretical lineshapes.

The shape of the strain well may be characterized by the shape of a luminescence spatial slit scan for excitons. As described in Section 42.1, if the exciton energy is parabolic in the distance r from the center of the well, then the luminescence intensity in a slit scan is given by the following:

$$I(x) = I(x_o) \exp\left(-\frac{\alpha_{ex}(x - x_o)^2}{kT}\right) \quad , \tag{5.6}$$

where $x = x_o$ is the center of the well. Here the excitons are assumed to act as an ideal gas. This assumption has been justified in studies of free excitons in a strain well in Si.[5.12] Figure 5.8 shows exciton slit scans for the x, y, and z directions as defined in Chapter 3 (see Fig. 3.8). These scans were obtained at T = 4.2K at an excitation level $P_{abs} = 1.1$ mW, which was below the threshold for EHL formation. The spatial resolution

was ≈85 μm. The open circles show Eq. (5.6) corrected for the spatial resolution. The data for the x and y directions (Figs. 5.8a and 5.8b respectively) are in excellent agreement with the theoretical profiles, showing that the strain well is quite accurately parabolic in these two directions. (This parabolicity is expected from the two-dimensional calculations such as in Fig. 5.5.) A more precise fit gives α_{ex}^{x} = 1.9 ± 0.1 meV/mm^2 and α_{ex}^{y} = 2.0 ± 0.2 meV/mm^2. The stated errors include the differences between the left and right halves of the scans, which were larger than the uncertainties for the individual half-scans. For the upper half of the z-scan ($z - z_o < 0$ in Fig. 5.8c) the well is reasonably parabolic, with α_{ex}^{z} = 5.5 ± 0.5 meV/mm^2. However, the lower half of the scan ($z - z_o > 0$) is not so accurately parabolic. (The lack of parabolicity is also expected from the two-dimensional calculations.) This must be kept in mind when comparing theory and experiment. However, as a starting point the well may be considered to consist of two hemi-ellipses (actually a hemi-ellipse and a hemisphere).

Finally, it is necessary to relate the variation of the exciton energy with position to the variation of the stress and the EHL spectroscopic energy with position. This is straightforward if the exciton energy is just a constant less than the band gap. The data used by Balslev[5.11] to deduce the deformation potentials of the band edges actually correspond to the exciton deformation potentials at T = 0. It may be noted from Fig. 2.11 that at finite temperature the exciton binding energy has a slight stress dependence, especially in the range of stresses of interest ($2.5 \leq -\sigma \leq 5.5$ kgf/mm^2). However, this is a small correction and will be neglected here. Thus the changes in the

band gap and the exciton energy with stress are taken to be equal. The well parameter α_{spec}, which describes the variation of the EHL spectroscopic energy E_{spec} with position, may be simply obtained from α_{ex} using Eq. (5.4) and the gap deformation potential given above. Thus

$$\alpha_{spec} = 0.89\, \alpha_{ex} \quad , \tag{5.7}$$

or α_{spec} = 1.7 ± 0.2 meV/mm^2. It is useful to estimate the change in stress over the volume of the largest drop size obtained, R ≈ 700 μm (see Fig. 4.15 and later sections of this chapter). Using Eq. (5.4) it is easily found that the stress only varies by ≤1.1 kgf even for the largest drop size studied here.

53. Theory

In this section the theoretical background is presented for the understanding of the variation of e-h pair density with position in the SCEHL. In Section 53.1 it is shown how the density variation arises. A first-order version[5.13] of the thoery is presented in order to gain physical insight. Then a more exact theory is presented. It is noted that the density variation can be exploited to study the compressibility of the SCEHL and to study certain properties of the SCEHL as a function of density. In Section 53.2 the manifestation of the density variation in luminescence experiments is described, including a method for the measurement of density profiles.

53.1. Prediction of the Variation in Pair Density with Position

The theoretical basis for understanding the variation in e-h pair density with position lies in two facts: the pair energy varies with

density in the electron-hole liquid, and the liquid sits in a potential energy well. In the absence of the potential well, i.e., for uniform (or zero) stress, at low temperature the equilibruim density is that for which the pair energy is a minimum. The liquid can have a density other than the equilibrium density only at the cost of an increase in energy. In the presence of the strain well, however, the energy varies with position in the crystal. For small drop sizes, the energy variation is small and the density is nearly uniform with the equilibrium value. As the drop grows larger, the average pair energy is forced to increase as the liquid occupies regions of higher strain energy. However, it turns out that the total drop energy can be reduced if the liquid becomes more dense at the center, where the strain energy is lower.[1] Thus the pair density varies with position, with densities higher than the equilibrium value occurring at the center of the drop. The condition which determines the density distribution is that the chemical potential is a constant throughout the drop volume.

It may be noted in advance that the variations in density as well as in stress are reasonably gradual. For example, even for a relatively large well parameter, $\alpha_{spec} = 10$ meV/mm^2, in the steepest part of the well for the largest possible drop size, the stress changes by less than 0.4% over a distance 1 μm; for the same conditions the density changes by less than ≈1.5%. This may be contrasted with a calculation of the EHL surface structure, in which the density falls to zero over a distance approximately equal to an exciton Bohr radius, or ≈0.02 μm. In the latter case calculations are usually done using an expansion in the density gradient.[5.14-5.17] However, for the present calculation

this is unnecessary.

In order to be more quantitative, suppose that the ground state free energy per pair is given by the following Taylor series expansion about the minimum:[5.13]

$$E = E_o + \tfrac{1}{2}E_o''(n - n_o)^2 + E_s(r) \quad . \tag{5.8}$$

(Because this is a simplified derivation, E instead of f is used for the pair energy.) Here n_o and E_o are the ground state equilibrium density and energy, and $E_o'' = d^2E/dn^2|_{n_o}$. The strain energy is assumed to be parabolic in the distance r from the center of the well:

$$E_s(r) = \alpha_{spec}\, r^2 \quad . \tag{5.9}$$

The well parameter α_{spec} was discussed in the previous section and measures the variation in the liquid energy with position relative to the valence band. Thus if E_o is measured relative to the valence band rather than the conduction band, so is the total energy E. Because of the energy variations with position, it is necessary to know the zero of energy and convenient to use the valence band maximum as that zero. Using Eq. (2.6a) the pressure is given by

$$P = n^2 \frac{dE}{dn} = n^2 E_o''(n - n_o) \quad . \tag{5.10}$$

The chemical potential is given by Eq. (2.6b). To first order in the deviation from the equilibrium density, $(n - n_o)$, it can be written as

$$\mu = E + \frac{P}{n} = E_o + n_o E_o''(n - n_o) + \alpha_{spec}\, r^2 \quad . \tag{5.11}$$

The chemical potential is constant throughout the drop volume. This just means that the liquid is in diffusive equilibrium: the time

required for particles to travel across the drop is much less than the drop lifetime. This may be verified by estimating the electron Fermi velocity

$$v_F = \sqrt{2E_F^e/m} \approx 6 \times 10^6 \text{ cm/sec} \quad , \qquad (5.12)$$

using $E_F^e \approx 2.2$ meV for the equilibrium density at $-\sigma = 5$ kgf/mm^2 and the electron density-of-states mass $m = 0.22\ m_o$. (The hole Fermi velocity is not very different.) Since the Fermi velocity increases with density, this represents a minimum value for v_F. The greatest distance to be traveled is the diameter of the largest drop studied, $2R = 1.4$ mm. Thus the transit time is less than ≈ 0.023 μsec, which is much shorter than the drop lifetime $\tau \approx 500$ μsec, and μ = constant is well justified.

In order to obtain an expression for the density as a function of position, Eq. (5.11) may be written for an arbitrary position r as well as for $r = R$. This may be solved to yield

$$n(r) = n(R)\left[1 + \frac{\alpha_{spec}(R^2 - r^2)}{n(R) n_o E_o''}\right] \quad . \qquad (5.13)$$

The density at the surface, $n(R)$, may be obtained by noting that the change in pressure crossing the drop surface is given by[5.18]

$$P_{liquid} - P_{gas} = \frac{\sigma}{R} \quad , \qquad (5.14)$$

where here σ is the surface tension rather than the stress. For the "ideal" intermediate stress corresponding to the Model 1 correlation energy of Chapter 2, the surface tension has been calculated[5.19] to be $\sigma \approx 1 \times 10^{-4}$ erg/cm^2. Even for the smallest drops studied here, $R \approx 50$ μm, the pressure difference ≈ 0.02 dyne/cm^2 corresponds to a

negligible correction in the liquid density, at least at low temperature. (At higher temperatures, near the critical temperature, the system becomes more difficult to describe, as discussed in Section 24.2.) In addition, at low temperature the gas pressure itself can be neglected. Thus for the liquid at low T, $P \approx 0$ at the drop surface and from Eq. (5.14)

$$n(R) = n_o \quad , \qquad (5.15)$$

i.e., the density at the surface of the drop is the equilibrium density. Actually, it is the equilibrium density for the value of stress corresponding to the drop surface and therefore changes with R. However, this density does not change very much over the relevant range of stresses for a typical experiment: the equilibrium density increases by 20% as the stress is reduced from -5 to -3 kgf/mm^2 and by only 10% as the stress is reduced from -5 to -4 kgf/mm^2, for Model 1.

It was noted in Section 52 that the latter stress range corresponds to the range of drop sizes studied in Sample CR50. This small change in the equilibrium density with drop size will be neglected, since it is much smaller than the density variation implied by Eq. (5.13), as will be shown shortly.

Equation (5.15) may be substituted into Eq. (5.13) to yield the following density distribution:

$$n(r,R) = n_o\left[1 + \beta(R)\left(1 - \frac{r^2}{R^2}\right)\right] \qquad (5.16)$$

where

$$\beta(R) = \frac{\alpha_{spec} R^2}{n_o^2 E_o''} \quad . \qquad (5.17)$$

Here the dependence of the density profile on drop size as well as on

position within the drop is noted explicitly. It is easily seen that the density increases from the equilibrium value at the drop surface to a higher value at the center, confirming the qualitative ideas presented at the beginning of this section. For this first-order theory the density distribution is parabolic. The density at the center of the drop is given by

$$n(0,R) = n_0[1+\beta(R)] \quad . \tag{5.18}$$

This can be estimated for Sample CR50 by noting that $n_0^2 E_0'' \approx 0.42$ meV for $-\sigma = 5$ kgf/mm^2 and $T = 0$, according to Model 1. Using $\alpha_{spec} = 1.7$ meV/mm^2 from Section 52 it can be seen that the density is unifrom to within 10% if $R \lesssim 160$ μm, while for the largest drop sizes ($R = 700$ μm) $n(0) \approx 3.0\ n_0$. The values given here differ from those given in Section 42.3 because the well parameter α_{spec} was smaller for Sample CR50 than for Sample CR38. It is clear, however, that the density variation with position is a large effect and should be evident in many experiments. Indeed, evidence of compression of the SCEHL has been pointed out in Chapter 4 and in Section 51; direct measurements are presented in Section 54.

The magnitude of the density variation for large drop sizes is perhaps surprising. Generally one thinks of a liquid as having a uniform density. In addition, it is relatively difficult to change the density appreciably; i.e., most liquids are not very compressible. This is because the interparticle spacing in the liquid is nearly the size of the sphere, using a hard-sphere model to describe the liquid molecules. In the electron-hole liquid the interparticle spacing still corresponds approximately to the size of the gas "atom," i.e., the

exciton Bohr radius. However, in contrast with ordinary liquids, the constituent particles (e-h pairs) can interpenetrate one another. A hard-sphere limit for electrons and holes would correspond to a density many orders of magnitude greater than the equilibrium density, and in fact is never attained due to the Coulomb interaction. It can be seen, however, that the compressibility of the EHL could be much larger than the compressibility of ordinary liquids.

An analogy may be drawn between the SCEHL and the ocean. The water at the bottom of the ocean is denser because of the weight of the column of water above any ocean-floor area. Consider a simple model in which the ocean is isothermal. The pressure exerted by a column with height h is $P = \rho h g$, where $\rho \approx 1$ gm/cm^3 and the change in g with height is neglected. The greatest ocean depth is ~10 km. Thus the pressure at the bottom of the ocean is $\sim 10^9$ dyne/cm^2. The compressibility of water is $\approx 4 \times 10^{-11}$ cm^2/dyne at 20°C and P = 1 atmosphere,[5.20] nearly independent of P. Using the definition of the isothermal compressibility from Eq. (2.70a) it can be seen that

$$-\frac{\Delta V}{V} = \Delta P\ K_T \approx 4\% \quad . \tag{5.19}$$

At the bottom of the deepest part of the ocean, then, the water is only 4% compressed, according to this simple model. Note from Fig. 2.20 that the compressibility of the EHL is $K_T = 2.7 \times 10^{-2}$ cm^2/dyne for $-\sigma =$ 5 kgf/mm^2, $T = 0$, and Model 1. Thus the EHL is nearly 10^9 times more compressible than water! A fairer comparison may be made by noting that the (particle) density for water is greater than the EHL density by a factor $\approx 6.6 \times 10^5$. The product nK_T is still larger for the EHL by ≈800. Even for liquid He^3, which is considered to be a highly

compressible liquid with $K_T \approx 3.9 \times 10^{-8}$ cm^2/dyne at T = 1K and saturated vapor pressure,[5.21] the product nK_T is smaller than for the EHL by about a factor of two. Thus the electron-hole liquid may be nature's most compressible liquid.

It is clear that the first-order theory given by Eqs. (5.16) and (5.17) is not valid for the largest experimentally accessible drop sizes, since the deviations from n_o are no longer small. Hence a more exact theoretical treatment is necessary. Before turning to the more exact theory, however, additional physical insight may be gained from the first-order theory. It is useful to estimate the effect of changing the temperature on the density profile. In particular, in attempting to study the phase diagram of the EHL and an exciton gas in a strain well it is necessary to account for the compression of the liquid at the smallest observable drop sizes at elevated temperatures. This may be accomplished approximately by using a low-T expansion for the pair energy in Eq. (5.8), following Eq. (2.67):

$$E = E_o + \tfrac{1}{2}E_o''(n - n_o)^2 - \tfrac{1}{2}\gamma(n)\,T^2 + \alpha_{spec}\,r^2 \,. \qquad (5.20)$$

This expression is equivalent to the following one:

$$E = E_o(T) + \tfrac{1}{2}E_o''(T)\,(n - n_o(T))^2 + \alpha_{spec}\,r^2 \,, \qquad (5.21)$$

in which the temperature dependence is distributed among the other terms. The formalism of Section 24.1 may be used, i.e.,

$$n_o(T) = n_o[1 - \delta_n(kT)^2] \qquad (5.22a)$$

$$E_o(T) = E_o - \frac{3}{2}\,n_o^2 E_o''\,\delta_n(kT)^2 \qquad (5.22b)$$

$$E_o''(T) = E_o''\left[1 - \frac{5}{3}\,\delta_n(kT)^2\right] \qquad (5.22c)$$

$$\delta_n = \frac{\gamma(n_o)}{3n_o^2\,E_o''} \,. \qquad (5.22d)$$

Here it is assumed that $\gamma(n) \propto n^{-2/3}$. This is true only for parabolic bands; however, it is accurate enough for the present discussion as long as the stress is not too near one of the critical stresses σ_e or σ_h, which are defined in Chapter 2. Using Eq. (5.21), the density profile may be immediately obtained as previously:

$$n(r,R,T) = n_o(T)\left[1 + \beta(R,T)\left(1 - \frac{r^2}{R^2}\right)\right] \qquad (5.23a)$$

where

$$\beta(R,T) = \frac{\alpha_{spec}\,R^2}{n_o^2(T)\,E_o''(T)} = \beta(R,0)\left[1 + \frac{11}{3}\,\delta_n(kT)^2\right] \qquad (5.23b)$$

to first order in T^2. This equation may be used to estimate the largest drop size for which the density is uniform to within a certain fraction at finite temperature, e.g., to within 20% at T = 4.2K for $-\sigma$ = 5 kgf/mm^2. According to Model 1, for this stress $\delta_n = 3.8$ meV^{-2}. Using the information given above for $\beta(R,0)$, it is easily seen that this drop size is $R \approx 130$ μm for the conditions of Sample CR50. It should be noted that for a sample with a steeper well, the requirement is more stringent: if $\alpha_{spec} \approx 8$ meV/mm^2, as is more typical, then 20% uniformity is achieved only if $R \lesssim 60$ μm. Thus at high temperatures the liquid may already be appreciably compressed at the smallest drop sizes for which enough luminescence can be collected for an accurate lineshape fit.

The density at the center of the drop can be obtained for finite temperature from Eq. (5.23) and rewritten as follows:

$$n(0,R,T) = n_o[1+\beta(R,0)] + n_o[\frac{8}{3}\beta(R,0) - 1]\,\delta_n(kT)^2 \quad . \qquad (5.24)$$

The sign of the temperature coefficient of the density at the center depends on the drop size through $\beta(R,0)$. For small drop radii the coefficient is negative and the density decreases with temperature; this is the usual behavior, as expected from Eq. (2.55a). For larger drops, however, where the density is larger at T = 0, the compressibility is more important and $n(0,R,T)$ actually increases with T. For the conditions of Sample CR50 the temperature coefficient changes sign at $R \approx 300$ μm, while for the conditions of Sample CR38 (larger α_{spec}) it changes sign at $R \approx 140$ μm. Finally, it may be noted that the temperature dependence of the compressibility may be obtained using Eqs. (2.71) and (5.22):

$$K_T(T) = K_T(0)\,[1 + \frac{14}{3}\,\delta_n(kT)^2] \quad . \qquad (5.25)$$

Here $K_T(T)$ is evaluated at the equilibrium density $n_o(T)$. Note that the temperature coefficient is nearly five times as large as that for $n_o(T)$; see Eq. (5.22). Thus the compressibility increases very rapidly with temperature.

The preceding remarks have been intended to give some physical insight into the variation of the e-h pair density with position in the SCEHL. While numerical examples were given, these must in some cases be taken as guidelines rather than as fixed values, since the first-order theory is not valid for large deviations from the equilibrium density. In order to be more quantitative, a more exact theory must be used. Instead of the Taylor series expansion given in Eq. (5.8) and

used up to this point, the full calculation of the pair free energy f versus density developed in Chapter 2 must be used. Figure 5.9 illustrates the differences between the two models. The free energy per pair and the chemical potential are shown as a function of density for $-\sigma = 5$ kgf/mm^2 and T = 1.9K, corresponding to Sample CR50. This solid curves show the full calculation according to Model 1, while the dashed curves show the first-order theory given by Eqs. (5.8) and (5.11). Here the strain energy term is omitted. It is clear that the full calculation must be used when the density deviates significantly from n_o.

In order to properly determine the density distribution, it is necessary to take into account the variation in stress with position. It was shown in Section 52 that the stress is very nearly uniaxial, with the magnitude varying parabolically with the distance from the center of the well. The liquid ground state energy was also shown to be parabolic in r, with a well parameter α_{spec}. The next step is to consider the variation in the free energy (or chemical potential) versus density over the range of stresses accessible to the SCEHL. Figure 5.10 shows the chemical potential as a function of density for the stresses $-\sigma = 3$ and 5 kgf/mm^2, using Model 1 at T = 1.9K. The difference between these two stresses is more than the stress range included in the largest drop studied in Sample CR50. To facilitate the comparison, the curve for $-\sigma = 3$ kgf/mm^2 has been shifted vertically to coincide with the curve for $-\sigma = 5$ kgf/mm^2 at approximately the equilibrium density. It can be seen that the two curves are very similar over a very wide density range (except for an additive constant). Combining this information with that given above, it is concluded that the strain well may be described

fairly accurately via a strain energy term $E_s(r) = \alpha_{spec} r^2$, in addition to a uniform stress with magnitude σ_M, the value at the bottom of the well. This was actually assumed implicitly in the discussion of the first-order theory.

The pair free energy can now be written as a function of density and position, measured from the valence band instead of from the conduction band. To make this distinction more clear, energies measured from the valence band are labeled with an asterisk. Thus the free energy per pair is given by

$$f^*(n,T,\sigma_M,r) = E_{gap}(\sigma_M) + f(n,T,\sigma_M) + E_s(r) \quad . \qquad (5.26)$$

Here $E_{gap}(\sigma_M)$ is the (minimum) gap for the stress σ_M, $f(n,T,\sigma_M)$ is the Model 1 calculation measured as usual with respect to the conduction band, and $E_s(r)$ is from Eq. (5.9). The pressure is given by

$$P(n,T,\sigma_M,r) = n^2 \frac{\partial f^*(n,T,\sigma_M,r)}{\partial n} = n^2 \frac{\partial f(n,T,\sigma_M)}{\partial n} \quad , \qquad (5.27)$$

while the chemical potential is given by

$$\mu^*(n,T,\sigma_M,r) = E_{gap}(\sigma_M) + f(n,T,\sigma_M) + n \frac{\partial f(n,T,\sigma_M)}{\partial n} + \alpha_{spec} r^2 \qquad (5.28a)$$

$$= E_{gap}(\sigma_M) + \mu(n,T,\sigma_M) + \alpha_{spec} r^2 \quad . \qquad (5.28b)$$

As discussed above for the first-order theory, the chemical potential μ^* is constant over the drop volume, with the value determined by the condition in Eq. (5.14). As long as the surface tension is negligible, $P_{liquid} = P_{gas}$ at the surface and

$$n(R,R,T) = n_o(T) \quad . \qquad (5.29)$$

This is the true equilibrium density for the temperature T, as determined by Eq. (2.5). That is, at low T this corresponds to the minimum in $f(n,T,\sigma_M)$; however, at higher T it does not correspond to the minimum in f, due to the pressure of the gas outside the drop. Equations (5.28b) and (5.29) may be used to write the chemical potential μ_R^* for a drop with radius R, which is equal to the chemical potential for the position r = R:

$$\mu_R^* = E_{gap}(\sigma_M) + \mu(n_o(T),T,\sigma_M) + \alpha_{spec} R^2 \quad . \qquad (5.30)$$

Note that the first two terms correspond to the limit of zero drop size:

$$\mu_o^* = E_{gap}(\sigma_M) + \mu(n_o(T),T,\sigma_M) \quad . \qquad (5.31)$$

Thus it can be seen that the chemical potential varies quadratically with drop radius, i.e.,

$$\mu_R^* = \mu_o^* + \alpha_{spec} R^2 \quad . \qquad (5.32)$$

This equation is true as long as the strain well is parabolic; deviations may be expected for very large drops. Equations (5.28b) and (5.30) may be combined as follows:

$$\mu(n(r,R,T),T,\sigma_M) = \mu(n_o(T),T,\sigma_M) + \alpha_{spec}(R^2 - r^2) \quad . \qquad (5.33)$$

In the LHS of this equation the dependence of the density on position is included explicitly: because the variation of the chemical potential with density depends on position, the density must vary with position.

The density profile $n(r,R,T)$ can now be obtained by solving the implicit equation, Eq. (5.33). Note that the spatial dependence is given by $(R^2 - r^2)$. Instead of expressing μ as a function of density,

it is convenient to express the density difference $n(r,R,T) - n_o(T)$ as a function of the chemical potential difference $\mu(n) - \mu(n_o)$. (This is equivalent to turning Fig. 5.10 on its side.) Thus $n-n_o$ may be fit to a power series in $\alpha_{spec}(R^2-r^2)$. The series should have enough terms so that it is accurate over the range of densities and drop sizes which are accessible. The maximum drop size R_{max} which is energetically possible for a given stress may be determined from Eqs. (5.31) and (5.32) by noting that the chemical potential μ_R^* cannot exceed the value for μ_o^* appropriate for a lower value of stress σ_{min}. This is because for stresses smaller in magnitude than σ_{min}, the ground state energy μ_o^* (measured from the valence band) does not decrease with stress, and it is not energetically favorable for the liquid to be in that part of the crystal. The stress σ_{min} is very close to σ_e, the critical stress at which the upper conduction bands become depopulated. Thus

$$\begin{aligned} \alpha_{spec} R_{max}^2 &= \mu_o^*(\sigma_{min}) - \mu_o^*(\sigma_M) \\ &= E_{gap}(\sigma_{min}) - E_{gap}(\sigma_M) + \mu(n_o(T,\sigma_{min}),T,\sigma_{min}) \\ &\quad - \mu(n_o(T,\sigma_M),T,\sigma_M) \quad . \end{aligned} \tag{5.34}$$

For $-\sigma_M = 5$ kgf/mm^2 and $-\sigma_{min} = 2.6$ kgf/mm^2, at T = 1.9K, $\alpha_{spec} R_{max}^2 = 1.8$ meV. Thus for Sample CR50, $R_{max} \approx 1$ mm, which is greater than the largest drop size obtained experimentally. This means that the well was not completely "filled up." The expression in Eq. (5.33) was actually fit for chemical potential differences up to 2 meV, using ten terms in the series, so that

$$n(r,R,T) = n_o(T) + \sum_{i=1}^{10} A_i[\alpha_{spec}(R^2 - r^2)]^i \quad . \tag{5.35}$$

The values for $n_o(T)$ and the coefficients A_i are given in Table 5.1 for $-\sigma = 5$ kgf/mm^2 and T = 1.9K. Several density profiles calculated according to Eq. (5.35) are shown in Fig. 5.11 for $\alpha_{spec} = 2$ meV/mm^2. In the figure the position variable x is normalized to the drop radius. As expected from the first-order theory presented above, the variation in density with position is still a very large effect when calculated exactly.

The density at the center of the drop may be computed easily using Eq. (5.35):

$$n(0,R,T) = n_o(T) + \sum_{i=1}^{10} A_i[\alpha_{spec} R^2]^i \quad . \tag{5.36}$$

This is shown in Fig. 5.12 for the same conditions as in Fig. 5.11. For comparison, n(0) is also shown for the corresponding first-order calculation, using Eq. (5.23) with $n_o^2(T)E_o''(T) = 0.34$ meV. Thus the first-order theory overestimates the increases in density. (This can actually be anticipated from Fig. 5.9.) It should be noted that the results in Figs. 5.11 and 5.12 can easily be reinterpreted for other values of α_{spec}, since the density at a given value of x/R depends only on $\alpha_{spec}R^2$. For example, from Fig. 5.12, when $\alpha_{spec}R^2 = 1$ meV the density increase $n(0)/n_o$ is 2.8 for the exact calculation and 3.85 for the first-order calculation; this is true both for $\alpha_{spec} = 2$ meV/mm^2, R = 700 μm and for $\alpha_{spec} = 8$ meV/mm^2, R = 350 μm.

In order to understand how to measure the density profiles predicted here and how to interpret other experimental measurements on drops with a density distribution, it is useful to try to simplify Eq. (5.35) in some way. The density profiles in Fig. 5.11 appear qualitatively to

be parabolic in shape. In fact, the profiles are very nearly parabolic, as illustrated in Fig. 5.13 for the case $\alpha_{spec}R^2 = 2$ meV. In this case the parabola was chosen to have the same values for n(0) and n(R) as the exact calculation. Since the agreement is so good the calculations of the next section, which include some measureable manifestations of the density variation, are performed using parabolic density distributions. It should be noted, however, that n(0) must be computed using Eq. (5.36) for the appropriate drop size. Thus the calculations of the next section are based on the following density profiles:

$$n(r,R,T) = n_0(T)\left[1 + \beta(R,T)\left(1 - \frac{r^2}{R^2}\right)\right] \qquad (5.37a)$$

where

$$\beta(R,T) = \frac{1}{n_0(T)} \sum_{i=1}^{10} A_i [\alpha_{spec} R^2]^i \quad . \qquad (5.37b)$$

In this approximation, which should be an excellent one, $\beta(R,T)$ is not simply proportional to R^2, as in the first-order theory of Eq. (5.23). Recall from Eq. (5.11) that in the first-order theory the chemical potential μ is simply linear with density. The parabolic approximation of Eq. (5.37a) then corresponds to a linear approximation for μ between the densities $n_0(T)$ and $n(0,R,T)$, where the latter density is properly adjusted as the drop size changes. It can be seen from Fig. 5.9 that this is reasonable for the range of densities considered here.

Before turning to the experimental manifestations of these density variations, it may be noted that the range of accessible densities is finite and depends on the maximum stress σ_M at the center of the well. As discussed above, $\mu_R^*(\sigma_M)$ cannot exceed $\mu_0^*(\sigma_{min})$, where σ_{min} is the

minimum stress for which the EHL energy is lowered. This limits the drop size to R_{max} given by Eq. (5.34). The maximum density which can be obtained, $n(0,R_{max},T)$, is in turn limited. This maximum density can be determined by using Eqs. (5.28b), (5.30), and (5.31) to obtain

$$\mu(n(0,R_{max},T),T,\sigma_M) = E_{gap}(\sigma_{min}) - E_{gap}(\sigma_M) + \mu(n_0(T,\sigma_{min}),T,\sigma_{min}) \qquad (5.38)$$

and then by computing μ versus n for the stress σ_M. For example, using $-\sigma_{min} = 2.6$ kgf/mm^2 as before, at T = 0 the maximum density increases with stress from ~2.2 x 10^{17} cm^{-3} at $-\sigma_M = 5$ kgf/mm^2 to ~4.5 x 10^{17} cm^{-3} at $-\sigma_M = 10$ kgf/mm^2. In fact, over the stress range $-\sigma_M = 3$ to 15 kgf/mm^2 the maximum density increases nearly linearly with stress. At the same time the minimum density, $n_0(T,\sigma_M)$, decreases (more gradually) with stress. Thus the range of densities available for a given stress increases with σ_M.

Because a range of densities can be obtained for a given value of the stress, it is possible to study certain properties of the SCEHL as a function of density by changing the drop size, i.e., by changing the excitation level. In particular, as shown in the next section, the chemical potential can be measured versus density. This in itself is of fundamental importance, since it is the chemical potential or free energy versus density which is calculated in all theories, such as the theory of Chapter 2. Because a wide range of densities can be studied, at a fixed value of the stress, this provides a very sensitive test of the many-body theories which are used in the calculation of the Coulomb energy. In addition, the EHL compressibility can be measured, using Eq. (2.70). Another problem of fundamental importance is the under-

standing of different recombination mechanisms and their density dependences. A kinetic study of the SCEHL provides information on the relative importance of these different recombination mechanisms.

Because the density variations occur within a single electron-hole drop, an experimental measurement will in general involve a superposition from all densities which are present. This is of course a complication in the interpretation of experimental results such as the luminescence lineshape or decay time. However, the density profiles can be measured directly, as shown in the next section, and the appropriate superpositions can be synthesized for comparison with experiment. Further, the entire range of densities is available for fixed temperature, fixed stress, and fixed magnetic field. Thus other complications which may occur as the stress or magnetic field are varied are eliminated; and larger density variations are possible than by changing the temperature.

53.2. Manifestation of the Density Variation in Luminescence Experiments

Because the density variations predicted in the last section can be so large, it may be expected that many types of luminescence experiments would be affected. Indeed, it was already noted in Section 42.3 that the variation of the density as well as the strain energy with position contribute to the increase of the luminescence linewidth with power illustrated in Figs. 4.8 and 5.3. Density changes alone can account for the decrease of the drop lifetime with power in Figs. 4.12 and 5.4 and the non-exponential decay in Fig. 4.11. However, these experiments only indicate that an average density increases with drop size; they do not indicate the density distribution. It may be noted, for example,

that if the density changes were due only to the change in equilibrium density with stress, the liquid would be denser at the surface rather than at the center of the drop. Furthermore, these density changes are too small to explain the experimental results -- indeed, it was argued in the last section that they may be neglected entirely. Power dependences of the peak luminescence intensity in a slit scan, on the other hand, when combined with size measurements as in Figs. 5.1 and 5.2, can be interpreted if the density increase occurs at the center of the drop, as shown in Section 51. In this section it is shown how to interpret luminescence experiments of the types described above. More importantly, a method is described to measure the density variations directly.

Since the measurements to be described here involve EHL luminescence, the first step is to introduce a quantity which indicates the rate at which e-h pairs decay radiatively from a small volume dV located at a particular position r in the liquid:

$$dI(r) = \frac{n(r)}{\tau_{rad}(n)}\, dV \quad . \tag{5.39}$$

This may be integrated over a finite volume and multiplied by the luminescence photon energy ≈0.71 eV to yield the radiated power P_{rad}, which is related to the luminescence signal or amplifier output via Eq. (3.20). The radiative lifetime is given by

$$\tau_{rad}^{-1}(n) = B\,n \tag{5.40}$$

(see Eq. (4.8)), where B is a constant which is proportional to $|D|^2|H|^2/|\Delta E|^2$. Here D is the optical matrix element, H is the

electron-phonon matrix element, and ΔE is an energy denominator. For simplicity B is generally assumed to be independent of stress and magnetic field, since its stress and field dependences are unknown but expected to be small.[5.23] Actually, B should depend on density through the radiative enhancement factor, i.e., $B = B_0\rho(n)$, where B_0 is really a constant and $\rho(n)$ is the enhancement factor. In this thesis $\rho(n)$ is omitted, although it should be included in a more complete treatment.[5.4,5.5] Many of the results of this chapter are not quantitatively affected by this omission, however, and no results are modified qualitatively.

The results of several types of luminescence experiments can be modeled using Eqs. (5.39) and (5.40) and the density profiles from the previous section, Eq. (5.37). In particular, luminescence spatial profiles can easily be modeled. For example, a slit scan profile is given by

$$I_{slit}(x) = B\int_{x-s/2}^{x+s/2} dx \int_{-R}^{R} dy \int_{-R}^{R} dz \; n^2(r) \quad , \tag{5.41}$$

where s is the effective slit width on the sample, $r^2 = x^2 + y^2 + z^2$, and R is the drop radius. The procedure for obtaining spatial slit and box scans is described in Section 34. Figure 5.14 shows the effect on a slit scan of the density distribution predicted in the previous section. The outer curve shows a theoretical slit scan for constant density, for which $I_{slit}(x) \sim (R^2 - x^2)$ for small slit widths. The inner curve uses the density distribution from Eq. (5.37), with $n(0) = 2.8\, n_0$. This condition should be readily obtainable in an experiment. For both curves

the slit width is 0.05 times the drop radius, so the effect of the finite slit width is small. It is immediately apparent that a density distribution which includes a sizeable density variation gives a luminescence profile which is significantly modified from the constant-density case. The profile is more peaked in the center, and the full width at half maximum of the profile (W_s) is reduced.

A similar calculation may be performed for a box scan profile. In this case,

$$I_{box}(x,z=0) = B\int_{x-s/2}^{x+s/2} dx \int_{-R}^{R} dy \int_{-s/2}^{s/2} dz \; n^2(r) \quad , \tag{5.42}$$

where all quantities are as in Eq. (5.41) and the two crossed slits have the same width. Figure 5.15 shows theoretical box scan luminescence profiles for the same conditions as for the slit scans in Fig. 5.14. For constant density and for a small slit width, $I_{box}(x) \sim (R^2-x^2)^{\frac{1}{2}}$, so that the edge of the drop is very well defined. The density variation over a factor 2.8 in the inner curve has an even larger effect on a box scan than on a slit scan. Indeed, the full width at half maximum, W_b, of the box scan has become almost as narrow as W_s. These qualitative features should be readily observable experimentally, as long as the slit width is small compared to the drop radius.

The primary factor, then, which determines the shape of the luminescence profiles in Figs. 5.14 and 5.15 is the density distribution. Because the observed luminescence depends only on the radiated term, Eq. (5.39), for a given drop size the profile shape is completely independent of the relative importance or density dependence of the non-radiative processes.

It may be noted that for a given drop size the actual luminescence intensities also depend rather strongly on the density distribution. Thus, for example, in Fig. 5.14 the peak intensity in the slit scan $I_{slit} = I_{slit}(0)$ should be ≈2.9 times as large for the inner curve as for the constant density curve. The corresponding ratio for the peak intensity in the box scan $I_{box} = I_{box}(0,0)$ in Fig. 5.15 is ≈3.7. (These differences are not seen in the figures because the curves are normalized to the same peak intensity.) These large differences are easily understood qualitatively: the drop having $n(0) = 2.8\ n_o$ contains considerably more e-h pairs than the drop having $n(r) = n_o$; in fact, that ratio is ≈1.7. A spatial region containing more e-h pairs emits more intense luminescence. In addition, it may be noted that the ratios of luminescence intensities given above depend on the geometry of the selected spatial region: the ratio for the box is greater than the ratio for the slit, which in turn is greater than the ratio of total e-h pairs in the drop. This trend can also be understood qualitatively. The quantity I_{slit} corresponds to a slice taken through the center of a sphere, while I_{box} corresponds to a core section through the center of the sphere. The central region, where the density is greatest, is relatively more important in the core section than in the slice, and in turn in the slice than in the entire sphere. Thus the effects of a density distribution in which the density is greater at the center of the drop are most pronounced in luminescence box scans.

Some of the features of Figs. 5.1 and 5.2 can be more fully understood by applying the types of reasoning given above. The total luminescence intensity I_{tot} is a measure of the number of e-h pairs in

the liquid. Its greater than linear power dependence in Fig. 5.1 indicates that the production efficiency is probably changing rather rapidly over that range of excitation levels.[5.24] For the case of constant-density spherical drops, it would be expected that $I_{box} \sim R \sim (P \times \epsilon_{prod})^{1/3}$ and that $I_{slit} \sim R^2 \sim (P \times \epsilon_{prod})^{2/3}$, using the geometrical arguments presented in Section 51. For the case of a density distribution, W_s should change more slowly than R while I_{box} should change more rapidly than R. In addition, I_{slit} should change more rapidly than R^2 (and thus more rapidly than W_s^2) but less rapidly than I_{box}^2. And I_{tot} should change more rapidly than R^3 (and thus more rapidly than W_s^3 or the "volume" of Fig. 5.2) but less rapidly than $I_{slit}^{3/2}$ or I_{box}^3. While the actual drop radii are not displayed in Figs. 5.1 and 5.2, it is nevertheless clear that the relationships just given are true. A more detailed interpretation of these figures is difficult due to the complications of the power-dependent production efficiency. (For example, this can depend on the excitation geometry in a complex manner.) However, these kinds of complications can be avoided by plotting quantities as a function of drop size. A convenient measure of the drop size is W_s, the full width at half maximum of a slit scan.

Some of the ideas presented above are summarized in Fig. 5.16. This figure shows the effect of the density distribution of Eq. (5.37) on the peak luminescence intensity in a box scan, the peak luminescence intensity in a slit scan, and the total luminescence intensity. These quantities are shown as a function of W_s for three cases: constant density ($n = n_o$), $\alpha_{spec} = 2$ meV/mm^2, and $\alpha_{spec} = 8$ meV/mm^2. It should be noted that a particular value for W_s corresponds to different radii for the three

cases, for the larger drop sizes. The calculations were performed using a slit width s = 35 μm. As expected, for the constant density case the I_{box} curve is essentially a straight line with slope =1, the I_{slit} curve has slope =2, and the I_{tot} curve has slope =3. (Deviations occur for small drop sizes as the slit width becomes important.) The deviations from the constant-density case become more pronounced as the strain well becomes steeper and as the drop size increases. In addition, the deviations are more pronounced for I_{box} than for I_{slit}, and for I_{slit} than for I_{tot}. These trends are all expected from the discussion above. Curves such as those shown in Fig. 5.16 can be directly compared to luminescence data such as those shown in Figs. 5.1 and 5.2 (see Section 54). Indeed, if the theoretical density distributions are correct, such a comparison can be used to estimate a value for the well parameter α_{spec} without studying the spatial distribution of the exciton luminescence. However, in order to test the correctness of the theory, α_{spec} was measured in Sample CR50 by an analysis of the exciton luminescence, as described in Section 52.

One further point may be made about the curves in Fig. 5.16. These curves were calculated assuming spherical drops. From the fit of the exciton slit scans discussed in Section 52, it was determined that for Sample CR50 the well could be adequately represented by $\alpha \approx 2$ meV/mm^2 for the x and y coordinates, while for the z coordinate one half looked like $\alpha \approx 5.5$ meV/mm^2 and the other half looked (rather poorly) like $\alpha \approx 2$ meV/mm^2. Thus the drop shape is approximately a hemisphere plus a hemi-ellipse, rather than a sphere. The curves of Fig. 5.16 should thus be modified according to the following line of reasoning:

In the sphere (and in the ellipse), the dependence on spatial coordinates is parabolic and is determined by a well parameter (or several well parameters). A certain density range, say n_1 to $n_1 + \Delta n$, corresponds to a spherical or elliptical shell. The fractional volume of that shell is the same for the sphere as for the ellipse. Thus, for example, a box scan would have the same shape for any scan direction, if plotted as in Fig. 5.15 as a function of a normalized coordinate (x/R_x, y/R_y, z/R_z) and normalized to the same peak intensity. This is because the luminescence signal would contain the same relative amounts corresponding to the different densities. However, the absolute amounts would be determined by the absolute volumes. If α_1 is the well parameter of the sphere and α_1, α_1, and α_2 are the well parameters of the ellipse, then the total volume of the ellipse is $\sqrt{\alpha_1/\alpha_2}$ times the total volume of the sphere. For a hemi-ellipse plus a hemisphere, the volume ratio becomes $(1 + \sqrt{\alpha_1/\alpha_2})/2$. The total luminescence intensity I_{tot} appropriate for a sphere must be multiplied by this ratio, in order to be appropriate for the hemi-ellipse plus hemisphere; so must the quantity I_{slit}, if the slit scan is taken along one of the directions represented by α_1. However, if the box scan is taken along one direction represented by α_1 and integrated through the other direction represented by α_1 (as will be the case in Section 54), then I_{box} does not need to be corrected. For the conditions in Sample CR50, i.e., $\alpha_1 \approx 2$ meV/mm^2 and $\alpha_2 \approx 5.5$ meV/mm^2, the ratio is ≈ 0.8. Thus in the quantitative comparison with experiment this adjustment should be made.

The analysis of experimental results corresponding to the theoretical curves in Fig. 5.16 can yield much useful semi-quantitative information

about the e-h pair density distribution in the SCEHL. However, it is actually possible to measure the density profile directly using a careful measurement of the luminescence intensity versus position and an Abel transform to convert the luminescence intensity to density. The technique is borrowed from plasma physics and astrophysics, where observations of plasma radiation are analyzed to yield the radial distribution of the emission.[5.25] The plasma is assumed to be optically thin (no reabsorption of the radiation by the plasma) and to have cylindrical or spherical symmetry. These conditions are applicable for the case of the EHL; the requirement of circular symmetry is easily relaxed to elliptical symmetry, as will be seen shortly. In addition, the technique has been used in order to study the e-h pair density distribution in the EHD cloud in unstressed Ge[5.26] and in a single drop confined in a strain well in inhomogeneously stressed Ge.[5.26,5.27] In these experiments the absorption of 3.39 μm light was studied, rather than luminescence. Thus the technique is rather general. Because of its extensive use in plasma diagnostics and astrophysics, many numerical methods have appeared in the literature.[5.29]

For the case of luminescence, the determination of the density distribution is based on the measurement of a luminescence box scan. For the mathematical formalism, consider the ideal case for infinitely narrow slits:

$$\phi(x) = B\int_{-R}^{R} dy\, n^2(r) \quad . \tag{5.43}$$

This expression is obtained from Eq. (5.42) by omitting the x and y integrations over the slit width and by dropping the explicit designation

z = 0. (The generalization to nonzero z is obvious.) It may be noted that the integrand depends on y only as y^2 and that n(r) = 0 for r > R. In addition, if the distribution is circularly symmetric in the x and y dimensions, then Eq. (5.43) may be rewritten as follows:

$$\phi(x) = 2B\int_{x}^{\infty} \frac{n^2(w)}{\sqrt{w^2 - x^2}}\, w\,dw \quad , \tag{5.44}$$

where $w^2 = x^2 + y^2$. For the case of elliptical symmetry relating the coordinates x and y, w^2 would be equal to $x^2 + ay^2$ and the RHS of Eq. (5.44) would be multiplied by $a^{-\frac{1}{2}}$; here $a = \alpha_y/\alpha_x$. Now $\phi(x)$ is simply the Abel transform[5.30,5.31] of $n^2(w)$. Thus in order to obtain the density distribution it is only necessary to perform the inverse transform. This may actually be done in two ways:[5.30,5.31]

$$n^2(w) = -\frac{1}{\pi B}\int_{w}^{\infty} \frac{\phi'(x)}{\sqrt{x^2 - w^2}}\, dx \tag{5.45a}$$

$$= -\frac{1}{\pi B w}\,\frac{d}{dw}\int_{w}^{\infty} \frac{\phi(x)}{\sqrt{x^2 - w^2}}\, x\,dx \quad , \tag{5.45b}$$

where $\phi'(x) = d\phi(x)/dx$. The primary difference between the two forms is whether the differentiation is performed before or after the integration. The first method, Eq. (5.45a), appears to be more common in the literature.[5.25,5.29,5.31] However, because the derivative $\phi'(x)$ is required and because in a real experiment the data points contain noise, much effort has been expended in the numerical methods[5.25,5.29] in order to smooth out the noise. In order to make this problem less important, the second method,[5.30] Eq. (5.45b), is used here, along with an extremely

simple smoothing method described in the next section. This method was found to give satisfactory results, even in the presence of rather large noise (i.e., when the signal was very small). The two methods were not directly compared.

A few details of the computation should be noted. The inverse Abel transform, Eq. (5.45b), was performed numerically on the Berkeley campus CDC 6400 computer. It may be noted that the transform appears to be singular at $w = 0$ and that the integrand is singular at $x = w$. The first problem was solved by making a change of variables: $u = w^2$, $v = x^2$, so that

$$n^2(u) = -\frac{1}{\pi B}\frac{d}{du}\int_u^{u_{max}} \frac{\phi(v)}{\sqrt{v-u}}\,dv \quad . \tag{5.46}$$

Here the integrand is zero for u (or v) greater than some maximum value. For this ideal case $u_{max} = R^2$; however, below this will change. The singularity in the integrand can be removed by writing $\phi(v) = [\phi(v) - \phi(u)] + \phi(u)$; then, after some rearrangement

$$n^2(u) = -\frac{1}{\pi B}\frac{d}{du}\left[\int_u^{u_{max}} \frac{\phi(v)-\phi(u)}{\sqrt{v-u}}\,dv + 2\sqrt{u_{max}-u}\;\phi(u)\right] . \tag{5.47}$$

The transform was evaluated using this equation.

In a real luminescence experiment the slits have a finite width, and $\phi(x)$ must be replaced by $I_{box}(x)$. As a result, the deduced density profile has the same slit width folded in as do the luminescence profiles. For s sufficiently small, the main effect is to wash out the abrupt density change which occurs at the surface of the drop: in the transform of a real box scan, the density appears to go smoothly to zero (see

Figs. 5.22 to 5.25). Also, for a real box scan, u_{max} in Eq. (5.47) is not R^2, but rather the square of the last point, where the luminescence intensity $I_{box}(x)$ has gone to zero.

It should be noted that the evaluation of Eq. (5.47) gives density profiles whose values can be directly compared for different drop sizes, different scan directions, or different values of the stress. The density scale is determined by the fit of the luminescence lineshape for small drop size. This method for determining the absolute scale for the density is thus quite accurate, i.e., as good as the lineshape fits or ±5 - 10% from Eqs. (4.6) and (5.5). This may be contrasted with the density determinations using the absorption of 3.39 μm radiation,[5.26,5.27,5.32,5.33] which rely on an absolute measurement of the hole absorption cross section at 3.39 μm. Values of the cross section varying over a factor of 5 have been used; in addition, values measured for unstressed Ge have been used to analyze absorption measurements in stressed Ge, since the stress dependence of the cross section is unknown.[5.34] Thus, as discussed in Section 42.4, measurements of the density using the absorption of 3.39 μm radiation have rather large uncertainties. The absolute accuracy of the density measurements reported here is crucial in the interpretation of the other measurements of properties of the EHL as a function of density.

The measurements of density profiles for different drop sizes can be used to determine how the EHL chemical potential changes with density. Equation (5.33) can be written for $r = 0$ and $r = R$ to yield

$$\mu(n(0,R,T),T,\sigma_M) = \mu(n_o(T),T,\sigma_M) + \alpha_{spec} R^2 \quad , \tag{5.48}$$

using Eq. (5.29). Note that the drop radius R is needed, rather than the FWHM of a slit scan W_s. The determination of R from the experimental measurements is discussed in the next section. Equation (5.48), then, gives a recipe for the change in μ (measured with respect to the conduction band) with the density $n(0,R)$. This may be compared directly with theory, such as the calculations of Chapter 2. As already mentioned, this provides a very sensitive test of the many-body theories used in the Coulomb energy. The measurement of $\mu(n)$ can be used to obtain the compressibility as follows, using Eqs. (2.70c) and (2.6b):

$$K_T(n) = \left(n^2 \frac{d\mu(n,T,\sigma_M)}{dn} \right)^{-1} . \qquad (5.49)$$

Note that this determines the compressibility as a function of density. Thus a series of measurements at different temperatures could in principle be used to determine K_T versus n and T. This may be contrasted with the case for unstressed Ge, where the measurements[5.35] determine K_T only for the ground state density $n_o(0)$.

54. Experimental Results and Discussion

In this section the experimentally observed manifestations of the variation of the SCEHL pair density with position are presented. Results are presented both for Sample CR38 and for Sample CR50, including detailed measurements of density profiles at several excitation levels. The deduced value for the compressibility, however, is more reliable for Sample CR50, since this sample was fully characterized (see Section 52). These results are compared with the theoretical predictions of Section 53.

A first type of experiment which shows clearly that density variations do occur in the SCEHL is the dependence of the luminescence intensity on drop size. Figure 5.17 shows the results for Sample CR38 from the set of runs discussed in Chapter 4. The total luminescence intensity without spatial selection, I_{tot}, and the peak intensity in a slit scan, I_{slit}, are shown as a function of the FWHM of the slit scan, W_s. The slit scan measurements are shown for y-scans (obtained from the face-view as shown in Fig. 3.8) and for x-scans (obtained from the end view). For each point I_{slit} and W_s were obtained from the same scan. The measurements of I_{tot} are shown versus W_s for the y-scans, for concreteness; however, the values for W_s for y-scans and x-scans at the same excitation level were virtually identical. Some of these measurements were shown previously in Figs. 4.17 and 4.18 as a function of excitation level. The curves in Fig. 5.17 are the results expected from the calculations of the last section for $\alpha_{spec} = 8$ meV/mm^2 and slit resolution s = 85 μm. This value of the well parameter is very close to the estimates made earlier: $\alpha^y_{spec} \approx 7$ meV/mm^2 from luminescence spectra of the center and the edge of a large drop (see Section 42.3), and $\alpha^x_{spec} \approx 10$ meV/mm^2 from an exciton slit scan (see Section 42.1 and Eq. (5.7)). The agreement over three orders of magnitude in the total luminescence intensity is excellent. Deviations can be seen for I_{slit} for small drop sizes. These deviations occur for both samples (see Figs. 5.17-5.20) and are due to a loss of resolution on a scale which apparently is larger than the slit resolution; see Section 34 for a fuller discussion.

From Fig. 5.16 it may be noted that the curves for I_{tot} and I_{slit} should be related by a specific scale factor. However, in this set of

experiments the measurements of I_{tot} and I_{slit} were performed in different runs, and the relative calibration of the collection optics was unknown. Hence the theoretical curves have been adjusted individually for the best fit. In addition, an overall loss in luminescence intensity for the end view is evident in the reduction in I_{slit} for the x-scans. These comments are intended to indicate the types of information which can be obtained from plots such as Fig. 5.17.

A more complete set of measurements is shown in Figs. 5.18 and 5.19 for Sample CR50. Figure 5.18 shows the total luminescence intensity I_{tot}, the peak intensity in a slit scan I_{slit}, the peak intensity in a luminescence wavelength spectrum $I_{\lambda\text{-scan}}$, and the peak intensity in a box scan I_{box}, all obtained using the side view. These quantities are shown as a function of drop size, given by the FWHM of the slit scan (x-scans). In Fig. 5.19 the quantities I_{slit} and I_{box} are shown as a function of W_s for y-scans obtained using the face view. In both cases, the curves show the theory of the previous section for α_{spec} = 2 meV/mm^2, which is very nearly the value obtained in Section 52 from exciton slit scans at 4.2K. (The theoretical curves for the correct values, α^x_{spec} = 1.7 meV/mm^2 and α^y_{spec} = 1.8 meV/mm^2, differ only negligibly from those shown.) In addition, in these two figures the theoretically predicted relative intensities of the curves are kept intact. This means that the calculated curves were all shifted together along the intensity scale in order to show the best agreement with the data. This was possible because the (small) daily variations in the overall system sensitivity were monitored and were taken into account in the display of the data. Here again, the agreement is excellent over nearly an order of magnitude

variation in drop size and three orders of magnitude variation in I_{tot}.[5.36]

Finally, Fig. 5.20 shows a partial set of data for Sample CR38 for different conditions from the results of Chapter 4 and Fig. 5.17. These data were obtained from the same scans used to obtain the density profiles shown below. The figure shows I_{box} versus drop size for y-scans using the face view. In this case the drop size was estmated by the FWHM of a box scan, W_b, since slit scans were not obtained in this set of runs. In addition, since the well parameter was not measured using either of the methods discussed in Chapter 4, these data are used to estimate α_{spec}. The curve shown in the figure corresponds to α_{spec} = 4 meV/mm^2 and agrees very well with the data. An estimate of the accuracy of such a determination of α_{spec} can be made from Fig. 5.16, which shows theoretical curves for α_{spec} = 2 and 8 meV/mm^2. (The changes in the curves as α_{spec} is varied are much more important than the changes which result from plotting versus W_s rather than W_b.) Thus this estimate of α_{spec} should be correct to within a factor ≈between 2/3 and 3/2.

The luminescence box scans used for Figs. 5.18 to 5.20 were also analyzed as described in the last section in order to obtain measurements of the e-h pair density as a function of position within the SCEHL. The scans were recorded automatically as described in Chapter 3. All data processing was handled by computer, i.e., no smoothing or baseline corrections were done by hand. However, a constant baseline correction was made by the computer. In addition, the raw data were smoothed as follows: each data point was replaced by the average of m points centered on the original point. For the data from Sample CR38, m = 5, while for the data from Sample CR50, m = 3. The density profiles were

obtained from the inverse Abel transform of the box scans, according to Eq. (5.47). Two scan directions were selected for analysis: side-view x-scans and face-view y-scans. These choices were deliberate. In a side-view x-scan the luminescence is integrated through the y-direction, while in a face-view y-scan the luminescence is integrated through the x-direction. Thus for both types of box scans the scanned and integrated coordinates are related via elliptical (indeed, essentially circular) symmetry, and the Abel transform is mathematically correct. This is not the case where the scanned or integrated coordinate is z, so scans involving z are not analyzed here.

An example of a box scan is shown in Fig. 5.21, while its transform is shown in Fig. 5.22. These data were obtained from Sample CR50, with P_{abs} = 400 mW. The resulting drop size, as seen here or in Fig. 4.15, is R ≈ 0.7 mm. Several points are illustrated in this pair of figures. First, it may be noted that an asymmetry occurs in both figures at the surface of the drop. The density measurements should appear to go smoothly to zero, as on the right-hand side of Fig. 5.22, due to the finite slit width, which smears out the ideally shapr density change at the drop surface. (Note that this means that the density n(R), which should be $\approx n_o$, cannot be measured from such a density profile.) However, the baseline on the left-hand side of Fig. 5.21 is higher than on the right. The extra luminescence comes from small droplets flowing from the excitation point into the well. The coordinate position x=0, or $x-x_o \sim -1.5$ mm, corresponds to the crystal face where the laser is incident (refer to Fig. 3.8). This extra baseline was not subtracted out before the data were transformed; as a result, the density does not appear to

go to zero at the left of Fig. 5.22.

In addition, it may be noted that the raw data in Fig. 5.21 show several small wiggles, which are apparently due to small imperfections on the crystal face through which the image was collected. These relatively small anomalies appear much larger in the transformed data. This is easily understood: the box scan is a superposition of luminescence from different densities through the depth of the well. In order for a dip (for example) in the box scan intensity to be real, it must correspond to a much larger dip in the density. Thus the transform automatically magnifies small anomalies in the raw data.

The most important feature of Fig. 5.22 is, of course, that the e-h pair density is found to have large variations with position. The density at the center of the drop is approximately three times the uncompressed density. (The determination of the absolute density scale is discussed below.) The form of the spatial density variation also agrees well with the theoretical prediction: the solid curve shows the transform of a theoretical box scan computed using Eq. (5.42) with α = 2 meV/mm^2, R = 0.7 mm, and s = 35 μm. For comparison, the figure also shows the expected form of the transform if the density were actually uniform, but still compressed over the equilibrium value. The dashed curve shows a "best fit" for such a constant density case. The essential validity of the density variations given by Eq. (5.37) is thus confirmed.

Figure 5.23 shows density profiles for Sample CR38 at a series of three excitation levels: P_{abs} = 2.5, 15 and 94 mW. All three sets of data are plotted on the same scale and show the increase in the density variation with drop size. The curves show transforms of theoretical

box scans computed according to Eqs. (5.42) and (5.37), with n(0,R) adjusted for a reasonable fit. The agreement is very good. Note that for the smallest drop size displayed in the figure, the liquid is already somewhat compressed above the equilibrium density $n_o \approx 0.5 \times 10^{17}$ cm^{-3}. For such a small drop size, when the radius is only a few times the slit resolution, it is difficult to tell from the transform of a single scan whether or not the density varies significantly with position, due to the scatter in the data and the finite slit width. This may possibly explain the null result of Mattos et al,[5.27] who found that the density appeared to be uniform in a drop with radius R ≈ 150 μm, using a probe with resolution ≈70 μm. For Sample CR38, the sample of Fig. 5.23, however, the density was lower for a smaller drop size, showing that the liquid was already compressed in the scan shown here. Thus it is important to study the density profiles for a range of drop sizes.

It may be noted that the density profiles shown in the figures are not perfectly symmetric. This is because the raw data are not quite symmetric — probably due to noise — and also because the left and right halves of the box scans are processed separately. In other situations, where the cylindrical symmetry is expected to be rigorous, it is common[5.25] to simply average the two halves of the original scans. Here, in order display any true asymmetries, the halves are processed separately. However, note that this requires that the center be accurately chosen. Figure 5.24 shows the effect of choosing the center of the box scan incorrectly. This is a transform of the same set of data for P_{abs} = 94 mW as in Fig. 5.23, except that the center, i.e., the point u=0 for the transform, is displaced from its true position by ≈35 μm. Now the density

n(0) should be the same whether determined from luminescence emitted from one half or the other of the drop. It is clear that unless the true drop center is located accurately, the resulting density profile is meaningless. Thus the center was chosen very carefully for all the scans analyzed in this thesis.

Finally, Fig. 52.5 shows a series of density profiles obtained for P_{abs} = 0.22, 7.4, and 400 mW in Sample CR50. The latter scan is the same as in Fig. 5.22. This illustrates the fact that it is possible to measure density profiles over more than three orders of magnitude in excitation intensity, corresponding to approximately one order of magnitude variation in drop size. The density at the center of the drop is found to vary by a factor of approximately three for this range of drop sizes.

The density profiles shown in Figs. 5.22 to 5.25 show conclusively that the e-h pair density varies with position in the SCEHL and that the magnitude of the variation increases with drop size. The form of the density profiles is in good agreement with the theoretical prediction of Eq. (5.37). A more quantitative comparison with theory is shown in Figs. 5.26 and 5.27. Here the density at the center of the drop n(0) is plotted as a function of drop size for the two samples studied here. One set of scans was analyzed for Sample CR38, while two more complete sets were analyzed for Sample CR50. The curves show the theoretical results for the values of the well parameter obtained previously: $\alpha_{spec} \approx$ 4 meV/mm^2 in Fig. 5.26 for Sample CR38, and $\alpha_{spec} \approx$ 2 meV/mm^2 in Fig. 5.27 for Sample CR50. Note that the calibration of the density scale for the profiles was performed using the data for these figures. The data were

plotted in arbitrary units; then the scale was adjusted to give the best agreement with the curve for the appropriate (measured) value of α_{spec}, normalized to the appropriate (measured) value for the equilibrium, uncompressed, density. The measured densities are slightly high for intermediate drop sizes and somewhat low for the largest drop sizes in Fig. 5.27. The latter result may be due to the shape of the strain well deviating from being truly parabolic; this is expected for sufficiently large drops. Overall, however, the agreement between experiment and theory is excellent.

The measurements of the density at the center of the drop versus drop size can be used to determine the variation of the EHL chemical potential with density, using Eq. (5.48): the chemical potential difference $\mu(n) - \mu(n_o)$ is simply given by $\alpha_{spec}R^2$. For the data from Sample CR38 shown in Fig. 5.26 the drop radius R was obtained from the drop size W_b using the theoretical relationship between W_b and R expected for $\alpha_{spec} = 4$ meV/mm^2. Since the <u>form</u> and magnitude of the density variations are well described by Eq. (5.37), the drop radii obtained in this way should be correct to within $\lesssim$10% even if α_{spec} if off by a factor up to $\lesssim$1.5. The results for Sample CR38 are shown in Fig. 5.28 using $\alpha_{spec} = 4$ meV/mm^2. The solid curve shows the theoretical chemical potential as a function of density according to Model 1. Here the data and theory appear to be in excellent agreement. However, it must be cautioned that the uncertainties in the values for the chemical potential are rather large, due to the uncertainties both in α_{spec} and in R. Indeed, the uncertainty in α_{spec} is amplified, rather than reduced, in the chemical potential.

On the other hand, the measurement of the chemical potential difference for Sample CR50 is much more accurate, since α_{spec} was measured rather carefully, as discussed in Section 52. The result is shown in Fig. 5.29, including both sets of data. Here the drop radius was determined using two methods: for large drop sizes the diameter was given by the points where the density profiles went to zero, with an appropriate correction for the finite slit width; for smaller drop sizes R was obtained from W_s using the theoretical relationship expected for $\alpha_{spec} = 1.7$ meV/mm^2, the correct value. As in Fig. 5.28, the solid curve shows the chemical potential difference $\mu(n) - \mu(n_o)$ given by Model 1. Here the accuracy of the measurement is greater, but the theory does not appear to agree with the experimental results. In fact, the disagreement appears to be outside the experimental uncertainty.

Indeed, from Fig. 5.29 the difference between the experimental and theoretical chemical potential versus density appears to be quite substantial and serious. Between $n = 0.5$ and 1.5×10^{17} cm^{-3}, the experimental chemical potential changes by $\approx$0.35 meV less than the theoretical chemical potential, whereas the <u>total</u> measured variation is $\approx$0.75 meV. However, this discrepancy is actually not as serious as it initially appears to be. Recall that the pair free energy consists of kinetic and Coulomb energy terms, that the kinetic energy is positive, and that the Coulomb energy is negative. Since the discrepancy occurs in the sum, the relative error in either quantity is much smaller. To be more specific, suppose that the theoretical kinetic energy is correct and that the error occurs in the FSC Coulomb energy used in Model 1. Then, according to Fig. 5.29, the theoretical Coulomb energy contribution to

the chemical potential, μ_{Coul}, varies too slowly with density by ≈0.35 meV over the density range 0.5 to 1.5×10^{17} cm^{-3}. But the total variation of μ_{Coul} is ≈2.85 meV in this density range, so the relative error is only ≈12%. Further, it may be noticed from Fig. 2.7 that the Coulomb contribution to the pair free energy f_{Coul} varies more rapidly with density in Model 6 than in Model 1. Indeed, over the density range in question, f_{Coul} changes by ≈0.25 meV more in Model 6 than in Model 1; and this difference should increase slightly for μ_{Coul} over the change for f_{Coul}. Thus it may be possible that the discrepancy between theory and experiment in Fig. 5.29 is no greater than between Models 1 and 6. If this is the case, then perhaps a different universal Coulomb energy should be used in the theory; or perhaps the universality proposed in Chapter 2 must be modified.

In order to test these possibilities in more detail, it would be desirable to measure the chemical potential using another method. For example, it should be possible to obtain the drop chemical potential μ_R^* (measured relative to the valence band) from an analysis of the luminescence spectrum. This is of course complicated by the density distribution and the energy variation with position. Thus far a model has not been developed to describe the composite luminescence lineshape for a drop whose density varies with position.

It should also be noted that the box scans were converted into density profiles neglecting a density-dependent radiative enhancement factor $\rho(n)$. The radiative lifetime in Eq. (5.40) should actually be written as follows:

$$\tau_{rad}^{-1}(n) = B_o \rho(n) n \quad , \qquad (5.50)$$

where B_o is a constant. The enhancement factor is the ratio of the probability of finding an electron and a hole at the same position within the EHL to the probability for an uncorrelated plasma. Thus the enhancement factor is a measure of the electron-hole correlation. It is expected[5.38] that $\rho(n)$ decreases with increasing density. This means that the density variations indicated in Figs. 5.22 - 5.29 actually underestimate the true density variations. An apparent density variation of 3 actually corresponds to a variation of 3 in the quantity $\rho^{\frac{1}{2}}n$, according to Eqs. (5.39) and (5.50). Thus, for example, if $\rho \sim n^{-\frac{1}{2}}$ then the true denstiy variation would be ≈4.3 – a significant difference. Thus the discrepancy between theory and experiment in Fig. 5.29 would actually become more pronounced.

Keeping the above points in mind, the chemical potential measurements in Figs. 5.28 and 5.29 yield values for the compressibility of the SCEHL, according to Eq. (5.49). Although K_T can be determined for any density in the range for which there are data, the analysis here is restricted to $K_T(n_o(T))$, where $n_o(T)$ is the equilibrium density for the temperature $T \approx 1.9K$ at which the density measurements were made. As mentioned previously, this is a quite accurately isothermal measurement. The derivative $d\mu(n)/dn|_{n_o}$ is determined by fitting a straight line to the data of Figs. 5.28 and 5.29; because of the curvature, only the points for which $n \leq 1.0 \times 10^{17}$ cm^{-3} are used. The best fit is indicated in the figures by a dashed line. Using the estimated value $n_o(T) \approx 0.5 \times 10^{17}$ cm^{-3}, for Sample CR38 the resulting value for the compressibility is $K_T = 0.023$ cm^2/dyne. Because of the possible errors discussed above, the uncertainty in this value is nearly a factor of 2. For Sample CR50,

the compressibility is given by

$$K_T^{expt} = 0.058\binom{+0.024}{-0.012}\ cm^2/dyne \quad (-\sigma = 5.5\ kgf/mm^2,\ n = 0.47 \times 10^{17}\ cm^{-3},\ T = 1.9K) \quad . \tag{5.51}$$

The uncertainty includes ±5% for n_o, ±5% for $d\mu/dn$ if α_{spec} is assumed to be correct, ±5% for α_{spec}, and +20% to allow for the density-dependent enhancement factor. Note that the uncertainties are so large primarily because several factors enter into the final result. This is a disadvantage of this method for measuring the compressibility: a series of careful ±5% measurements result in a ±20% estimate. However, the measurement of any property of the EHL which depends on the curvature of the free energy E_o'' is very difficult. Thus the final uncertainty is not excessive. The theoretical value for the compressibility is as follows for Model 1:

$$K_T^{theo} = 0.041\ cm^2/dyne \quad (-\sigma = 5.5\ kgf/mm^2,\ n_o = 0.46 \times 10^{17}\ cm^{-3},\ T = 2K,\ Model\ 1) \quad . \tag{5.52}$$

In view of the comments made above concerning different models for the Coulomb energy, the agreement between theory and experiment is quite satisfactory.

Two points should be made concerning the experimental value for K_T in Eq. (5.51). First, this represents a significant modification of a preliminary value $K_T \approx 0.03\ cm^2/dyne$ obtained for the same sample.[5.2] Several factors enter: the densities and drop radii have been re-checked;

the equilibrium density has been measured more carefully; the well parameter has been measured more carefully; the slope $d\mu/dn$ has been measured in a more controlled way; and a second set of data has been included. Each of these factors has contributed to the modification of the final result. The value given here in Eq. (5.51) is believed to be correct, within the stated limits.

Secondly, a comment is in order concerning the rather large difference between the values for K_T for the two samples. It may be noted that the ratio of the two values for K_T is almost exactly the same as the ratio of the well parameters. In other words, the quantity $1/\alpha_{spec}\ d\mu/dn = dR^2/dn(0,R)$ is nearly the same for the two samples. Similarly, the graphs of $n(0)$ versus drop size (W_s or W_b) are nearly identical for small drop sizes, although significant differences are evident for the larger drop sizes which are not used to determine the slope $d\mu/dn$. The results for $n(0)$ versus drop size actually should vary slightly for small drop size, depending on the value of α_{spec}. However, it is evident from these sets of data that it is extremely difficult to measure these quantities for small drops with sufficient accuracy to distinguish between different values for α_{spec}. Thus the well parameter must be determined separately.

55. Density Dependence of the EHL Lifetime

In this section the density variations measured in the previous section are exploited in order to obtain information about the density dependence of the EHL lifetime and about the relative importance of different recombination mechanisms. The EHL lifetime varies with density as follows:

$$\tau^{-1}(n) = \tau_{di}^{-1} + \tau_{rad}^{-1}(n) + \tau_{Aug}^{-1}(n) \qquad (5.53a)$$

$$= A + Bn + Cn^{S} \quad . \qquad (5.53b)$$

Here the first term represents processes independent of density; the second term represents the usual radiative recombination process; and the third term represents Auger processes, where s is expected to be 2 or 3. This expression is similar to Eq. (4.8), except that a density-independent term has been added. The analysis of this section will omit a density dependent enhancement factor; the implications of that omission will be discussed briefly at the end of the section. Efficiencies may be defined for the recombination processes, as follows:

$$\varepsilon_{di}(n) = \tau(n)/\tau_{di} \quad ,$$

$$\varepsilon_{rad}(n) = \tau(n)/\tau_{rad}(n) \quad , \qquad (5.54)$$

$$\varepsilon_{Aug}(n) = \tau(n)/\tau_{Aug}(n) \quad .$$

In addition, the rates at which e-h pairs in a small volume dV located at a particular position r within the SCEHL decay in the different recombination processes can be written as follows, following Eq. (5.39):

$$dI_{di}(r) = \frac{n(r)}{\tau_{di}}\, dV \quad ,$$

$$dI_{rad}(r) = \frac{n(r)}{\tau_{rad}(n)}\, dV \quad , \qquad (5.55)$$

$$dI_{Aug}(r) = \frac{n(r)}{\tau_{Aug}(n)}\, dV \quad .$$

It is possible, then, to model the decay of a drop with a given size

using Eqs. (5.53) and (5.55), the density distribution in Eq. (5.37), and various assumptions about the coefficients A, B, and C (or the efficiencies).

First, however, a description of the experiment and the experimental results is in order. Actually, two types of experiment will be discussed here. In the first experiment the initial luminescence decay time was measured for different drop sizes. The luminescence was collected from the entire drop, without spatial or spectral selection, and recorded as a function of time after laser cutoff for a series of different excitation levels. Because the average density increases with drop size, the decay of a large drop is markedly non-exponential, as shown for example in Fig. 4.11b. Therefore the initial decay time was measured, as well as the initial drop size, given as usual, by W_s. The results of this experiment are shown as the dots in Fig. 5.30 for Sample CR50. Note that the same data are shown as a function of excitation level in Figs. 5.2 and 5.4. The initial decay time is found to decrease from ≈500 μsec to ≈300 μsec with increasing drop size.

The change in τ_i with drop size may be modeled using the density distributions of the previous sections as follows: Note that the rate dN/dt at which e-h pairs decay via all processes is given by

$$\frac{dN}{dt} = \int \frac{n(r)}{\tau_{di}}\, dV + \int \frac{n(r)}{\tau_{rad}(n)}\, dV + \int \frac{n(r)}{\tau_{Aug}(n)}\, dV = \frac{N}{\tau_N} \quad . \qquad (5.56)$$

The first line uses Eq. (5.55), while the second line defines τ_N, the effective (initial) decay time for the number of e-h pairs N in a drop. The total luminescence intensity is proportional to

$$I_{rad} = \int \frac{n(r)}{\tau_{rad}(n)}\, dV \quad , \qquad (5.57)$$

which represents the radiated portion of dN/dt. The initial rate at which the total luminescence signal decays in time is given by

$$\frac{dI_{rad}}{dt} = \frac{I_{rad}}{\tau_i} \quad , \tag{5.58}$$

following Eq. (5.56); this defines τ_i. The left-hand side of Eq. (5.58) must be calculated numerically: I_{rad} is evaluated at times t=0 and Δt, where the radius $R(\Delta t)$ is obtained from $N(\Delta t)$, which is in turn calculated from Eq. (5.56). This procedure is necessary because of the density distribution. For the case of a constant density, τ_i is simply equal to τ_N. However, for the density distributions expected and observed here, the initial luminescence decay time τ_i is shorter than τ_N.

The curves in Fig. 5.30 represent different sets of values for the coefficients A, B, and C in Eq. (5.53). The dot-dashed curve represents the case for which $\varepsilon_{di}(n_o) = 0$, $\varepsilon_{rad}(n_o) = 0.75$, $\varepsilon_{Aug}(n_o) = 0.25$, and s = 2 in Eqs. (5.53) and (5.54). Here n_o is the uncompressed density $n_o = 0.47 \times 10^{17}$ cm^{-3}. Note that the equilibrium lifetime is $\tau(n_o) \approx$ 485 μsec. This model was formulated using the indications discussed in Section 44.2 that ε_{rad}(SCEHL) ≈ 3 ε_{rad} (unstressed EHL), along with the evidence obtained by Betzler et al[5.39] that A is negligible and that $\varepsilon_{rad} \approx 0.25$ for unstressed Ge. This model is clearly unsatisfactory; the initial decay time decreases too much as the average density increases, indicating that the Auger term is too large. Thus an Auger process is not dominant here, in contrast to the case of unstressed Ge.[5.39-5.41] It can be seen that this represents a problem: the best available information for unstressed Ge cannot simply be scaled to the densities appropriate for the SCEHL. Either some of the coefficients

A, B, C change with stress, or the coefficients are determined incorrectly for unstressed Ge, or both.

It may be noted that a slightly refined value for the ratio of the radiative efficiencies for stressed and unstressed Ge can be obtained using Eq. (5.54), as follows:

$$\frac{\varepsilon_{rad}(n_1)}{\varepsilon_{rad}(n_o)} = \frac{\tau(n_1)\tau_{rad}(n_o)}{\tau_{rad}(n_1)\tau(n_o)} \tag{5.59a}$$

$$= \frac{\tau(n_1)n_1}{\tau(n_o)n_o} \quad , \tag{5.59b}$$

where n_o and n_1 are two EHL densities. Using the values appropriate for unstressed Ge and for the SCEHL, the ratio is found to be

$$\frac{\varepsilon_{rad}(\text{unstressed EHL})}{\varepsilon_{rad}(\text{SCEHL})} = 0.36 \quad . \tag{5.60}$$

This value is found directly from measured quantities and does not depend on the production efficiencies; thus it represents an improvement over Eq. (4.11). The value for this ratio puts an absolute upper limit on the radiative efficiency for the EHL in unstressed Ge.[5.42]

The dashed curve in Fig. 5.30 represents $\varepsilon_{di}(n_o) = 0$, $\varepsilon_{rad}(n_o) = 1.0$, and $\varepsilon_{Aug}(n_o) = 0$. In this model, the change in τ_i^{-1} with drop size corresponds to the change in a kind of average density. This model is also unsatisfactory. In the first two models, a density independent term was omitted, following the situation for unstressed Ge.[5.39] It is clear, however, that within the framework of Eq. (5.53b), it is necessary to include a recombination process which is independent of density.

The solid curve in Fig. 5.30 represents an approximate fit to the data: $\varepsilon_{di}(n_o) = 0.75$, $\varepsilon_{rad}(n_o) = 0.24$, $\varepsilon_{Aug}(n_o) = 0.01$, and $s = 2$. While some adjustments are possible in these efficiencies, two points may be made. First, the density independent recombination mechanism actually dominates. Secondly, the Auger term is severely reduced. For example, if $\varepsilon_{Aug} \approx 0.75$ for unstressed Ge, then $C \approx 3.94 \times 10^{-31}$ cm^6/sec; however, if $\varepsilon_{Aug} \approx 0.01$ for the SCEHL, then the Auger coefficient is reduced to $C \approx 9.3 \times 10^{-33}$ cm^6/sec.

Additional supporting evidence is obtained from a second experiment. In this experiment the luminescence intensity from the entire drop was monitored as a function of magnetic field at discrete times after a short (≈0.2 μsec) pulse from a GaAs laser. Under these conditions the drpp grows very rapidly, within a time much shorter than the EHL lifetime,[5.43] to a maximum size; it then decays in the same way as a drop formed by cw excitation. The total energy per pulse was chosen to produce a drop with radius $R \approx 125$ μm, so that the density was essentially uniform. The application of the external magnetic field provides a second method to vary the density, similar to the case for unstressed Ge, where the density oscillates with magnetic field as electron Landau levels pass through the Fermi level.[5.39] Density oscillations of ~10% are obtained for $H \lesssim 20$ kOe. For the SCEHL, for the relatively small drop size given above, an essentially uniform density is varied without the complications of compression. The magneto-oscillations of the luminescence from Sample CR50 are shown in Fig. 5.31 for $H \leq 18$ kOe at several delay times. It can be seen that at t=1 msec the oscillations are reduced in amplitude but have not changed sign; note that t=1 msec is approximately twice the

zero-field decay time $\tau(n_o) \approx 485$ μsec. This is in contrast to the case for unstressed Ge, where the oscillations change sign after approximate one-third of the zero-field decay time.[5.39] These two results give information about the relative importance of the different decay mechanisms.

To understand the significance of these results it is necessary to consider the kinetics of a pulsed experiment. Because the drop lifetime is much longer than the laser pulse width (~500 μsec compared to ~0.2 μsec), the drop initially contains a constant number N(t=0) e-h pairs, if the efficiency of pumping carriers into the strain well is independent of magnetic field. The luminescence intensity as a function of time is given by

$$I(H,t) = \frac{N(t)}{\tau_{rad}(n(H))} \qquad (5.61a)$$

$$= B\, n(H)\, N(0)\, e^{-t/\tau(n)} \quad . \qquad (5.61b)$$

Here it is assumed that the density variation with position can be neglected, so that only the density variation with H is important. For the experimental situation, the average density for H=0 is expected to be ≈1.03 n_o, less than the magneto-oscillations; thus this assumption is justified. At a magnetic field for which the equilibrium density n(H) is higher than the zero-field value n_o, the initial luminescence intensity, I(H,0), is greater than I(0,0) and the lifetime $\tau(n)$ is shorter than $\tau(n_o)$. Therefore at some later time t_T the luminescence intensities are equal:

$$I(H,t_T) = I(0,t_T) \quad . \qquad (5.62)$$

At this turnover time t_T the magneto-oscillations change sign. As long as $|(n(H) - n_o)/n_o| \ll 1$, it is straightforward to show from Eqs. (5.61) and (5.62) that

$$t_T^{-1} = n_o \left.\frac{d\tau^{-1}(n)}{dn}\right|_{n_o} \tag{5.63a}$$

$$= Bn_o + sCn_o^s \quad . \tag{5.63b}$$

It is convenient to rewrite this equation slightly in order to define a useful quantity:

$$\xi \equiv \frac{\tau(n_o)}{t_T} = n_o \tau(n_o) \left.\frac{d\tau^{-1}(n)}{dn}\right|_{n_o} \tag{5.64a}$$

$$= \varepsilon_{rad}(n_o) + s\,\varepsilon_{Aug}(n_o) \quad . \tag{5.64b}$$

The quantities ξ and[5.44]

$$1 - \xi = \varepsilon_{di}(n_o) - (s-1)\varepsilon_{Aug}(n_o) \tag{5.65}$$

appear throughout the analysis of magneto-oscillatory phenomena. Other combinations of recombination efficiencies cannot easily be obtained from these experiments. If $\xi < 1.0$, it can be seen from Eq. (5.64a) that $\tau^{-1}(n)$ varies more slowly with density than $n^{1.0}$, i.e., that the density independent mechanism is more important than the Auger mechanism. Conversely, if $\xi > 1.0$, then $\tau^{-1}(n)$ varies more rapidly than $n^{1.0}$ and the Auger mechanism is more important than the density independent mechanism (for $s = 2$).

The data displayed in Fig. 5.31 give direct information about ξ, using Eq. (5.64a). Since the turnover time $t_T \gtrsim 2\tau(n_o)$, it must be the

case that

$$\xi \lesssim 0.50 \text{ (Sample CR50)}. \tag{5.66}$$

In addition, using Eq. (5.65), $\varepsilon_{di}(n_o) \gtrsim 0.50$, in agreement with the results of Fig. 5.30. On the other hand, the data of Betzler et al[5.39] indicate that

$$\xi \sim 2 \text{ (unstressed EHL)}. \tag{5.67}$$

This indicates that the Auger mechanism dominates the decay in unstressed Ge. In addition, note from Eq. (5.64a) that

$$\xi \leq s \ ; \tag{5.68}$$

the value of s for the Auger term cannot be smaller than the value for ξ. This has important consequences for unstressed Ge. Some of the experimental results of Betzler et al[5.39] indicate that ξ may be greater than 2. In this case, or if the enhancement factor is included in the Auger process, then it is necessary that the Auger exponent s is greater than 2.

A comment is in order concerning the omission of a density independent mechanism in the analysis of Betzler et al.[5.39] They concluded that $\varepsilon_{di} < 0.1\ \varepsilon_{Aug}$ for unstressed Ge and therefore set $\varepsilon_{di} = 0$. However, in the present analysis for the SCEHL, $\varepsilon_{di} = 0.75$ corresponds to $\tau_{di} \approx 645$ μsec. For the EHL in unstressed Ge the <u>same</u> density independent decay time corresponds to $\varepsilon_{di} = 0.056$. It is clear that such a process which can be neglected in unstressed Ge can at the same time dominate the decay of the SCEHL.

It should be noted that if a density-dependent enhancement factor is included in the analysis, somewhat different values for the efficiencies will be required for a good fit to the SCEHL data, compared to the values

corresponding to the solid curve in Fig. 5.30. The value for $\varepsilon_{di}(n_o)$ will decrease, while the values for $\varepsilon_{rad}(n_o)$ and $\varepsilon_{Aug}(n_o)$ will increase. However, it is likely that $\varepsilon_{di}(n_o)$ will still be substantial, while $\varepsilon_{Aug}(n_o)$ will still be smaller than expected simply by scaling from the results for unstressed Ge. There is also a question of what enhancement factor is appropriate to use. From a theoretical point of view, the calculation of Vashishta et al[5.38] corresponding to the Model 1 Coulomb energy of Chapter 2 is probably the most appropriate. Recently Chou and Wong[5.45] claim to have actually measured $\rho(n)$. However, in their analysis they omitted a density independent recombination mechanism. Consequently, in order to interpret their results they proposed such a rapid density dependence for $\rho(n)$ that $\tau_{rad}(n)$ was nearly independent of density. However, the experimental results of Chou and Wong are essentially consistent with those presented here: i.e., they can be interpreted using a term independent of density and a term linear in the density, with negligibly small higher order terms. Further theoretical work as well as experiments on different types of samples will be required to resolve this question.

Some of the experimental results for Sample CR50 can be used to estimate the radiative efficiency of the SCEHL. Consider drop sizes which are small enough that the effects of compression are not large. Then the number of e-h pairs which decay radiatively per sec is given by Eq. (5.57), and the radiated power is given by

$$P_{rad} = h\nu_{lum} \frac{n_o V}{\tau(n_o)} \varepsilon_{rad}(n_o) \quad , \qquad (5.69)$$

where $h\nu_{lum}$ is the energy of a luminescence photon, ≈0.71 eV. The

quantity P_{rad} is related to the actual recorded luminescence signal via Eq. (3.20). The data for drop sizes W_s between ≈100 μm and 200 μm yield the following result:

$$\varepsilon_{rad}(n_o) \approx 0.32/c \ ,$$

where the value of c is estimated to be between 0.5 and 1.0. In view of the difficulty of measuring the absolute detector sensitivity (indeed, such a measurement was <u>not</u> performed), this value is consistent with the other values proposed here.

Returning once again to the density independent recombination mechanism, a recombination time τ_{di} ~ several hundred μsec seems reasonable for Ge. Possible recombination sites include shallow traps and deep traps. While a detailed calculation is beyond the scope of this thesis, crude estimates can be made of the required concentrations of shallow or deep recombination centers. First, it may be noted that several groups[5.46-5.48] have measured the EHL decay time in doped unstressed Ge. While there is some variation in the results, the lifetime generally starts to decrease when the impurity concentration N_i is greater than ~10^{15} to 10^{16} cm^{-3}. For example, Zhurkin et al[5.48] report τ = 24 μsec for $N_i = 2 \times 10^{16}$ cm^{-3} As impurities. If the e-h pair density remains constant at these doping levels, the decrease in lifetime may be attributed to impurity-induced recombination. The change in lifetime then corresponds to τ_{di} ~ 70 μsec for $N_i = 2 \times 10^{16}$ cm^{-3}. Assuming further that this recombination time is inversely proportional to the impurity concentration, τ_{di} ~ 1 msec would correspond to N_i ~ 1×10^{15} cm^{-3} of shallow impurities. As discussed in Section 3l, it is known that the concentration of shallow impurities is $\lesssim 10^{11}$ cm^{-3} in all

the samples studied here. Thus shallow impurities are not responsible for the observed density-independent lifetime in Sample CR50.

An estimate can also be made for deep levels, where nonradiative recombination could take place via multiphonen emission.[5.49] Experimental values for nonradiative capture cross-sections at room temperature have been tabulated for Ge[5.50] and lie in the range $\sigma_{cap} \sim 10^{-14}$ to 10^{-16} cm^2. A simple model consists of a three-step process: very rapid capture of the first carrier, slower capture of a second carrier, followed by rapid recombination of the e-h pair. The rate for the slowest step is given by[5.51]

$$\tau^{-1} = \sigma_{cap} \, v \, N_i \quad , \tag{5.71}$$

where v is the carrier velocity, which can be taken to be the Fermi velocity for carriers in the EHL (see Eq. (5.12)). In this case $\tau_{di} \sim 1$ msec would correspond to $N_i \sim 10^{10}$ to 10^{12} cm^{-3}. The level associated with the divacancy-hydrogen complex is present in approximately this range of concentrations, as discussed in Section 31. While it is premature to suggest that these levels may be responsible for the observed density independent decay time, an experiment should be performed in which the concentrations of these and other deep levels are varied in a controlled manner. It may be noted that there are preliminary indications that the quantity ξ does vary between samples (e.g., for Sample CR38, ξ appears to be $\gtrsim 1$). Thus the study of the SCEHL in differently prepared samples may prove to be a sensitive test of impurity-induced recombination.

CHAPTER 6. SUMMARY AND CONCLUSIONS

In this chapter the main results of this thesis are summarized. In addition, some suggestions are made for further work.

Chapter 2 presented the results of a detailed calculation of properties of the electron-hole liquid in uniaxially stressed Ge and Si. Results were presented for a number of properties as a function of (111) stress in Ge and (100) stress in Si. These properties included the ground state (T=0) equilibrium density, the ground state pair energy, the electron-hole drop charge, the electron and hole Fermi energies, the luminescence linewidth, and the compressibility. The importance of including the non-parabolic valence band density of states in the fitting of luminescence lineshapes was emphasized. The possibility was discussed of a phase transition in Ge as a function of stress, as the upper electron valleys are depopulated. Either a phase transition should occur between two types of EHL, or the liquid should exhibit rather large density fluctuations. A careful series of experiments in this very interesting range of stresses would be highly desirable.

Theoretical results for the systematic variation of the liquid density, Fermi energy, and chemical potential with temperature were also presented. In addition, the high temperature properties were discussed, including the critical temperature and density. The theoretical results were found to be in reasonably good agreement with the available experimental data. However, a more extensive experimental study of the stress dependence of EHL properties should be done, especially in Si, where less data are currently available. As discussed here, of particular interest are the EHL properties in the infinite-stress limit, the

approach to the infinite-stress limit, and the nature of the gas in equilibrium with the liquid at high temperatures. Finally, the theoretical machinery developed here can also be used to calculate the stress dependence of EHL properties for the other primary stress directions: ⟨100⟩ and ⟨110⟩ in Ge, and ⟨111⟩ and ⟨110⟩ in Si. The availability of theoretical predictions will hopefully encourage experimental studies to be made.

In Chapter 4 the properties of the strain-confined electron-hole liquid in Ge were studied experimentally, and comparisons were drawn with clouds of small EHD formed in unstressed Ge. These properties were determined from spectrally, spatially, and time resolved measurements of the recombination luminescence as a function of excitation level, magnetic field, and, to a lesser extent, temperature and stress. The luminescence linewidth was found to increase at high excitation levels, and the recombination lifetime was found to decrease, indicating qualitatively that the liquid becomes compressed. For small drop sizes, however ($R \leq 150$ μm), the equilibrium properties may be studied. From a fit of the luminescence lineshape the density was found to be $0.50 \pm 0.05 \times 10^{17}$ cm^{-3} for stresses $-\sigma \approx 4$ to 7 kgf/mm^2 and $T = 1.6 - 2.0K$, nearly a factor of 5 lower than in unstressed Ge. The lifetime was found to be 500 ± 50 μsec at the above stresses and temperatures, over ten times longer than in unstressed Ge. This enhanced lifetime is qualitatively expected when the density is reduced.

Spatial luminescence profiles of the strain-confined liquid were studied for different conditions, thus providing information about how the drop size changes with excitation level, magnetic field, and time.

The drop radius was measured in this way from less than 100 μm up to the largest drops studied, $R \approx 700$ μm. The drops were found to flatten in a magnetic field. The size and shape of drops confined in strain wells were contrasted with the size and shape of clouds of EHD in unstressed Ge. The SCEHL was found to decay as a single entity, while the cloud retains the initial size or even grows slightly after laser cutoff.

The compression which was hinted at in Chapter 4 was investigated in detail in Chapter 5, both theoretically and experimentally. It was shown theoretically that the e-h pair density should vary with position in the strain-confined EHL. For small drops the density should be uniform to within 10-20%, depending on a parameter describing the strain well. However, for the largest drops the density should vary by $\approx$ a factor of 3 with position, depending on the maximum stress at the bottom of the well. The density is largest at the center of the drop, decreasing to the equilibrium value at the surface of the drop. Experimentally, density profiles were measured directly using luminescence box scans and an Abel transform. The magnitude and form of the density variations with position and with drop size were in excellent agreement with the theoretical predictions. This experimental technique could be extended to study density profiles at higher temperatures, where the compression becomes even stronger, and in a magnetic field. Such magnetic field studies could be compared with recent theoretical predictions by Markiewicz.

In addition, it was shown that the density variation can be exploited to study properites of the SCEHL as a function of density. In particular, the liquid chemcial potential versus density was measured

in Chapter 5. This provides a very stringent test of the many-body theories used to describe the EHL, in particular of the Coulomb energy used in the calculations of Chapter 2. The deviations from theory which were observed experimentally indicate that some modifications in the theoretical Coulomb energy may be necessary to describe the EHL at finite stress. The density dependent chemical potential also provided a measurement of the EHL compressibility. The experimentally measured value is $K_T^{expt} = 0.058\ ^{+0.024}_{-0.012}$ cm^2/dyne ($-\sigma \approx 5.5$ kgf/mm^2, $n = 0.47 \times 10^{17}$ cm^{-3}, T = 1.9K), compared to the theoretical value $K_T^{theo} = 0.041$ cm^2/dyne. These values are an order of magnitude larger than the EHL compressibility in unstressed Ge, due largely to the reduction in density. While the experimental and theoretical values are in reasonable agreement, their difference directly reflects a difference in the density-dependent chemical potential. It would be useful to have an independent measurement of the chemical potential: a proper analysis of the composite luminescence lineshape from a drop with varying density would provide such a measurement.

Finally, the EHL lifetime was studied as a function of density via the analysis of the luminescence decay time for different drop sizes. The data indicated that for the equilibrium density, the radiative efficiency $\varepsilon_{rad} \approx 0.24$, the Auger efficiency $\varepsilon_{Aug} \approx 0.01$, and the efficiency for a density-independent recombination mechanism $\varepsilon_{di} \approx 0.75$. The analysis here omitted a density-dependent enhancement factor $\rho(n)$. Although the inclusion of $\rho(n)$ would change the above values for the recombination efficiencies, the following conclusions may be drawn: (1) the lifetime changes more slowly than the density; (2) a density

independent recombination mechanism appears to be significant; (3) the Auger recombination coefficient is significantly reduced from its value in unstressed Ge. The importance of a density independent mechanism could be studied by varying the concentration of deep levels, particularly those associated with a divacancy-hydrogen complex which is known to be present in the samples studied here. In addition, it should be possible to obtain a direct measurement of the enhancement factor at the equilibrium SCEHL density, by studying both excitons and the EHL at 4.2K. Because of the geometry of the strain well, the number of pairs can be measured for either phase. This would provide a useful comparison with theory.

ACKNOWLEDGMENTS

I am very grateful to Prof. C. D. Jeffries for providing the opportunity to do research in a fascinating area of solid state physics, and for providing continual and active support, advice, and encouragement throughout the course of this work. I thank Dr. J. P. Wolfe, Dr. R. S. Markiewicz, and J. E. Furneaux for sharing uncounted hours in the lab and in discussions of results and theories. I also thank Dr. P. Vashishta for providing unpublished results of his calculations and for numerous discussions of the calculations. Dr. E. E. Haller and Dr. W. L. Hansen very generously provided Ge samples and the infrared-sensitive vidicon. I thank Dr. E. E. Haller in addition for providing detector crystals and for much advice about the science and art of detectors.

The Jeffries EHD group has had many members and visitors during the period of this research, with whom I have had many useful conversations. In particular, I thank Dr. R. M. Westerwelt, Dr. A. D. A. Hansen, B. S. Black, J. C. Culbertson, and Dr. I. Balslev. I also thank Prof. C. Kittel, Prof. L. Falicov, and A. Manoliu, who have been closely associated with the group and have provided useful input. I have also enjoyed useful conversations with Dr. G. A. Thomas, Dr. T. M. Rice, Dr. W. F. Brinkman, P. L. Gourley, and Dr. B. Chakraborty.

I especially thank D. W. Bowden for encouragement and support throughout the course of this work; and L. M. Billard, T. Doizaki, and R. Steiner for encouragement at a particularly crucial stage in my graduate student career. I would like to thank D. E. Aspnes and T. M. Rice for their patience during the final stages of writing this thesis.

I also thank J. Amoroso for dealing with administrative matters and for supervising many of the last-minute details in my absence.

This work was supported in part by the Division of Materials Sciences, Office of Basic Energy Sciences, U. S. Department of Energy under contract No. W-7405-Eng-48.

CHAPTER 1 REFERENCES

1.1. L. V. Keldysh, in Proc. IX Intern. Conf. on Phys. Semic., Moscow (Nauka, Leningrad, 1968), p. 1303; L. V. Keldysh, Eksitony v Poluprovodnikakh (Excitons in Semiconductors) (Izd. Nauka, Moscow, 1971), p. 5.

1.2. V. M. Asnin, A. A. Rogachev, and S. M. Ryvkin, Fiz. Tekh. Poluprovodn. 1, 1742 (1967) [Soviet Phys.-Semic. 1, 1447 (1968)].

1.3. Ya. Pokrovskii, Phys. Stat. Sol. (b) 11, 385 (1972).

1.4. C. D. Jeffries, Science 189, 955 (1975).

1.5. J. C. Hensel, T. G. Phillips, and G. A. Thomas, Solid State Physics, H. Ehrenreich, F. Seitz, and D. Turnbull, eds. (Academic Press, New York, 1977), vol. 32, p. 88.

1.6. T. M. Rice, ibid., p. 1.

1.7. Ya. E. Pokrovkii and K. I. Svistunova, Zh. Eksp. Teor. Fiz. Pis'ma Red. 13, 297 (1971) [JETP Lett. 13, 212 (1971)].

1.8. J. M. Worlock, T. C. Damen, K. L. Shaklee, and J. P. Gordon, Phys. Rev. Lett. 33, 771 (1974).

1.9. Ya. E. Pokrovskii and K. I. Svistunova, Fiz. Tekh. Poluprovodn. 4, 491 (1970) [Soviet Phys.-Semic. 4, 409 (1971)].

1.10. C. Benoît à la Guillaume, M. Voos, and F. Salvan, Phys. Rev. B 5, 3079 (1972).

1.11. G. A. Thomas, T. G. Phillips, T. M. Rice, and J. C. Hensel, Phys. Rev. Lett. 31, 386 (1973); G. A. Thomas, A. Frova, J. C. Hensel, R. E. Miller, and P. A. Lee, Phys. Rev. B 13, 1692 (1976).

1.12. T. K. Lo, Sol. St. Comm. 15, 1231 (1974).

1.13. C. Benoît à la Guillaume, M. Capizzi, B. Etienne, and M. Voos, Sol. St. Comm. 15, 1031 (1974).

1.14. R. M. Westervelt, T. K. Lo, J. L. Staehli, and C. D. Jeffries, Phys. Rev. Lett. 32, 1051 (1974); 32, 1331 (E) (1974).

1.15. B. B. Zubov, V. P. Kalinushkin, T. M. Murina, A. M. Prokhorov, and A. A. Rogachev, Fiz. Tekh. Poluprov. 7, 1614 (1973) [Soviet Phys.-Semic. 7, 1077 (1974)].

1.16. V. I. Sidorov and Ya. E. Pokrovskii, Fiz. Tekh. Poluprov. 6, 2405 (1972) [Soviet Phys.-Semic. 6, 2015 (1973)].

1.17. G. A. Thomas, T. M. Rice, and J. C. Hensel, Phys. Rev. Lett. 33, 219 (1974).

1.18. W. Miniscalco, C.-C. Huang, and M. B. Salamon, Phys. Rev. Lett. 39, 1356 (1977).

1.19. T. K. Lo, B. J. Feldman, and C. D. Jeffries, Phys. Rev. Lett. 31, 224 (1973); T. K. Lo, Thesis (University of California, Berkeley, 1973) (unpublished).

1.20. R. M. Westervelt, Thesis (University of California, Berkeley, 1977) (LBL Report No. LBL-6619).

1.21. R. M. Westervelt, J. L. Staehli, and E. E. Haller, Phys. Stat. Sol. (b) (to be published).

1.22. R. M. Westervelt, J. L. Staehli, E. E. Haller, and C. D. Jeffries, Lecture Notes in Physics, vol. 57, M. Ueta and Y. Nishina, eds. (Springer-Verlag, Berlin, 1976), p. 270; R. M. Westervelt, Proc. XIII Intern. Conf. on Phys. Semic., Rome, F. G. Fumi, ed. (Tipografia Marves, Rome, 1976), p. 902.

1.23. W. F. Brinkman and T. M. Rice, Phys. Rev. B 7, 1508 (1973).

1.24. M. Combescot and P. Noziéres, J. Phys. C. 5, 2369 (1972).

1.25. P. Bhattacharyya, V. Massida, K. S. Singwi, and P. Vashishta, Phys. Rev. B 10, 5127 (1974).

1.26. P. Vashishta, S. G. Das, and K. S. Singwi, Phys. Rev. Lett. 33, 911 (1974).

1.27. C. Kittel, Quantum Theory of Solids (Wiley, New York, 1963).

1.28. G. E. Pikus and G. L. Bir, Fiz. Tverd. Tela. 1, 1642 (1959) [Soviet Phys.-Solid State 1, 1502 (1959)].

1.29. I. Balslev, Phys. Rev. 143, 636 (1966).

1.30. J. C. Hensel and G. Feher, Phys. Rev. 129, 1041 (1963).

1.31. J. C. Hensel and K. Suzuki, Phys. Rev. B 9, 4219 (1974).

1.32. This notation was suggested by C. Kittel.

1.33. P. Vashishta, et al., to be published.

1.34. R. K. Kalia and P. Vashishta, Phys. Rev. B 17, 2655 (1978).

1.35. P. Vashishta, P. Bhattacharyya, and K. S. Singwi, Phys. Rev. B 10, 5108 (1974).

1.36. V. S. Bagaev, T. I. Galkina, O. V. Gogolin, and L. V. Keldysh, Pis'ma Zh. Eksp. Teor. Fiz. 10, 309 (1969) [JETP Lett. 10, 195 (1969)]; V. S. Bagaev, T. I. Galkina, and O. V. Gogolin, Proc. X Intern. Conf. on Phys. Semic., Cambridge, Mass., S. P. Keller, J. C. Hensel, and F. Stern, eds. (U. S. AEC, 1970), p. 500.

1.37. B. J. Feldman, H.-h. Chou, and G. K. Wong, Sol. St. Comm. 24, 521 (1977); 26, 209 (1978).

1.38. H.-h. Chou and G. K. Wong, Phys. Rev. Lett. 41, 1677 (1978).

1.39. Ya. E. Pokrovskii and K. I. Svistunova, Zh. Eksp. Teor. Fiz. 68, 2323 (1975) [Soviet Phys.-JETP 41, 1161 (1976)]; G. A. Thomas and Ya. E. Pokrovskii, Phys. Rev. B 18, 864 (1978).

1.40. B. M. Askkinadze, I. P. Kretsu, A. A. Patrin, and I. D. Yaroshetskii, Fiz. Tekh. Poluprovodn. 4, 2206 (1970) [Soviet Phys.-Semic. 4, 1897 (1970)].

1.41. V. D. Kulakovskii and V. S. Timofeev, Pis'ma Zh. Eksp. Teor. Fiz. 25, 487 (1977) [JETP Lett. 25, 458 (1977)]; V. D. Kulakovskii and V. S. Timofeev, Zh. Eksp. Teor. Fiz. 74, 372 (1978) [Soviet Phys.-JETP 47, 193 (1978)].

1.42. P. L. Gourley and J. P. Wolfe, Phys. Rev. Lett. 40, 526 (1978); J. P. Wolfe and P. L. Gourley, Proc. XIV Intern. Conf. on Phys. Semic., Edinburgh, B. J. H. Wilson, Inst. Phys. Conf. Ser. No. 43 (The Institute of Physics, London, 1979), p. 367; P. L. Gourley and J. P. Wolfe, unpublished results.

1.43. Preliminary or less detailed calculations have appeared in R. S. Markiewicz and S. M. Kelso, Sol. St. Comm. 25, 275 (1978); L. Liu, Sol. St. Comm. 25, 805 (1978); L. Liu and L. S. Liu, Sol. St. Comm. 27, 801 (1978); G. Kirczenow and K. W. Singwi, Phys. Rev. B 19, 2117 (1979).

1.44 R. S. Markiewicz, J. P. Wolfe, and C. D. Jeffries, Phys. Rev. Lett. 32, 1357 (1974); 34, 59 (E)(1975); C. D. Jeffries, R. S. Markiewicz, and J. P. Wolfe, Proc. XII Intern. Conf. on Phys. Semic., Stuttgart, M. H. Pilkuhn, ed. (Teubner, Stuttgart, 1974), p.101.

1.45. J. P. Wolfe, R. S. Markiewicz, C. Kittel, and C. D. Jeffries, Phys. Rev. Lett. 34, 275 (1975).

1.46. J. P. Wolfe, W. L. Hansen, E. E. Haller, R. S. Markiewicz, C. Kittel, and C. D. Jeffries, Phys. Rev. Lett. 34, 1292 (1975).

1.47. J. P. Wolfe, R. S. Markiewicz, and C. D. Jeffries, Proc. of the Third Intern. Conf. on Light Scatt. in Solids, Campinas, R. C. C. Leite, ed. (Flammarion, Paris, 1975), p.173; C. D. Jeffries, J. P. Wolfe, and R. S. Markiewicz, Proc. XIII Intern. Conf. on Phys. Semic., Rome, F. G. Fumi, ed. (Tipografia Marves, Rome, 1976), p. 879; C. D. Jeffries, J. P. Wolfe, S. M. Kelso, R. S. Markiewicz, and J. E. Furneaux, J. Lumin. 12, 659 (1976).

1.48. R. S. Markiewicz, Thesis (University of California, Berkeley, 1975) (unpublished).

1.49. R. S. Markiewicz, J. P. Wolfe, and C. D. Jeffries, Phys. Rev. B 15, 1988 (1977).

1.50. J. P. Wolfe, R. S. Markiewicz, S. M. Kelso, J. E. Furneaux, and C. D. Jeffries, Phys. Rev. B 18, 1479 (1978).

1.51. This may be contrasted with the situation in Si, where there is evidence that the strain-confined liquid may consist of a cloud of smaller drops. J. P. Wolfe, private communication.

1.52. Ya. E. Pokrovskii and K. I. Svistunova, Zh. Eksp. Teor. Fiz. Pis'ma Red. 23, 110 (1976) [JETP Lett. 23, 95 (1976)]; Ya. E. Pokrovskii and K. I. Svistunova, Proc. XIII Intern. Conf. on Phys. Semic., Rome, F. G. Fumi, ed. (Tipografia Marves, Rome, 1976), p. 849.

1.53. J. C. V. Mattos, J. M. Worlock, and T. C. Damen, Sol. St. Comm. 22, 13 (1977).

1.54. R. S. Markiewicz, Phys. Rev. B 10, 1766 (1974).

1.55. J. E. Furneaux, J. P. Wolfe, and C. D. Jeffries, Sol. St. Comm. 20, 317 (1976).

1.56. R. S. Markiewicz, Phys. Rev. B 18, 4260 (1978).

1.57. J. P. Wolfe, J. E. Furneaux, and R. S. Markiewicz, Proc. XIII Intern. Conf. on Phys. Semic., Rome, F. G. Fumi, ed. (Tipografia Marves, Rome, 1976), p. 954; J. P. Wolfe, R. S. Markiewicz, J. E. Furneaux, S. M. Kelso, and C. D. Jeffries, Phys. Stat. Sol. (b) 83, 305 (1977).

1.58. H. L. Störmer and D. Bimberg, Comments Phys. 1, 131 (1976); D. Bimberg and H. L. Störmer, Nuovo Cimento B 39, 615 (1977).

1.59. R. S. Markiewicz, Phys. Rev. B 17, 4788 (1978); R. S. Markiewicz, H. Hurwitz, Jr., and R. S. Likes, Phys. Rev. B 18, 2780 (1978).

1.60. J. C. Culbertson and R. M. Westervelt, Bull. Am. Phys. Soc. 24, 342 (1979).

1.61. S. M. Kelso and E. J. Pakulis, Bull. Amer. Phys. Soc. 34, 344 (1979); J. P. Wolfe, R. S. Markiewicz, and S. M. Kelso, unpublished results.

1.62. J. P. Wolfe, Bull. Amer. Phys. Soc. 34, 341 (1979); P. L. Gourley, post-deadline paper presented at the American Physical Society Meeting, Chicago, March 1979; P. L. Gourley and J. P. Wolfe, preprint.

1.63. A. Nakamura and K. Morigaki, Sol. St. Comm. 14, 1213 (1974).

1.64. I. Balslev, Sol. St. Comm. 26, 247 (1978).

CHAPTER 2 REFERENCES

2.1. W. F. Brinkman and T. M. Rice, Phys. Rev. B 7, 1508 (1973).

2.2. M. Combescot and P. Nozières, J. Phys. C 5, 2369 (1972).

2.3. P. Bhattacharyya, V. Massida, K. S. Singwi, and P. Vashishta, Phys. Rev. B 10, 5127 (1974).

2.4. P. Vashishta, P. Bhattacharyya, and K. S. Singwi, Phys. Rev. B 10, 5108 (1974).

2.5. P. Vashishta, R. K. Kalia, and K. S. Singwi, Lecture Notes in Physics, edited by M. Ueta and Y. Nishina, vol. 57 (Springer-Verlag, Heidelberg, 1976), p. 187.

2.6. P. Vashishta, et al., to be published.

2.7. P. Vashishta, S. G. Das, and K. S. Singwi, Phys. Rev. Lett. 33, 911 (1974).

2.8. M. Combescot, Phys. Rev. Lett. 32, 15 (1974).

2.9. G. A. Thomas, T. M. Rice, and J. C. Hensel, Phys. Rev. Lett. 33, 219 (1974).

2.10. R. N. Silver, Phys. Rev. B 8, 2403 (1973).

2.11. T. M. Rice, Solid State Physics, edited by H. Ehrenreich, F. Seitz, and D. Turnbull, vol. 32 (Academic Press, 1977), p. 1.

2.12. V. S. Bagaev, T. I. Galkina, O. V. Gogolin, and L. V. Keldysh, Pis'ma Zh. Eksp. Teor. Fiz. 10, 309 (1969) [JETP Lett. 10, 195 (1969)]; V. S. Bagaev, T. I. Galkina, and O. V. Gogolin, Proc. X Int'l. Conf. on Phys. Semic., Cambridge, Mass., edited by S. P. Keller, J. C. Hensel, and F. Stern (USAEC, 1970), p. 500.

2.13. C. Benoît à la Guillaume, M.Voos, and F. Salvan, Phys. Rev. B 5, 3079 (1972).

2.14. B. M. Ashkinadze, I. P. Kretsu, A. A. Patrin, and I. D. Yaroshetskii, Fiz. Tekh. Poluprovodn. 4, 2206 (1970) [Soviet Phys.—Semic. 4, 1897 (1970)].

2.15. R. S. Markiewicz, J. P. Wolfe, and C. D. Jeffries, Phys. Rev. Lett. 32, 1357 (1974); 34, 59 (E)(1975); J. P. Wolfe, R. S. Markiewicz, C. Kittel, and C. D. Jeffries, Phys. Rev. Lett. 34, 275 (1975); C. D. Jeffries, J. P. Wolfe, S. M. Kelso, R. S. Markiewicz, and J. E. Furneaux, J. Lumin. 12, 659 (1976).

2.16. B. J. Feldman, H.-h. Chou, and G. K. Wong, Sol. St. Comm. 24, 521 (1977); 26, 209 (1978).

2.17. H.-h. Chou and G. K. Wong, Phys. Rev. Lett. 41, 1677 (1978).

2.18. Ya. E. Pokrovskii and K. I. Svistunova, Zh. Eksp. Teor. Fiz. 68, 2323 (1975) [Soviet Phys.—JETP 41, 1161 (1976)]; G. A. Thomas and Ya. E. Pokrovskii, Phys. Rev. B 18, 864 (1978).

2.19. V. D. Kulakovskii and V. S. Timofeev, Pis'ma. Zh. Eksp. Teor. Fiz. 25, 487 (1977) [JETP Lett. 25, 458 (1977)]; V. D. Kulakovskii, V. S. Timofeev, and V. M. Edel'shtein, Zh. Eksp. Teor. Fiz. 74, 372 (1978) [Soviet Phys. — JETP 47, 193 (1978)].

2.20. P. C. Gourley and J. P. Wolfe, Phys. Rev. Lett. 40, 526 (1978).

2.21. J. P. Wolfe and P. L. Gourley, Proc. XIV Int'l. Conf. on Phys. Semic., Edinburgh, edited by B. L. H. Wilson, Inst. Phys. Conf. Ser. No. 43 (The Institute of Physics, London, 1979), p. 379.

2.22. J. C. Hensel, T. G. Phillips, and G. A. Thomas, Solid State Physics, edited by H. Ehrenreich, F. Seitz, and D. Turnbull, vol. 32 (Academic Press, 1977), p. 88.

2.23. R. S. Markiewicz and S. M. Kelso, Sol. St. Comm. 25, 275 (1978).

2.24. S. M. Kelso, Bull. Am. Phys. Soc. 24, 343 (1979); S. M. Kelso, submitted to Phys. Rev. B.

2.25. G. Kirczenow and K. S. Singwi, Phys. Rev. B 19, 2117 (1979).

2.26. L. Liu, Sol. St. Comm. 25, 805 (1978).

2.27. L. Liu and L. S. Liu, Sol. St. Comm. 27, 801 (1978).

2.28. J. P. Wolfe, R. S. Markiewicz, S. M. Kelso, J. E. Furneaux and C. D. Jeffries, Phys. Rev. B 18, 1479 (1978).

2.29. P. Vashishta, private communication (1977).

2.30. C. Kittel, Thermal Physics (Wiley, NY, 1969), see especially Chapters 14 and 18-20.

2.31. R. S. Markiewicz, J. P. Wolfe, and C. D. Jeffries, Phys. Rev. B 15, 1988 (1977).

2.32. C. Kittel, Introduction to Solid State Physics, 5th edition (Wiley, NY, 1976), see especially Chapter 6.

2.33. H.-h. Chou, G. K. Wong, and B. J. Feldman, Phys. Rev. Lett. 39, 959 (1977).

2.34. B. J. Feldman, H.-h. Chou, and G. K. Wong, to be published.

2.35. G. Kirczenow and K. S. Singwi, Phys. Rev. Lett. 41, 326 (1978); 42, 1004 (1979).

2.36. B. J. Feldman and R. S. Markiewicz, Sol. St. Comm. 29, 411 (1979).

2.37. V. D. Kulakovskii, I. B. Levinson, and V. B. Timofeev, Fiz. Tverd. Tela 20, 399 (1978)[Soviet Phys.—Solid State 20, 230 (1978)].

2.38. G. E. Pikus and G. L. Bir, Fiz. Tverd. Tela 1, 1642 (1959) [Soviet Physics—Solid State 1, 1502 (1959)].

2.39. I. Balslev, Phys. Rev. 143, 636 (1966).

2.40. G. Dresselhaus, A. F. Kip, and C. Kittel, Phys. Rev. 98, 368 (1955).

2.41. J. C. Hensel and G. Feher, Phys. Rev. 129, 1041 (1963).

2.42. J. C. Hensel and K. Suzuki, Phys. Rev. B 9, 4219 (1974).

2.43. Hensel and Feher (Ref. 2.41) give formulas involving compliance constants S_{ij}. The experimental values to be used (see Table 2.1) are given as stiffness constants C_{ij}, so these are used in the equations. There has traditionally been a great deal of confusion over engineering vs. tensor notation for these quantities. As long as either notation is used consistently, then $S_{44} = (C_{44})^{-1}$, $S_{11}-S_{12} = (C_{11}-C_{12})^{-1}$, and $S_{11} + 2S_{12} = (C_{11} + 2C_{12})^{-1}$. It must then be assumed that Hensel and Feher (Ref. 2.41), Fine, and McSkimin (see Table 2.1) used the same type of notation.

2.44. B. Lax and J. G. Mavroides, Phys. Rev. 100, 1650 (1955).

2.45. Ya. Pokrovskii, A. Kaminskii, and Svistunova, Proc. X Int'l. Conf. on Phys. Semic., Cambridge, edited by S. P. Keller, J. C. Hensel, and F. Stern (USAEC, 1970), p. 504.

2.46. C. Benoît à la Guillaume and M. Voos, Phys. Rev. B 7, 1723 (1973).

2.47. W. P. Dumke, Phys. Rev. 105, 139 (1957).

2.48. The selection rules for Ge and Si are given in M. Lax and J. J. Hopfield, Phys. Rev. 124, 115 (1961).

2.49. G. A. Thomas and M. Capizzi, Proc. XIII Int'l. Conf. on Phys. Semic, Rome, edited by F. G. Fumi (Topografia Marves, Rome, 1976), p. 914; G. A. Thomas, E. I. Blount, and M. Capizzi, Phys. Rev. B 19, 702 (1979).

2.50. R. B. Hammond, T. C. McGill and J. W. Mayer, Phys. Rev. B 13, 3566 (1976).

2.51. M. Vouk and E. C. Lightowlers, J. Phys. C 8, 3695 (1975).

2.52. H. L. Störmer, R. W. Martin, and J. C. Hensel, Proc. XIII Int'l. Conf. on Phys. Semic., Rome, edited by F. G. Fumi (Tipografia Marves, Rome, 1976), p. 950.

2.53. R. W. Martin and H. L. Störmer, Sol. St. Comm. 22, 523 (1977).

2.54. P. T. Landsberg, Phys. Stat. Sol. 15, 623 (1966).

2.55. G. A. Thomas, T. G. Phillips, T. M. Rice, and J. C. Hensel, Phys. Rev. Lett. 31, 386 (1973).

2.56. R. S. Markiewicz, private communication.

2.57. P. Vashishta, private communication (1978). The author is grateful for many discussions with Dr. Vashishta concerning his unpublished calculations.

2.58. R. K. Kalia and P. Vashishta, Phys. Rev. B 17, 2655 (1978).

2.59. H. Büttner, Festkörperprobleme XIII (1973), p. 145; E. P. Wigner, Trans. Faraday Soc. 34, 678 (1938).

2.60. H. Hasegawa, Phys. Rev. 129, 1029 (1963).

2.61. An error in the calculation of the optical mass in Ref. 2.23 has been corrected here, so the results for Model 3 in Ge differ somewhat.

2.62. N. O. Lipari and M. Altarelli, Phys. Rev. B 15, 4883 (1977).

2.63. A. Frova, G. A. Thomas, R. E. Miller, and E. O. Kane, Phys. Rev. Lett. 34, 1572 (1975).

2.64. M. Capizzi, F. Evangelisti, A. Frova, and P. Valfre, Proc. XIII Int'l. Conf. on Phys. Semic, Rome, edited by F. G. Fumi (Tipografia Marves, Rome, 1976), p. 857.

2.65. M. A. Buchanan and T. Timusk, Proc. XIII Int'l. Conf. on Phys. Semic Rome, edited by F. G. Fumi (Tipografia Marves, Rome, 1976), p. 821.

2.66. M. Altarelli and N. O. Lipari, Phys. Rev. B 15, 4898 (1977).

2.67. R. B. Hammond, D. L. Smith, and T. C. McGill, Phys. Rev. Lett. 35, 1535 (1975); D. L. Smith, R. B. Hammond, M. Chen, S. A. Lyon, and T. C. McGill, Proc. XIII Int'l. Conf. on Phys. Semic, Rome, edited by F. G. Fumi (Tipografia Marves, Rome, 1976), p. 1077.

2.68. I. Balslev, Sol. St. Comm. 23, 205 (1977).

2.69. M. Capizzi, J. C. Merle, P. Fiorini, and A. Frova, Sol. St. Comm. 24, 451 (1977).

2.70. V. I. Sidorov and Ya. E. Pokrovskii, Fiz. Tekh. Poluprovodn. 6, 2405 (1972) [Soviet Phys.—Semicond. 6, 2015 (1973)].

2.71. K. L. Shaklee and R. E. Nahory, Phys. Rev. Lett. 24, 942 (1970).

2.72. W. Kohn and J. M. Luttinger, Phys. Rev. 97, 1721 (1955); 98, 915 (1955).

2.73. K. Muro and S. Narita, Proc. XIII Int'l. Conf. on Phys. Semic., Rome, edited by F. G. Fumi (Tipografia Marves, Rome, 1976), p. 853.

2.74. J. B. Mock, M. Capizzi, and G. A. Thomas, J. Phys. Chem. Sol. 39, 1231 (1978).

2.75. T. Ohyama, T. Sanada, and E. Otsuka, Phys. Rev. Lett. 33, 647 (1974).

2.76. B. M. Ashkinadze, I. P. Kretsu, A. A. Patrin, and I. D. Yaroshetskii, Phys. Stat. Sol. (b) 46, 495 (1971).

2.77. F. Bassani and D. Brust, Phys. Rev. 131, 1524 (1963).

2.78. P. Vashishta, S. G. Das, and K. S. Singwi, Phys. Rev. B 13, 4490 (1976).

2.79. Other methods for estimating the density of the strain-confined liquid are discussed in Sec. 42.4.

2.80. J. E. Furneaux, R. S. Markiewicz, and S. M. Kelso, Bull. Am. Phys. Soc. 22, 270 (1977).

2.81. J. P. Wolfe, private communication.

2.82. T. M. Rice, Phys. Rev. B 9, 1540 (1974).

2.83. Ya. E. Pokrovskii and K. I. Svistunova, Zh. Eksper. Teor. Fiz. Pis. Red. 19, 92 (1974) [JETP Lett. 19, 56 (1974)].

2.84. Ya. E. Pokrovskii and K. I. Svistunova, Fiz. Tverd. Tela 16, 3399 (1974) [Soviet Phys.—Sol. St. 16, 2202 (1975)]; Proc. XII Int'l Conf. on Phys. Semic., Stuttgart, edited by M. H. Pilkuhn (Teubner, Stuttgart, 1974), p. 71.

2.85. T. M. Rice, Il Nuovo Cimento 23B, 226 (1974).

2.86. A renormalization of carrier masses was also predicted in the context of a theoretical lineshape analysis by M. Rösler and R. Zimmermann, Phys. Stat. Sol. (b) 67, 525 (1975). Their results are similar to those of Rice (Ref. 2.85).

2.87. R. W. Martin, H. L. Störmer, W. Ruhle, and D. Bimberg, J. Lum. 12/13, 645 (1976); H. L. Störmer and R. W. Martin, Proc. of the Conf. on the Application of High Mag. Fields in Semic. Physics Oxford (edited by J. F. Ryan, Clarendon Laboratory, Oxford, UK, 1978), p. 269.

2.88. V. I. Gavrilenko, V. L. Kononenko, T. S. Mandel'shtam, and V. N. Murzin, Pis'ma Zh. Eksp. Teor. Fiz. 23, 701 (1976) [JETP Lett. 23, 645 (1976)].

2.89. See, for example, R. P. Feynman, Statistical Mechanics (Benjamin, 1972), pp. 36-37.

2.90. J. Shah, M. Combescot, and A. H. Dayem, Phys. Rev. Lett. 38, 1497 (1977).

2.91. A. F. Dite, V. D. Kulakovskii and V. B. Timofeev, Zh. Eksp. Teor. Fiz. 72, 1156 (1977) [Soviet Phys.--JETP 72, 604 (1977)].

2.92. G. A. Thomas, J. B. Mock, and M. Capizzi, Phys. Rev. B 18, 4250 (1978) and references therein.

2.93. W. D. Kraeft and W. Fennel, Phys. Stat. Sol. (b) 73, 487 (1976).

2.94. T. L. Reinecke and S. C. Ying, Phys. Rev. Lett. 35, 311 (1975); 35, 547 (E) (1975).

2.95. T. L. Reinecke, M. C. Lega, and S. C. Ying, to be published.

2.96. T. L. Reinecke and S. C. Ying, Sol. St. Electronics 21, 1385 (1978).

2.97. N. F. Mott, Metal-Insulator Transitions (Barnes & Noble, NY, 1974).

2.98. G. Mahler, Phys. Rev. B 11, 4050 (1975); G. Mahler and J. L. Birman, Phys. Rev. B 16, 1552 (1977).

2.99. L. M. Sander and D. K. Fairobent, Sol. St. Comm. 20, 631 (1976).

2.100. W. Ebeling, W. D. Kraeft, D. Kremp, and K. Kilimann, Phys. Stat. Sol. (b) 78, 241 (1976).

2.101. R. Zimmermann, Phys. Stat. Sol. (b) 76, 191 (1976).

2.102. H. Haug and D. B. Tran Thoi, Phys. Stat. Sol. (b) 85, 561 (1978). There may be an error in these calculations (I. Balslev, private communication).

2.103. D. Kremp, W. Ebeling, and W. D. Kraeft, Phys. Stat. Sol. (b) 69, K59 (1975); W. D. Kraeft, K. Kilimann, and D. Kremp, Phys. Stat. Sol. (b) 72, 461 (1975).

2.104. T. M. Rice, Proc. XII Int'l Conf. on Phys. Semic., Stuttgart, edited by M. H. Pilkuhn (Teubner, Stuttgart, 1974), p. 23.

2.105. The possibility of two critical points was first considered for the case of Hg in L. D. Landau and G. Zeldovich, Acta, Phys.-Chim. USSR 18, 194 (1973), translated in Collected Papers of L. D. Landau, edited by D. Ter Haar (Gordon & Breach, NY, 1975), p. 380.

2.106. T. Timusk, Phys. Rev. B. 13, 3511 (1976).

2.107. W. Miniscalco, C.-C. Huang, and M. B. Salamon, Phys. Rev. Lett. 39, 1356 (1977).

2.108. G. A. Thomas and T. M. Rice, Sol. St. Comm. 23, 359 (1977).

2.109. J. E. Furneaux and I. Balslev, Bull. Am. Phys. Soc. 24, 280 (1979); I. Balslev and J. E. Furneaux, preprint (1979).

2.110. E. A. Guggenheim, J. Chem. Phys. 13, 253 (1945).

2.111. M. Droz and M. Combescot, Phys. Lett. A51, 473 (1975).

2.112. G. A. Thomas, A. Frova, J. C. Hensel, R. E. Miller, and P. A. Lee, Phys. Rev. B 13, 1692 (1976); G. A. Thomas, Il Nuovo Cimento 39B, 561 (1977).

2.113. See, for example, A. H. Wilson, The Theory of Metals (Cambridge University Press, 1953); J. S. Blakemore, Semiconductor Statistics (Pergamon Press, 1962).

2.114. See, for example, F. B. Hildebrand, Introduction to Numerical Analysis (McGraw-Hill, NY, 1956), p. 447.

2.115. A. A. Kastal'skii, Fiz. Tverd. Tela 20, 1241 (1978) [Soviet Phys. — Solid State 20, 715 (1978)].

CHAPTER 3 REFERENCES

3.1. W. L. Hansen and E. E. Haller, IEEE Trans. Nucl. Sci. 21, 251 (1974); E. E. Haller and W. L. Hansen, ibid., p. 279.

3.2. E. E. Haller, G. S. Hubbard, W. L. Hansen, and A. Seeger, Inst. Phys. Conf. Ser. No. 31, edited by N. B. Urli and J. W. Corbett (Inst. of Physics, London, 1977), p. 309.

3.3. E. E. Haller, G. S. Hubbard, and W. L. Hansen, IEEE Trans. Nucl. Sci. NS24, 48 (1977).

3.4. R. S. Markiewicz, J. P. Wolfe, and C. D. Jeffries, Phys. Rev. B 15, 1988 (1977).

3.5. H. Hertz, J. Rein. Ang. Math. 92, 156 (1881).

3.6. R. S. Markiewicz, Thesis (University of California, Berkeley, 1975) (unpublished).

3.7. A. D. A. Hansen, Thesis (University of California, Berkeley, 1977) (LBL Report No. LBL-7326).

3.8. See, for example, H. Kogelnik and T. Li, Applied Optics 5, 1550 (1966).

3.9. L. F. Mollenauer, C. D. Grandt, W. B. Grant, and H. Panepucci, Rev. Sci. Instr. 39, 1958 (1968).

3.10. R. M. Westervelt, Thesis (University of California, Berkeley, 1977)(LBL Report No. LBL-6619).

3.11. See, for example, S. M. Sze, Physics of Semiconductor Devices (Wiley-Interscience, New York, 1969), p. 89.

3.12. R. A. Faulkner, Phys. Rev. 184, 713 (1969).

3.13. D. M. Chang and J. G. Ruch, Appl. Phys. Lett. 12, 111 (1968); G. O. Haviani, C. Canali, F. Nava, and J. W. Mayer, J. Appl. Phys. 44, 2917 (1973).

3.14. G. G. Macfarlane, T. P. McLean, J. E. Quarrington, and V. Roberts, Phys. Rev. 108, 1377 (1957); J. Phys. Chem. Sol. 8, 388 (1959).

3.15. R. F. Potter, Phys. Rev. 150, 562 (1966).

3.16. Ya. Pokrovskii, Phys. Stat. Sol. (a) 11, 385 (1972).

3.17. R. W. Martin, Thesis (Stuttgart, 1974) (unpublished); R. W. Martin, Physica Status Solidi (b) 61, 223 (1974).

3.18. C. D. Jeffries, J. P. Wolfe, S. M. Kelso, R. S. Markiewicz, and J. E. Furneaux, J. Lumin. 12, 659 (1976).

3.19. J. P. Wolfe, R. S. Markiewicz, S. M. Kelso, J. E. Furneaux, and C. D. Jeffries, Phys. Rev. B 18, 1479 (1978).

3.20. G. W. Cleek, J. J. Villa, and C. H. Hahner, J. Opt. Soc. Amer. 49, 1090 (1959).

3.21. Such a discussion is not generally found in optics textbooks. See, however, B. Sherman, Modern Photography (Nov. 1978), p. 46.

3.22. Y.-R. Shen, private communication.

3.23. See, for example, C. Kittel, Introduction to Solid State Physics, 5th edition (Wiley, NY, 1976), p. 138.

3.24. A. A. Manenkov, G. N. Mikhailova, A. S. Seferov, and V. D. Chernetskii, Fiz. Tverd. Tela. 16, 2719 (1974) [Sov. Phys.—Sol. St. 16, 1757 (1974)].

CHAPTER 4 REFERENCES

4.1. R. S. Markiewicz, J. P. Wolfe, and C. D. Jeffries, Phys. Rev. B 15, 1988 (1977).

4.2. R. S. Markiewicz, Thesis, University of California, 1975 (unpublished).

4.3. J. P. Wolfe, R. S. Markiewicz, and C. D. Jeffries, in Proc. of the Third Intern. Conf. on Light Scattering in Solids, Campinas, R. C. C. Leite, ed. (Flammarion, Paris, 1975), p. 173; C. D. Jeffries, J. P. Wolfe, and R. S. Markiewicz in Proc. of the Thirteenth Intern. Conf. on the Physics of Semiconductors, Rome, F. G. Fumi, ed. (Tipografia Marves, Rome, 1976), p. 879.

4.4. Ya. E. Pokrovskii and K. I. Svistunova, Zh. Eksp. Teor. Fiz. Pis'ma Red. 13, 297 (1971) [JETP Lett. 13, 212 (1971)]; J. M. Worlock, T. C. Damen, K. L. Shaklee, and J. P. Gordon, Phys. Rev. Lett. 33, 771 (1974).

4.5. M. Voos, K. L. Shaklee, and J. M. Worlock, Phys. Rev. Lett. 33, 1161 (1974).

4.6. R. W. Martin, Thesis, Stuttgart, 1974 (unpublished); R. W. Martin, Phys. Stat. Sol. (b) 61, 223 (1974).

4.7. J. P. Wolfe, R. S. Markiewicz, S. M. Kelso, J. E. Furneaux, and C. D. Jeffries, Phys. Rev. B 18, 1479 (1978).

4.8. J. P. Wolfe, R. S. Markiewicz, J. E. Furneaux, S. M. Kelso, and C. D. Jeffries, Phys. Stat. Sol. (b) 83, 305 (1977).

4.9. For reviews see (a) Ya. Pokrovskii, Phys. Stat. Sol. (b) 11, 385 (1972); (b) C. D. Jeffries, Science 189, 955 (1975); (c) J. C. Hensel, T. G. Phillips, and G. A. Thomas, Solid State

Physics, H. Ehrenreich, F. Seitz, and D. Turnbull, eds. (Academic, New York, 1978), vol. 32, p. 88; (d) T. M. Rice, ibid., p. 1.

4.10. J. P. Wolfe, R. S. Markiewicz, C. Kittel, and C. D. Jeffries, Phys. Rev. Lett. 34, 275 (1975).

4.11. See, for example, R. M. Westervelt, Proc. of the Thirteenth Intern. Conf. on the Physics of Semiconductors, Rome, F. G. Fumi, ed., (Tipografia Marves, Rome, 1976), p. 902; J. C. Hensel, T. G. Phillips, and T. M. Rice, Phys. Rev. Lett. 30, 227 (1973); T. K. Lo, B. J. Feldman, and C. D. Jeffries, Phys. Rev. Lett. 31, 224 (1973).

4.12. J. E. Furneaux, R. S. Markiewicz, and S. M. Kelso, Bull. Am. Phys. Soc. 22, 270 (1977).

4.13. J. E. Furneaux, et al., to be published; see also the thesis of J. E. Furneaux.

4.14. G. A. Thomas, A. Frova, J. C. Hansel, R. E. Miller, and P. A. Lee, Phys. Rev. B13, 1692 (1976).

4.15. R. M. Westervelt, in Ref. 4.11; R. M. Westervelt, Thesis (University of California, 1977)(LBL Report No. LBL-6619); R. M. Westervelt, Phys. Stat Sol. (b), to be published.

4.16. C. Benoît à la Guillaume, M. Voos, and F. Salvan, Phys. Rev. B 5, 3079 (1972).

4.17. In principle, the strains could be calibrated by observing the strain-induced birefringence pattern (see Ref. 4.1). In practice, this is difficult, since the birefringence represents a two-dimensional average of the three-dimensional strain pattern. Furthermore, great care must be taken to avoid interference

effects. If the crystal surfaces are not optically smooth, or if the polarized beam is not everywhere perpendicular to the surface, there will be interference between different rays of light, which tends to blur the pattern, reducing the number of fringes. Thus, while the fringes shown in Ref. 4.1 correctly reflect the distribution of strain in the crystal, they probably underestimate the magnitudes of the strains by about a factor of two.

4.18. B. J. Feldman, H.-h. Chou, and G. K. Wong, Sol. St. Comm. 24, 521 (1977); 26, 209 (1978).

4.19. H.-h. Chou and G. K. Wong, Phys. Rev. Lett. 41, 1677 (1978).

4.20. Ya. E. Pokrovskii and K. I. Svistunova, Zh. Eksp. Teor. Fiz. 68, 2323 (1975) [Soviet Phys.—JETP 41, 1161 (1976)]; G. A. Thomas and Ya. E. Pokrovskii, Phys. Rev. B 18, 864 (1978).

4.21. See, for example, A. S. Alekseev, V. S. Bagaev, and T. I. Galkina, Zh. Eksp. Teor. Fiz. 63, 1020 (1972). [Soviet Phys. JETP 36, 536 (1973)]; T. Ohyama, T. Sanada, K. Fujii, and E. Otsuka, in Proc. of the Twelfth Intern. Conf. on the Physics of Semiconductors, Stuttgart, M. H. Pilkuhn, ed. (Teubner, Stuttgart, 1974), p. 66; and Ref. 4.16. The greatly decreased lifetime and luminescence intensity observed in these experiments may have been due to non-uniformity in the stress, driving the drops into rapid recombination centers at the crystal surface. Also, shorter lifetimes are observed for γ-drops when dislocated samples are used. Pokrovskii (Ref. 4.43) has reported lifetimes of ≈400 μsec in dislocation-free Ge under uniaxial ⟨111⟩ stress, where the lifetime did not vary greatly with stress.

4.22. H. Hertz, J. Rein. Ang. Math. 92, 156 (1881).

4.23. Note that, for the sample stressed along ⟨100⟩, the luminescence is scarcely shifted from its unstressed position; indeed, the peak is actually shifted to higher energy than in the unstressed sample. This does not mean that drops are not attached to the well. A uniaxial ⟨100⟩ stress raises the EHL pair energy (Ref. 4.16), but in the inhomogeneously-stressed sample, the pair energy is raised everywhere except in the wells, as shown in Fig. 10 of Ref. 4.1. Actually, the γ-drop luminescence line in Fig. 4.7 is sufficiently narrow that the high energy edge is at a lower energy than in the unstressed sample, showing that the γ-drop has a lower ground-state energy.

4.24. The density is also expected to vary with position in the well, due to the change in stress. However, as shown in Chapter 2, n varies only weakly with uniform stress over the range relevant to this discussion ($-\sigma$ = 4 to 6 kgf/mm^2 for a 400 μm radius drop).

4.25. R. S. Markiewicz and S. M. Kelso, Sol. St. Comm. 25, 275 (1978).

4.26. At low P, the lines shown here are slightly narrower than those observed by others (see Fig. 2.14). This may be because of inhomogeneous broadening due to small inhomogeneities in the "uniform" stress experiments. This is a problem of considerable difficulty attending all experiments of uniform stress on EHD. See Ref. 4.21.

4.27. H. L. Störmer, R. W. Martin, and J. C. Hensel, in Proc. of the Thirteenth Intern. Conf. on the Physics of Semiconductors, Rome, F. G. Fumi, ed. (Tipografia Marves, Rome, 1976), p. 950; R. W. Martin and H. L. Störmer, Sol. St. Comm. 22, 523 (1977).

4.28. G. A. Thomas and M. Capizzi, in Proc. of the Thirteenth Intern. Conf. on the Physics of Semiconductors, Rome, F. G. Fumi, ed. (Tipografia Marves, Rome, 1976), p. 914.

4.29. V. S. Bagaev, T. I. Galkina, N. A. Penin, V. B. Stopachinskii, and M. N. Churaeva, Zh. Eksp. Teor. Fiz. Pis'ma Red. 16, 120 (1972) [JETP Lett. 16, 83 (1972)].

4.30. K. Betzler, B. G. Zhurkin, and A. L. Karuzskii, Sol. St. Comm. 17, 577 (1975); K. Betzler, B. G. Zhurkin, A. L. Karuzskii, and B. M. Balter, J. Lumin. 12, 651 (1976).

4.31. V. N. Murzin, V. A. Zayats, and V. L. Kononenko, Fiz. Tverd. Tela 15, 3634 (1973) [Soviet Phys.-Solid State 15, 2421 (1974)].

4.32. K. Fujii and E. Otsuka, J. Phys. Soc. Japan 38, 742 (1975).

4.33. Oscillations in the photocurrent initially ascribed to holes in EHD, in V. F. Gantmakher and V. N. Zverev, Zh. Eksp. Teor. Fiz. Pis'ma Red. 18, 180 (1973) [JETP Lett. 18, 105 (1973)], have been reinterpreted. See V. F. Gantmakher and V. N. Zverev, Zh. Eksp. Teor. Fiz. 69, 695 (1975). [Sov. Phys. JETP 42, 352 (1975)].

4.34. Some experimental results are given in Ref. 4.7 and will be discussed in more detail in the thesis of J. E. Furneaux.

4.35. T. Ohyama, A. D. A. Hansen, and J. L. Turney, Sol. St. Comm. 19, 1083 (1976); A. D. A. Hansen, T. Ohyama, and J. L. Turney, Lecture Notes of Third Intern. Conf. on the Application of High Magnetic Fields in Semiconductor Physics, Würzburg (Physikalisches Institut der Universitat Würzburg, 1976), p. 580.

4.36. A. D. A. Hansen, private communication.

4.37. C. D. Jeffries, J. P. Wolfe, S. M. Kelso, R. S. Markiewicz, and J. E. Furneaux, J. Luminescence 12, 659 (1976).

4.38. R. S. Markiewicz, J. P. Wolfe, and C. D. Jeffries, Phys. Rev. Lett. 32, 1357 (1974); 34, 59 (E) (1975).

4.39. R. S. Markiewicz, Phys. Rev. B 10, 1766 (1974).

4.40. R. S. Markiewicz, Phys. Rev. B 18, 4260 (1978).

4.41. Reference 4.37 quoted a value $n_\gamma = 0.7 \times 10^{17}$ cm^{-3} while Ref. 4.2 quoted a value $n_\gamma = 1 \times 10^{17}$ cm^{-3}. This difference is due to an overall decrease in drop volume in a magnetic field, which was taken into account only in Ref. 4.2. However, experiments subsequent to those in Refs. 4.2 and 4.37, involving simultaneous imaging and Alfvén absorption measurements, showed the distortion of the drop shape in a magnetic field. Assuming the primary resonance observed is the longitudinal magnetic dipole resonance, the field configurations indicate that the drop dimension perpendicular to the external field would be measured (see Ref. 4.2, especially Fig. IV.1a-1b). Since this is generally the larger dimension, the lower value for n is more nearly correct.

4.42. Ya. E. Pokrovskii and K. I. Svistunova, Zh. Eksp. Teor. Fiz. Pis'ma Red. 23, 110 (1976) [JETP Lett. 23, 95 (1976)].

4.43. Ya. E. Pokrovskii and K. I. Svistunova, Proc. of the Thirteenth Intern. Conf. on the Physics of Semiconductors, Rome, F. G. Fumi, ed. (Tipografia Marves, Rome, 1976), p. 849.

4.44. J. C. V. Mattos, J. M. Worlock, and T. C. Damen, Sol. St. Comm. 22, 13 (1977).

4.45. For a recent measurement of σ_a, see M. Glicksman, S. A. Mittleman, and J. R. Meyer, Sol. St. Comm. 27, 523 (1978).

4.46. R. L. Aurbach, L. Eaves, R. S. Markiewicz, and P. L. Richards, Sol. St. Comm. 19, 1023 (1976).

4.47. M. Combescot and P. Nozières, Sol. St. Comm. 10, 302 (1972).

4.48. V. N. Murzin, Fiz. Tekh. Poluprovodn. 7, 1610 (1973) [Soviet Phys.-Semiconductors 7, 1074 (1974)]; V. N. Murzin, V. A. Zayats, and V. L. Kononenko, Fiz. Tverd. Tela 17, 2684 (1975) [Soviet Phys.-Solid State 17, 1783 (1976)].

4.49. J. H. Rose, H. B. Shore, and T. M. Rice, Phys. Rev. B 17, 752 (1978).

4.50. R. N. Silver and C. H. Aldrich, Phys. Rev. Lett. 41, 1249 (1978).

4.51. A similar calculation for γ-drops is complicated by the inhomogeneous strain, but this strain also weakens the intensity of interband transitions. A Manoliu, private communication, 1975.

4.52. A. D. A. Hansen and T. Ohyama, Bull. Am. Phys. Soc. 22, 269 (1977); and A. D. A. Hansen, Thesis (University of California, Berkeley, 1977) (LBL Report No. LBL-7326), especially Fig. 81.8.

4.53. See, for example, C. Kittel, Introduction to Solid State Physics, 5th edition (Wiley, New York, 1976), p. 227.

4.54. Rice has calculated renormalized carrier masses in EHD in unstressed Ge, and finds for electrons $m_\parallel$ (EHD) $\approx 0.99\, m_\parallel$ (Ge), $m_\perp$ (EHD) $\approx 1.10\, m_\perp$ (Ge); for holes m_{LH}(EHD) $\approx 1.10\, m_{LH}$(Ge), m_{HH}(EHD) $\approx 1.14\, m_{HH}$(Ge). See T. M. Rice, Nuovo Cimento 23B, 226 (1974) and the discussion in Section 23.3.

4.55. In general, there can be an unequal population of electrons in the various valleys corresponding to non-integer ν_e. The result given in the text can be taken to indicate that the population of three of the four valleys is much less than the remaining valley.

4.56. R. S. Markiewicz, unpublished results.

4.57. A. S. Alekseev, V. S. Bagaev, T. I. Galkina, O. V. Gogolin, and N. A. Penin, Fiz. Tverd. Tela 12, 3516 (1970) [Soviet Phys.-Solid State 12, 2855 (1971)]; C. Benoît à la Guillaume and M. Voss, Sol. St. Comm. 11, 1585 (1972); R. W. Martin and R. Sauer, Phys. Stat. Sol. (b) 62, 443 (1974).

4.58. Ya. E. Pokrovskii, private communication; R. M. Westervelt, private communication.

4.59. R. M. Westervelt, T. K. Lo, J. L. Staehli, and C. D. Jeffries, Phys. Rev. Lett. 32, 1051 (1974); 32, 1331 (E) (1974).

4.60. C. Benoît à la Guillaume, M. Capizzi, B. Etienne, and M. Voos, Sol. St. Comm. 15, 1031 (1974).

4.61. J. C. Hensel, T. G. Phillips and T. M. Rice, Phys. Rev. Lett. 30, 227 (1973).

4.62. Ya. E. Pokrovskii and K. I. Svistunova, Fiz. Tekh. Poluprovodn. 4, 491 (1970) [Soviet Phys.-Semiconductors 4, 409 (1970)].

4.63. C. Benoît à la Guillaume, M. Voos, and F. Salvan, Phys. Rev. Lett. 27, 1214 (1971).

4.64. R. F. Leheny, J. Shah, and M. Voos, Sol. St. Comm. 20, 819 (1976).

4.65. Ya. E. Pokrovskii, private communication. This value is somewhat lower than some published values (see Refs. 4.30, 4.62-4.64). However, the absolute measure of ε_{rad} is experimentally very difficult and is subject to error. Pokrovskii and Svistunova (Ref. 4.43) have found that the quantum efficiency is at least three times greater in their uniformly stressed samples than in unstressed Ge.

4.66. J. P. Wolfe, W. L. Hansen, E. E. Haller, R. S. Markiewicz, C. Kittel, and C. D. Jeffries, Phys. Rev. Lett. 34, 1292 (1975).

4.67. P. Vashishta, R. K. Kalia, and K. S. Singwi, Sol. St. Comm. 19, 935 (1976); R. K. Kalia and P. Vashishta, Phys. Rev. B 17, 2655 (1978).

4.68. R. S. Markiewicz, Phys. Rev. B 17, 4788 (1978).

4.69. L. V. Keldysh, Zh. Eksp. Teor. Fiz. Pis'ma Red. 23, 100 (1976) [JETP Lett. 23, 86 (1976)].

4.70. V. S. Bagaev, L. V. Keldysh, N. N. Sibel'din, V. A. Tsvetkov, Zh. Eksp. Teor. Fiz. 70, 702 (1976) [Soviet. Phys.-JETP 43, 362 (1976)].

4.71. J. Doehler, J. C. V. Mattos, and J. M. Worlock, Phys. Rev. Lett. 38, 726 (1977); J. Doehler and J. M. Worlock, Sol. St. Comm. 27, 229 (1978); J. Doehler and J. M. Worlock, Phys. Rev. Lett. 41, 980 (1978).

4.72. J. C. Hensel and R. C. Dynes, Phys. Rev. Lett. 39, 969 (1977); J. C. Hensel, Bull. Am. Phys. Soc. 23, 421 (1978).

4.73. M. Greenstein and J. P. Wolfe, Phys. Rev. Lett. 41, 715 (1978).

4.74. R. S. Markiewicz, to be published.

4.75. B. J. Feldman, Phys. Rev. Lett. 33, 359 (1974).

4.76. J. C. V. Mattos, K. L. Shaklee, M. Voos, T. C. Damen, and J. M. Worlock, Phys. Rev. B 13, 5603 (1976).

4.77. Other possible mechanisms for producing the "cloud" have been proposed. See M. Combescot, Phys. Rev. B 12, 1591 (1975); I. Balslev and J. M. Hvam, Phys. Stat. Sol. (b) 65, 531 (1974); J. M. Hvam and I. Balslev, Phys. Rev. B 11, 5053 (1975); and the discussion in Refs. 4.70 and 4.72.

4.78. R. S. Markiewicz, Phys. Stat. Sol. (b) 83, 659 (1977); Phys. Stat. Sol. (b), to be published.

4.79. R. M. Westervelt, Thesis, in Ref. 4.15.

4.80. T. C. Damen and J. M. Worlock, Proc. Third Intern. Conf. on Light Scatt. in Solids, Campinas, R. C. C. Leite, ed. (Flammarion, Paris, 1975), p. 183.

4.81. J. E. Furneaux, J. P. Wolfe, and C. D. Jeffries, Sol. St. Comm. 20, 317 (1976).

4.82. Fore more details, see Ref. 4.8 and the thesis of J. E. Furneaux.

4.83. J. P. Wolfe, J. E. Furneaux, and R. S. Markiewicz, Proc. of the 13th Intern. Conf. on the Physics of Semic., Rome, F. G. Fumi, ed. (Tipografia Marves, Rome, 1976), p. 954.

4.84. H. L. Störmer and D. Bimberg, Comm. on Physics 1(5), 131 (1976).

4.85. D. Bimberg and H. L. Störmer, Proc. of Conf. on Recent Developments in Optical Spectroscopy of Solids, Taormina, Nuovo Cimento 39B, 615 (1977).

4.86. A. S. Kaminskii and Ya. E. Pokrovskii, Zh. Eksp. Teor. Fiz. Pis'ma Red. 21, 431 (1975) [JETP Lett. 21, 197 (1975)].

4.87. R. S. Markiewicz, H. Hurwitz, Jr., and R. S. Likes, Phys. Rev. B 18, 2780 (1978).

4.88. F. Salvan, Ph. Mathiez, J. C. McGroddy, D. Bimberg, and H. Störmer, Nuovo Cimento 39B, 645 (1977).

CHAPTER 5 REFERENCES

5.1. Note that for constant production efficiency, the slope for I_{tot} should simply be 1. Evidently the production efficiency increases significantly at low excitation levels, since the well is relatively far from the excited face of the crystal.

5.2. S. M. Kelso, Proceedings of XIV Int'l. Conf. on Phys. Semic., Edinburgh, edited by B. L. H. Wilson, Inst. Phys. Conf. Ser. No. 43 (The Institute of Physics, London, 1979), p.363.

5.3. S. M. Kelso and J. E. Furneaux, Sol. State Elec. 21, 1377 (1978).

5.4. S. M. Kelso, manuscript in preparation.

5.5. S. M. Kelso, manuscript in preparation.

5.6. R. S. Markiewicz, thesis (University of California, 1975) (unpublished).

5.7. R. S. Markiewicz, J. P. Wolfe, and C. D. Jeffries, Phys. Rev. B 15, 1988 (1977).

5.8. For the geometry of part (a) of Figs. 5.5 and 5.6 ($\langle 111 \rangle$ stress, $(1\bar{1}0)$ face), one cannot define a true shear stress in two dimensions. Thus the formulas given here are only approximate.

5.9. C. Benoît à la Guillaume, M. Voos, and F. Salvan, Phys. Rev. B 5, 3079 (1972).

5.10. J. C. Hensel, T. G. Phillips, and G. A. Thomas, Solid State Physics, edited by M. Ehrenreich, F. Seitz, and D. Turnbull (Academic Press, New York, 1978), Vol. 32, p.88.

5.11. I. Balslev, Phys. Rev. 143, 636 (1966).

5.12. P. L. Gourley and J. P. Wolfe, Phys. Rev. Lett. 40, 526 (1978).

5.13. R. S. Markiewicz and S. M. Kelso, Sol. St. Comm. 25, 275 (1978).

5.14. T. M. Rice, Phys. Rev. B 9, 1540 (1974).

5.15. L. M. Sander, H. B. Shore, and L. J. Sham, Phys. Rev. Lett. 31, 533 (1973).

5.16. T. L. Reinecke and S. C. Ying, Sol. St. Comm. 14, 381 (1974); T. L. Reinecke, F. Crowne, and S. C. Ying, Proc. XII Int'l. Conf. on Phys. Semic., Stuttgart, edited by M. H. Pilkuhn (Teubner, Stuttgart, 1974), p.61.

5.17. P. Vashishta, R. K. Kalia, and K. S. Singwi, Sol. St. Comm. 19, 935 (1976); P. Vashishta, R. K. Kalia, and K. S. Singwi, Proc. Oji Seminar on the Physics of Highly Excited States in Solids, edited by M. Ueta and Y. Nishina (Springer-Verlag, Berlin, 1976), Vol. 57, p.187.

5.18. L. D. Landau and E. M. Lifshitz, Fluid Mechanics (Pergamon, London, 1959), p.230.

5.19. R. K. Kalia and P. Vashishta, Phys. Rev. B17, 2655 (1978).

5.20. American Institute of Physics Handbook, edited by D. E. Gray, 3rd edition (McGraw-Hill, New York, 1972), p. 2-184.

5.21. R. H. Sherman and F. J. Edeskuty, Ann. Phys. 9, 522 (1960).

5.22. C. Benoît à la Guillaume and M. Voos, Phys. Rev. B 7, 1723 (1973).

5.23. The quantity B is expected to change by ~10%, for example, as the electron degeneracy is reduced from 4 to 1, as occurs under stress (R. S. Markiewicz, private communication).

5.24 Actually, $I_{tot} \propto P_{abs} \times \varepsilon_{prod} \times \varepsilon_{rad}$ so that something must be known about the power dependence (i.e., the drop size or density dependence) of the radiative efficiency ε_{rad}. It may be noted that if nonradiative recombination processes which depend more

strongly on density than the radiative process (e.g., an Auger process) are more important than nonradiative processes which depend more weakly on density than the radiative process (e.g., a density-independent process), then ε_{rad} decreases with increasing density or excitation level. For the opposite case, ε_{rad} increases with increasing density or excitation level. As long as $\varepsilon_{rad} \gtrsim$ 50%, however, this consideration is not important for the interpretation of Figs. 5.1 and 5.2.

5.25. See, for example, K. Bockasten, J. Opt. Soc. Amer. 51, 943 (1961); W. L. Barr, J. Opt. Soc. Amer. 52, 885 (1962).

5.26. J. C. V. Mattos, K. L. Shaklee, M. Voos, T. C. Damen, and J. M. Worlock, Phys. Rev. B 13, 5603 (1976).

5.27. J. C. V. Mattos, J. M. Worlock, and T. C. Damen, Sol. St. Comm. 22, 13 (1977).

5.28. The results of this experiment are discussed in Section 54.

5.29. See, for example, R. Piessens, Comp. Phys. Commun. 5, 294 (1973); C. Fleurier and J. Chapelle, Comp. Phys. Commun. 7, 200 (1974); and references therein.

5.30. I. N. Sneddon, The Use of Integral Transforms (McGraw-Hill, New York, 1972), pp.210-211, 318-319.

5.31. R. Bracewell, The Fourier Transform and Its Applications (McGraw-Hill, New York, 1965), pp.262-266.

5.32. Ya. E. Pokrovskii and K. I. Svistunova, Pis'ma Zh. Eksp. Teor. Fiz. 23, 110 (1976) [JETP Lett. 23, 95 (1976)].

5.33. Ya. E. Pokrovskii and K. I. Svistunova, Proc. XIII Int'l. Conf. on Phys. Semic., Rome, edited by F. G. Fumi (Tipografia Marves, Rome, 1976), p.849.

5.34. Indeed, if the absorption of 3.39 μm radiation is combined with an analysis of the luminescence lineshape, an accurate measurement of the absorption cross-section under stress would be obtained.

5.35. G. A. Thomas, T. G. Phillips, T. M. Rice, and J. C. Hensel, Phys. Rev. Lett. 31, 386 (1973).

5.36. The theoretical curve for $I_{\lambda\text{-scan}}$ was computed using an incorrect model to account for the luminescence lineshape from a drop containing a variation in the pair density. Although this curve is not expected to change greatly when the model is corrected, the agreement here may be fortuitous.

5.37. However, if the Model 6 Coulomb energy were used instead of Model 1, it is clear from Fig. 2.9 that the equilibrium density would not be as close to the experimental value. Thus neither model is ideal.

5.38. P. Vashishta, P. Bhattacharyya, and K. S. Singwi, Phys. Rev. B 10, 5108 (1974).

5.39. K. Betzler, B. G. Zhurkin, A. L. Karuzskii, and B. M. Balter, J. Lumin. 12, 651 (1976); K. Betzler, B. G. Zhurkin, and A. L. Karuzskii, Sol. St. Comm. 17, 577 (1975); A. L. Karuzskii, K. Betzler, B. G. Zhurkin, and B. M. Balter, Pis'ma. Zh. Eksp. Teor. Fiz. 22, 65 (1975) [JETP Lett. 22, 29 (1975)].

5.40. C. Benoît à la Guillaume, M. Voos, and F. Salvan, Phys. Rev. Lett. 27, 1214 (1971).

5.41. R. F. Leheny, J. Shah, and M. Voos, Sol. St. Comm. 20, 819 (1976).

5.42. Note that Eq. (5.59a) is rigorously correct, while Eq. (5.59b) omits the density-dependent enhancement factor. If $\rho(n) \sim n^{-\frac{1}{2}}$, for example, the ratio in Eq. (5.60) is reduced to 0.16.

5.43. J. E. Furneaux, J. P. Wolfe, and C. D. Jeffries, Sol. St. Comm. 20, 317 (1976).

5.44. Note that the efficiencies must add up to one: $\epsilon_{di} + \epsilon_{rad} + \epsilon_{Aug} = 1.0$.

5.45. H.-h. Chou and G. K. Wong, Phys. Rev. Lett. 41, 1677 (1978).

5.46. C. Benoît à la Guillaume and M. Voos, Sol. St. Comm. 11, 1585 (1972).

5.47. A. L. Karuzskii, K. Betzler, B. G. Zhurkin, and V. P. Aksenov, Fiz. Tverd. Tela 17, 3104 (1975) [Sov. Phys.-Solid State 17, 2058 (1975)].

5.48. B. G. Zhurkin, A. L. Karuzskii, R. L. Korchazhkina, and V. A. Fradkov, Sol. St. Comm. 20, 341 (1976).

5.49. C. H. Henry, J. Lumin. 12, 47 (1976).

5.50. É. P. Sinyavskii and V. A. Kovarskii, Fiz. Tverd. Tela 9, 1464 (1967) [Soviet Phys.-Solid State 9, 1142 (1967)].

5.51. T. M. Rice, Solid State Physics, edited by H. Ehrenreich, F. Seitz, and D. Turnbull, Vol. 32 (Academic Press, New York, 1977), p.77.

Table 2.1. Values for parameters used in the calculation of hole masses.

Parameter	Ge	Ref.	Si	Ref.
A	13.38	*a,b*	4.28	*c*
B	8.48	*a,b*	0.75	*c*
C	13.14	*a,b*	4.85	*c,d*
b	2.21 eV	*a,e*	1.36 eV	*c,e*
d	4.40 eV	*a,e*	3.09 eV	*c,e*
C_{11}	13360 kgf/mm^2	*f*	17100 kgf/mm^2	*g*
C_{12}	4996 kgf/mm^2	*f*	7093 kgf/mm^2	*g*
C_{44}	7016 kgf/mm^2	*f*	8180 kgf/mm^2	*g*
$E^h_{spl}/\|\sigma\|$	0.362 meV/(kgf/mm^2)	*h*	0.272 meV/(kgf/mm^2)	*h*

[a] J. C. Hensel and K. Suzuki, Phys. Rev. B 9, 4219 (1974).

[b] Reference *a* gives values for γ_1, γ_2, and γ_3, where $A = -\gamma_1$, $B = -2\gamma_2$, $C^2 = 12(\gamma_3^2 - \gamma_2^2)$. Defined in this way, valence band energies are negative. Following convention in EHL calculations, the signs of A and B have been changed in order to make the energies positive (C enters only as C^2). These quantities are expressed as multiples of $(\hbar^2/2m_o)$.

[c] J. C. Hensel and G. Feher, Phys. Rev. 129, 1041 (1963).

[d] The value for C obtained from Ref. *c* was later updated in P. Lawaetz, Phys. Rev. B 4, 3460 (1971). The value given here is generally used in EHL calculations at zero stress.

[e] References *a* and *c* give values for D_u and D'_u, which are related to b and d via $b = -2/3\ D_u$ and $d = -2/\sqrt{3}\ D'_u$. Again, following convention for EHL calculations, the signs are changed to make the energies E(k) positive.

[f] M. E. Fine, J. Appl. Phys. 26, 862 (1955). The values used are from the lowest temperature of the experiment, T = 1.7 K.

[g] H. J. McSkimin, J. Appl. Phys. 24, 988 (1953). The data were extrapolated to helium temperatures from 78 K by multiplying by 1.002, a factor obtained by comparison with data for Ge in Ref. *f*.

[h] For ⟨111⟩ stress (Ge), $E^h_{spl}/|\sigma| = d/(\sqrt{3}\ C_{44})$. For ⟨100⟩ stress (Si), $E^h_{spl}/|\sigma| = 2b/(C_{11} - C_{12})$.

Table 2.2. Selected numerical results for hole masses.

Quantity	Ge	Si
ZERO STRESS		
m_{dHH}/m_o	0.347	0.5231
m_{dLH}/m_o	0.0423	0.1548
m_{dh}/m_o	0.3568	0.5778
m_{oh}/m_o	0.2244	0.3354
$frac_{LH}$	0.0410	0.1387
INFINITE STRESS	⟨111⟩ STRESS	⟨100⟩ STRESS
m_{ht}/m_o	0.1301	0.2561
m_{hl}/m_o	0.04038	0.1988
m_{dh}/m_o	0.08809	0.2354
m_{oh}/m_o	0.07474	0.2336

Table 2.3. Other parameters used in the calculation.

Parameter	Ge	Ref.	Si	Ref.
Electrons				
m_{et}/m_o	0.08152	*a*	0.1905	*b*
m_{el}/m_o	1.588	*a*	0.9163	*b*
m_{de}/m_o	0.2193	*c*	0.3216	*c*
m_{oe}/m_o	0.1192	*d*	0.2588	*d*
Ξ_u	16.6 eV	*e*	8.6 eV	*e*
$E^e_{spl}/\lvert\sigma\rvert$	1.05 meV/(kgf/mm^2)	*f*	0.86 meV/(kgf/mm^2)	*f*
$\phi(\rho_e)$	0.8401	*g*	0.9490	*g*
Zero Stress				
ν_e	4		6	
$\psi(\rho_h)$	0.710	*h*	0.746	*h*
$E^h_F(0)/E^e_F(0)$	1.55	*i*	1.84	*i*
Infinite Stress				
ν_e	1 (⟨111⟩ stress)		2 (⟨100⟩ stress)	
$\psi(\rho_h)$	0.9698	*g*	0.9986	*g*
$E^h_F(0)/E^e_F(0)$	2.50	*i*	2.17	*i*
Miscellaneous				
κ	15.36	*j*	11.40	*j*
a (Model 2)	0.1917	*k*	0.2128	*k*
c (Model 2)	4.461	*k*	8.552	*k*

[a] B. W. Levinger and D. R. Frankl, J. Phys. Chem. Solids 20, 281 (1961).

[b] J. C. Hensel, H. Hasegawa, and M. Nakayama, Phys. Rev. 138, A225 (1965).

[c] Use Eq. (2.33).

[d] Use Eq. (2.30).

[e] I. Balslev, Phys. Rev. 143, 636 (1966).

[f] For ⟨111⟩ stress (Ge), $E^e_{spl}/|\sigma| = (4/9)\Xi_u/C_{44}$. For ⟨100⟩ stress (Si), $E^e_{spl}/|\sigma| = \Xi_u/(C_{11} - C_{12})$.

[g] Use Eq. (2.43).

[h] W. F. Brinkman and T. M. Rice, Phys. Rev. B 7, 1508 (1973).

[i] Use Eq. (2.40)

[j] R. A. Faulkner, Phys. Rev. 184, 713 (1969).

[k] Model 2 is described in the text; if n is expressed in units of 10^{17} cm^{-3} and the masses as multiples of the free electron mass, then a is dimensionless and c is in meV.

Table 2.4. Selected numerical results for the ground state properties of the EHL in stressed Ge and Si.

Material, Stress Direction	$-\sigma$ (kgf/mm^2)	Model	n_o (10^{17} cm^{-3})	$-f_G$ (meV)	E_F^e (meV)	E_F^h (meV)	E_F^{tot} (meV)	E_o'' (10^{-34} meV cm^6)
Ge, ⟨111⟩	Zero	Expt.[a]	2.3±0.1	6.1±0.2	2.53±0.02	3.90±0.02	6.43±0.04	0.2±0.05
		5	2.21	5.88	2.40	3.73	6.13	0.186
		1	2.70	6.14	2.75	4.27	7.02	0.137
		2	2.24	6.03	2.43	3.77	6.20	0.193
	3	1	0.642	4.06	2.66	2.16	4.82	1.31
		2	0.659	4.06	2.71	2.19	4.90	1.58
	7	1	0.435	3.66	2.05	2.32	4.37	2.02
		2	0.492	3.65	2.23	2.45	4.68	2.16
	20	1	0.200	3.22	1.22	2.19	3.41	8.62
		2	0.259	3.15	1.45	2.49	3.94	6.05
	Infinite	1	0.098	2.96	0.76	1.92	2.68	52.9
		2	0.112	2.82	0.83	2.10	2.93	40.5
		6	0.109	3.07	0.81	2.06	2.87	34.9
Si, ⟨100⟩	Zero	Expt.[a]	33±1	23	7.8±0.1	14.4±0.1	22.2±0.2	0.005±0.003
		5	32.3	21.97	7.50	13.79	21.29	0.00311
		1	31.8	22.52	7.43	13.64	21.07	0.00290
		2	29.3	22.42	7.03	12.91	19.94	0.00384
	12	1	13.6	17.42	8.75	9.32	18.07	0.0159
		2	13.1	17.42	8.55	9.14	17.69	0.0156
	40	1	9.04	15.47	6.68	10.25	16.93	0.0293
		2	8.18	15.54	6.25	9.74	15.99	0.0287

Table 2.4 (continued)

Material, Stress direction	$-\sigma$ (kgf/mm^2)	Model	n_0 (10^{17} cm^{-3})	$-f_G$ (meV)	E_F^e (meV)	E_F^h (meV)	E_F^{tot} (meV)	E_0'' (10^{-34} meV cm^6)
	100	1	6.22	14.60	5.20	9.94	15.14	0.0616
		2	5.41	14.78	4.74	9.17	13.91	0.0699
	Infinite	1	4.74	14.09	4.34	9.46	13.80	0.106
		2	4.20	14.35	4.01	8.73	12.74	0.131
		6	4.46	14.71	4.17	9.08	13.25	0.118

[a]The experimental data at zero stress are compiled from J. C. Hensel, T. G. Phillips, and G. A. Thomas, Solid State Physics, ed. by H. Ehrenreich, F. Seitz, and D. Turnbull, Vol. 32 (Academic Press, 1977), p.88.

Table 2.5. Selected numerical results for properties of the EHL in stressed Ge and Si at finite temperature.

Material, Stress Direction	$-\sigma$ (kgf/mm^2)	Model	δ_n (meV^{-2})	δ_μ (meV^{-1})	δ_E (meV^{-2})	T_c (K)	n_c (10^{17} cm^{-3})
Ge, (111)	Zero	Expt.	0.9-1.4[a,b]	2.2±0.9[b]	0.71±0.14[b]	6.5-7.0[f,g,h]	0.5-1.0[f,g,h]
		5	1.24	1.69	0.92	8.18[j]	0.50[j]
		1	0.98	1.47	0.73	6.95	0.28
		2	1.15	1.67	0.85	7.96	0.31
	3	1	2.91	2.41	1.91	5.05	0.065
		2	2.25	2.37	1.52	5.92	0.087
	7	1	3.90	2.75	2.47	4.59	0.042
		2	2.67	2.57	1.76	5.39	0.062
	20	1	5.65	3.53	3.61	3.95	0.018
		2	4.19	3.07	2.66	4.53	0.028
	Infinite	1	5.94	4.53	4.52	3.61	0.010
		2	5.41	4.14	4.07	3.99	0.014
		6	6.84	4.23	5.05	3.72[j]	0.017[j]
Si, (100)	Zero	Expt.	0.055±0.020[c,d]	0.3-1.7[c,d,e]	0.05±0.025[c,d,e]	26-30[e,i]	10-14[e,i]
		5	0.104	0.508	0.078	28.6[j]	5.1[j]
		1	0.117	0.513	0.086	27.4	3.7
		2	0.110	0.542	0.082	26.7	3.5
	12	1	0.136	0.599	0.094	23.2	1.7
		2	0.152	0.613	0.104	22.6	1.6

Table 2.5 (continued)

Material, Stress direction	$-\sigma$ (kgf/mm^2)	Model	δ_n (meV^{-2})	δ_μ (meV^{-1})	δ_E (meV^{-2})	T_c (K)	n_c (10^{17} cm^{-3})
	40	1	0.169	0.685	0.113	20.4	0.90
		2	0.222	0.727	0.146	20.0	0.82
	100	1	0.193	0.750	0.135	19.2	0.63
		2	0.246	0.823	0.175	18.8	0.58
	Infinite	1	0.231	0.829	0.174	18.6	0.52
		2	0.258	0.898	0.196	18.3	0.48
		6	0.246	0.864	0.186	24.4[k]	0.78[k]

[a] T. K. Lo, Sol. St. Comm. 15, 1231 (1974).

[b] G. A. Thomas, T. G. Phillips, T. M. Rice, and J. C. Hensel, Phys. Rev. Lett. 31, 386 (1973).

[c] R. B. Hammond, T. C. McGill, and J. W. Mayer, Phys. Rev. B 13, 3566 (1976).

[d] M. A. Vouk and E. C. Lightowlers, J. Phys. C 8, 3695 (1975).

[e] A. F. Dite, V. D. Kulakovskii, and V. B. Timofeev, Zh. Eksp. Teor. Fiz. 72, 1156 (1977) [Sov. Phys. -- JETP 72, 604 (1977)].

[f] G. A. Thomas, T. M. Rice, and J. C. Hensel, Phys. Rev. Lett. 33, 219 (1974).

[g] W. Miniscalco, C.-C. Huang, and M. B. Salamon, Phys. Rev. Lett. 39, 1356 (1977).

[h] G. A. Thomas, J. B. Mock, and M. Capizzi, Phys. Rev. B 18, 4250 (1978).

[i] J. Shah, M. Combescot, and A. H. Dayem, Phys. Rev. Lett. 38, 1497 (1977).

[j] Computed using T^2 expansion. The values differ from those given in P. Vashishta, S. G. Das, and K. S. Singwi, Phys. Rev. Lett. 33, 911 (1974), as explained in the text.

Table 3.1. Ge samples and characteristics

Sample	LBL Single crystal number[a]	Dimensions (mm)	Stress direction	Face	Surface preparation
CR50	145	3.85 x 3.95 x 2.80	⟨111⟩	$(1\bar{1}0)$	"White" etch[b]
CR38	146	3.85 x 3.85 x 1.75	⟨111⟩	$(1\bar{1}0)$	"White" etch, followed by Syton for imaging faces
CR37	145	4 x 4 x 2	⟨111⟩	$(1\bar{1}0)$	"White" etch
CR36	145 or 146	4 x 4 x 2	⟨111⟩	$(1\bar{1}0)$	"White" etch
CR16	145	3.95 (dia), 1.40 (thick)	⟨110⟩	(100)	"White" etch
CR14	145	3.95 (dia), 1.40 (thick)	⟨110⟩	(100)	"White" etch

[a] LBL single crystals 145 and 146 are virtually identical, with a net acceptor concentration $N_A \approx 2 \times 10^{11}$ cm^{-3} due to a hydrogen-divacancy complex; both are dislocation-free.

[b] "White" etch is a $3HNO_3$:HF solution.

TABLE 5.1. Coefficients for Density Power Series.

$$n(r,R,T) = n_o(T) + \sum_{i=1}^{10} A_i[\alpha_{spec}(R^2 - r^2)]^i$$

$-\sigma$ = 5 kgf/mm^2, T = 1.9K

Coefficient	Value	Unit
$n_o(T)$	0.493	10^{17} cm^{-3}
A_1	1.391	10^{17} cm^{-3} meV^{-1}
A_2	-1.703	10^{17} cm^{-3} meV^{-2}
A_3	3.413	10^{17} cm^{-3} meV^{-3}
A_4	-4.524	10^{17} cm^{-3} meV^{-4}
A_5	3.651	10^{17} cm^{-3} meV^{-5}
A_6	-1.725	10^{17} cm^{-3} meV^{-6}
A_7	0.491	10^{17} cm^{-3} meV^{-7}
A_8	-0.125	10^{17} cm^{-3} meV^{-8}
A_9	0.0401	10^{17} cm^{-3} meV^{-9}
A_{10}	-0.0070	10^{17} cm^{-3} meV^{-10}

CHAPTER 1 FIGURE CAPTIONS

Fig. 1.1. Schematic energy band structure for Ge along the (111) crystallographic direction. The valence and conduction bands are shown, along with bands for free excitons (FE) and the electron-hole liquid (EHL). Several characteristic energies of the system are shown: the FE and EHL ground state energies E_x and $-f_G$ measured down from the conduction band edge, the liquid condensation energy ϕ, and the liquid Fermi energy E_F. The quantity $\hbar\omega_{ph}$ is the energy of the phonon emitted with the photon in the radiative recombination process. Thus the energies E_x', μ', and E_{BB}' are photon or spectroscopic values for the FE ground state energy, the EHL ground state energy, and the energy of the bottom of the EHL band respectively.

Fig. 1.2. Luminescence spectrum of FE and EHD in unstressed ultrapure Ge at 2.10 K. The LA phonon assisted lines are labelled FE and EHD; the small bump at the low energy side of the EHD line is the TO replica of the FE line. From Ref. 1.20.

Fig. 1.3. Splitting of the conduction and valence bands for uniaxial compression along the ⟨111⟩ direction in Ge and the ⟨100⟩ direction in Si. The configurations Ge (ν_e:ν_h) and Si (ν_e:ν_h) indicate the number ν_e of electron bands and ν_h of hole bands which are (partially) below the Fermi level.

Fig. 1.4. Photograph of the luminescence from the electron-hole liquid confined in a strain well in a 4 mm x 4 mm x 3 mm crystal of Ge inhomogeneously stressed along the ⟨111⟩ direction. The large central bright region is a single electron-hole drop with diameter ≈1.4 mm. The edges of the crystal and the stressing rod are marked by scattered luminescence. Sample CR50, absorbed power 400 mW, T = 1.9 K.

CHAPTER 2 FIGURE CAPTIONS

Fig. 2.1. Local and integrated density-of-states masses for heavy and light holes in stressed Ge, as a function of reduced energy $E' = E/|\sigma_{111}|$. The arrows indicate the values at zero stress.

Fig. 2.2. Local and integrated density-of-states masses for heavy and light holes in stressed Si, as a function of reduced energy $E' = E/|\sigma_{100}|$. The arrows indicate the values at zero stress.

Fig. 2.3. Longitudinal and transverse optical masses for heavy and light holes and total optical hole mass for stressed Ge, as a function of reduced energy $E' = E/|\sigma_{111}|$. The arrows indicate zero-stress values for the heavy and light masses.

Fig. 2.4. Longitudinal and transverse optical masses for heavy and light holes and total optical hole mass for stressed Si, as a function of reduced energy $E' = E/|\sigma_{100}|$. The arrows indicate zero-stress values for the heavy and light masses.

Fig. 2.5. Theoretical luminescence lineshapes for Ge, for $-\sigma_{111}$ = 5.6 kgf/mm^2, $n = 0.50 \times 10^{17}$ cm^{-3}, and T = 1.8 K. Solid line: uses energy-dependent density-of-states mass from Fig. 2.1. Dashed curve: uses constant mass $m_{dh} = M_{dHH}(E_F^h)$ with E_F^h = 2.28 meV from the previous case. The Fermi energy $E_F^e + E_F^h$ is shown.

Fig. 2.6. Theoretical luminescence lineshapes for Si stressed along ⟨100⟩, with the Fermi energy chosen so that the full width at half maximum ΔE = 6.8 meV (T = 1.4 K). Solid curve: uses energy-dependent density-of-states mass from Fig. 2.2, with $-\sigma$ = 55 kgf/mm^2 and $n = 5.53 \times 10^{17}$ cm^{-3}. Dashed curve:

uses infinite-stress mass and $n = 3.79 \times 10^{17}$ cm^{-3}. The electron and hole Fermi energies E_F^e and E_F^h are shown for the dashed curve. The sum $E_F^e + E_F^h$ is also shown, in each case measured from the low-energy edge of the curve.

Fig. 2.7. Coulomb energy per e-h pair vs. pair density for several models of the Coulomb energy in Ge. The models are discussed in the text.

Fig. 2.8. Coulomb energy per e-h pair vs. pair density for several models of the Coulomb energy in Si. The models are discussed in the text.

Fig. 2.9. Equilibrium density vs. stress for the EHL in Ge uniaxially stressed along ⟨111⟩. (a) Models 1, 5, and 6; (b) Models 2, 3, and 4. The models are discussed in the text. Compressional stresses are negative. Arrows indicate the "correct" zero-stress (Model 5) and infinite-stress (Model 6) densities.

Fig. 2.10. Equilibrium density vs. stress for the EHL in Si uniaxially stressed along ⟨100⟩. (a) Models 1, 5, and 6; (b) Models 2, 3, and 4. The models are discussed in the text. Compressional stresses are negative. Arrows indicate the "correct" zero-stress (Model 5) and infinite-stress (Model 6) densities.

Fig. 2.11. Ground state pair energy versus stress for the EHL in Ge stressed along ⟨111⟩, for the same models as shown in Fig. 2.9. The dashed curve is the exciton binding energy, estimated as described in the text.

Fig. 2.12. Ground state pair energy vs stress for the EHL in Si stressed along ⟨100⟩, for the same models as shown in Fig. 2.10. The

dashed curve is the exciton binding energy, estimated as described in the text.

Fig. 2.13. Equilibrium density vs. stress for Ge-like bands. The calculation is identical to Model 1 (see the text for a description) except that as 1 conduction valley is lowered, it is assumed that ν_2 valleys are raised, in the calculation of the electron kinetic energy. The magnitude and abruptness of the change in density associated with the emptying of the upper valleys thus depends on the magnitude of the change in fractional occupation of the lower valley. (The curve with $\nu_2 = 3$ corresponds to "real" Ge.)

Fig. 2.14. Equilibrium density as a function of ⟨111⟩ stress for Ge at T = 2K. The curves are the results for Models 1 and 2. The data points are taken from Refs. 2.16 (●), 2.18 (▲), 2.17 (■), and 2.28 (+).

Fig. 2.15. Electron and hole Fermi energies E_F^e and E_F^h, total Fermi energy $E_F^{tot} = E_F^e + E_F^h$, and luminescence linewidth ΔE as a function of ⟨111⟩ stress for Ge at T = 2 K, using Model 1. The arrows show the results for the zero and infinite stress limits. The dashed lines are the energy splitting between upper and lower bands for electrons (E_{spl}^e) and for holes (E_{spl}^h).

Fig. 2.16. Electron and hole Fermi energies E_F^e and E_F^h, total Fermi energy $E_F^{tot} = E_F^e + E_F^h$, and luminescence linewidth ΔE as a function of ⟨100⟩ stress for Si at T = 2 K, using Model 1. The arrows show the results for the zero and infinite stress

limits. The dashed lines are the energy splittings between upper and lower bands for electrons (E^e_{spl}) and for holes (E^h_{spl}). The experimental values for ΔE are from Refs. 2.50 (□, zero stress), 2.19 (○) and 2.20, 2.21 and 2.81 (△).

Fig. 2.17. The ratio of the total Fermi energy to the luminescence linewidth as a function of stress for Ge (⟨111⟩ stress) and Si (⟨100⟩ stress) at T = 2K for Models 1 and 2.

Fig. 2.18. Equilibrium density n and luminescence linewidth ΔE vs. $1/\sigma$ for Ge at 2K, for Models 1 and 2. The data points for n are replotted from Fig. 2.14.

Fig. 2.19. Equilibrium density n and luminescence linewidth ΔE vs $1/\sigma$ for Si at 2 K, for Models 1 and 2. The data points for ΔE are plotted from Fig. 2.16.

Fig. 2.20. Isothermal compressibility K_T of the EHL ground state as a function of ⟨111⟩ uniaxial stress in Ge, for Models 1 and 2.

Fig. 2.21. Isothermal compressibility K_T of the EHL ground state as a function of ⟨100⟩ uniaxial stress in Si, for Models 1 and 2.

Fig. 2.22. (a) δ_n, (b) δ_μ, (c) δ_E vs. stress for the EHL in Ge stressed along ⟨111⟩. Models 1 and 2 are shown.

Fig. 2.23. (a) δ_n, (b) δ_μ, (c) δ_E vs. stress for the EHL in Si stressed along ⟨100⟩. Models 1 and 2 are shown.

Fig. 2.24. Critical temperature T_c vs. ⟨111⟩ stress for the electron-hole liquid in Ge, for Models 1 and 2.

Fig. 2.25. Critical density n_c vs. ⟨111⟩ stress for the electron-hole liquid in Ge, for Models 1 and 2.

Fig. 2.26. Critical temperature T_c vs. ⟨100⟩ stress for the electron-hole liquid in Si, for Models 1 and 2.

Fig. 2.27. Critical density n_c vs. ⟨100⟩ stress for the electron-hole liquid in Si, for Models 1 and 2.

CHAPTER 3 FIGURE CAPTIONS

Fig. 3.1. Diagram of sample head, showing arrangement for stressing a Ge sample and for viewing the sample from three different mutually perpendicular directions. The diagram is to the scale shown.

Fig. 3.2. Apparatus for applying stress via a calibrated steel spring. This apparatus was outside the helium cryostat and allowed changing the stress while the sample and holder were immersed in liquid helium.

Fig. 3.3. Schematic plan view of the experimental apparatus. The deflection mirror can be automatically scanned about two axes, vertical and horizontal, thus translating the image of the crystal in the image plane of the spectrometer.

Fig. 3.4. Circuit for Si photodiode and amplifier used with mechanical chopper.

Fig. 3.5. Method for mounting Ge detector in cold-finger Dewar. The temperature of the detector is higher than that of the cold finger, due to the low thermal conductivity of the standoffs.

Fig. 3.6. Detector response versus wavelength for several detector temperatures. The peak wavelengths for free exciton (FE) and electron-hole droplet (EHD) luminescence from unstressed Ge are indicated by arrows. The actual detector temperature was estimated to be ~20 K higher than the thermocouple readings given here (see text).

Fig. 3.7. Reverse bias and amplifier circuits for the Ge detector. The amplifier response time is given by $R_F C_F$, chosen here to be 10 μsec.

Fig. 3.8. Definition of the coordinate system used in this thesis. In a z-scan, either the face view or the side view is scanned vertically across a slit or box (crossed slits) aperture. In a y-scan, either the face view or the end view is scanned horizontally past the aperture. In an x-scan, the end view is scanned vertically or the side view is scanned horizontally. The zero points for the x, y, and z coordinates are as shown. The face view is obtained directly, while the end and side views are obtained using the 45° mirrors shown in Fig. 3.1.

CHAPTER 4 FIGURE CAPTIONS

Fig. 4.1. Luminescence spectrum of a γ-drop in sample CR38 of Ge at T = 1.8 K, P_{abs} = 11 mW and applied force F = 9 kgf, along ⟨111⟩, showing the three phonon-assisted lines. The absolute intensities have not been corrected to account for a wavelength-dependent detector sensitivity. Monochromator resolution (FWHM) is 0.66 meV. The shift of about -2.5 meV from the α-drop spectrum corresponds to a stress $\sigma \approx -6.4$ kgf/mm^2, estimated as in Fig. 4.5. (Compressional stresses are taken to be negative.)

Fig. 4.2. Luminescence spectra from a stressed Ge sample at 4.2K, showing both the EHL and FE lines (LA phonon-assisted). The stress was approximately -5.5 kgf/mm^2 along ⟨111⟩. A sharp excitation threshold in the liquid luminescence is observed. Sample CR38.

Fig. 4.3. Dependence of the EHL and FE peak intensities on excitation level, at 4.2 K. A sharp threshold at $P_{abs} \approx 0.15$ mW in the EHL luminescence is observed, characteristic of the gas-liquid phase transition. The pumping efficiency is different from that in Fig. 4.2 due to a translation of the excitation point. Sample CR38.

Fig. 4.4. Spatial luminescence profiles at 4.2 K, showing that the gas and liquid are both in the strain well in the sample. The laser is incident on the face at x = 0. Spatial resolution ≈80 μm. (a) FE gas phase, near threshold. The open circles are Eq. (4.2) with α = 11 meV/mm^2. (b) Liquid phase, at a somewhat higher excitation level. Sample CR38.

Fig. 4.5. (a) Luminescence peak energy vs. applied force F in kilograms force (kgf), for a sample stressed along ⟨111⟩. The determination of the σ-scale is discussed in the text. The γ-drop is formed above a threshold force $F_c \approx 3$ kgf. (b) EHL linewidth ΔE vs. applied force. The linewidth is the full width at half maximum of the luminescence spectrum. (c) EHL lifetime τ vs. applied force, taken from the tail of the decay curve, as described in Section 43. (d) Total luminescence intensity vs applied force. $P_{abs} = 3.2$ mW, T = 1.8 K. Sample CR38.

Fig. 4.6. (a) EHL luminescence peak energy, (b) linewidth ΔE, and (c) decay time τ vs. applied force F for a sample stressed along ⟨110⟩. Because the force was applied with a metal rod, the stress was not linearly proportional to the applied force (see text). The solid curve in (a) corresponds to $F^{1/3}$. $P_{abs} = 25$ mW, T = 1.8 K. Sample CR 16.

Fig. 4.7. EHL luminescence spectra from samples with approximately equal applied stresses (permanent stress geometry) and for unstressed Ge. (a) Force ∥ ⟨111⟩, (b) force ∥ ⟨110⟩, (c) force ∥ ⟨100⟩, and (d) unstressed Ge.

Fig. 4.8. Comparison of the FWHM linewidths ΔE for the α- and γ-drop LA-assisted lines as a function of excitation level. At low powers both ΔE are constant, as expected for a constant-density liquid phase. At $P_{abs} \gtrsim 5$ mW, corresponding to $R_\gamma \gtrsim 200$ μm, the γ-drop linewidth becomes noticeably broadened by the strain gradient and by compression of the liquid, as explained in the text. T = 1.8 K. Sample CR38.

Fig. 4.9. (a) EHL luminescence spectrum from a slit centered on a large drop, with R ≈ 350 μm at $P_{abs} = 58$ mW; (b) spectrum from a region near the surface of the same drop; (c) spectrum from a smaller drop with R ≈ 150 μm, at $P_{abs} = 1.4$ mW. The effective slit resolution on the sample is 80 μm. T = 1.8 K. Sample CR38.

Fig. 4.10. Experimental luminescence spectrum from a sample stressed in the ⟨111⟩ direction. The stress is $\sigma \approx -6.8$ kgf/mm^2 from the shift of the peak energy. $P_{abs} \approx 0.17$ mW, T = 2.0 K. Sample CR36. The open circles are the theoretical lineshape using Eqs. (2.38) and (2.39), with $\sigma = -6.8$ kgf/mm^2, $n = 0.50 \times 10^{17}$ cm^{-3}, T = 2.0 K.

Fig. 4.11. (a) EHL luminescence intensity as a function of time after the light source is switched off, for a sample stressed along ⟨111⟩ (F = 9 kgf), for $P_{abs} = 1.1$ mW. (b) Same as (a), with $P_{abs} = 119$ mW. (c) α-drop luminescence intensity vs. time for the same sample after the stress was removed, for $P_{abs} = 19$ mW. T = 1.8 K. Sample CR38.

Fig. 4.12. Initial luminescence decay time τ_i as a function of absorbed power P_{abs} for the same sample and strain configuration as in Figs. 4.11a and 4.11b.

Fig. 4.13. Luminescence intensity vs. temperature. (a) γ-drop in a ⟨111⟩ stressed sample, $P_{abs} = 1.2$ mW. (b) α-drops in the same sample after the stress was removed, $P_{abs} = 24$ mW. (c) Same as (b), except $P_{abs} = 2.2$ mW. Sample CR38. Directly above the λ-point of liquid helium, 2.17 K, the luminescence

intensity is reduced, apparently due to light scattering by helium bubbles.

Fig. 4.14. Initial luminescence decay time τ_i as a function of absorbed power P_{abs} for the same sample as in Fig. 4.12, with T = 4.2 K.

Fig. 4.15. Luminescence images from a sample stressed in the ⟨111⟩ direction, for a series of excitation levels. The image is viewed through a (110) face and displayed using an infrared vidicon and standard TV monitor. T = 1.8 K. Sample CR50.

Fig. 4.16. Luminescence profiles (slit scans) at two different excitation levels for a sample stressed along ⟨111⟩. The small peaks, e.g., at y ≈ ±1.9 mm, are due to scattered light from the edges of the crystal. The upper row of scans is for P_{abs} = 55 mW; the lower row is for P_{abs} = 0.26 mW. T = 1.8 K. Sample CR38.

Fig. 4.17. γ-drop radii vs. absorbed power P_{abs} for a ⟨111⟩-stressed sample. Sample CR38. The effective spatial resolution was 80 μm, which equals the slit width divided by the image magnification. The solid line has a slope of 1/3.

Fig. 4.18. Integrated luminescence intensity vs. absorbed power for the same sample as in Figs. 4.16 and 4.17 (●), and for the same sample after the stress was removed (o). The solid line has a slope of 1. The relative intensities of the two sets of data cannot be directly compared due to a change in detector sensitivity between the two runs.

Fig. 4.19. Results of a two-dimensional calculation of (a) the EHL energy shift and (b) the "acceleration potential" E^* for a crystal inhomogeneously stressd along the ⟨111⟩ direction. The force on an EHD is normal to the curves in (a), while the droplet acceleration is normal to the curves in (b), due to the carrier mass anisotropy in Ge.

Fig. 4.20. Luminescence slit scans showing motion of the EHD tail observed in Fig. 4.15 at the highest excitation level. The image is obtained from a region centered approximately 2.8 mm below the top of the crystal, for three different laser pumping positions shown in the inset.

Fig. 4.21. Luminescence profiles for a sample before and after the stress is removed. The upper row of scans is for a γ-drop in the stressed sample, while the lower row of scans is for a cloud of α-drops after the stress is removed. P_{abs} = 2.8 mW, T = 1.8 K. Sample CR38.

Fig. 4.22. Luminescence profiles for an unstressed sample. The upper row of scans is for P_{abs} = 47 mW, the middle row is for P_{abs} = 5.1 mW, and the lower row is for P_{abs} = 0.45 mW. T = 1.8K. Sample CR38.

Fig. 4.23. Luminescence x-scan for an unstressed sample at moderate excitation, P_{abs} = 11 mW, showing the peak of the cloud to be separated from the face at x = 0, where the laser is incident on the crystal. Resolution is ≈50 μm. T = 1.8 K. Sample CR38.

Fig. 4.24. Luminescence x-scans for an unstressed sample at 3 moderate to high excitation levels. The laser is incident on the crystal face at x = 0. The extra small peak at x ≈ 2 mm is due to light scattered from the edge of the end-view mirror (see Fig. 3.1). T = 1.8 K. Sample CR38.

Fig. 4.25. Radius of the α-cloud in unstressed Ge vs. absorbed laser power P_{abs}. The solid line has a slope of 1/3. T = 1.3K. Sample CR38.

Fig. 4.26. Luminescence profiles for t = 0 and 1000 μsec for a sample stressed along ⟨111⟩. P_{abs} = 100 mW, T = 1.8K. Sample CR38.

Fig. 4.27. Luminescence profiles for t = 0 and 100 μsec for an unstressed sample. P_{abs} = 11 mW, T = 1.8K. Sample CR38. Due to decreased spatial resolution (~330 μm) the edge effects at x = 1.8 mm are particularly broad.

Fig. 4.28. Radii obtained from luminescence profiles. (a) γ-drop radii, for the same sample and conditions as in Fig. 4.26. (b) α-cloud radii, for the same conditions as in Fig. 4.27. The solid line assumes exponential decay at 1/3 of the total luminescence decay rate, Fig. 4.11c.

Fig. 4.29. Radius as a function of time for a sample stressed along ⟨110⟩, in the "permanent stress" geometry of Ref. 4.1. (This stress direction would usually result in two strain wells. However, in this experiment the stress plunger was applied close to one edge of the sample, so that only a single minimum actually occurred inside the crystal.) ● , o from luminescence profiles, for P_{abs} = 96 mW. ▩ from Alfvén

resonances, in a pulsed excitation experiment with 0.75 μJ/pulse, giving a smaller initial drop size; the radius was obtained from the resonant field as in Refs. 4.38 and 4.81, using n = 0.5 x 10^{17} cm^{-3}. T = 1.8 K. Sample CR14.

Fig. 4.30. (a) Drawing of the crystal mounting and orientation. (b) Infrared vidicon images showing face and end views for zero field. (c) Distortion in drop shape when H∥⟨11$\bar{2}$⟩ axis. (d) Distortion in drop shape when H∥⟨1$\bar{1}$0⟩ axis. P_{abs} = 50 mW, T = 1.7 K. Sample CR37.

Fig. 4.31. Field dependence of the drop distortion. The γ-drop radii $R_{\parallel}$ and $R_{\perp}$ are measured parallel and perpendicular to H. These data correspond to the geometry of Fig. 4.30d. P_{abs} ≈ 3 mW, T = 1.7 K. Sample CR38.

Fig. 4.32. (a) Schematic diagram showing recombination currents of electrons (solid arrows) and holes (dashed arrows) in zero magnetic field. (b) Modification of these drift currents caused by the Lorentz forces in an applied magnetic field parallel to the x-axis. A net circulating current results.

Fig. 4.33. Parallel and perpendicular radii as a function of time in a magnetic field H = 20 kOe ∥ ⟨111⟩ ∥ stress. P_{abs} = 90 mW, T = 1.7 K. Sample CR37.

CHAPTER 5. FIGURE CAPTIONS

Fig. 5.1. Total luminescence intensity I_{tot}, peak intensity in a slit scan I_{slit}, and peak intensity in a box scan I_{box} versus absorbed power P_{abs}. The inset shows the schematic arrangement for slit and box scans. The straight lines are drawn in for the same range of excitation levels; the slopes are discussed in the text. Sample CR50, T = 1.9K.

Fig. 5.2. Drop size and volume versus absorbed power. The drop size is given by the full width at half maximum of a slit scan, which is related approximately to the radius via Eq. (3.15). The volume is obtained from the measured radii for three mutually perpendicular directions. The straight lines are drawn as in Fig. 5.1 and are discussed in the text. Sample CR50, T = 1.9K.

Fig. 5.3. Full width at half maximum ΔE of luminescence spectra as a function of excitation level. The curve is a visual aid. Sample CR50, T = 1.9K.

Fig. 5.4. Initial luminescence decay time τ_i as a function of absorbed power P_{abs}. The curve is a visual aid. Sample CR50, T = 1.9K.

Fig. 5.5. Two-dimensional calculations of the ⟨111⟩ component of stress σ_{111}, with parameters chosen to reproduce experimental conditions. (a) Corresponds to face view of sample. (b) Corresponds to side view of sample.

Fig. 5.6. Two-dimensional calculations of the deviation from uniaxial ⟨111⟩ stress $|\sigma_{non\text{-}111}/\sigma_{111}|$. (a) Face view. (b) Side view.

Fig. 5.7. Luminescence spectra from stressed and unstressed Ge samples. The open circles give the theoretical lineshapes for the best fit,

including the spectrometer slit resolution and the change in detector response with wavelength. Unstressed Ge: P_{abs} = 25 mW, $n = 2.20 \pm 0.05 \times 10^{17}$ cm^{-3}. Stressed Ge: (Sample CR50) P_{abs} = 0.8 mW, $n = 0.47 \pm 0.03 \times 10^{17}$ cm^{-3}, $-\sigma_M$ = 5 kgf/mm^2. The shift of the luminescence peak energy ΔE_{peak} and the shift of the spectroscopic energy ΔE_{spec} are indicated. T = 1.9K.

Fig. 5.8. Exciton slit scans obtained at 4.2K and P_{abs} = 1.1 mW, below the threshold for EHL formation. The open circles are Eq. (5.4) with the values of α_{ex} indicated on the figures. (a) x-scan, (b) y-scan, (c) z-scan. Sample CR50.

Fig. 5.9. Free energy per e-h pair and chemical potential versus density calculated for $-\sigma$ = 5 kgf/mm^2 and T = 1.9K. (a) Free energy -- full Model 1 calculation. (b) Free energy -- first order theory. (c) Chemical potential -- full Model 1 calculation. (d) Chemical potential -- first order theory.

Fig. 5.10. Chemical potential versus density for two values of the stress. The curve for $-\sigma$ = 3 kgf/mm^2 has been shifted vertically to coincide with the curve for $-\sigma$ = 5 kgf/mm^2 at approximately the equilibrium density.

Fig. 5.11. Theoretical density profiles for different drop sizes, calculated according to Eq. (5.35) for $-\sigma$ = 5 kgf/mm^2, T = 1.9K, and α_{spec} = 2 meV/mm^2. Note that the position x is normalized to the drop radius R.

Fig. 5.12. Calculated density at the center of the drop versus drop size for the same conditions as in Fig. 5.11. Exact calculation: uses Eq. (5.36). Simple parabola: uses Eq. (5.23) with the same values for $n_0(T)$ and $E_0''(T)$ as in the exact calculation.

Fig. 5.13. Comparison of a theoretical density profile using the exact calculation and a simple parabolic profile. For the simple profile, both n(0) and n(R) were chosen to agree with the exact calculation.

Fig. 5.14. Theoretical slit scan luminescence profiles according to Eq. (5.41). Outer curve: uniform density. Inner curve: uses the density distribution given in Eq. (5.37), with $n(0) = 2.8\ n_o$. The slit width is 0.05 times the drop radius R.

Fig. 5.15. Theoretical box scan luminescence profiles according to Eq. (5.42). Outer curve: uniform density. Inner curve: uses the density distribution given in Eq. (5.37), with $n(0) = 2.8\ n_o$. The slit width is 0.05 times the drop radius R.

Fig. 5.16. Calculation of the peak luminescence intensity in a box scan (I_{box}), the peak luminescence intensity in a slit scan (I_{slit}), and the total luminescence intensity (I_{tot}) as a function of drop size, which is determined by the full width at half maximum of a slit scan (W_s). These quantities are shown for a constant density $n = n_o$ and for the density distributions of Eq. (5.37) with two values for the well parameter α. The slit width was 35 μm.

Fig. 5.17. Total luminescence intensity (I_{tot}) and peak intensity in a slit scan (I_{slit}) for both y-scans and x-scans, shown as a function of drop size (W_s). The drop size is given by the full width at half maximum of a slit scan. The curves are the theory of Section 53.2 with $\alpha_{spec} = 8$ meV/mm^2 and slit resolution 85 μm. Sample CR38, T = 1.8K.

Fig. 5.18. Total luminescence intensity (I_{tot}), peak intensity in a slit scan (I_{slit}), peak intensity in a luminescence wavelength spectrum ($I_{\lambda\text{-scan}}$), and peak intensity in a box scan (I_{box}), shown as a function of drop size (W_s). The drop size is given by the full width at half maximum of a slit scan. The curves are the theory of Section 53.2 with $\alpha_{spec} = 2$ meV/mm^2 and slit resolution 35 μm. Sample CR50, x-scans obtained from the side view, T = 1.9K.

Fig. 5.19. Peak luminescence intensity in a slit scan (I_{slit}) and in a box scan (I_{box}), shown as a function of drop size (W_s). These data are similar to Fig. 5.18 except that they were obtained from y-scans using the face view.

Fig. 5.20. Peak luminescence intensity in a box scan (I_{box}) as a function of drop size. Here the drop size is given by the full width at half maximum of a box scan, W_b. The curve is the theory of Section 53.2 with $\alpha_{spec} = 4$ meV/mm^2 and slit resolution 50 μm. Sample CR38, y-scans from the face view, T = 1.9K.

Fig. 5.21. Luminescence box scan obtained by scanning the luminescence image of the Ge crystal across a small aperture. Sample CR50, $P_{abs} = 400$ mW, T = 1.85K.

Fig. 5.22. Electron-hole pair density profile obtained by performing an Abel transform on the box scan in Fig. 5.21. The solid curve shows the transform of a theoretical box scan, Eq. (5.42), including a finite slit $s \approx 35$ μm. The dashed curve shows a "best fit" for a constant density. The uncompressed density is indicated by the arrow.

Fig. 5.23. Electron-hole pair density profiles obtained as in Fig. 5.22 for a series of excitation levels: P_{abs} = 2.5, 15, and 94 mW. The curves show transforms of theoretical box scans with slit resolution ≈50 μm using the density distribution given in Eq. (5.37). Sample CR38, T = 1.9K.

Fig. 5.24. The effect of choosing the center of the scan incorrectly. The raw data corresponding to the largest drop size in Fig. 5.23 were transformed with y=0 assumed to be displaced by ≈35 μm from its true position (shown by the arrow). The density at the drop center, n(0), should be the same for both the left and right halves of the scan.

Fig. 5.25. Electron-hole pair density profiles obtained for a series of excitation levels: P_{abs} = 0.22, 7.4, and 400 mW. Sample CR50.

Fig. 5.26. Density at the center of the drop n(0) versus drop size W_b for Sample CR38. The curve shows the theoretical result for α_{spec} = 4 meV/mm^2.

Fig. 5.27. Density at the center of the drop n(0) versus drop size W_s for Sample CR50. Two sets of data are shown. The curve shows the theoretical result for α_{spec} = 2 meV/mm^2.

Fig. 5.28. Chemical potential difference $\mu(n) - \mu(n_o)$ versus e-h pair density n, using the results from an entire set of density profiles. The solid curve is the theoretical chemical potential using Model 1. The dashed line is used to obtain the compressibility, as discussed in the text. Sample CR38.

Fig. 5.29. Chemical potential difference $\mu(n) - \mu(n_o)$ versus e-h pair density n, using the results of two complete sets of density

profiles. The solid curve is the theoretical chemical potential using Model 1. The dashed line is used to obtain the compressibility as discussed in the text. Sample CR50.

Fig. 5.30. Initial decay time τ_i for the total luminescence intensity plotted as a function of the FWHM of a slit scan. The dots represent the experimental results; the three curves are calculations discussed in the text. Sample CR50, T = 1.9K.

Fig. 5.31. Total luminescence intensity as a function of magnetic field H for several different delay times after a short excitation pulse. The vertical scale is offset from zero by an arbitrary amount. The symbols at the right indicate 10% of the total zero-field intensity. Sample CR50, $H \| \langle 1\bar{1}0 \rangle$, T = 1.6K.

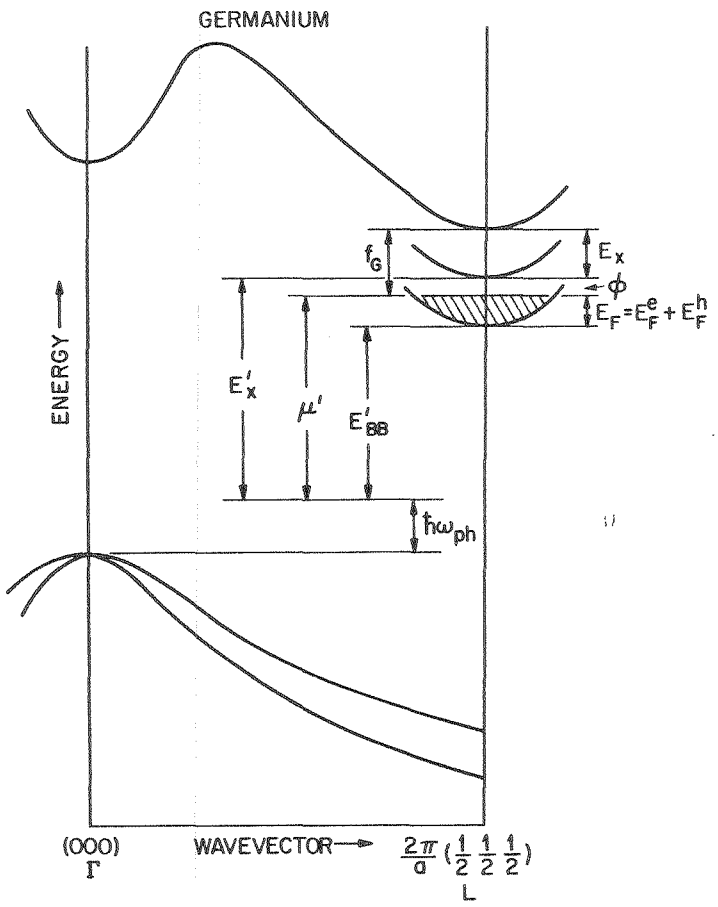

XBL 795-9623

Figure 1.1

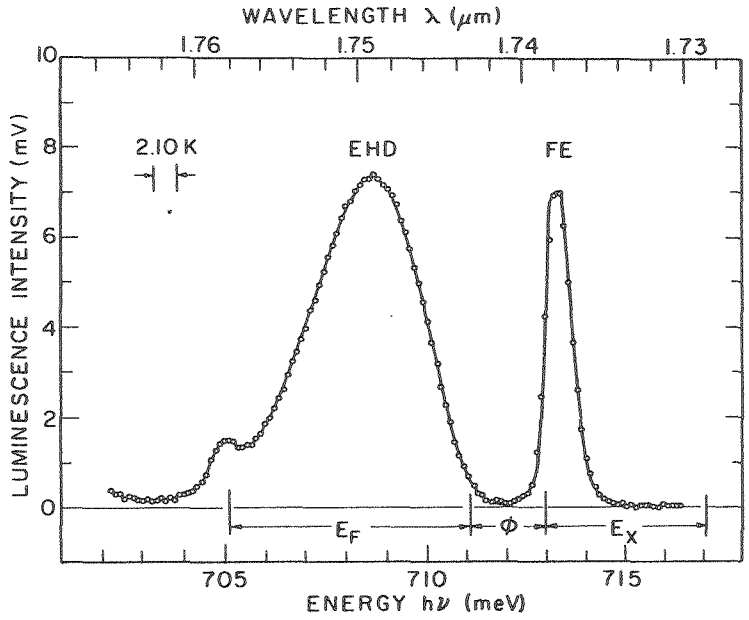

XBL778-5964

Figure 1.2

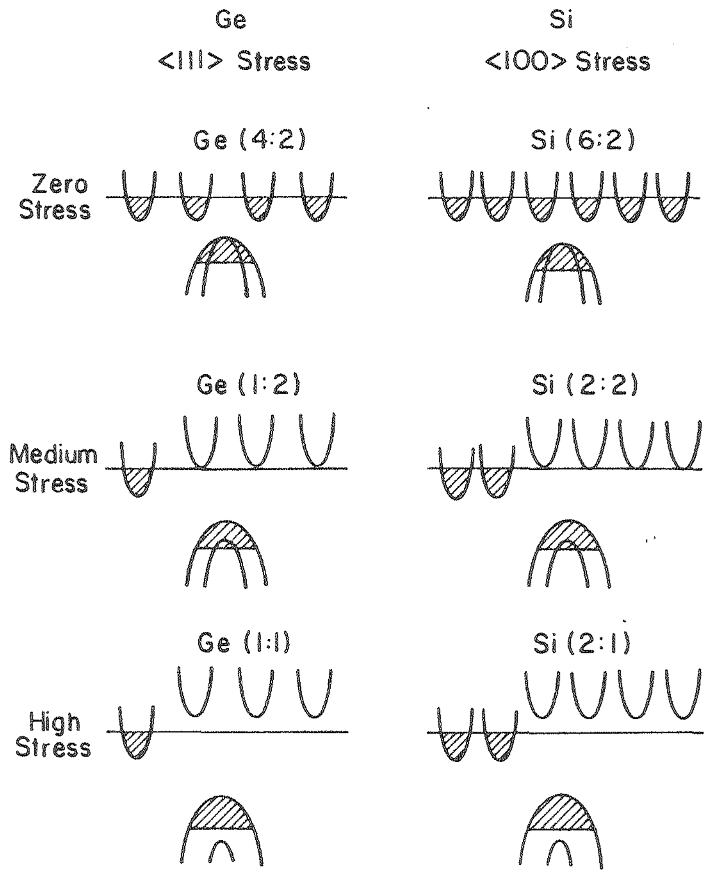

Figure 1.3

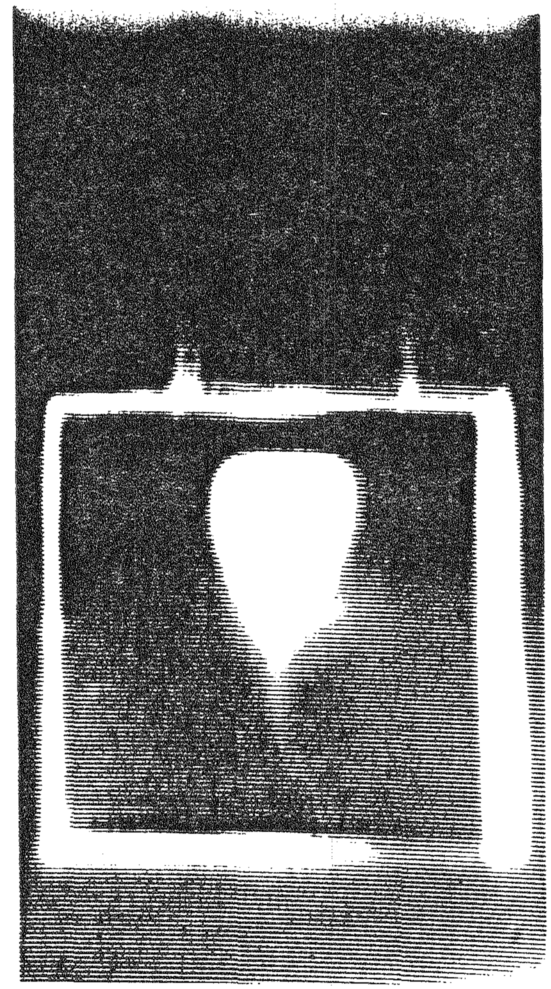

XBB 781-490

Figure 1.4

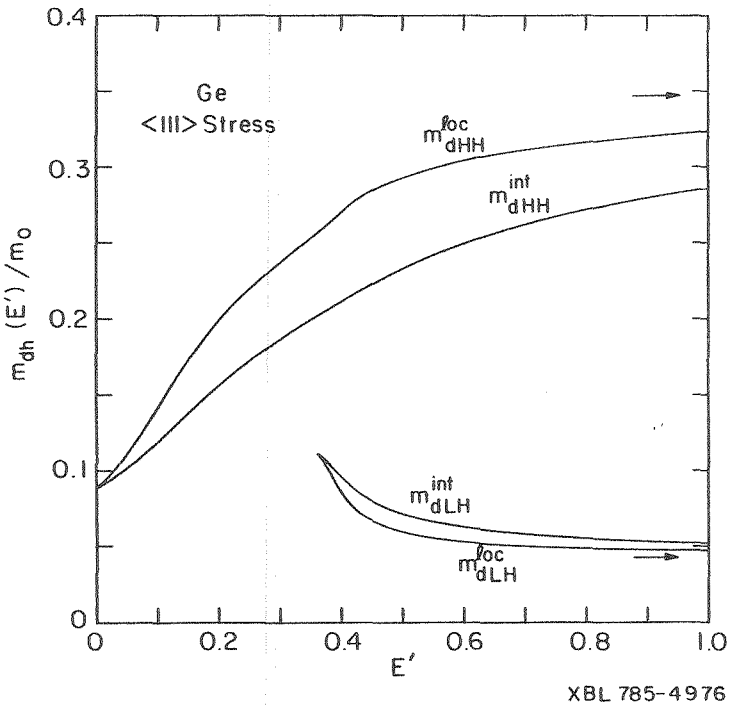

Figure 2.1

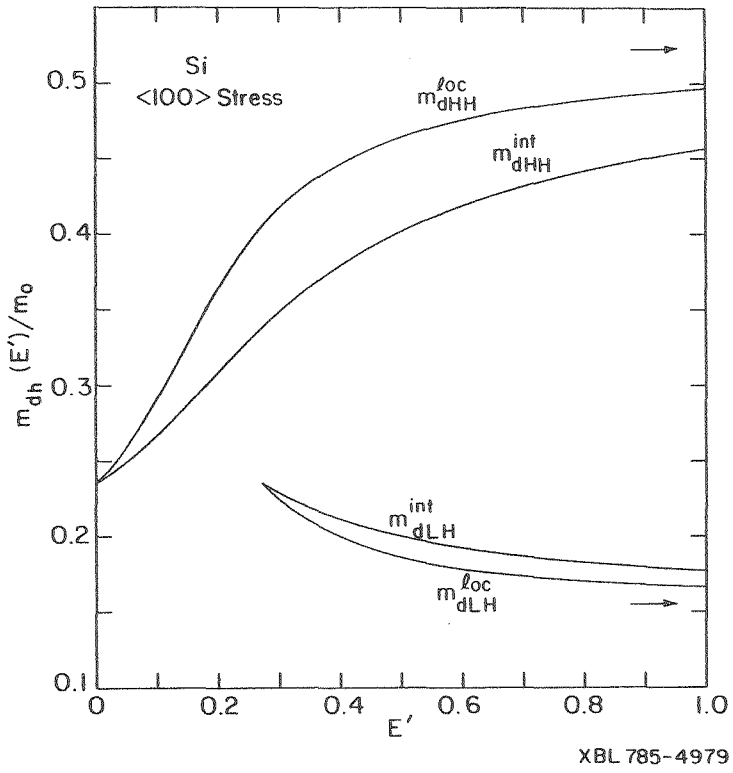

Figure 2.2

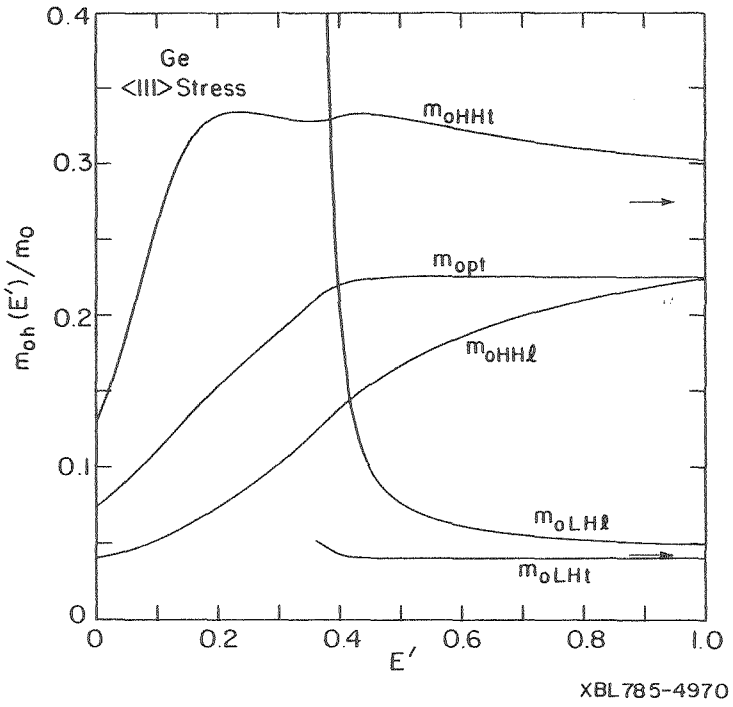

Figure 2.3

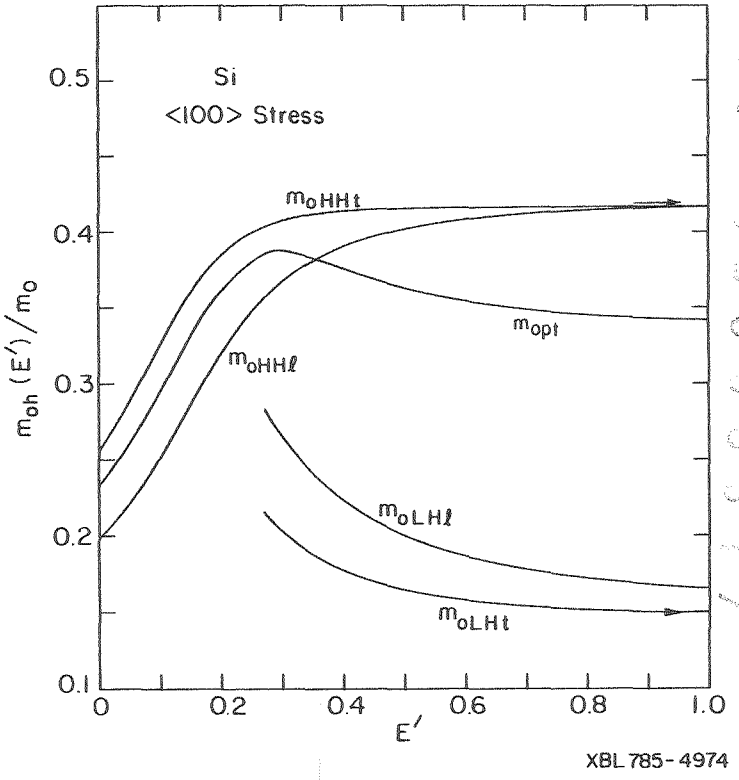

Figure 2.4

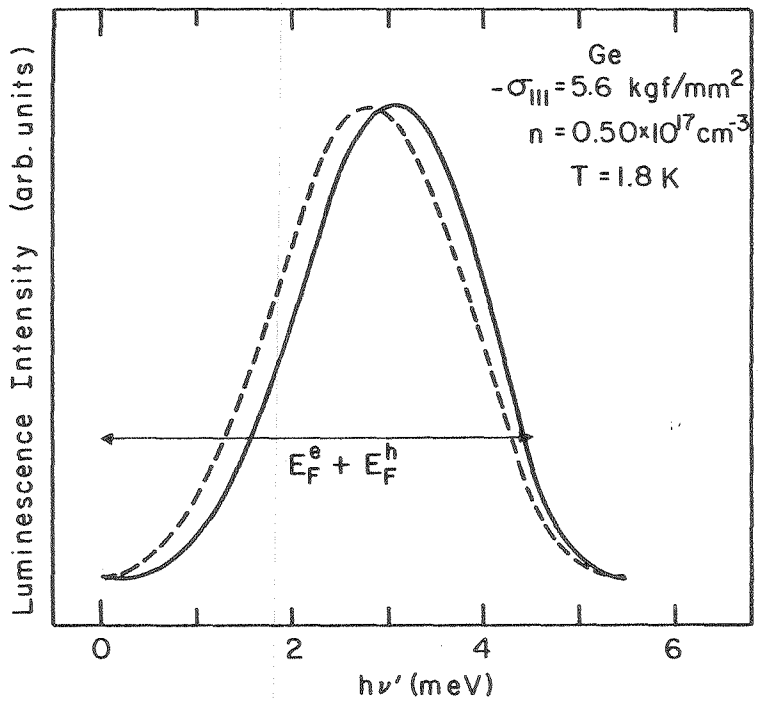

XBL7812-6301

Figure 2.5

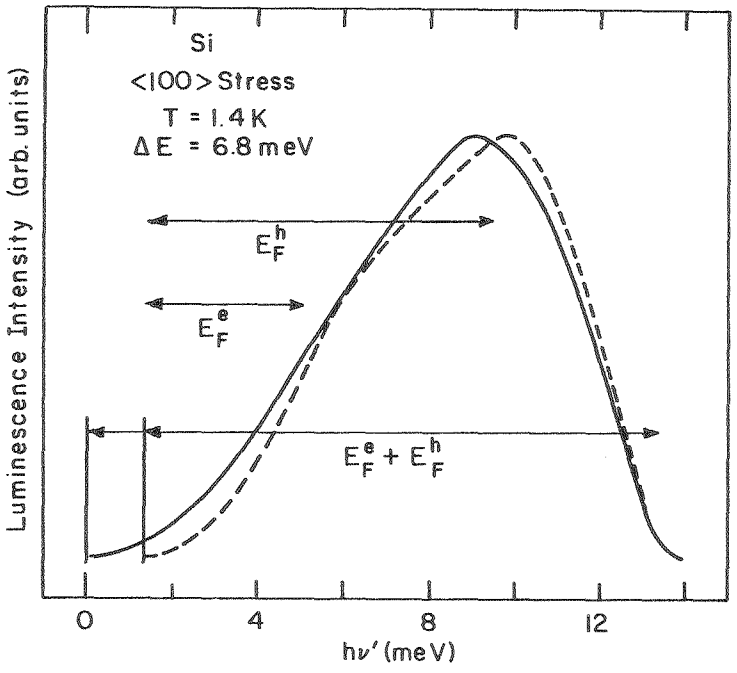

XBL7812-6302

Figure 2.6

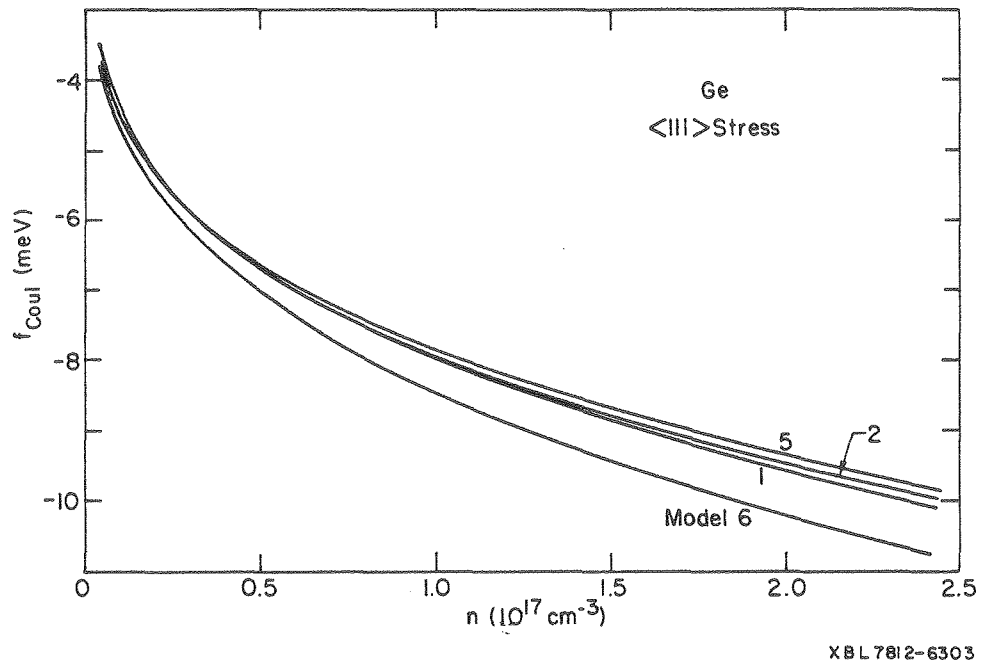

Figure 2.7

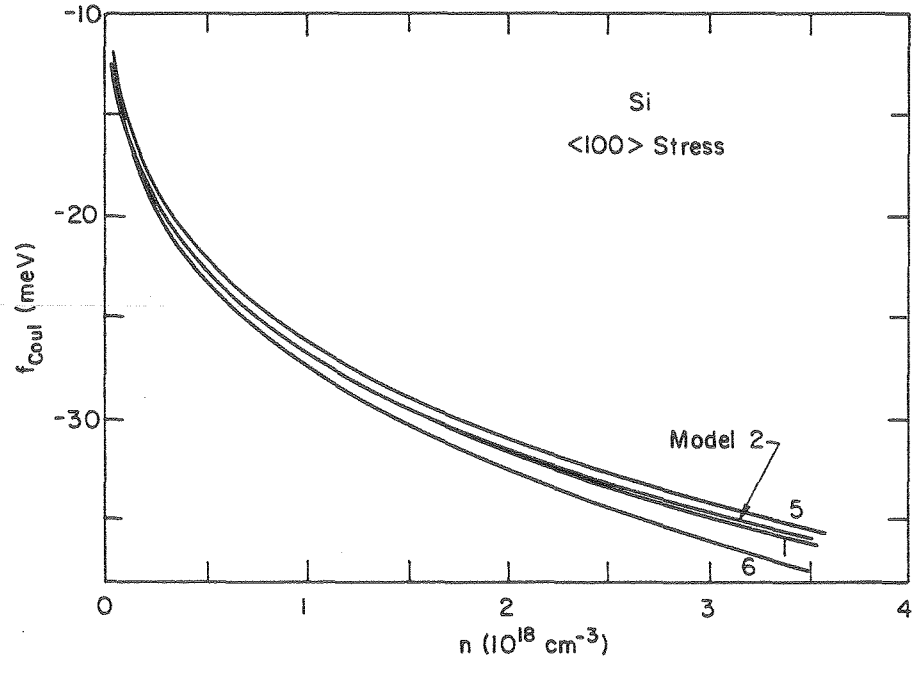

Figure 2.8

81 0 0 0 9 7 0 0

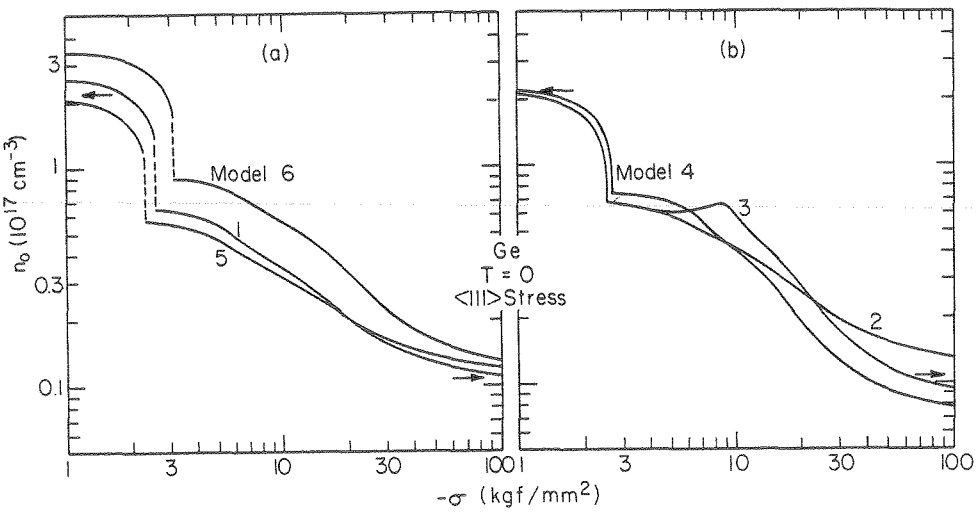

Figure 2.9

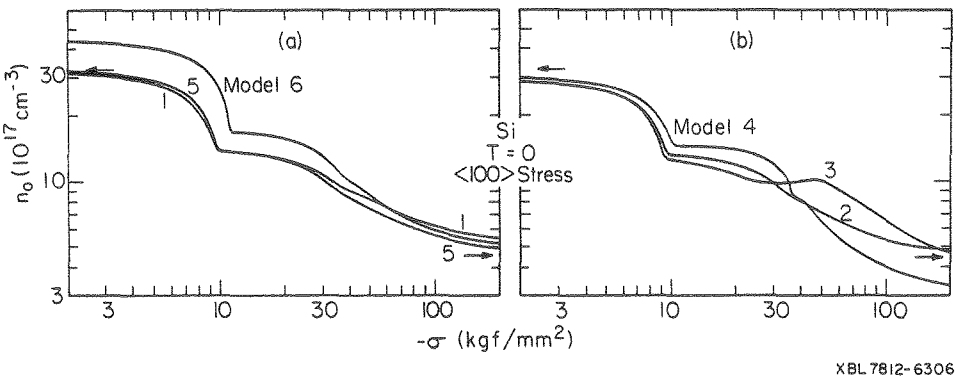

Figure 2.10

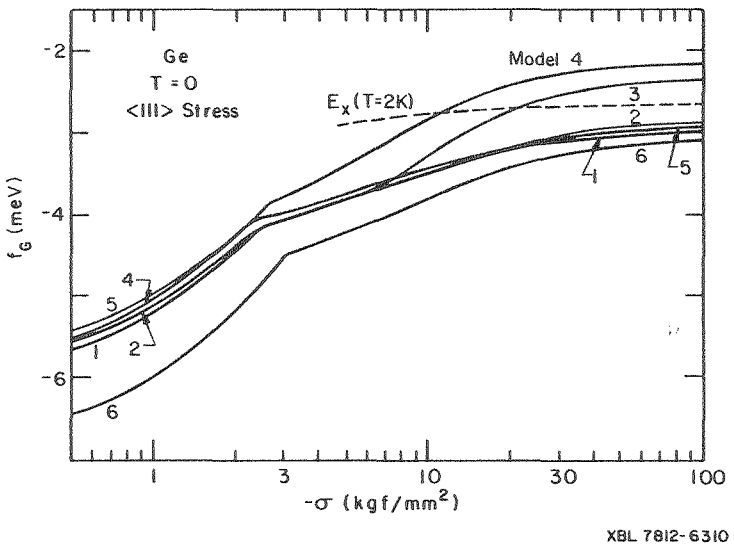

Figure 2.11

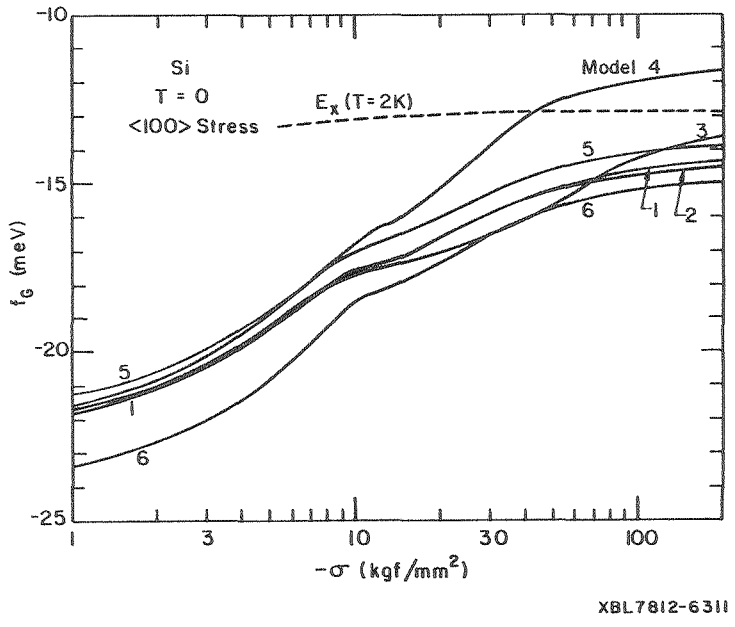

Figure 2.12

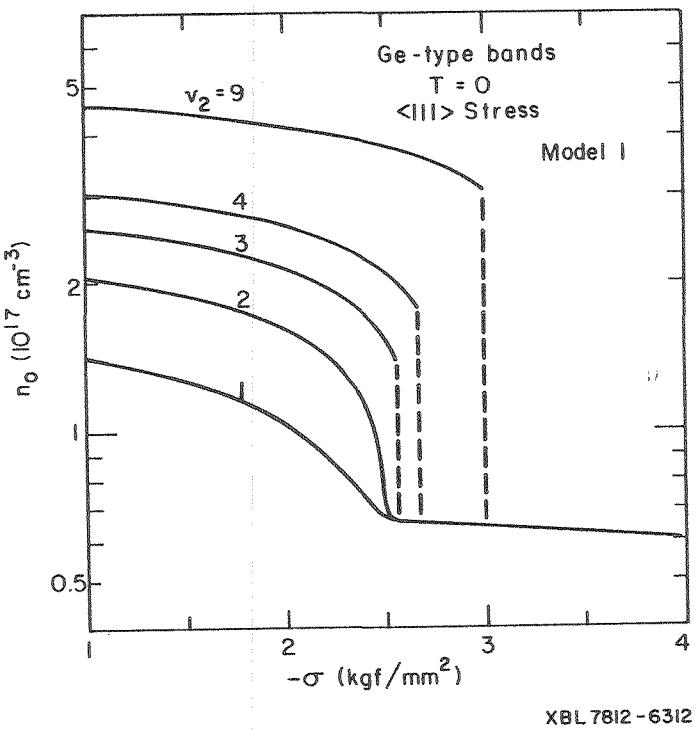

Figure 2.13

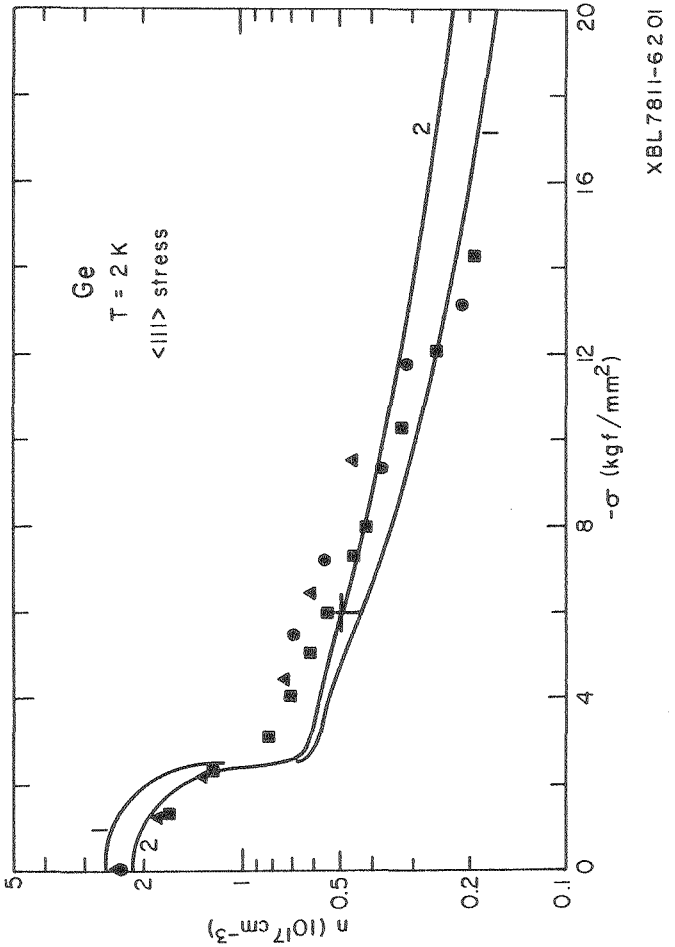

Figure 2.14

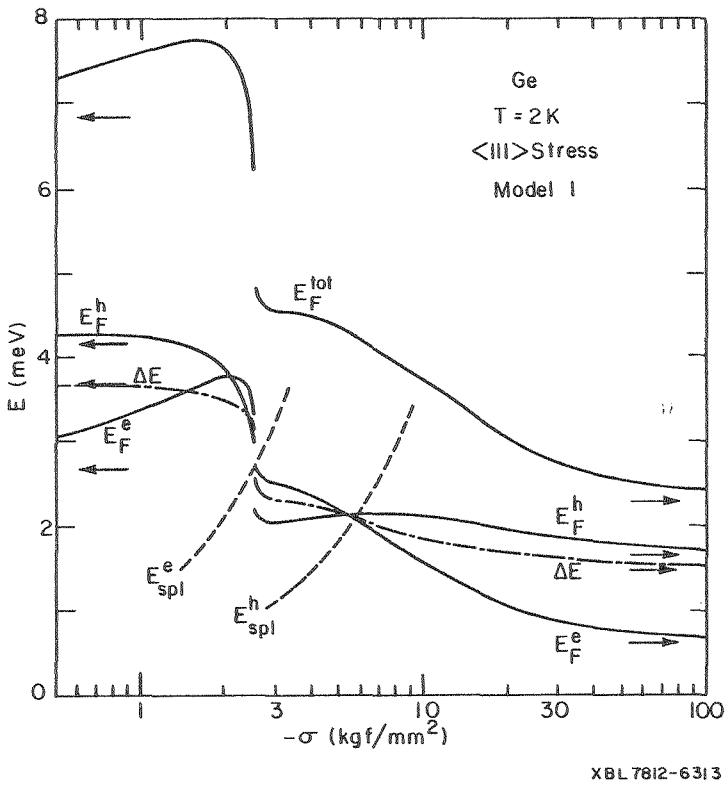

Figure 2.15

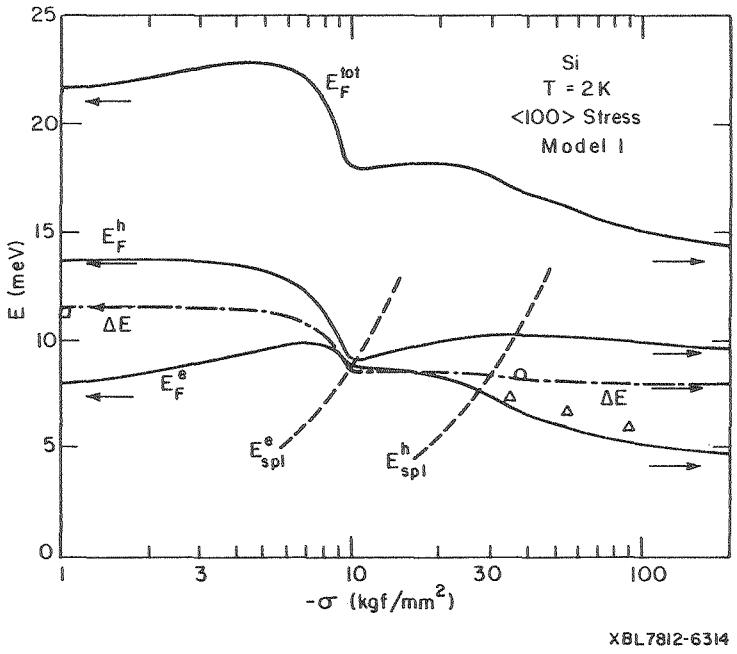

Figure 2.16

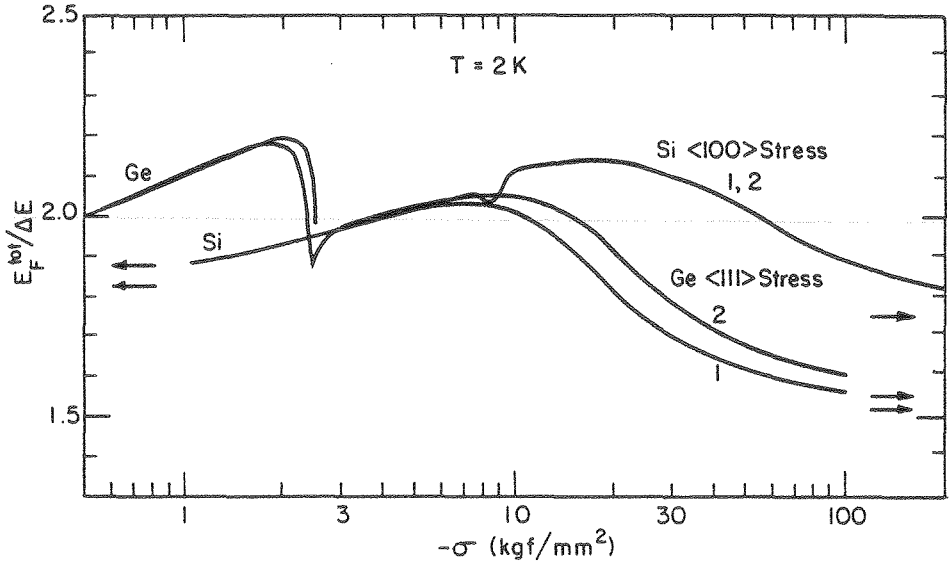

XBL 7812-6315

Figure 2.17

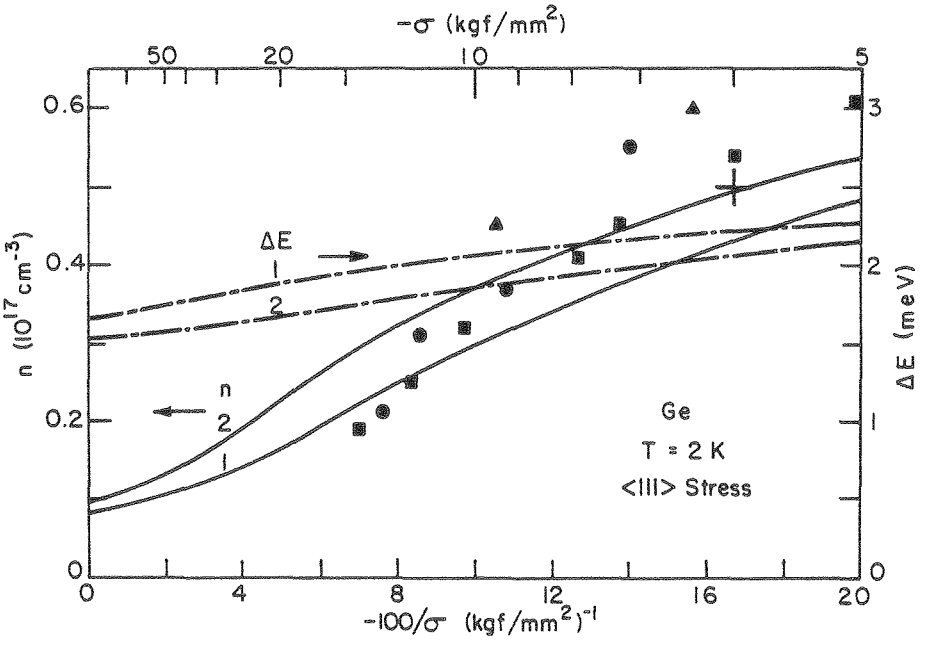

XBL 7812-6316

Figure 2.18

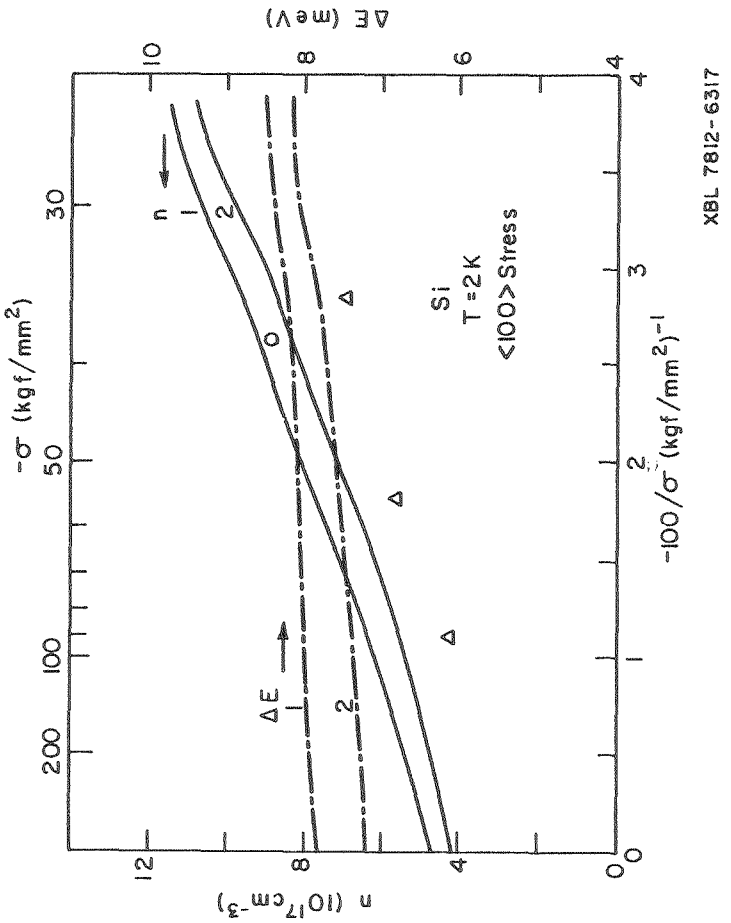

Figure 2.19

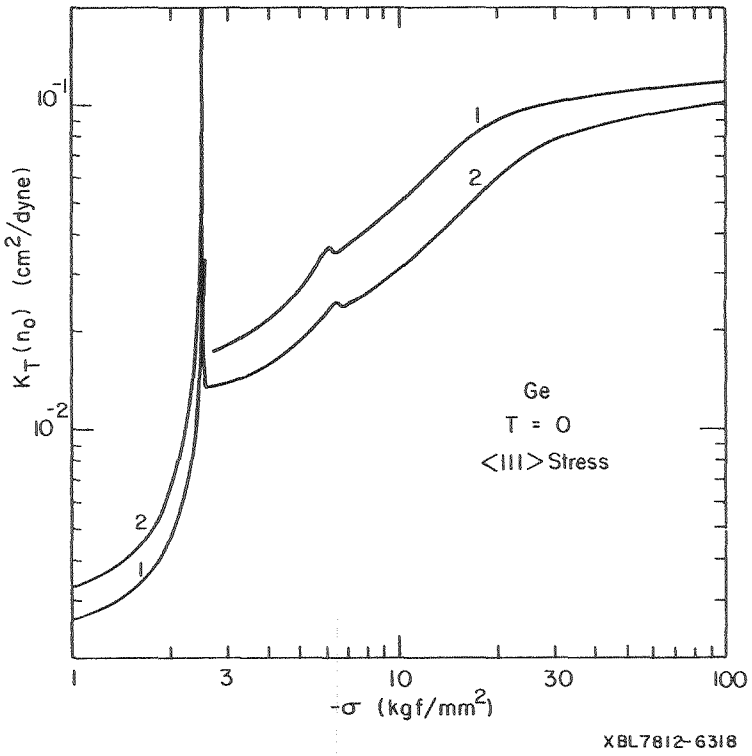

Figure 2.20

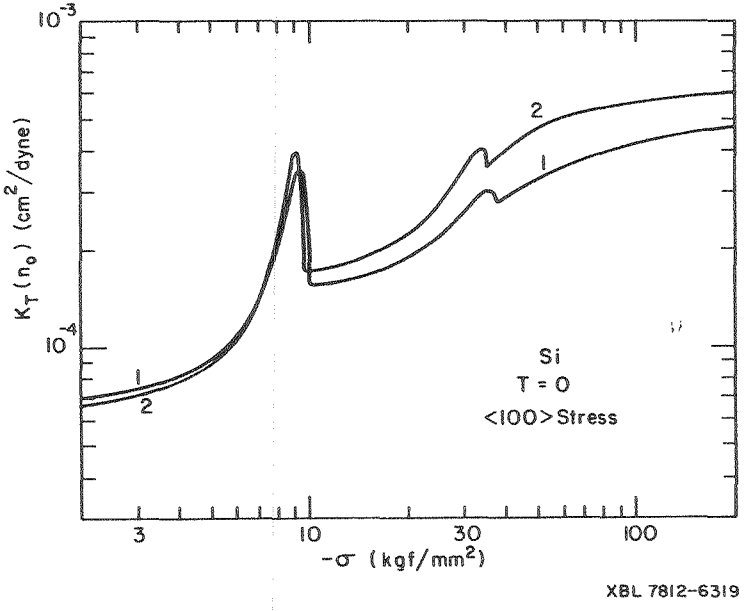

Figure 2.21

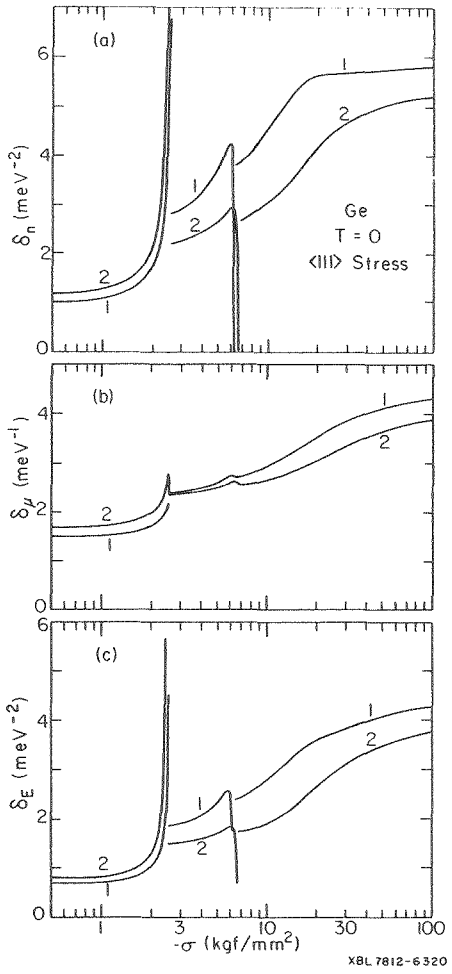

Figure 2.22

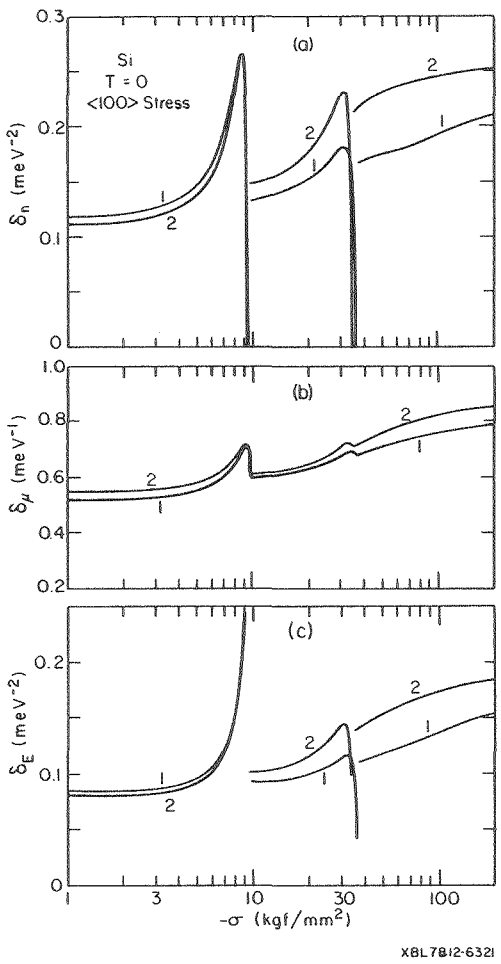

Figure 2.23

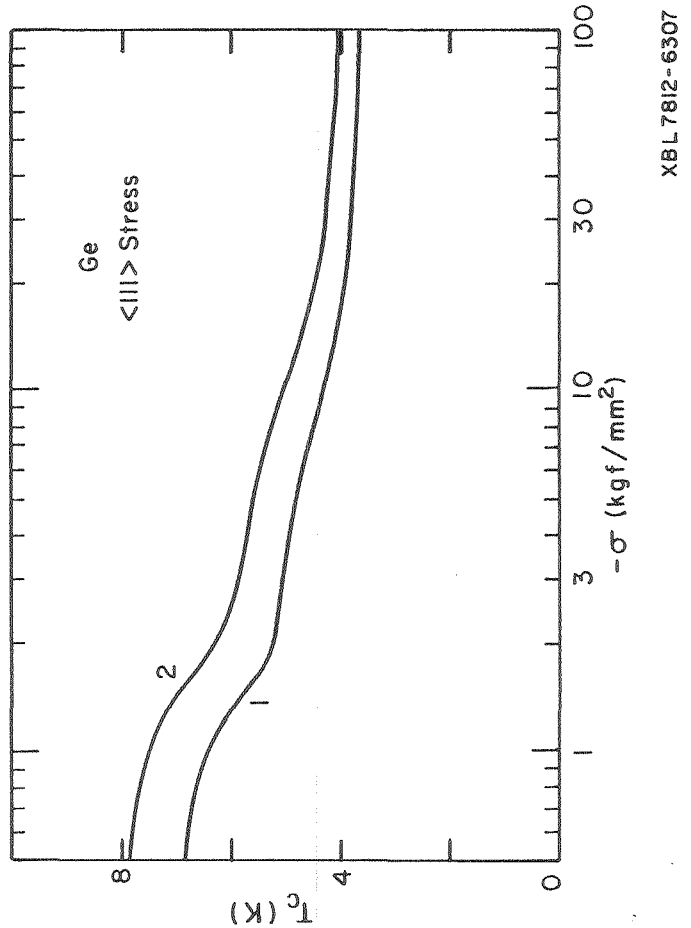

Figure 2.24

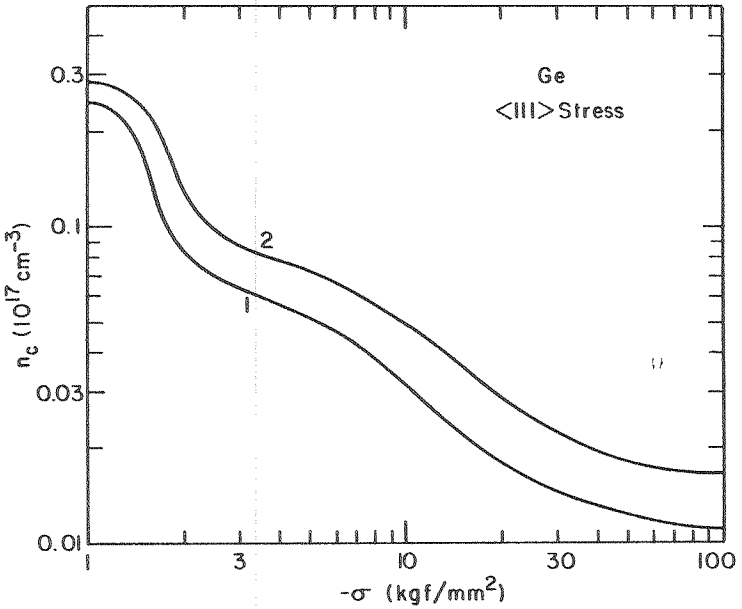

Figure 2.25

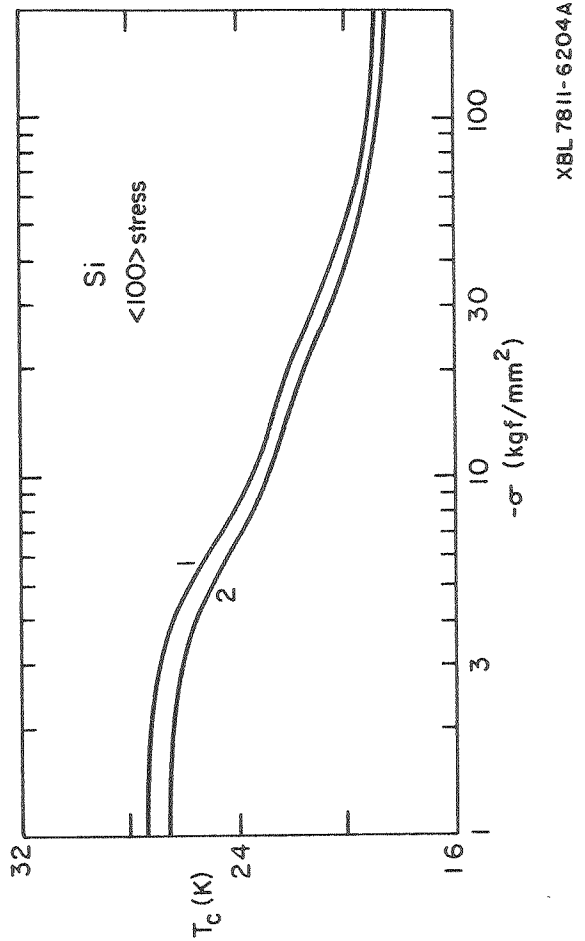

Figure 2.26

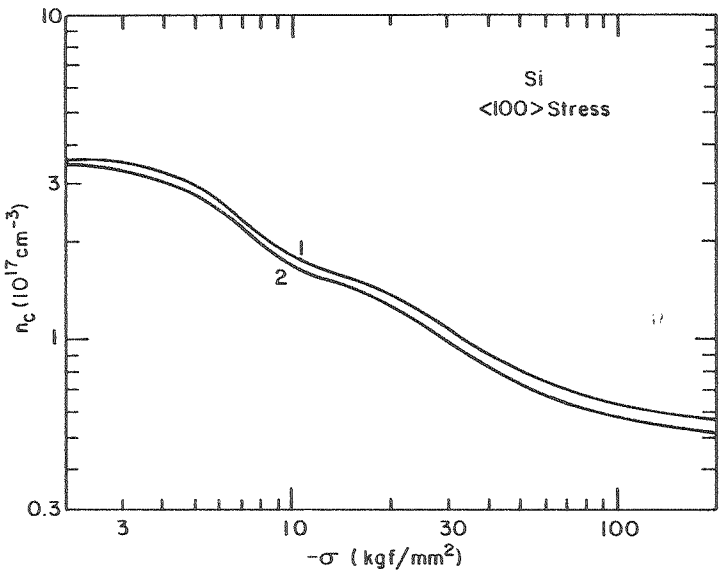

Figure 2.27

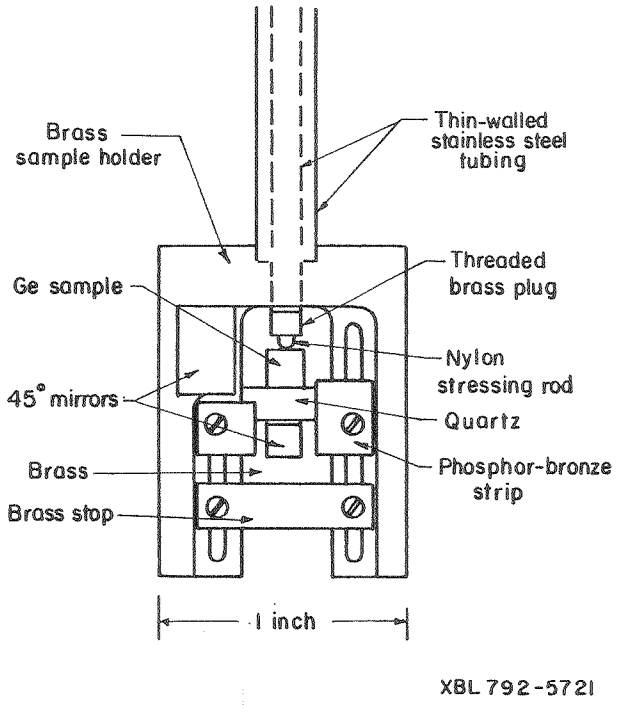

Figure 3.1

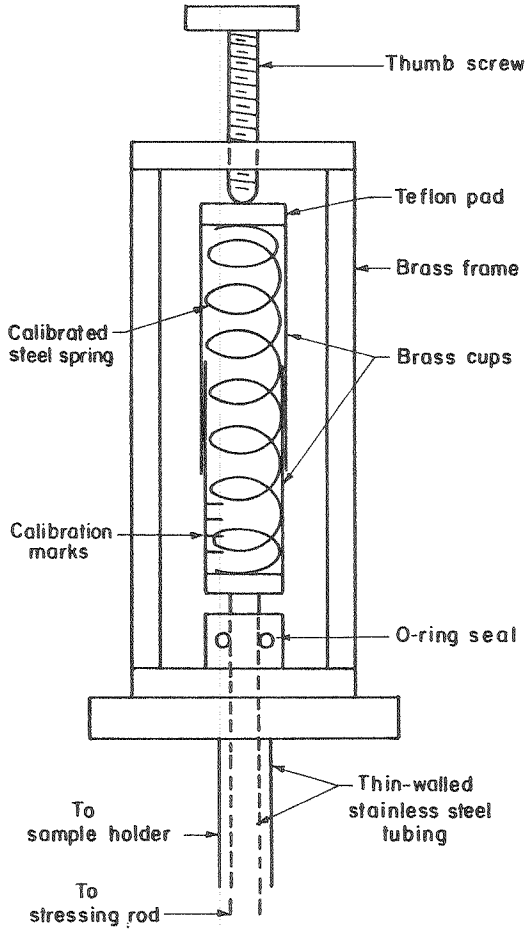

Figure 3.2

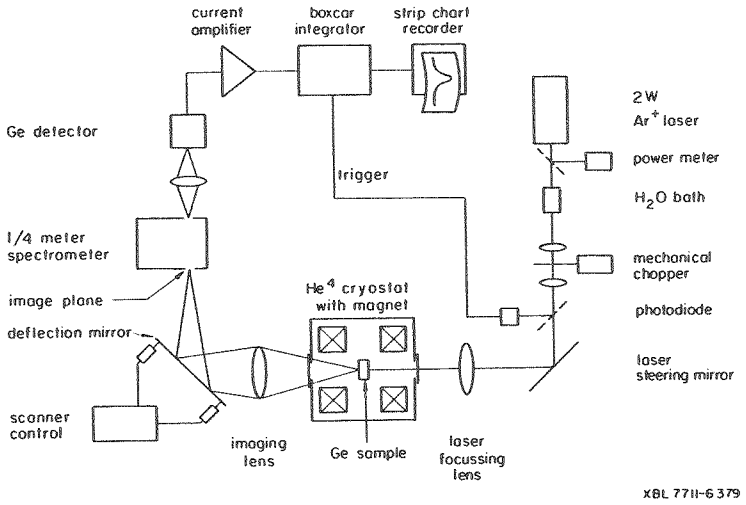

Figure 3.3

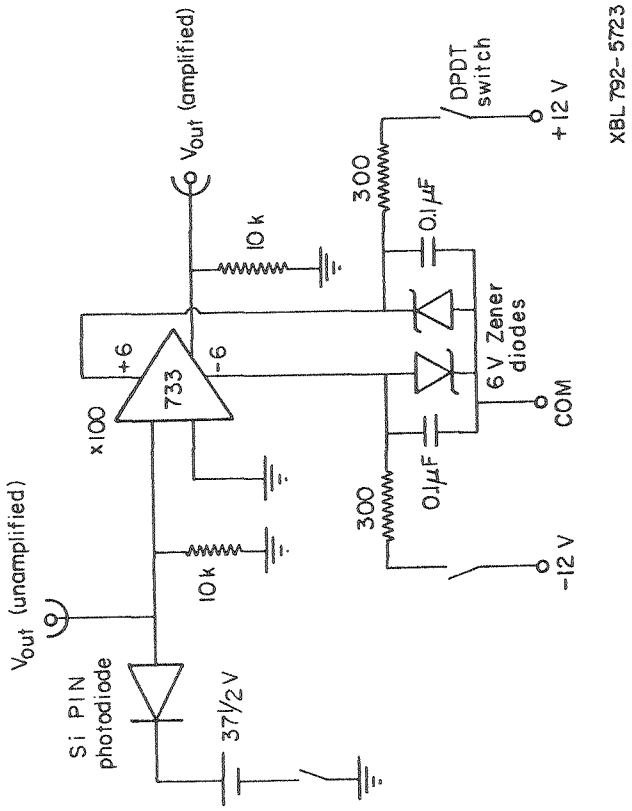

Figure 3.4

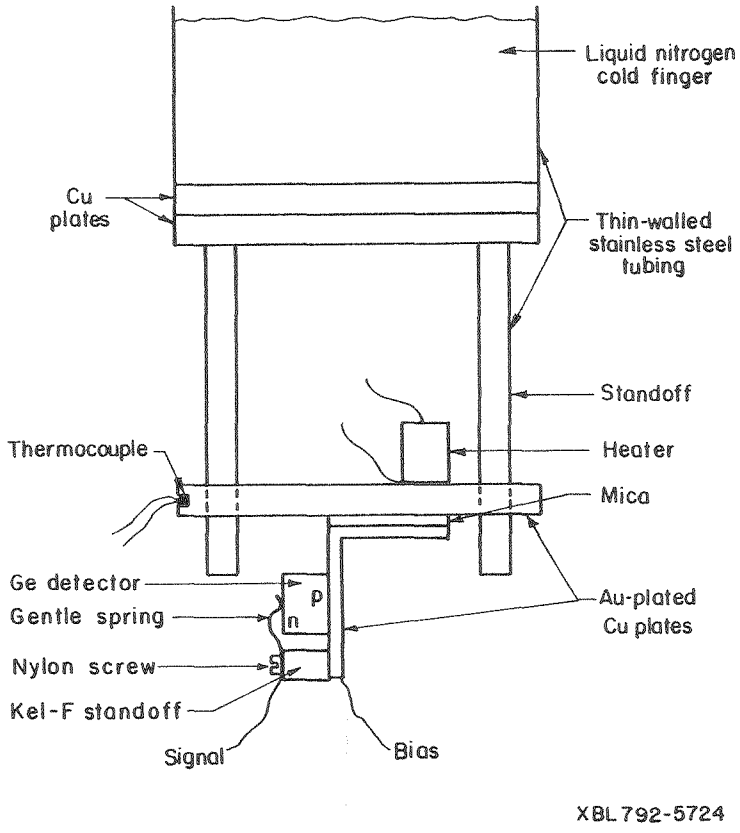

Figure 3.5

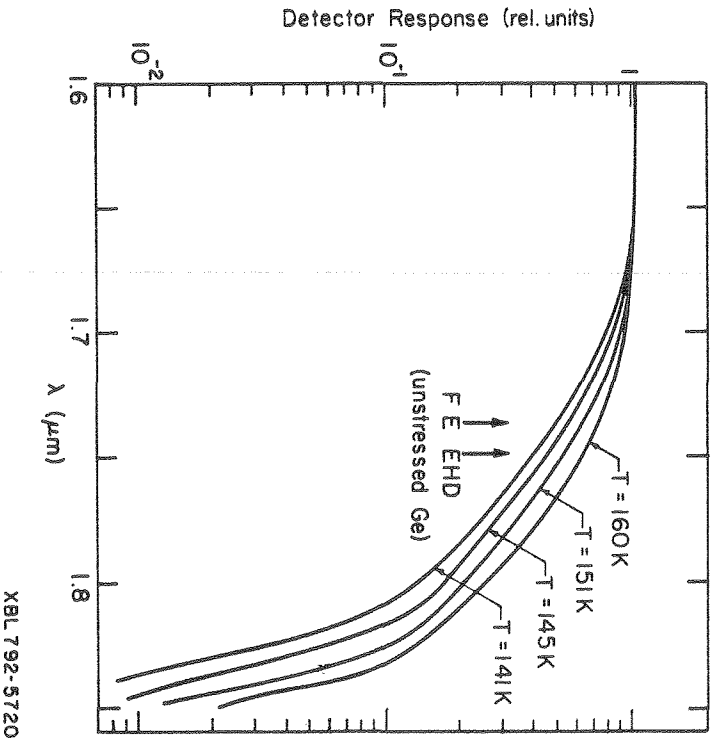

Figure 3.6

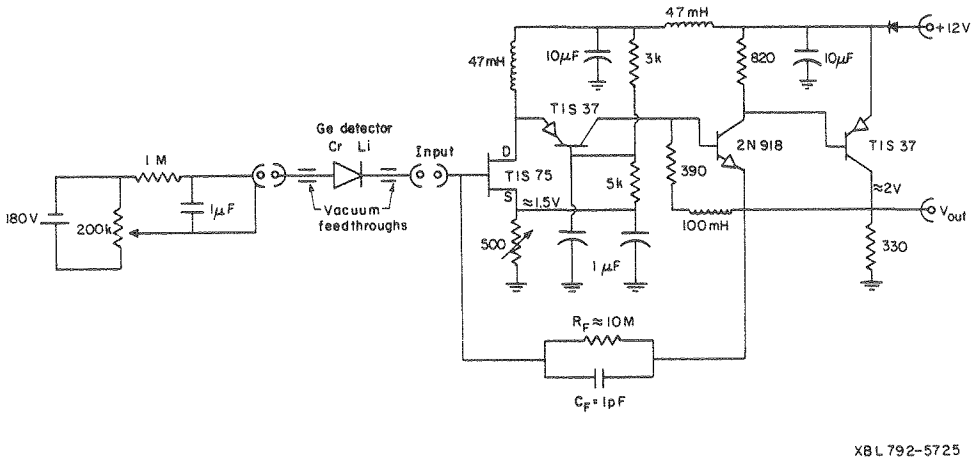

Figure 3.7

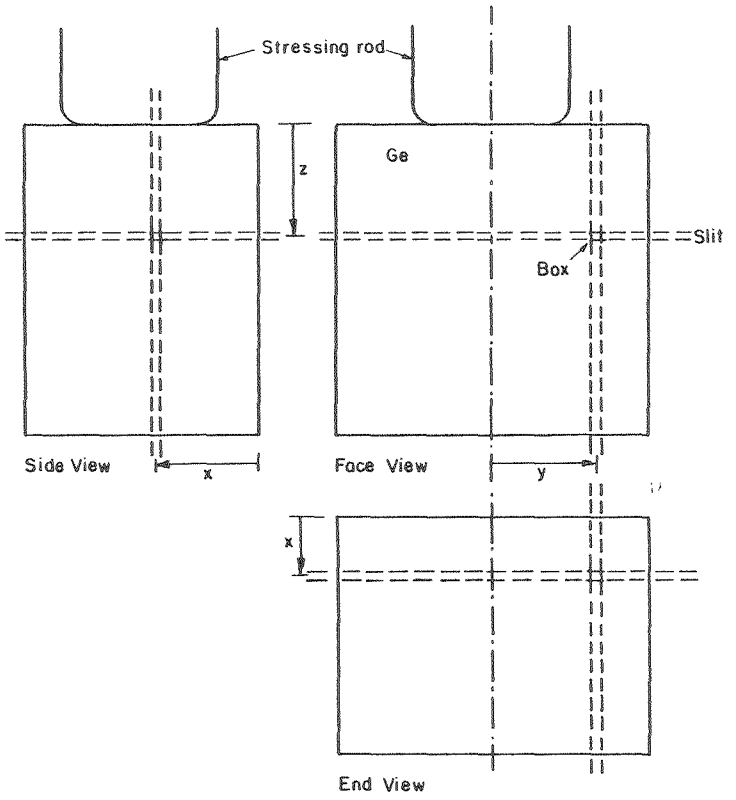

Figure 3.8

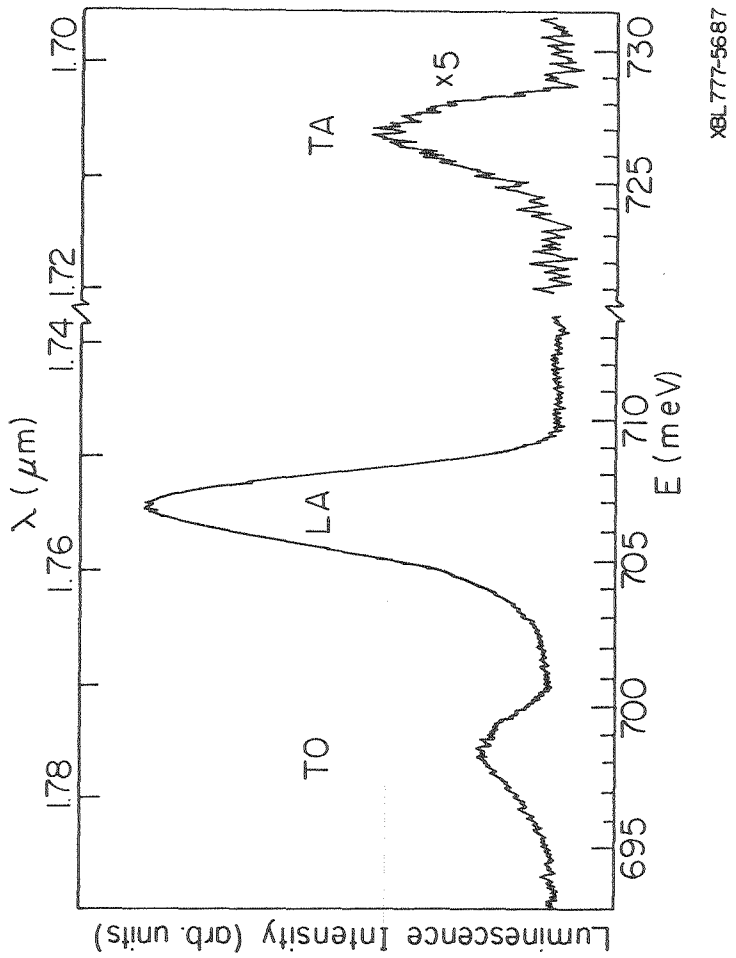

Figure 4.1

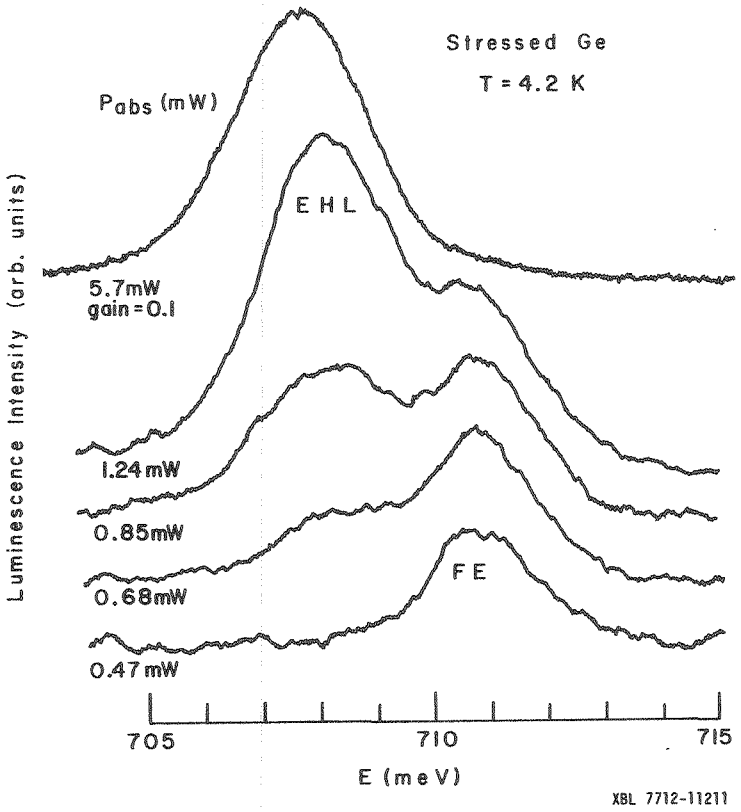

Figure 4.2

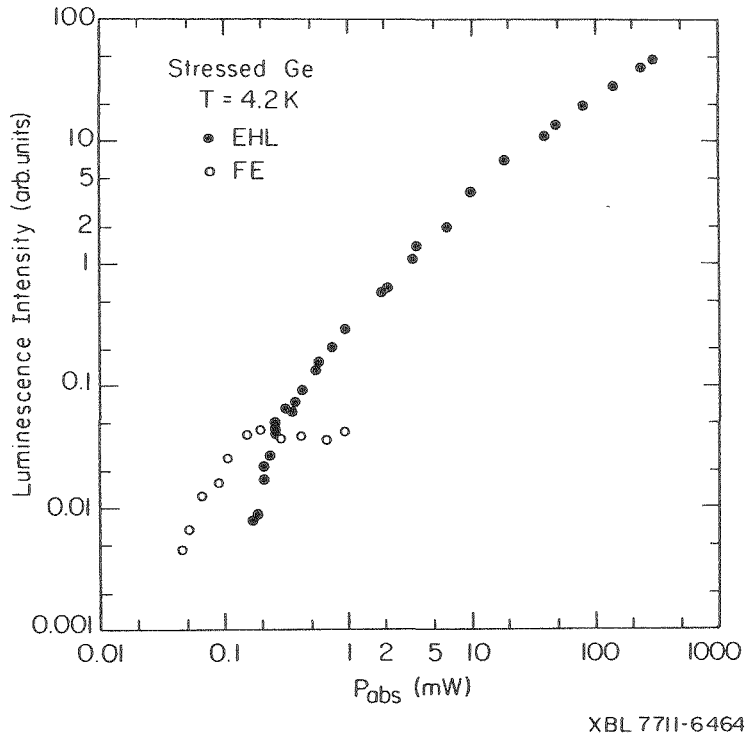

Figure 4.3

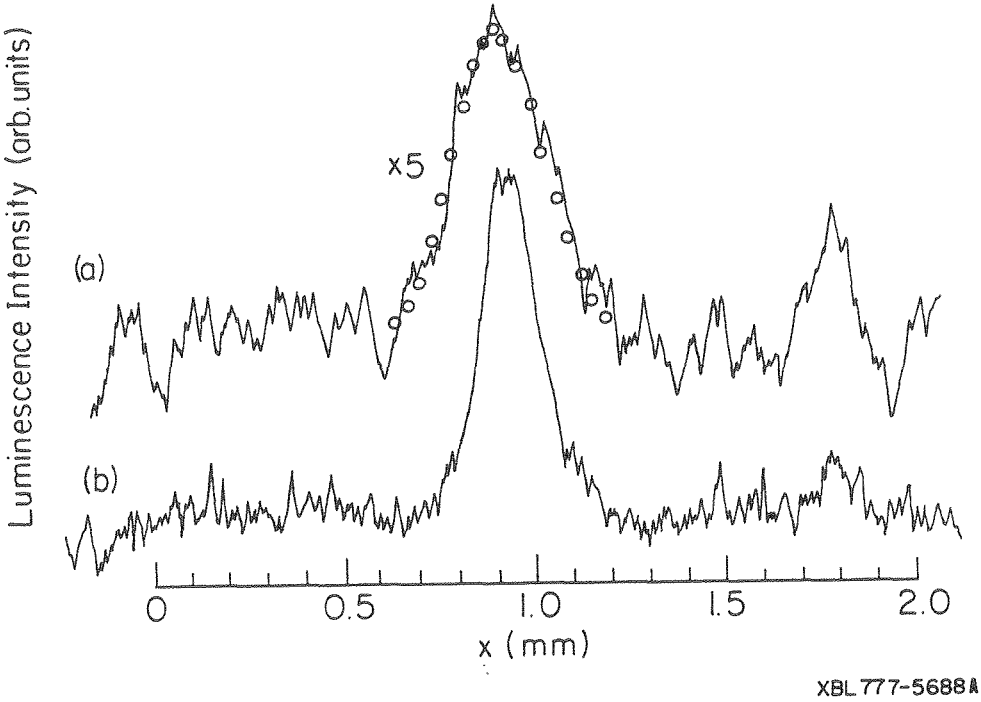

Figure 4.4

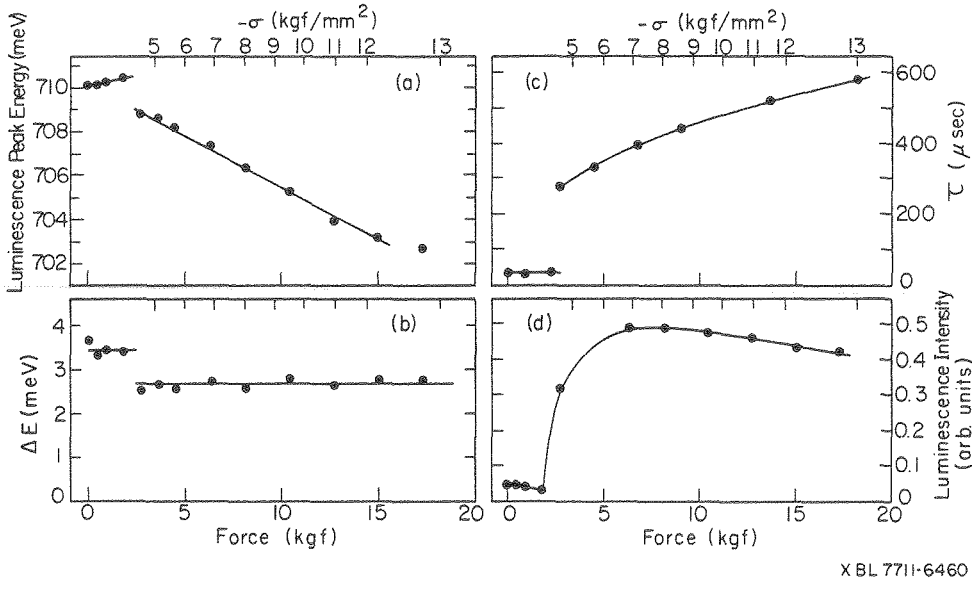

Figure 4.5

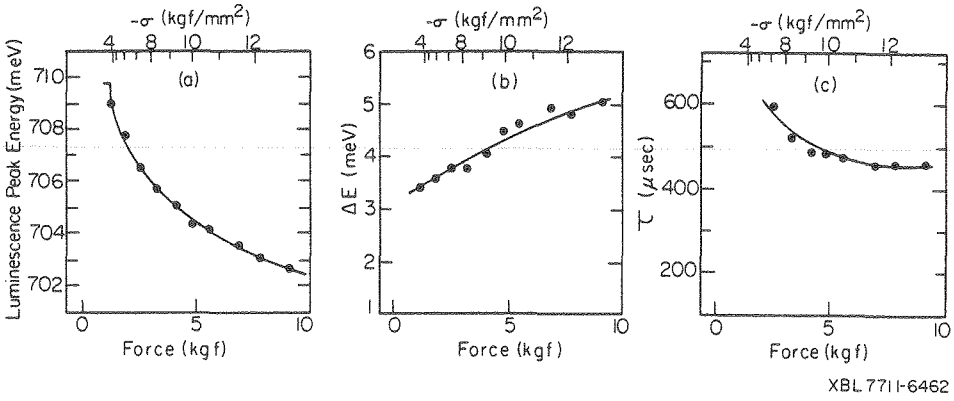

Figure 4.6

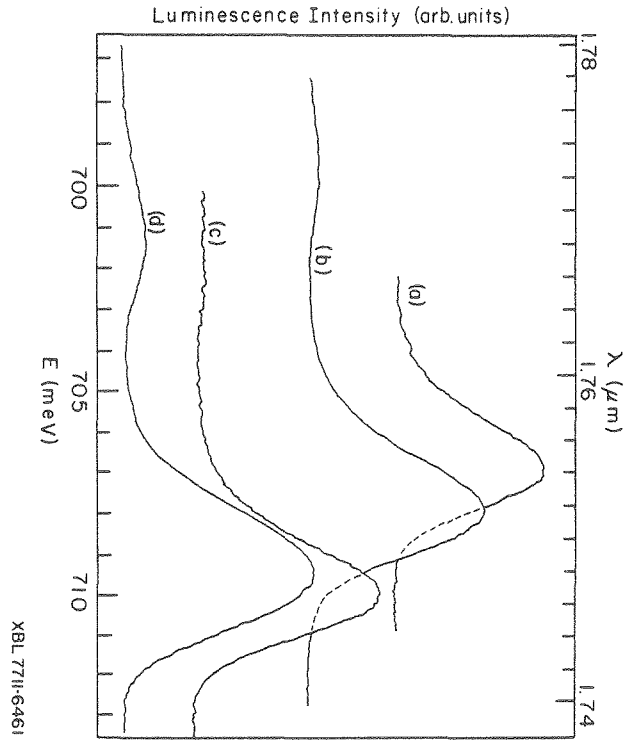

Figure 4.7

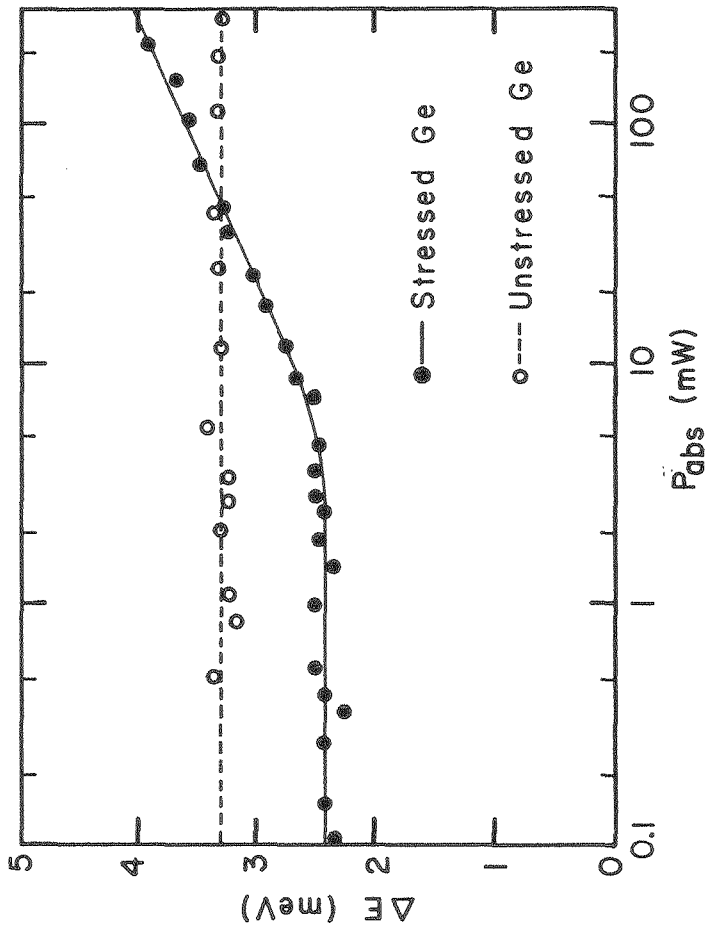

Figure 4.8

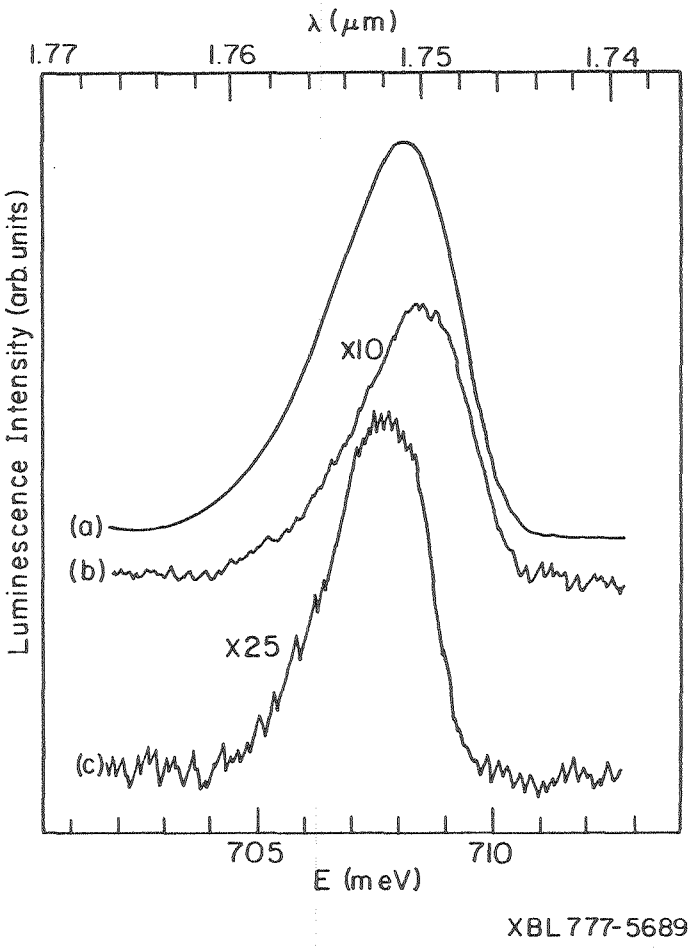

Figure 4.9

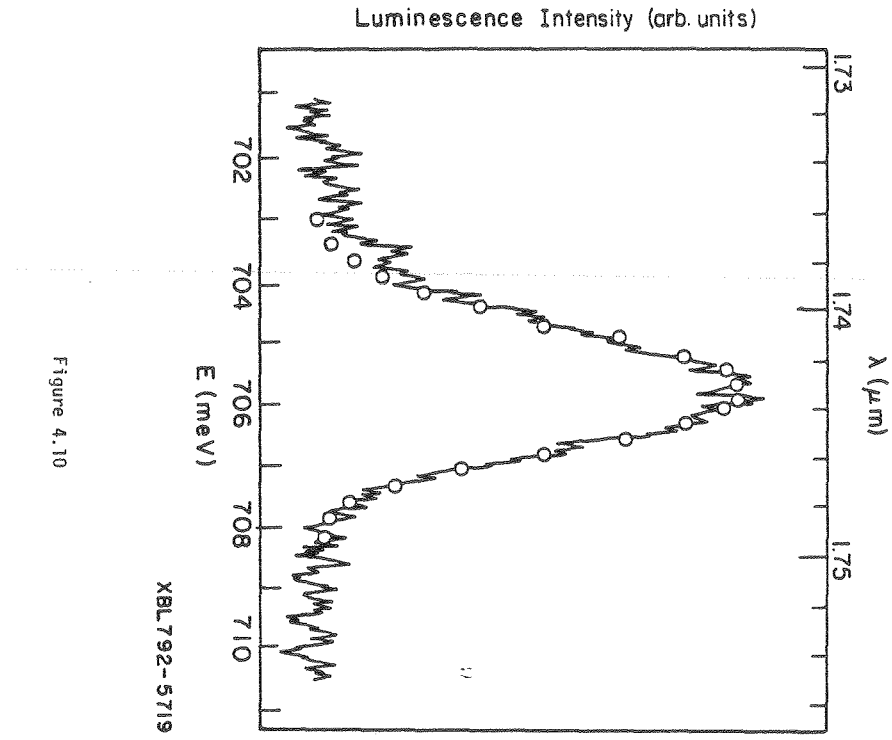

Figure 4.10

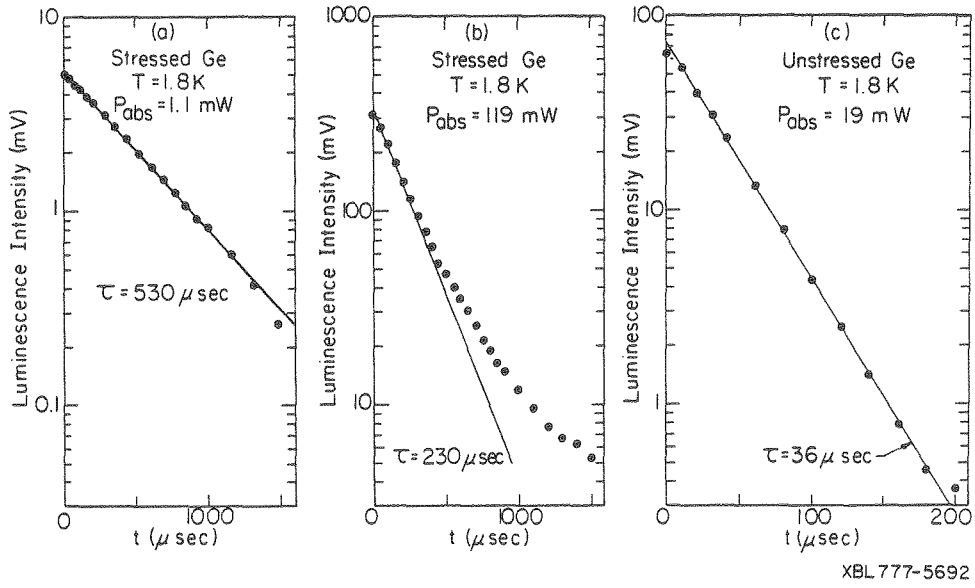

Figure 4.11

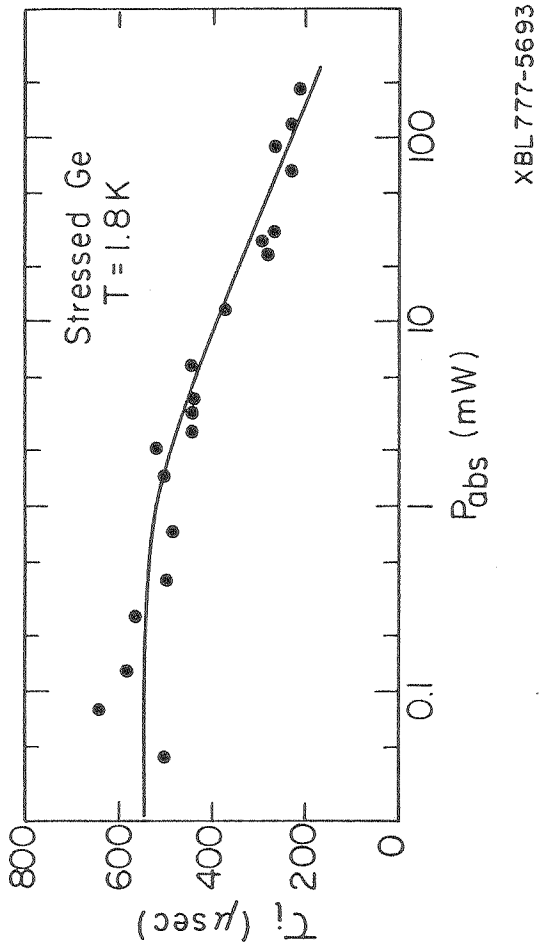

XBL 777-5693

Figure 4.12

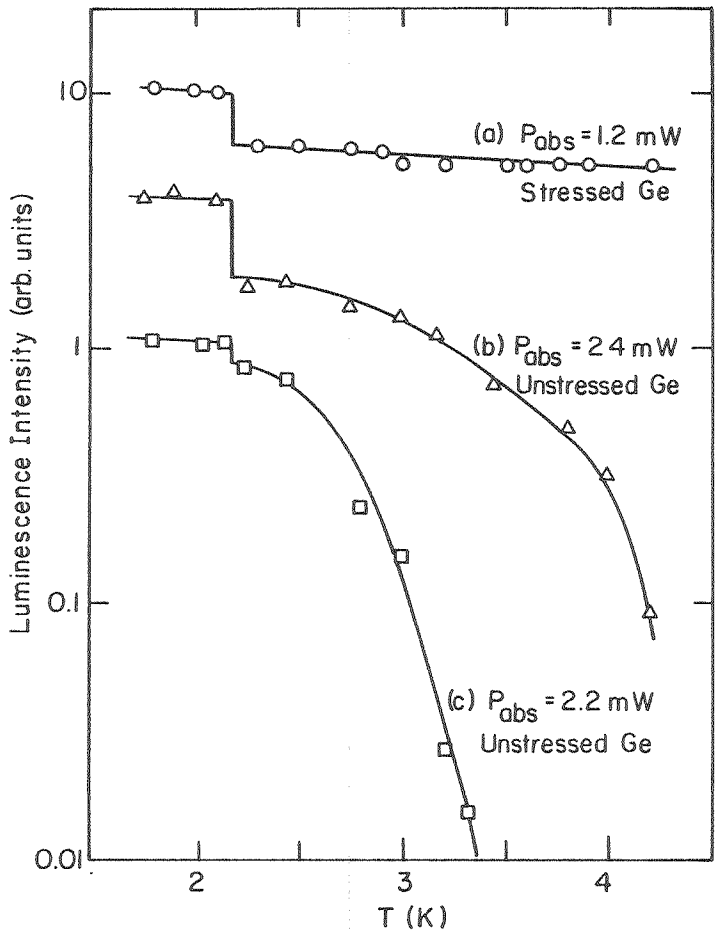

XBL 777-5695

Figure 4.13

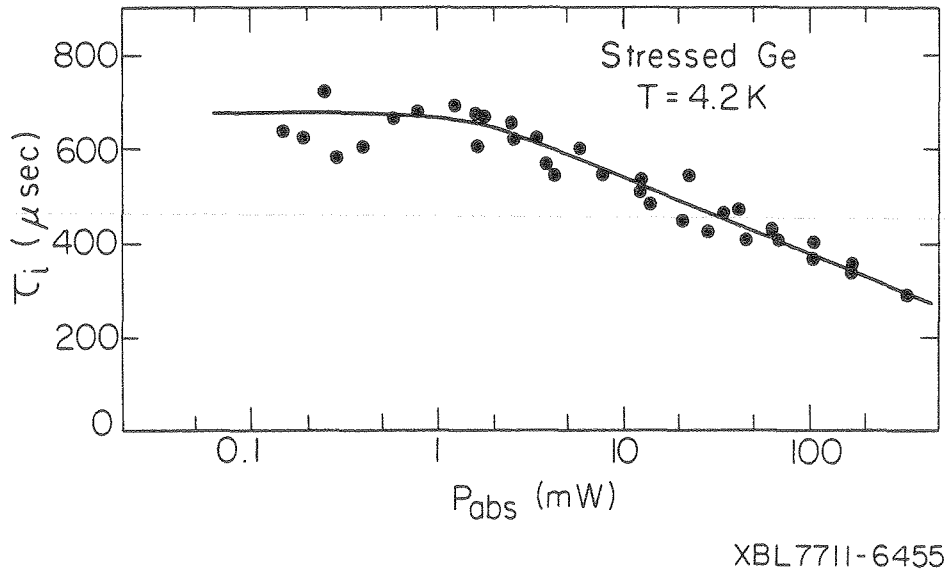

Figure 4.14

⟨111⟩ Stress

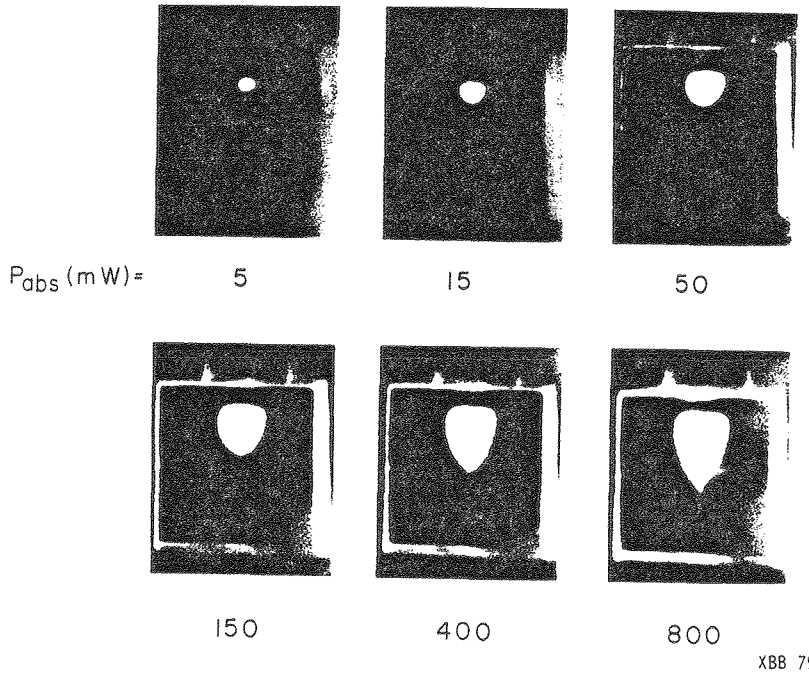

Figure 4.15

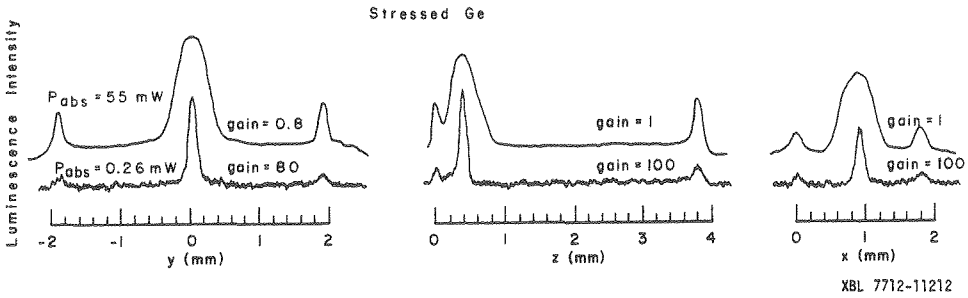

Figure 4.16

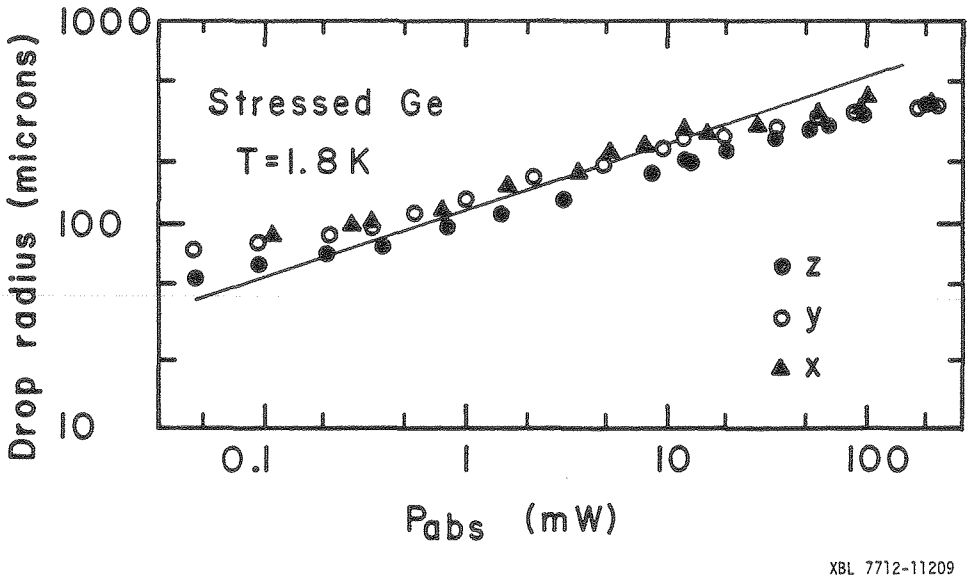

Figure 4.17

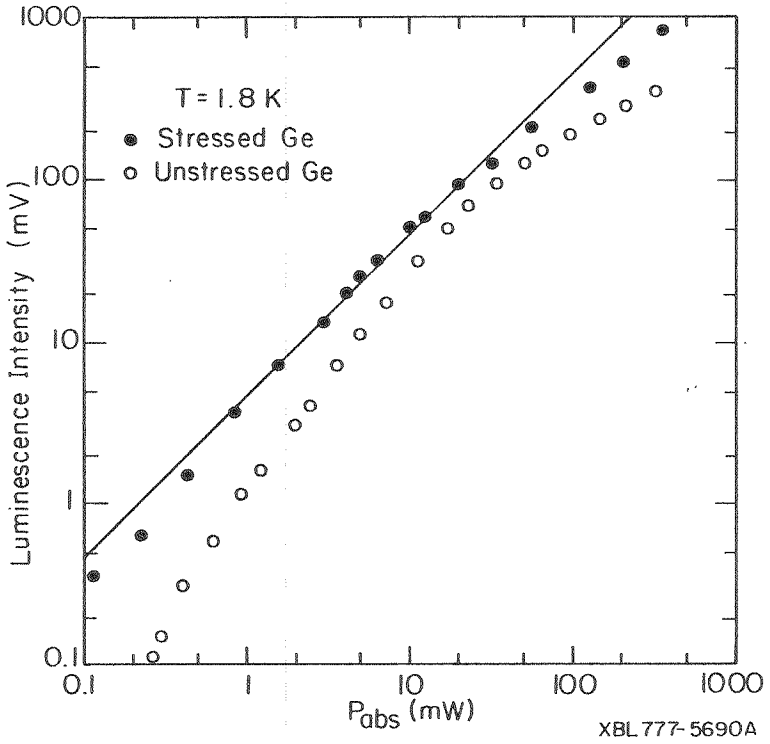

Figure 4.18

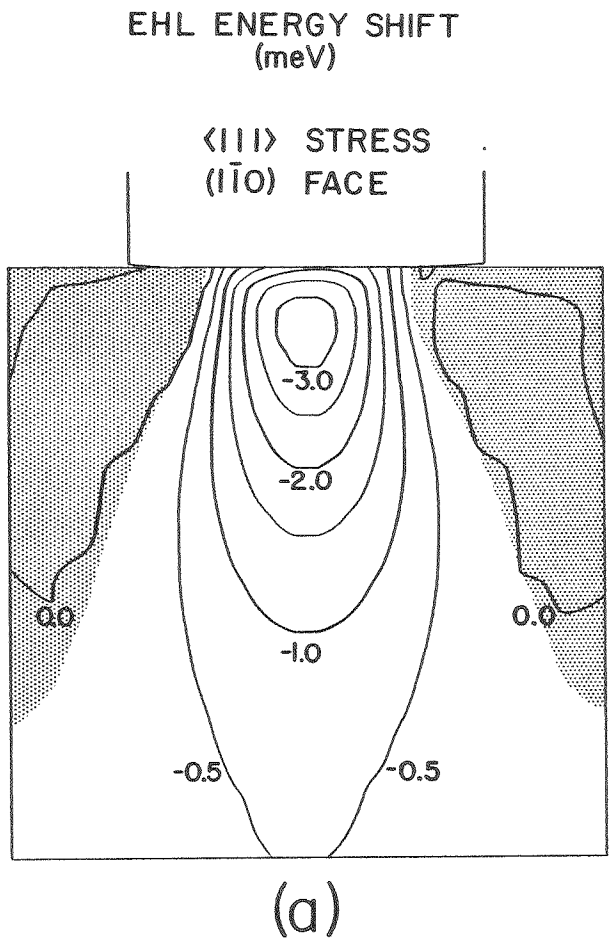

Figure 4.19a

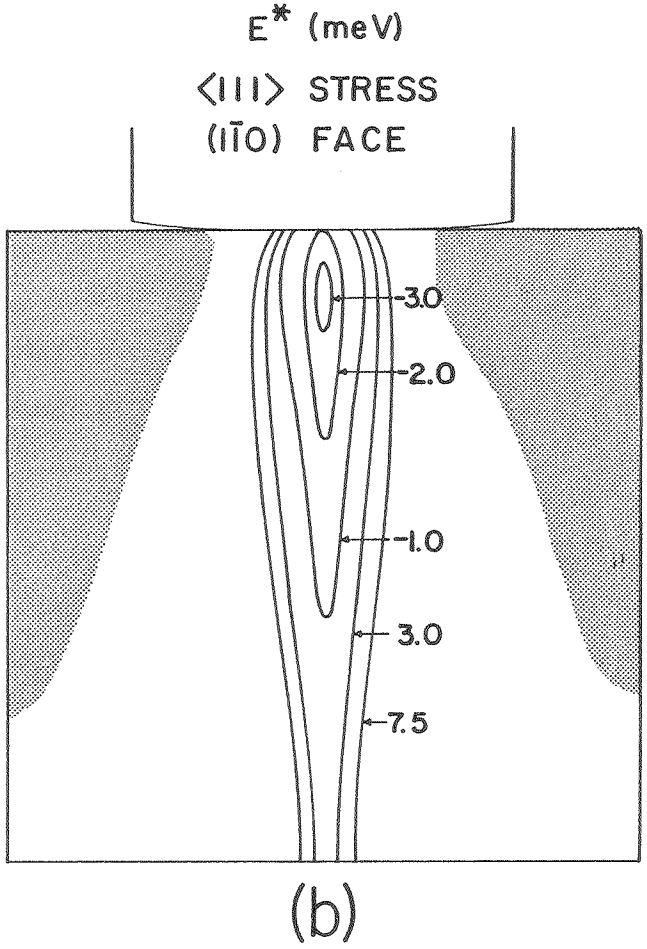

Figure 4.19b

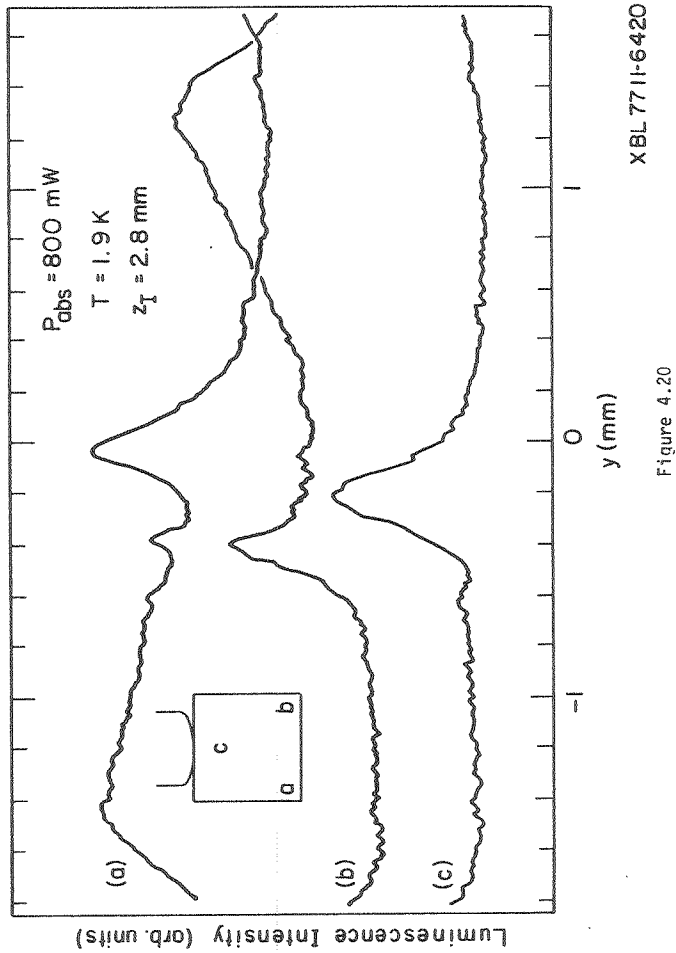

Figure 4.20

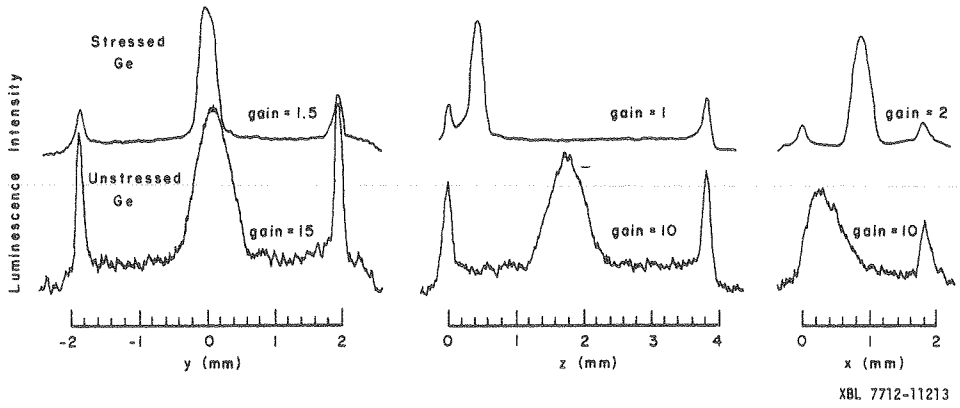

Figure 4.21

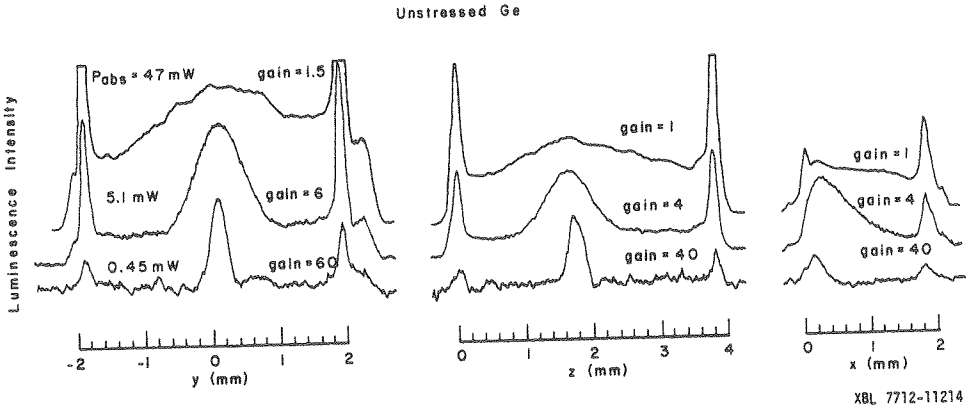

Figure 4.22

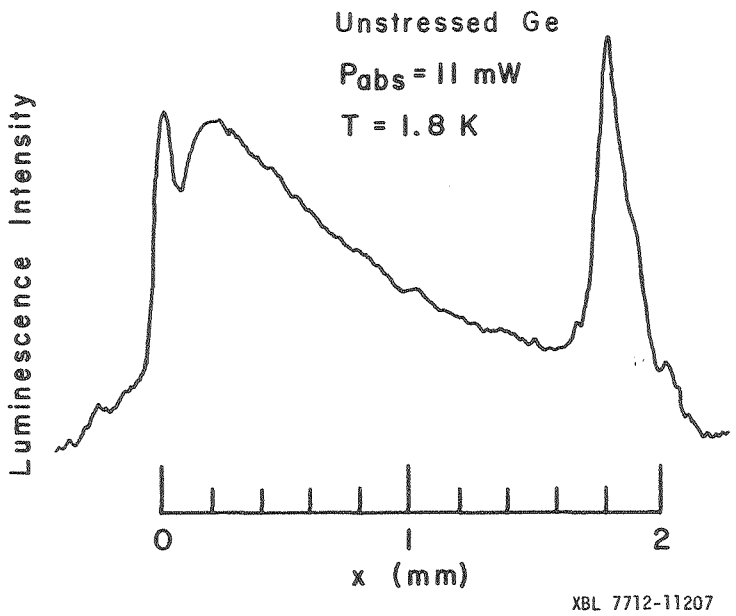

Figure 4.23

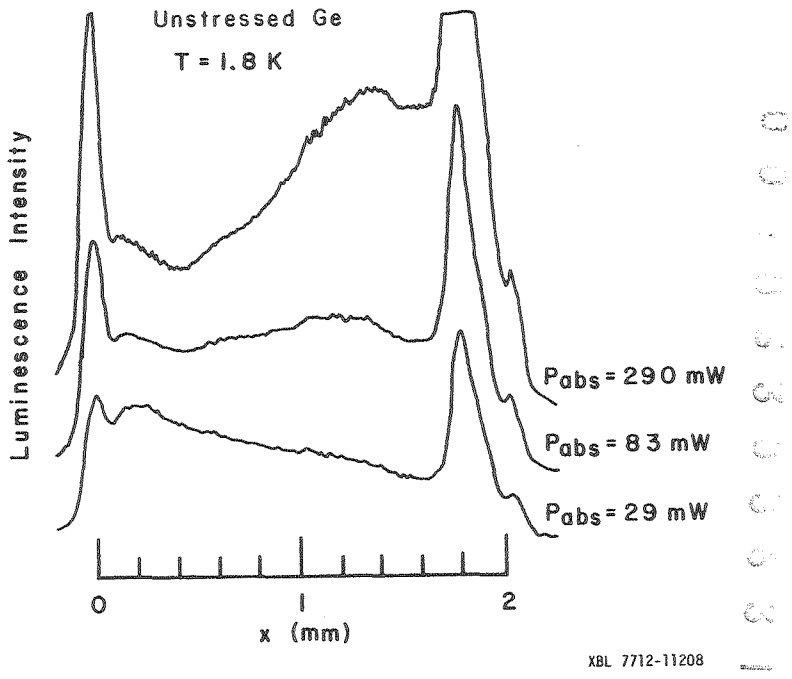

Figure 4.24

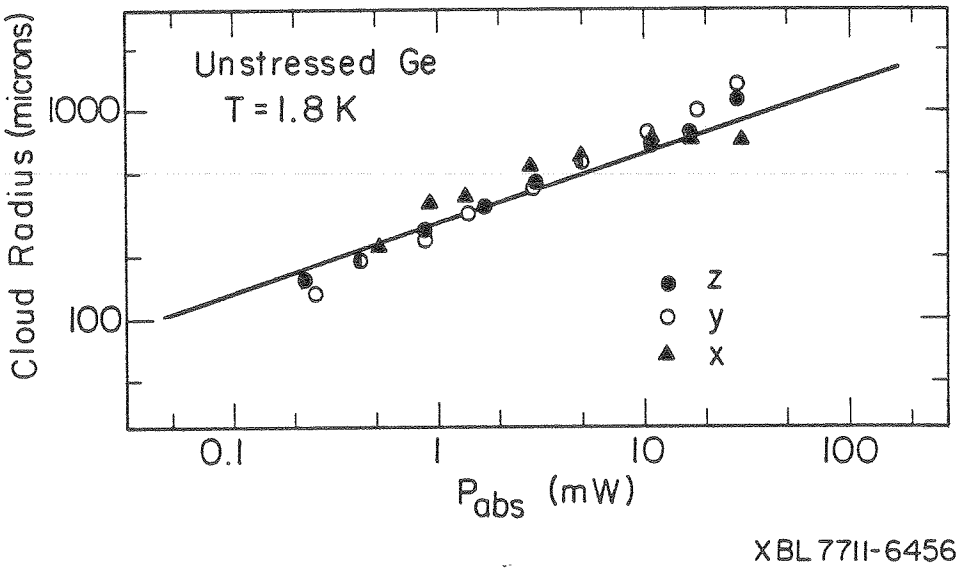

Figure 4.25

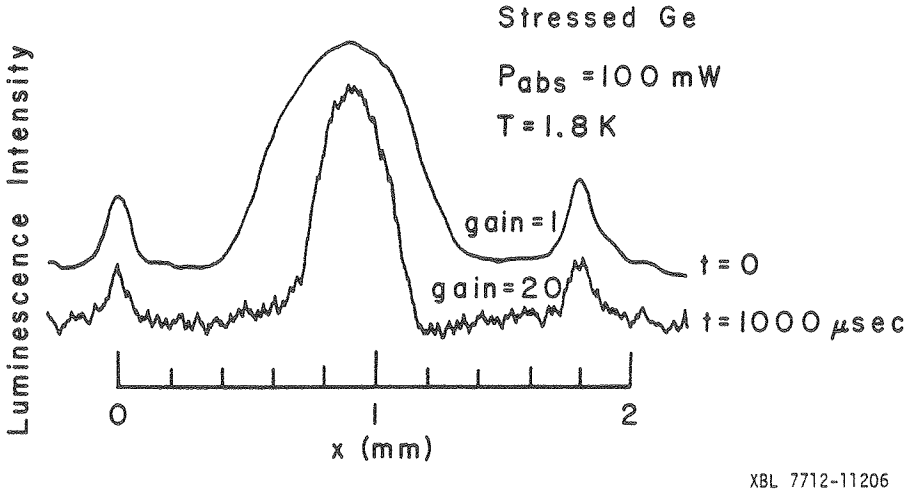

Figure 4.26

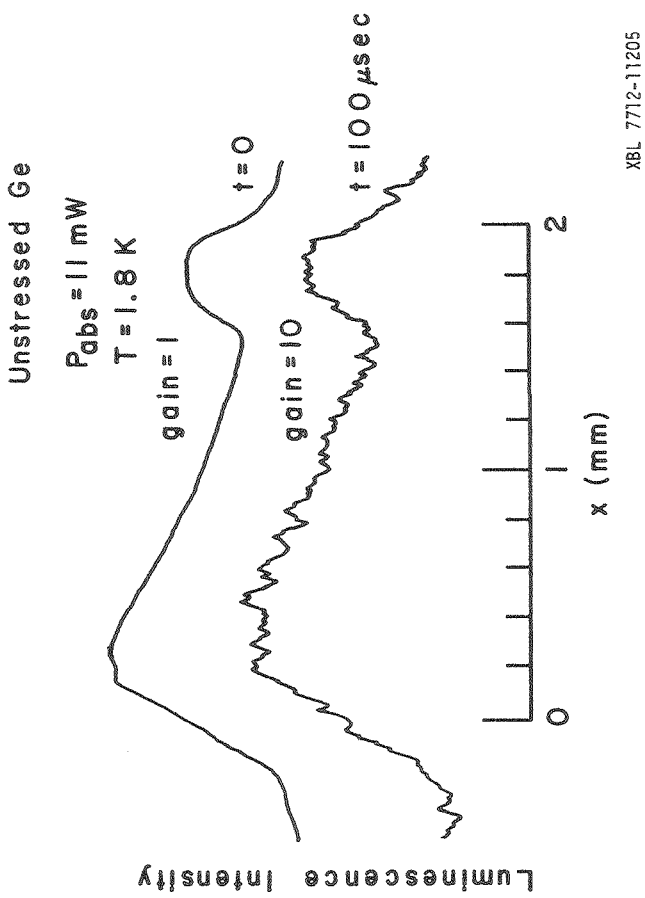

XBL 7712-11205

Figure 4.27

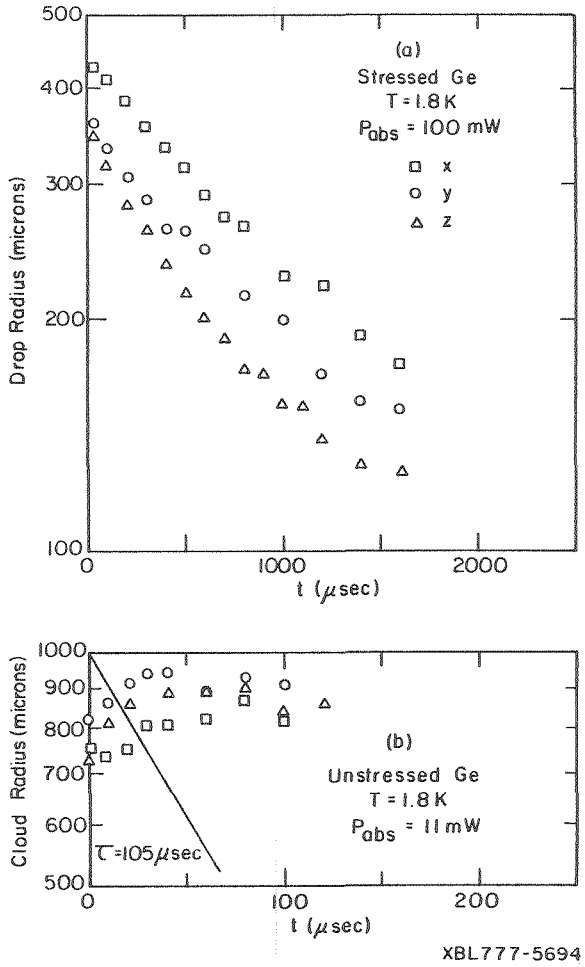

XBL777-5694

Figure 4.28

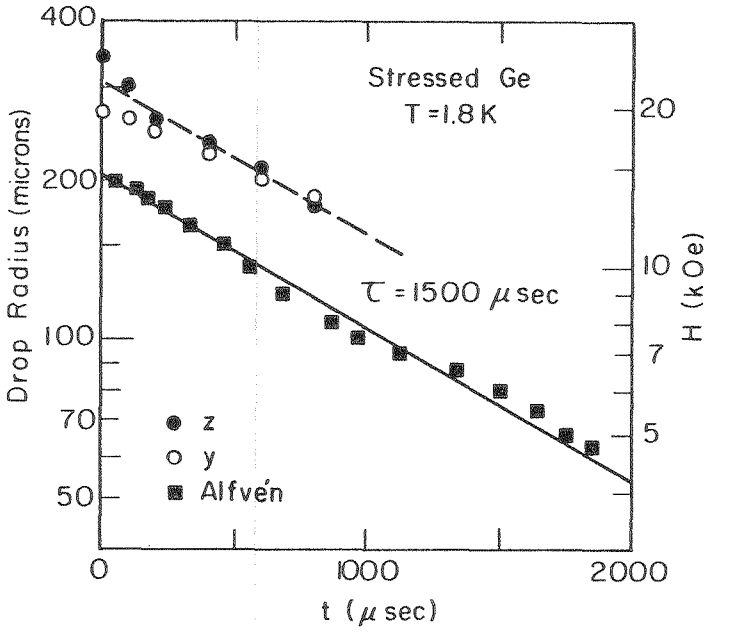

XBL 7711-6457

Figure 4.29

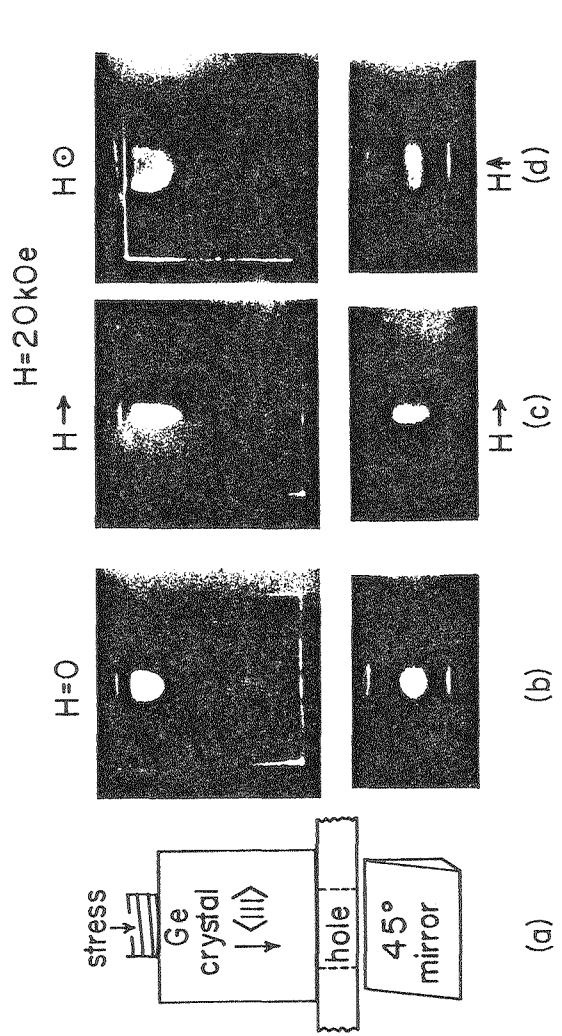

XBB 773-2139

Figure 4.30

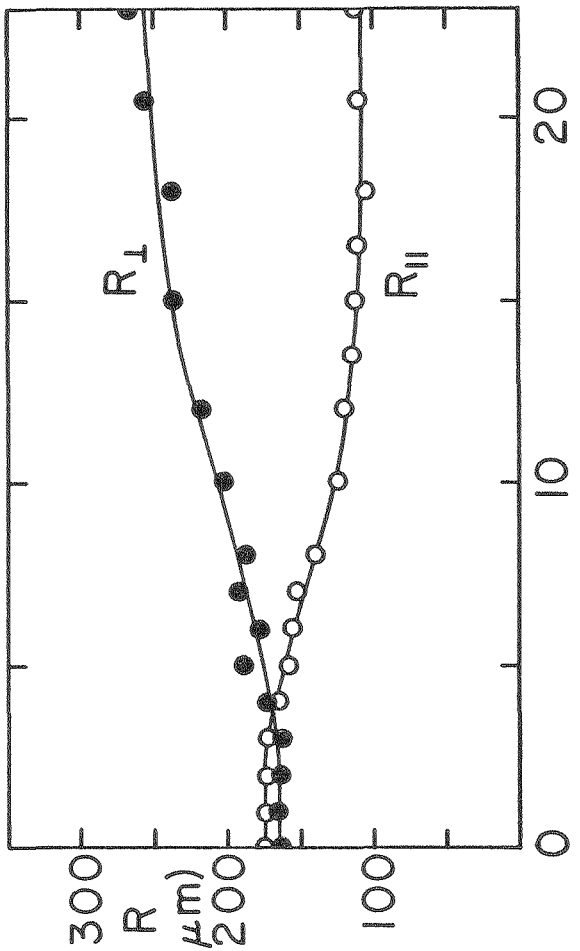

XBL 773-8032

Figure 4.31

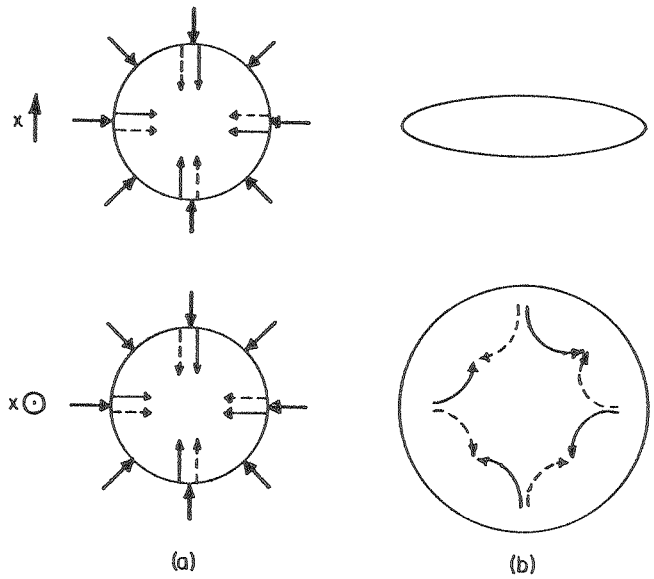

XBL792-5727

Figure 4.32

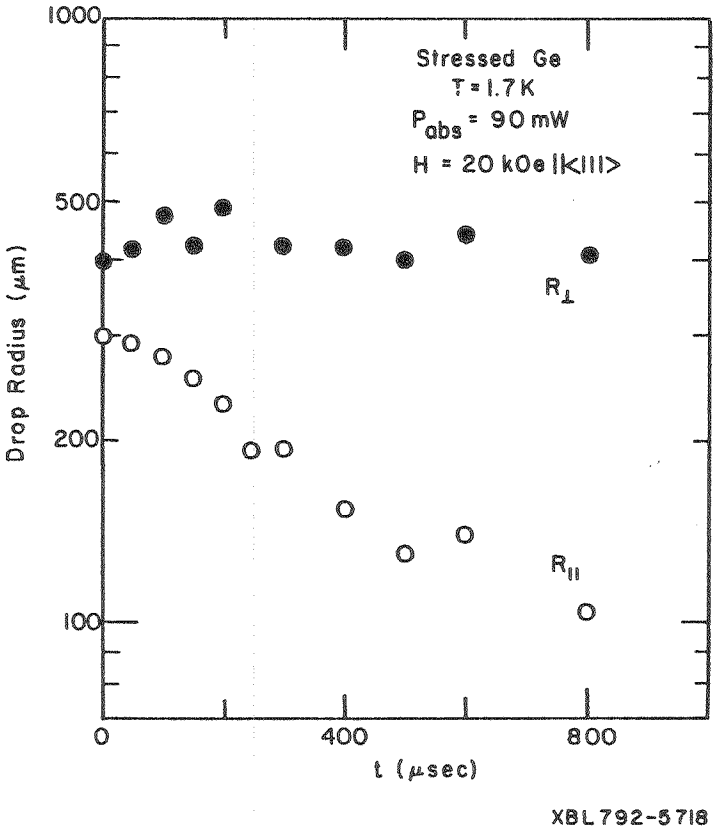

Figure 4.33

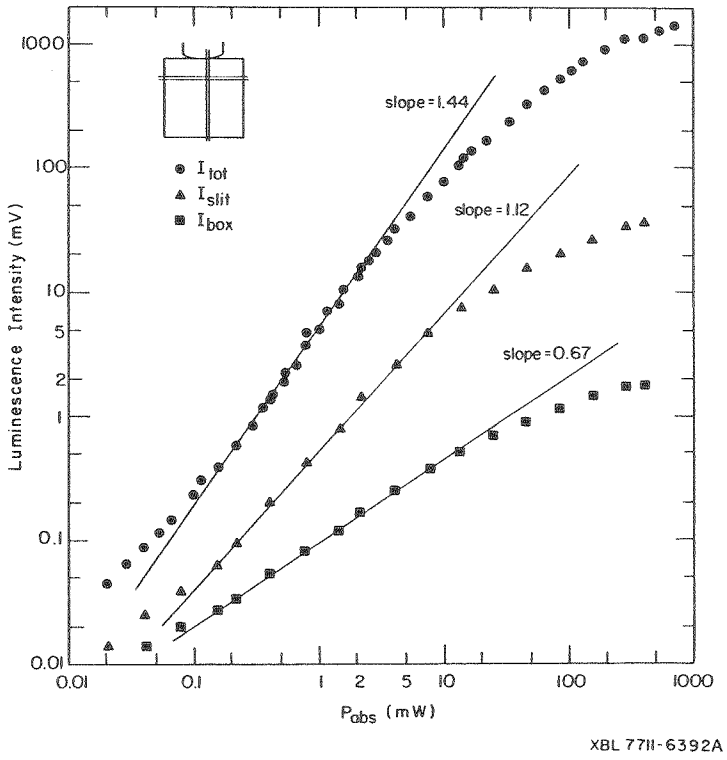

Figure 5.1

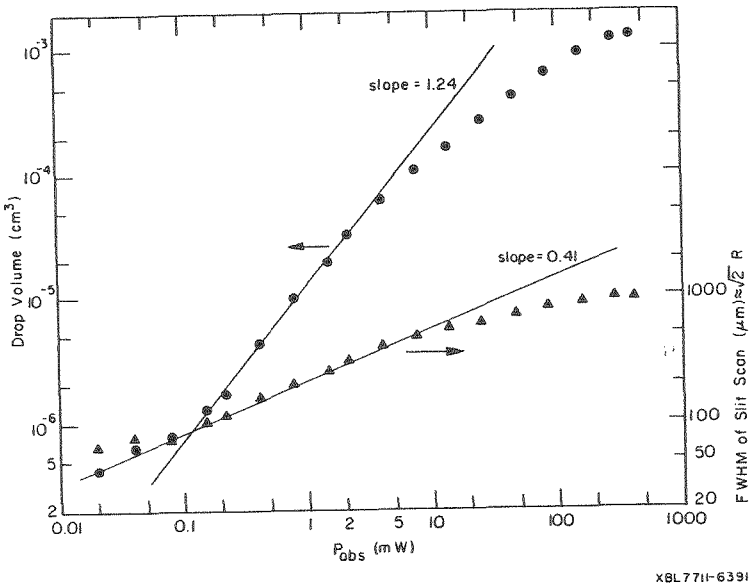

Figure 5.2

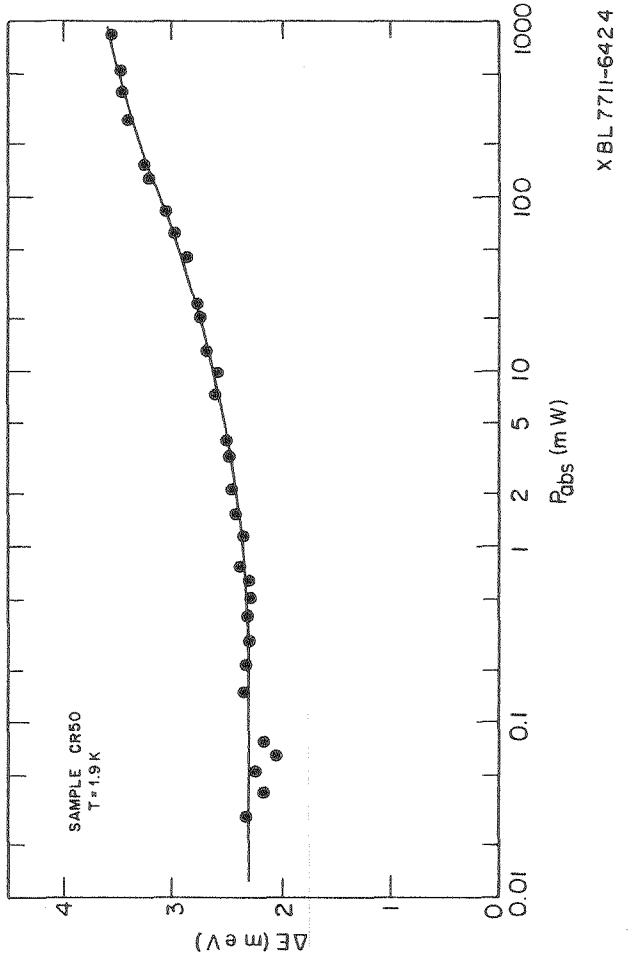

Figure 5.3

This report was prepared as an account of work sponsored by the United States Government. Neither the United States nor the United States Energy Research and Development Administration, nor any of their employees, nor any of their contractors, subcontractors, or their employees, makes any warranty, express or implied, or assumes any legal liability or responsibility for the accuracy, completeness or usefulness of any information, apparatus, product or process disclosed, or represents that its use would not infringe privately owned rights.

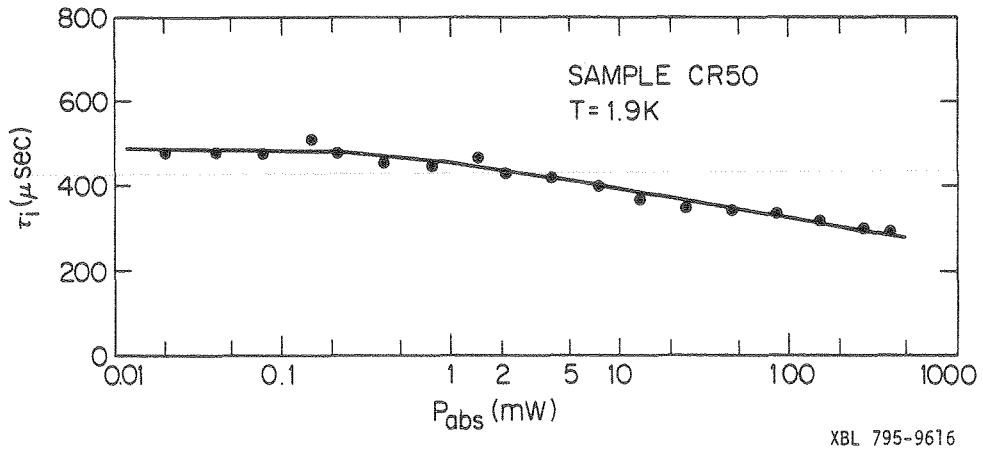

Figure 5.4

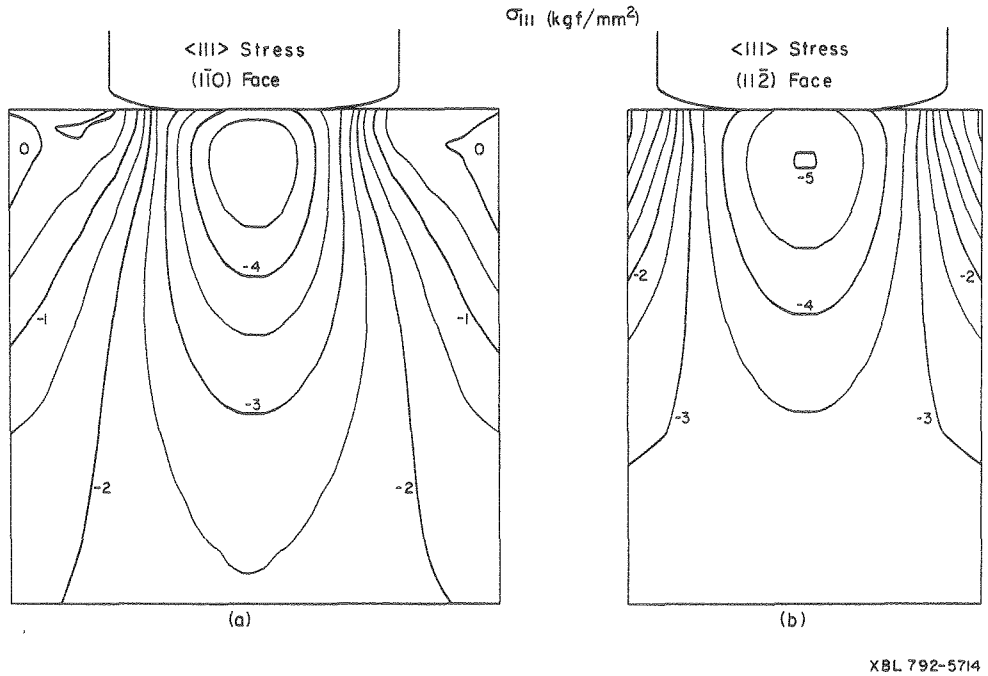

Figure 5.5

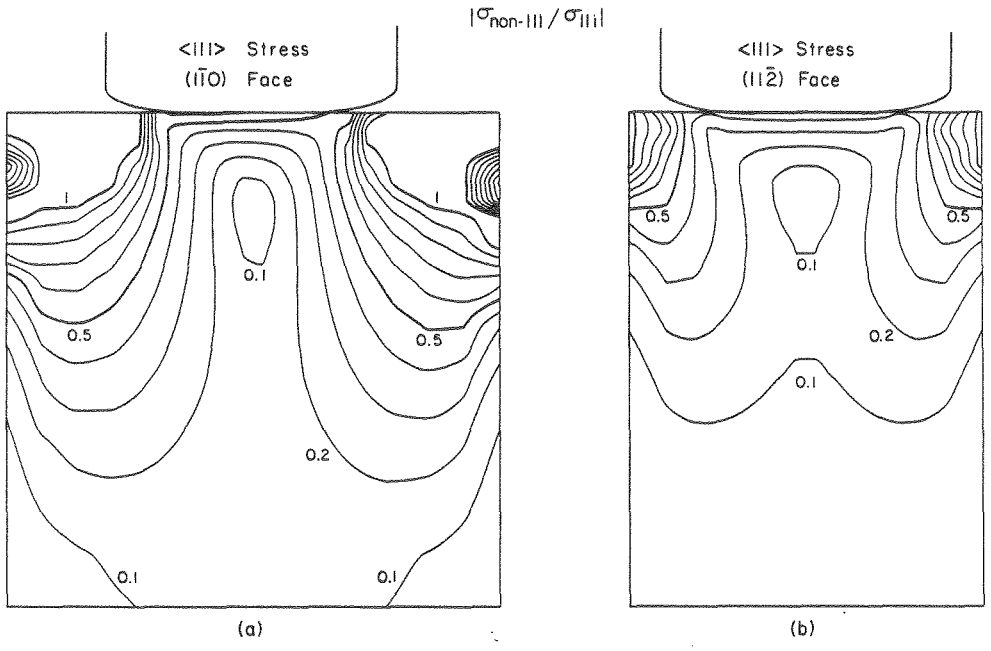

XBL792-5716

Figure 5.6

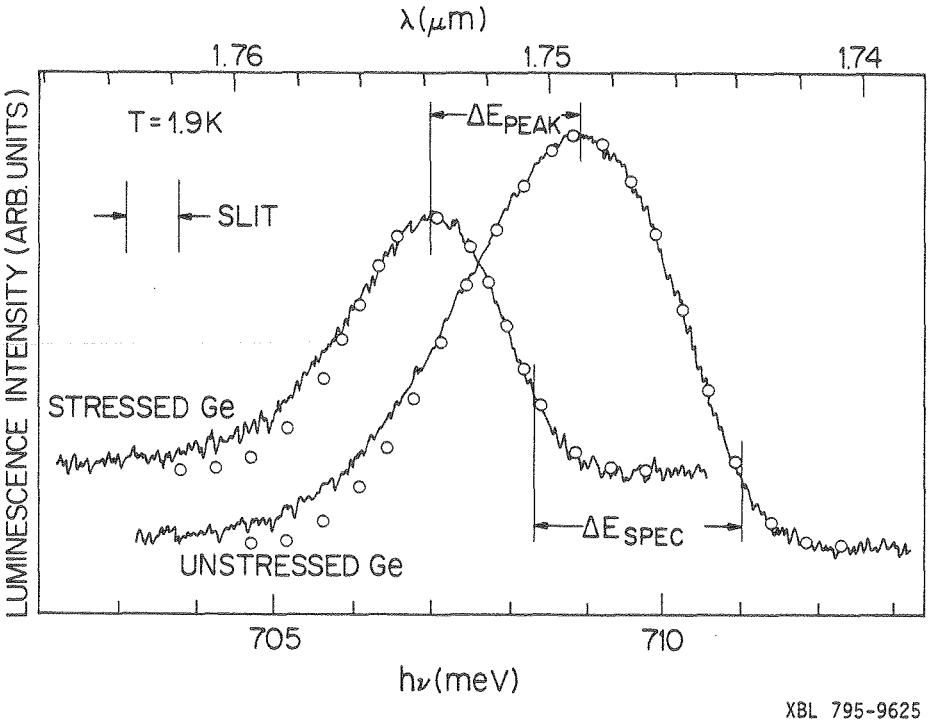

XBL 795-9625

Figure 5.7

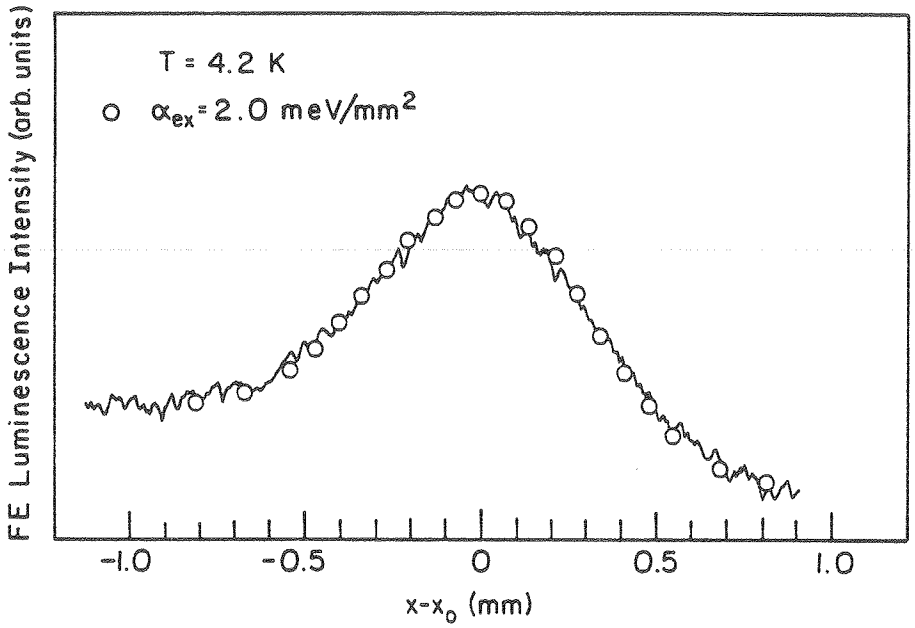

Figure 5.8a

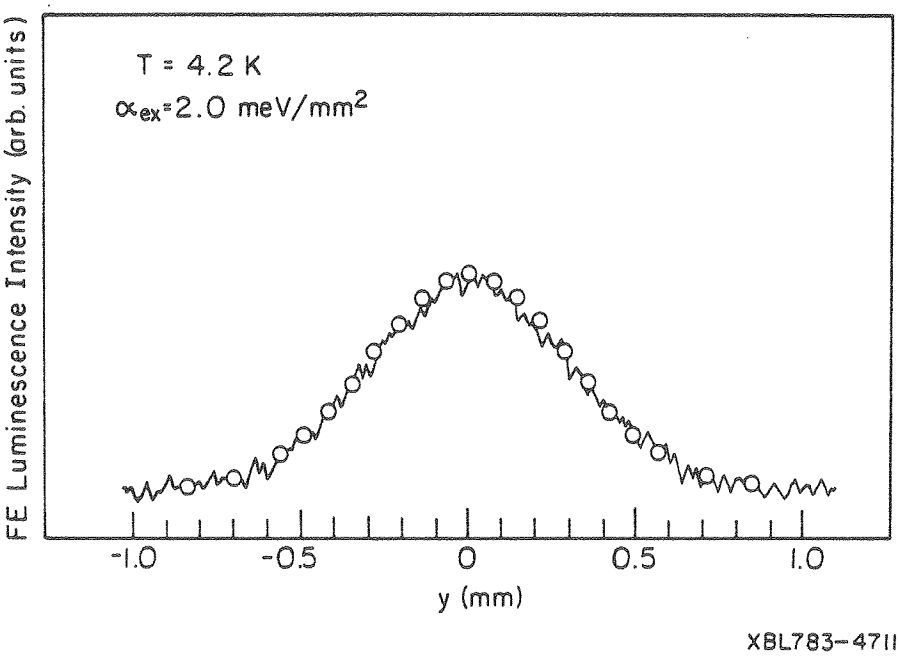

Figure 5.8b

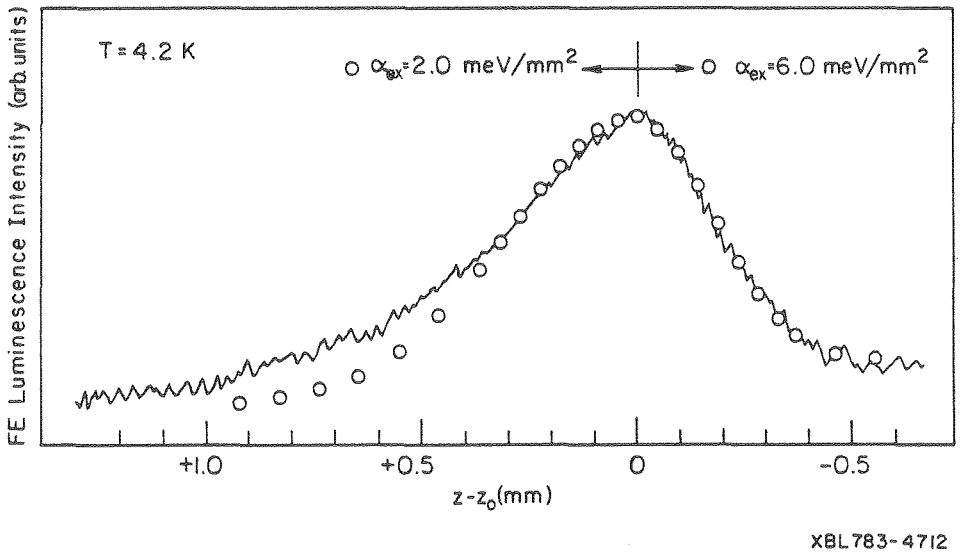

Figure 5.8c

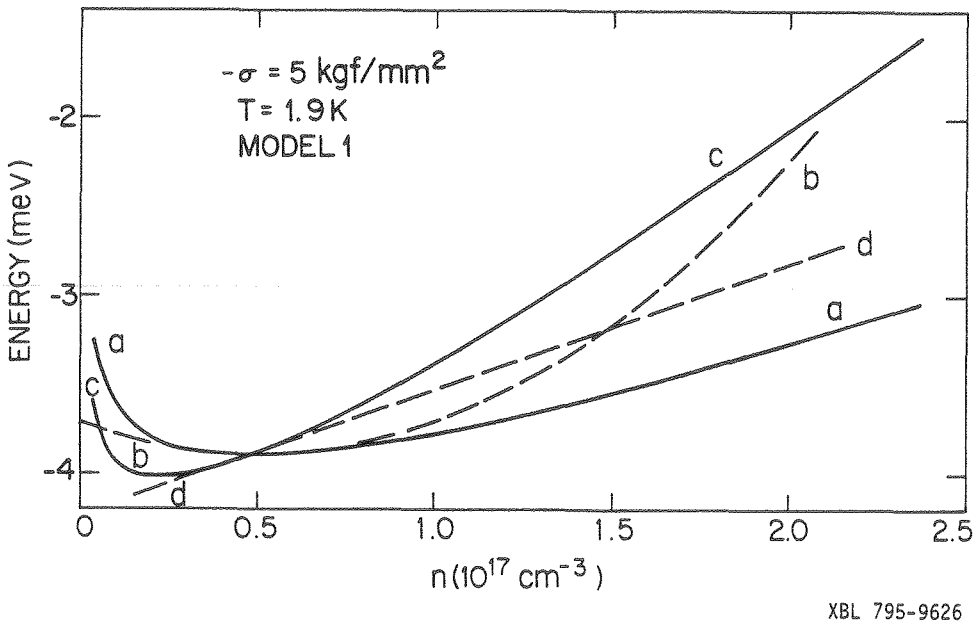

Figure 5.9

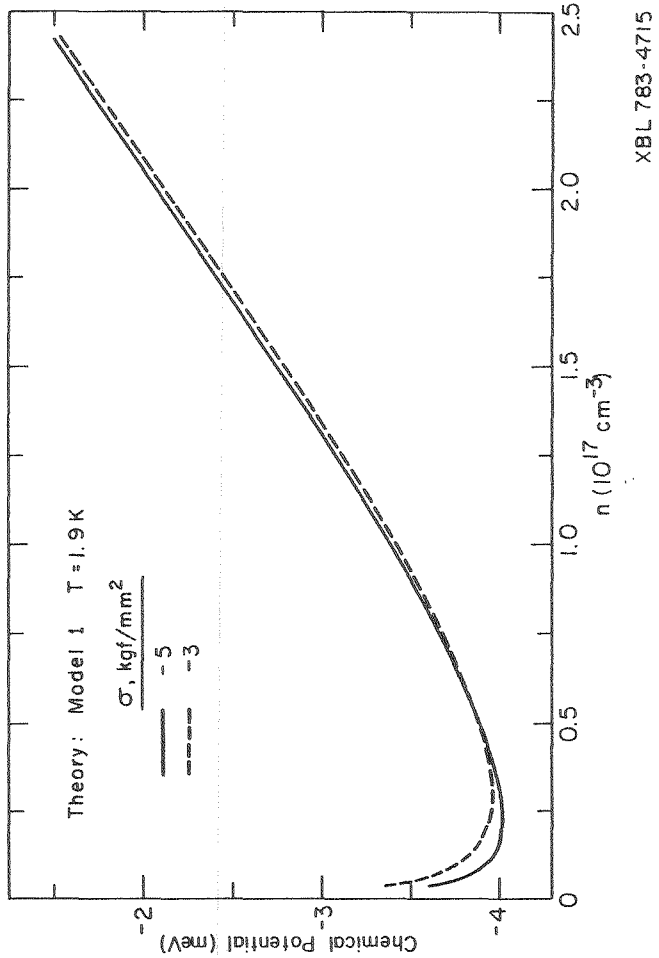

Figure 5.10

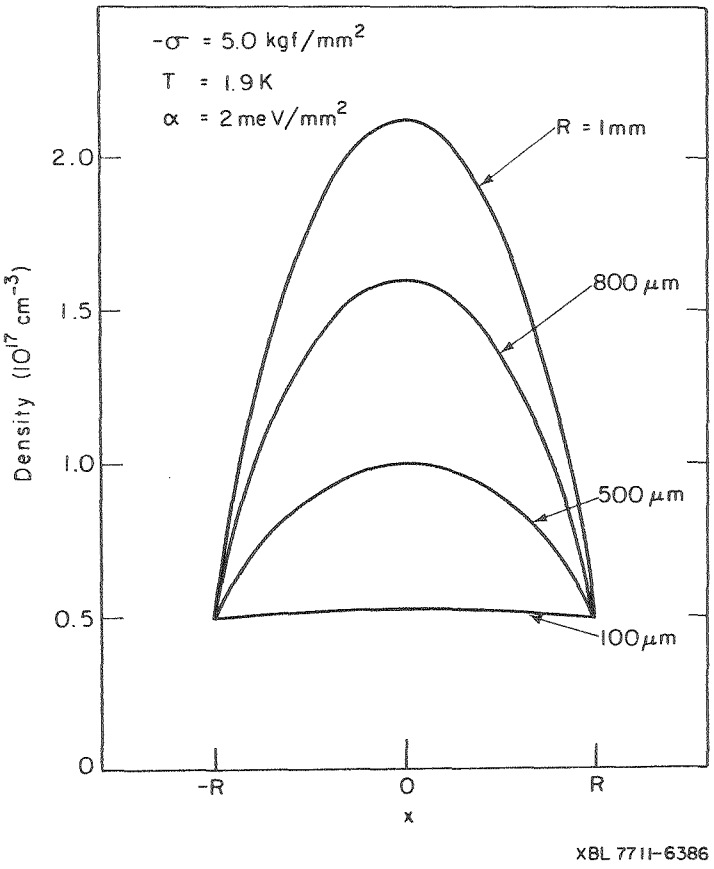

Figure 5.11

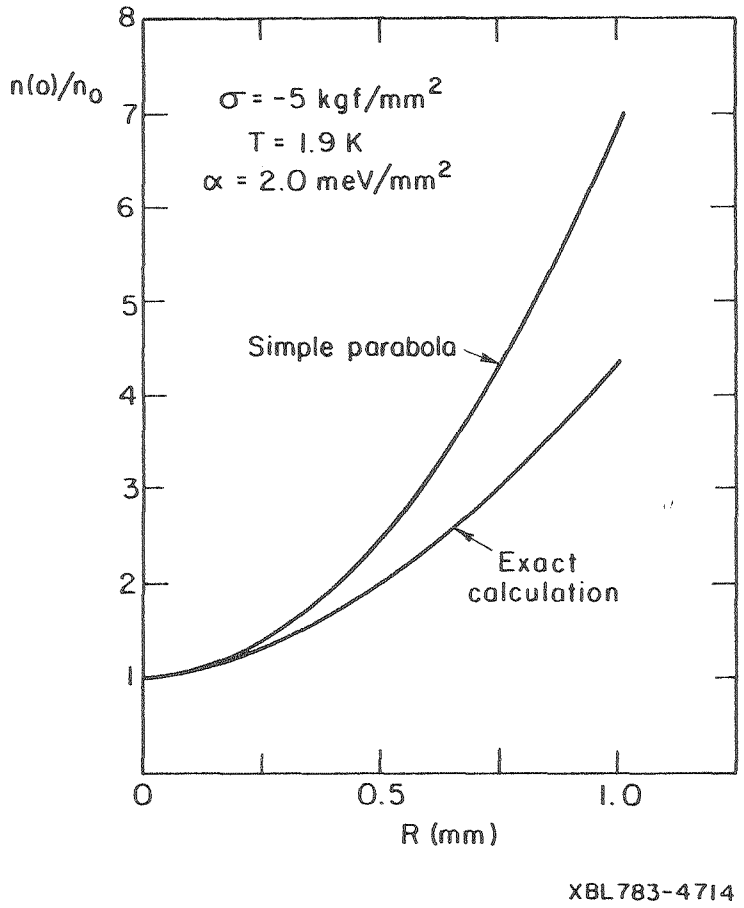

Figure 5.12

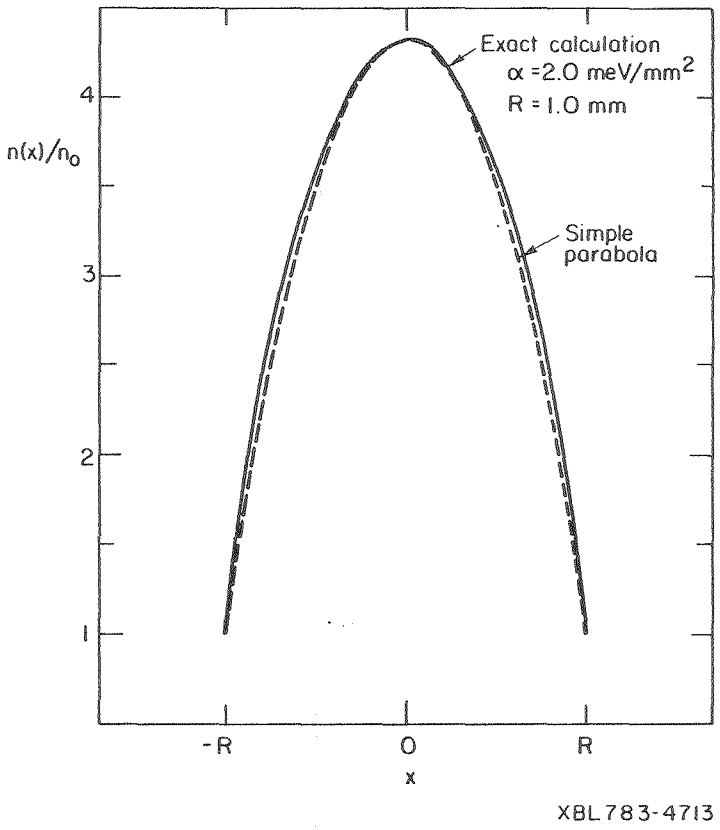

Figure 5.13

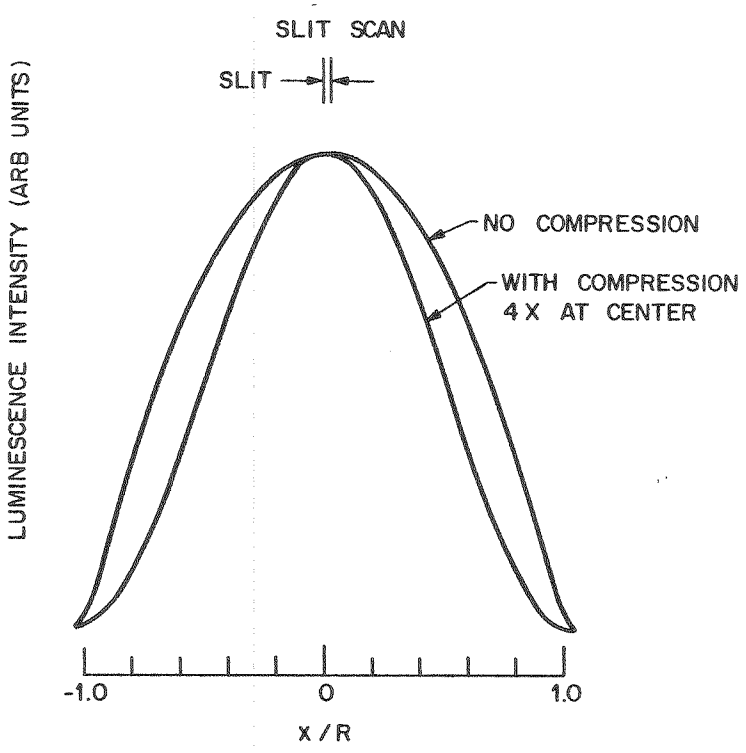

Figure 5.14

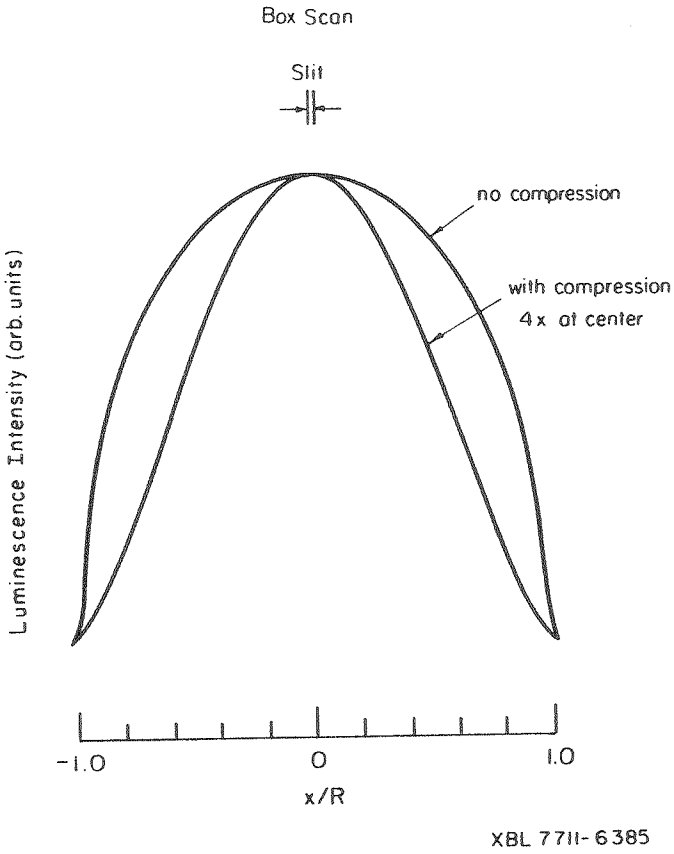

Figure 5.15

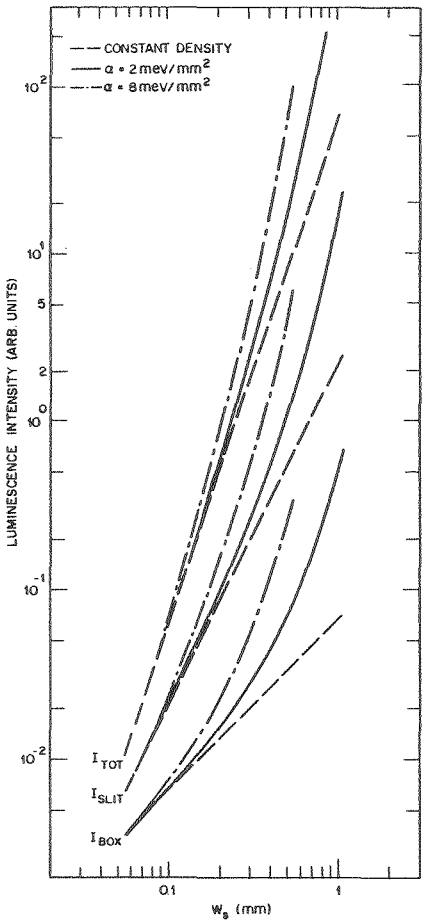

Figure 5.16

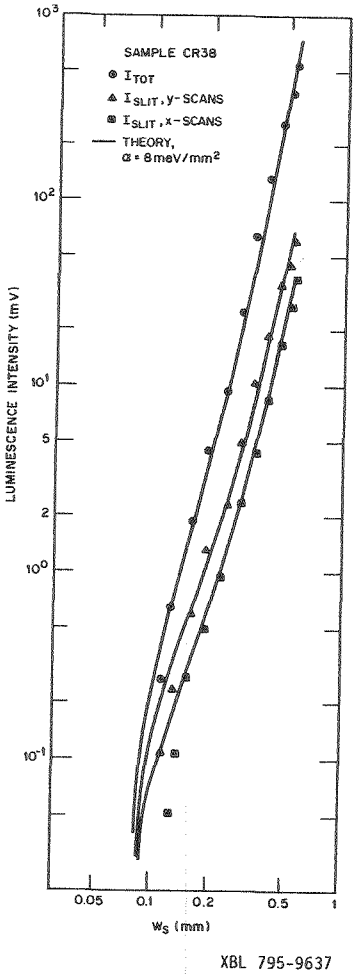

Figure 5.17

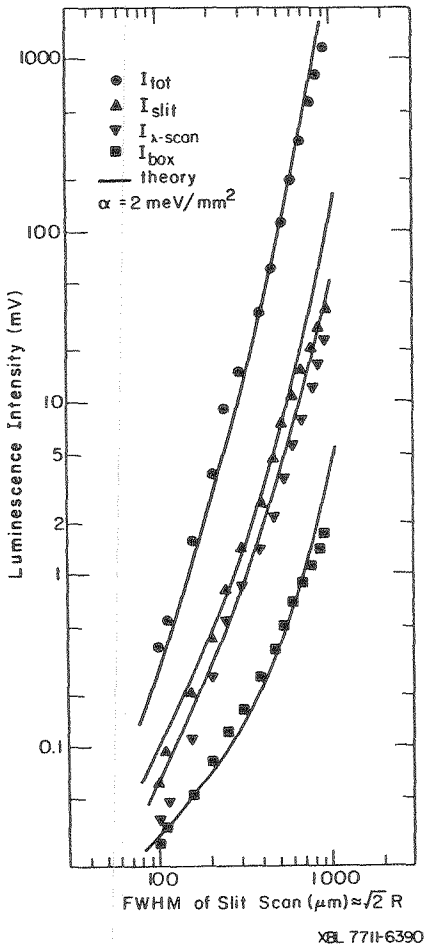

Figure 5.18

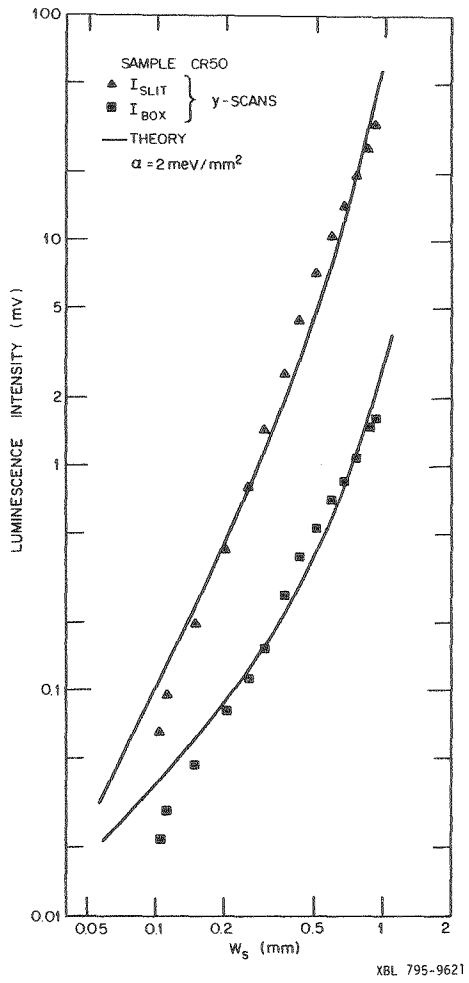

Figure 5.19

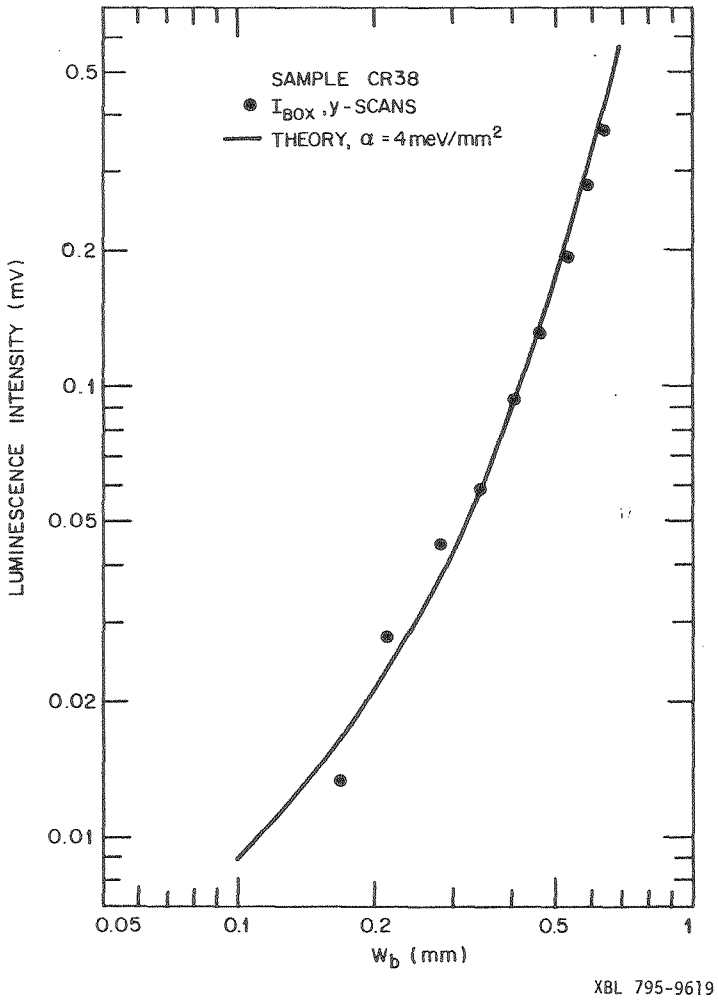

Figure 5.20

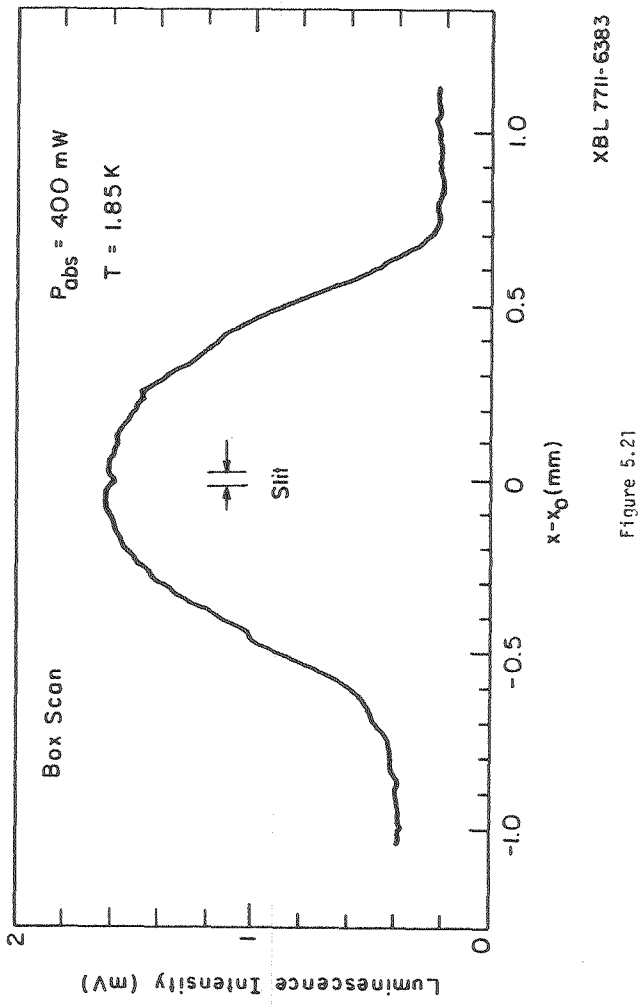

Figure 5.21

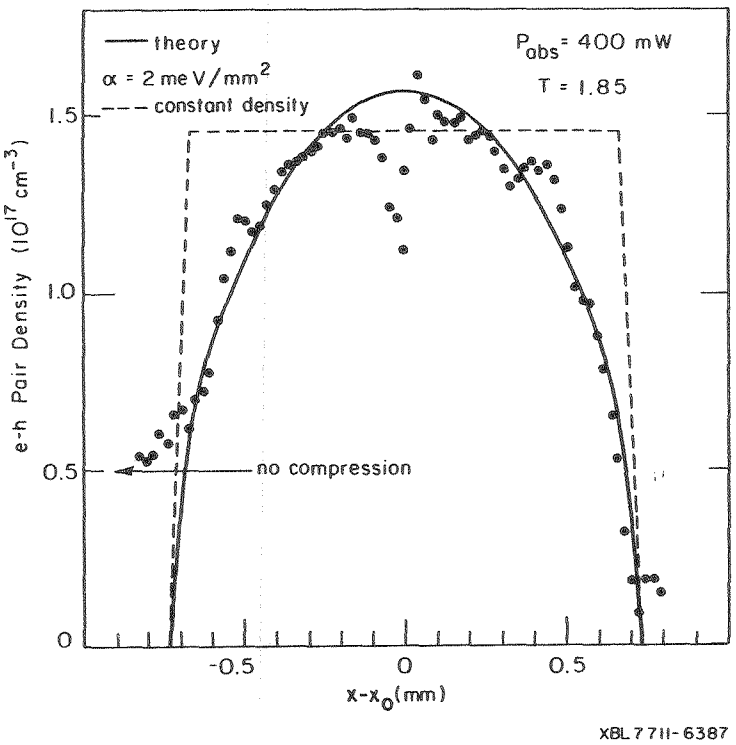

Figure 5.22

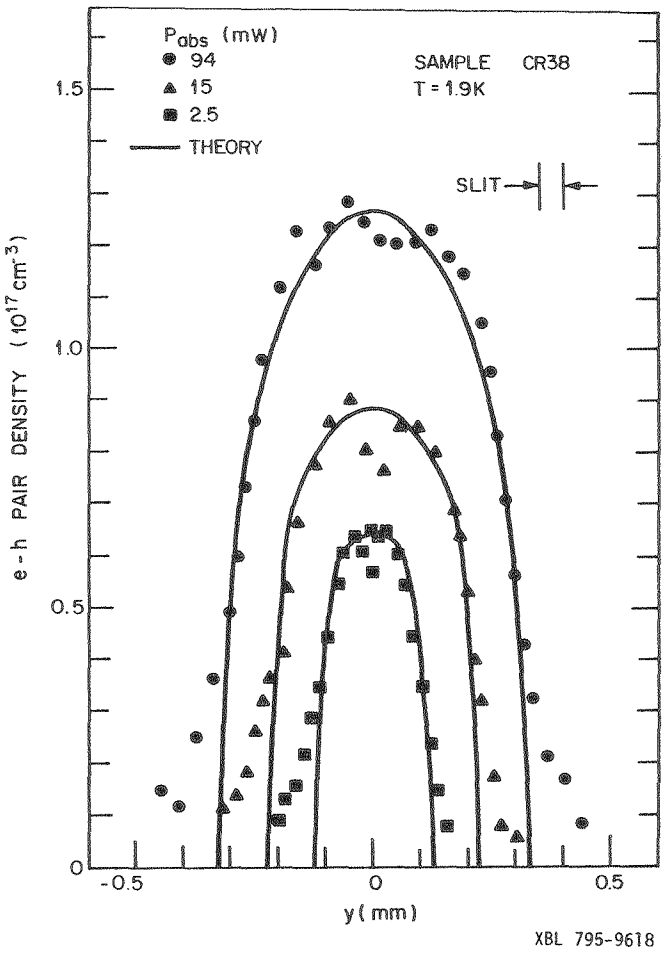

Figure 5.23

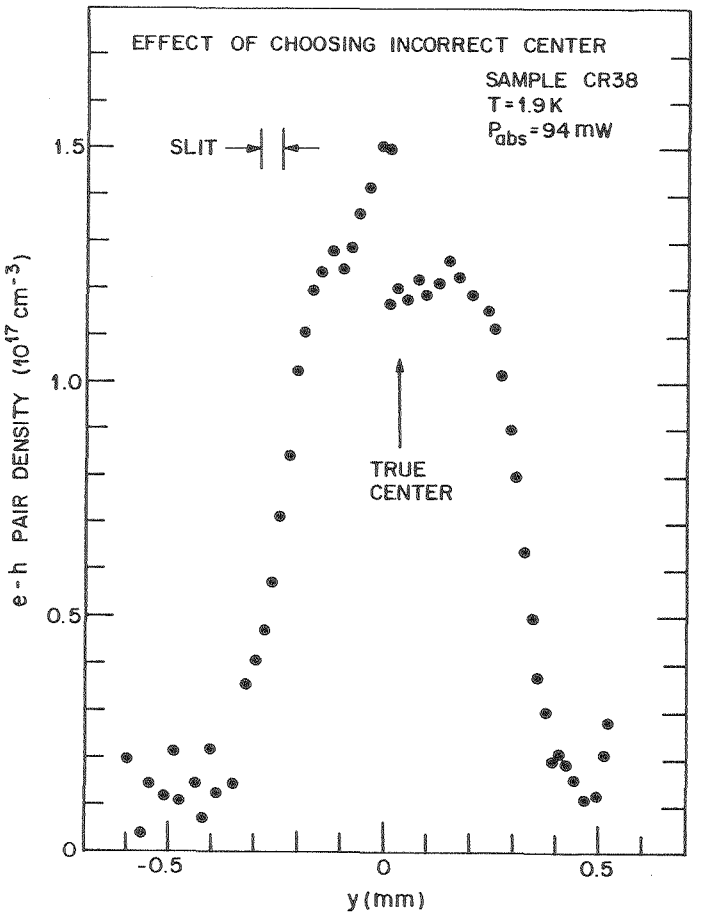

Figure 5.24

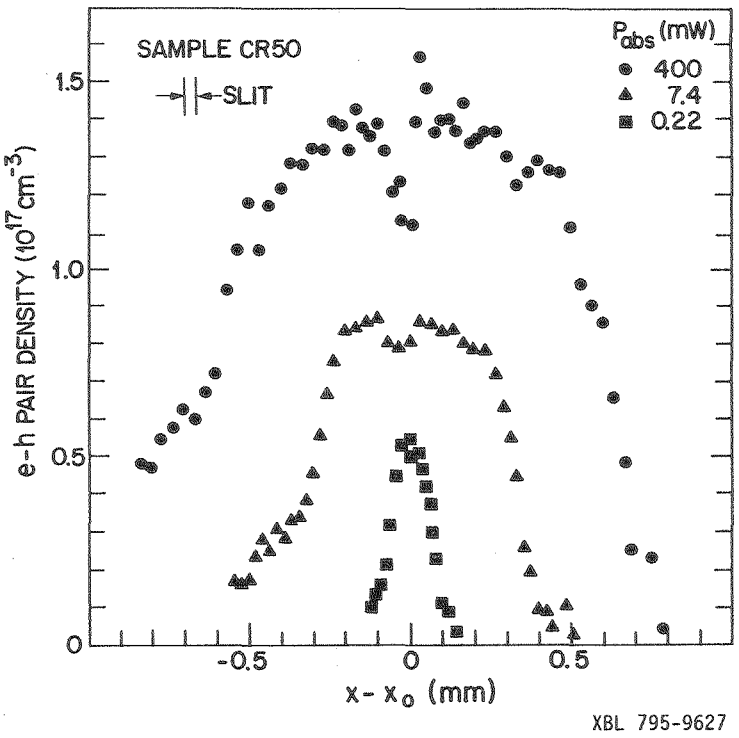

Figure 5.25

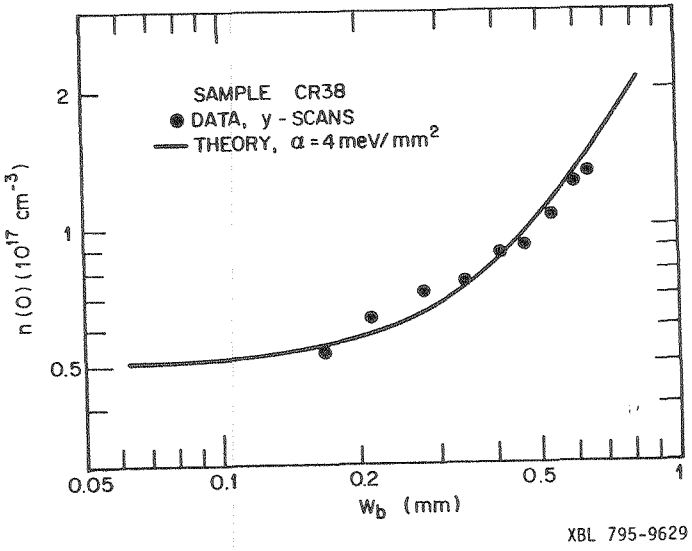

Figure 5.26

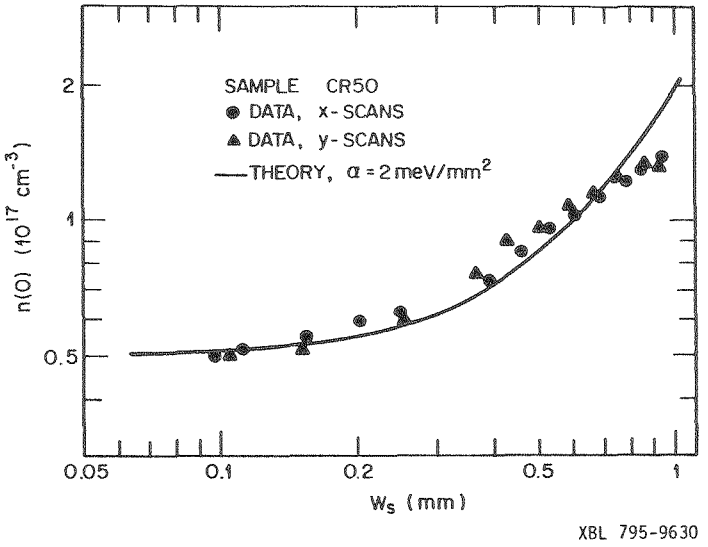

Figure 5.27

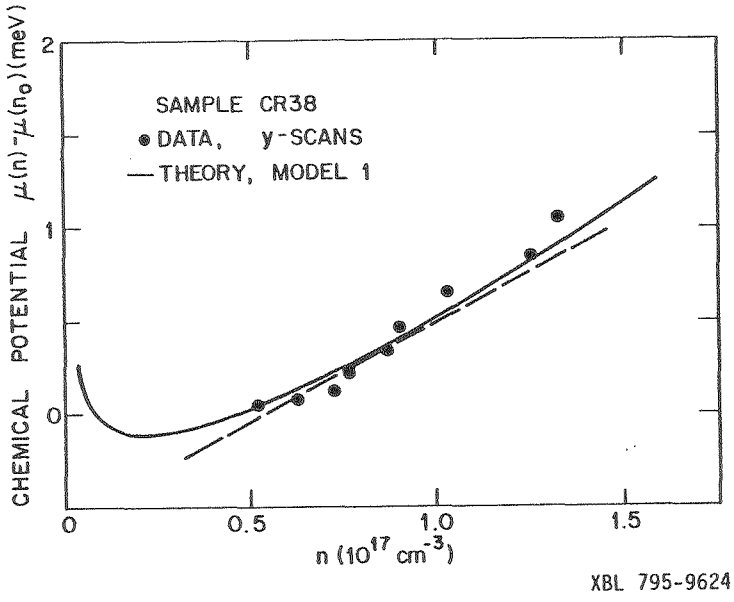
SAMPLE CR38
● DATA, y-SCANS
— THEORY, MODEL 1
CHEMICAL POTENTIAL $\mu(n)-\mu(n_0)$(meV)
n (10^{17} cm^{-3})
0
0.5
1.0
1.5
2
1
0
XBL 795-9624

Figure 5.28

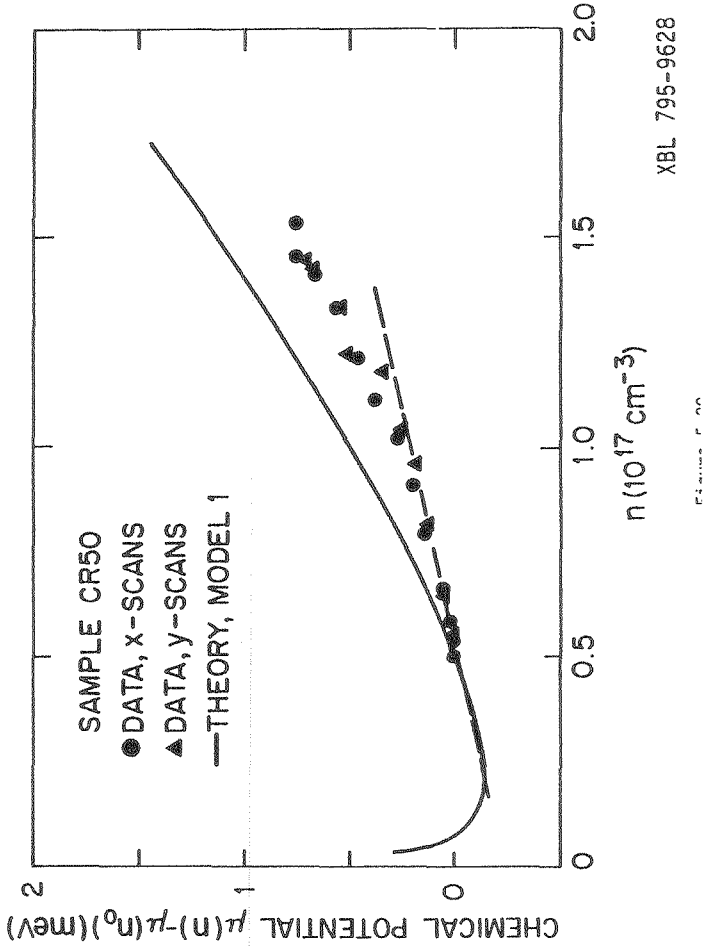
SAMPLE CR50
● DATA, x-SCANS
▲ DATA, y-SCANS
— THEORY, MODEL 1
CHEMICAL POTENTIAL $\mu(n)-\mu(n_0)$(meV)
n (10^{17} cm^{-3})
0
0.5
1.0
1.5
2.0
2
1
0
XBL 795-9628

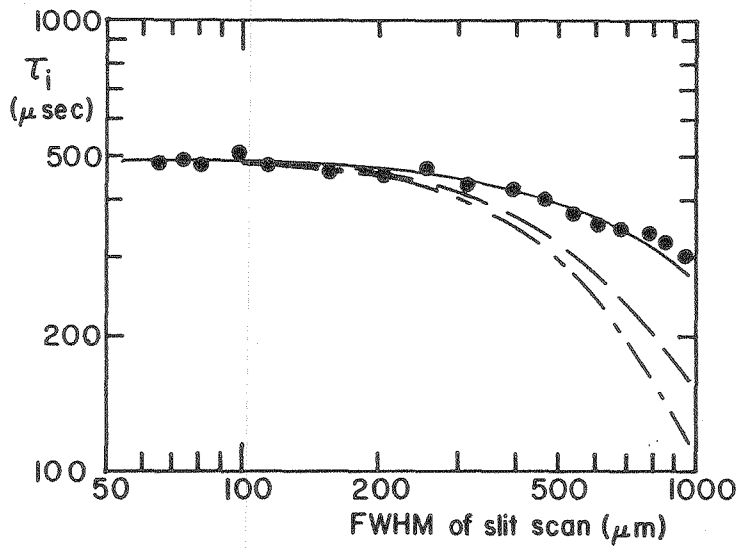

XBL 7812-13244

Figure 5.30

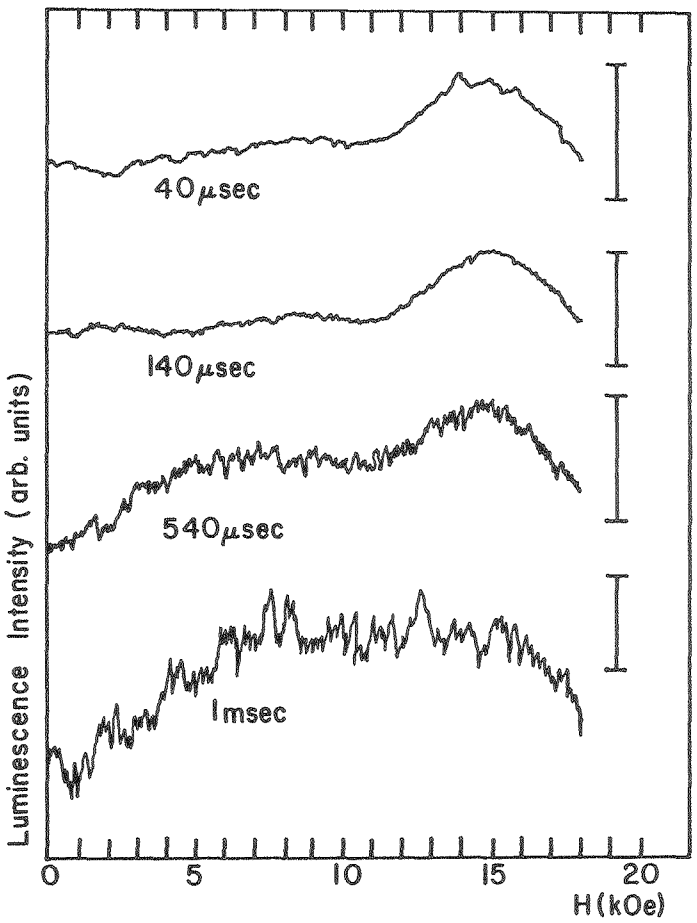

XBL 7812-13245

Figure 5.31

0 0 0 0 5 5 3 0 3 6 4 0

This report was done with support from the Department of Energy. Any conclusions or opinions expressed in this report represent solely those of the author(s) and not necessarily those of The Regents of the University of California, the Lawrence Berkeley Laboratory or the Department of Energy.

Reference to a company or product name does not imply approval or recommendation of the product by the University of California or the U.S. Department of Energy to the exclusion of others that may be suitable.

TECHNICAL INFORMATION DEPARTMENT
LAWRENCE BERKELEY LABORATORY
UNIVERSITY OF CALIFORNIA
BERKELEY, CALIFORNIA 94720